Gas-Sensitive Holographic Sensors

Juan Leonardo Martínez-Hurtado

Department of Chemical Engineering and Biotechnology

University of Cambridge

∼ Girton College ∼

This dissertation is submitted for the degree of

Doctor of Philosophy

September 28, 2012

This dissertation is the result of my own work and includes nothing which is the outcome of work done in collaboration except where specifically indicated in the text.

The document comprises 15 Tables, 111 Figures and 51,887 words, product of research carried out from $October 1, 2008$ to $September 28, 2012$.

<div style="text-align:right">

_____

Juan Leonardo Martínez-Hurtado

</div>

To the ones who forged me Leonardo Martínez, M Lourdes Hurtado, Mónica, Mariana, Pepe and Lulú – my family.

To those who taught me important things and to the ones whom I remember.

Acknowledgements

I would like to thank my supervisor Professor Chris Lowe for the opportunity to pursue a doctoral degree at Cambridge; for his guidance and example on how to develop science in an innovative and competitive world.

I would also like to thank the people in Chris' group for their discussion and valuable comments that have contributed directly or indirectly to the realization of this project. Particularly, to the ones doing holography, it would not have been amusing without them.

Many thanks to the members of the Institute of Biotechnology, the technical and administrative staff for their assistance and for making my time in the labs enjoyable.

Special gratitude to my college friends and colleagues and everyone else I met in Cambridge for their encouragement and support during my time here. Also, to those whose patience and caring helped me throughout my studies.

Abstract

Holographic sensors are photonic layered structures contained in analyte sensitive films that upon illumination produce monochromatic reflections (λ). The present work reports the fabrication of oxygen and ammonia sensors in Nafion membranes and hydrocarbon and volatile organic compound sensors in poly(dimethylsiloxane) (PDMS) films. A holographic recording technique was developed to suit these materials consisting of the *in situ* formation of nanoparticles of $\sim$18nm average diameter and their subsequent ordered ablation with a 300mJ laser. The wavelength of the monochromatic reflections depends principally on the refractive index of the resulting layers (n) and the separation between them (Λ). Changes in these parameters are generated by the analyte-sensor interactions and their magnitude can be correlated to the analyte concentration. The strength of these interactions is determined by the thermodynamic properties of the analytes, such as the cohesive energy density (δ^2), and this, was coupled with a photonic model for the prediction of the holographic response. After exposure to different concentrations of the analytes, the kinetics of the responses were determined and the lowest detection limits (LDL) established as follows: Hydrocarbons in PDMS holograms 1% (v/v) in $\sim$3s for a range of concentrations from 0-100%; ammonia in Nafion holograms 0.16% in $\sim$100s in the 0-12.5% range; the LDL for oxygen sensing could not be determined although the response was recorded down to 12.5% and up to 100% in $\sim$100s. Holographic sensors show competitive responses comparable to commercially available gas sensors for biomedical diagnostics and industrial process monitoring because of their facile fabrication and their shared sensing platform allowing multiplexing.

Contents

List of Figures

List of Tables

Acronyms and Symbols

$dn/d\overline{T}$	Thermo-optic coefficient of the material. 19
E	Young's modulus. 80
E^c	Cohesive energy density. 105
E_π	Pi energy. 178
ϵ	Dielectric constant. 13
ε	Strain. 80
ε_0	The permittivity of free space. 20
ϵ_j	The energy of an orbital j. 178
ε_r	The permittivity of a medium. 20
$\varepsilon(T)$	The temperature dependent permitivity of a medium. 19
η	Tilted optical admittance for the matrix method. 20
E_v	Electron affinity. 178
F	Applied force in the forces diagram. 40
F_i	Molar attraction values for each chemical group in a given molecule. 105
FIB	Focused Ion Beam. 35
g	Gravity constant $9.81 m/s^2$. 40
G_m	Gibbs free energy of mixing. 104
H	Height of the hologram. 79
h	Separation between the layers L_r and L_{r+1} along the x axis. 63
H_m	Enthalpy of mixing. 104
HQ	Hydroquinone. 27, 53
H_v	Heat of vaporization. 105
I	The incident wave amplitude. 21
i	Imaginary unit. 20
I	Analyte-sensor Interactions. 4
I_0	Reflection intensity at the start of the experiment. 157
IDLL	Immediate Danger to Life Limit. 8
I_v	Ionization potential. 178
K	Grating vector perpendicular to the grating fringes. 18
k	Complex part of the refractive index N. 20
k_1	Component of the wave vector for the layer a. 21
κ	Boltzmann's constant. 103
k_2	Component of the wave vector for the layer b. 21

K_{ow}	Octanol-water partition coefficient. 97
L	Number of layers in a hologram of thickness l. 20
l	Thickness of the hologram. 79
L_0	The first layer corresponding to the incident medium. 20
Λ	The distance between the fringes. 18, 23, 32
λ	The wavelength of the light. 23
λ_0	Wavelength at the start of the experiment. 157
Λ_r	Distance between adjacent fringes for layer r. 20
LDL	Lower Detection Limit. 188
L_r	The rth layer. 20
$\bar{m}$	Mass of the objects in the forces diagram. 40
m	Suffix for the variables at the final emerging layer. 20
M	Sensing mechanism. 4
MD	Molecular Dynamics. 45
M_i	Molarity [mol/L]. 172
m_i	Molality [mol/kg]. 172
MR_{calc}	Molar refractivity. 178
μ_0	The relative permeability of free space. 20
μ_β	Dipole moment of the β bond. 178
μ_I	Ionic strength defined as: $\mu_I = 1/2 \sum m_i z_i^2$. 172
μ_r	The relative permeability of a medium. 20
μ_x	Molecular dipole. 178
MW	Molecular weight. 178
N	Average complex refractive index defined as: $N = n - \imath k$. 20
n	Average real refractive index. 18, 23
N_0	Complex refractive index of the incident medium. 20
N_1	Represents the total number of polymer molecules in the Flory-Huggins lattice model. 104
n_1	Refractive index of an alternating layer of material thickness a. 20
N_2	Represents the total number of analyte molecules in the Flory-Huggins lattice model. 104
n_2	Refractive index of an alternating layer of material thickness b. 20
NA	Numerical aperture. 63

N_e	Total number of electrons in a molecule. 178
n_i	Refractive index of the external medium of incidence. 12
n_j	The number of electrons in the jth orbital. 178
N_m	Complex refractive index of the emergent medium. 20
N_r	Complex refractive index of the layer r. 20
n_r	Refractive index of the layer r. 12
n_s	Refractive index of the last layer or substrate. 18
N_t	Total number of molecules. 104
n_{T_0}	The material's refractive index at temperature T_0. 19
ν	Wave frequency. 12
Ω	Number of ways of arranging N molecules in the probability function. 103
ω	Angular frequency of the wave. 21
P	Pressure in the forces diagram. 40
PCA	Principal Component Analysis. 102, 193
PDMS	Poly(dimethylsiloxane). 26, 27, 40, 41, 45–47, 71, 101, 108
PEM	Proton Exchange Membrane. 124, 149
Φ	Diameter of the area in the forces diagram. 40
ϕ	Angle of the grating vector K to a normal of the surface. 18, 30
π	The constant 3.14159(...). 18
q	Total number of layers. 20
R	Total reflectance at the incident point. 20, 23
r	Suffix for the variables at the rth layer. 20
RC	Recognition Component. 4
RH	Relative Humidity. 156
ρ	Density. 178
ϱ	Bond charge. 178
r_q	Coefficient of reflection in the matrix model, $r_q = R/I$. 21
r_{xy}	Pearson's correlation coefficient for the linear fits defined as: $r_{xy} = \frac{N \sum x_i y_i - \sum x_i \sum y_i}{\sqrt{N \sum x_i^2 - (\sum x_i)^2}\sqrt{N \sum y_i^2 - (\sum y_i)^2}}$. 75
r_z	Reflection coefficient based on refractive index differences. 18
S	Measurable signal. 4
§	Section. 32

SEM	Scanning Electron Microscopy. 35, 57
σ	Stress. 80
S_m	Entropy of mixing. 103
SPR	Surface Plasmon Resonance. 66, 127
T	Transducer. 4
T_0	A temperature for which n_{T_0} is measured. 19
τ	Emerging wave amplitude, transmitted wave. 20
τ_A	Polarizability of each atom in a molecule. 178
TE	Transverse electric or s-polarised wave. 20, 21, 73
TEM	Transmission Electron Microscopy. 35, 54
$\overline{T}$	Temperature. 104
θ	Angle of incidence to the normal of the surface, $\theta = \theta_i$. 12
θ_1	Angle of the light refracted on layer a. 21
θ_2	Angle of the light refracted on layer b. 21
θ_B	Angle of incidence to the normal of the surface that satisfies the Bragg condition. 18
ϑ_m	Angle of the emerging wave. 20
θ_r	Angle of refraction to the normal of the surface. 12
ϑ_r	Angle of refracted light at the layer r. 20
ϑ	Angle of incidence to the normal of the grating layers, $\phi - \theta$. 18
ϑ_B	Angle of incidence to the normal of the grating layers that satisfies the Bragg condition, $\vartheta_B = \phi - \theta_B$. 18, 30
THF	Tetrahydrofuran. 27
TM	Transverse magnetic or p-polarised wave. 20, 21, 73
u	Stretching gain length. 80
Υ	Optical admittance of free space. 20
V	Volume of the hologram. 79
V_m	Molar volume. 105
VOC	volatile organic compound. 2, 8, 46, 47, 82, 97, 101, 115, 189
υ_2	Volume fraction of the polymer in Flory-Huggins lattice model. 104
W	Matrix component of the Bloch wave equations. 21
w	Width of the hologram. 79
X	Matrix component of the Bloch wave equations. 21

Introduction

Gaseous substances in the environment play a key role in the chemostasis of many biological processes, from respiration in animals to photosynthesis in plants. Our atmosphere is, in fact, conformed by a mixture of highly concentrated gases like oxygen, nitrogen, carbon dioxide and water vapour; other types of gases are also present in minor quantities. The concentration and abundance of atmospheric gases varies for certain regions and times of the year [1]; for example, ozone and carbon dioxide concentrations in the stratosphere differ from those in other atmospheric layers [2–4]. In fact, with industrialization and increased consumption of gas products for daily use, certain gas molecules accumulate in cities and indoor environments [5].

Numerous human activities including industries, healthcare facilities and homes require a continuous supply of certain gases. For example, methane, propane and butane are commonly used as domestic comburants for cooking and heating or as a fuel for vehicles. Other gases such as ammonia or noble gases are widely used in refrigeration processes. Thus, gases are extensively used, in aerosols, as chemical reactants, in compression systems and scientific instruments, amongst others [6].

Undesired changes in the concentration of gaseous substances can be catastrophic. For example, controlled oxygen atmospheres in plane cabins ensure that the right concentration is delivered to the crew and passengers, since even slight increments or decrements can result in lethal events. Carbon monoxide or carbon dioxide resulting from the combustion of fossil fuels can accidentally accumulate in enclosed environments and thereby endanger individuals. Reactive gases such as oxygen can cause a number of problems when dissolved in water and can drastically affect the fauna and flora in the surroundings. Oxygen's reactivity can affect industrial processes and uncontrolled concentrations impose danger to

1

human health [7]. Industrial gases are often transported and stored in different locations; Thus, leaks are likely to occur, changing the local concentration, and putting operators and economic revenue at risk. Hence, there is a need to avoid these undesirable changes and, moreover, to develop technologies that measure accurate concentrations of gases in the atmosphere. Gas monitoring has also grown in importance in biomedical diagnostics, particularly, in the non-invasive detection of disease via breath analysis [8]. Several studies have pointed out the correlation between the incidence of gas molecules in exhaled breath with certain pathologies and show that it is possible to extract a fingerprint of gases in breath for a non-invasive health diagnosis [9]. Another common use for gases in the biomedical sector is respiration apparatuses that deliver oxygen to patients and require continuous accurate monitoring of concentrations [10].

Thus, not surprisingly, there is a major concern for some toxic or noxious gas molecules and their impact on human wellbeing or industrial processes. For instance, ammonia, oxygen, ozone, hydrogen sulphide, hydrogen, nitrogen oxides, carbon oxides, sulphur oxides, aromatics, hydrocarbons and other volatile organic compounds (VOCs) are often used and considered as potential threats [11, 12]. Volatile compounds have attracted interest as potentially harmful substances to human health as indoor pollutants originating from domestic products such as building or furnishing materials, paints, adhesives and solvents for cleaning, also from road transport and other industrial processes [13].

1.1 Gas sensors

The chemical sensors market for medical, industrial and environmental applications is estimated to be worth £31.6 billion per annum, divided among the key sectors at 66%, 21% and 9% respectively[a]. The sole gas sensors market estimated in £421.1 million in 2005 is expected to reach £586.6 million by the end of 2012 with a 4.9% growth over that period [15]. This figure is for the internal sensing components only, whilst the market for the completed instruments is estimated at £1.5 billion per annum [14–17]. Industrial safety, fire and domestic gas detection are the most profitable sectors with an anual market size of £160 million; gas

---

[a]Percentages of market share from US data only [14].
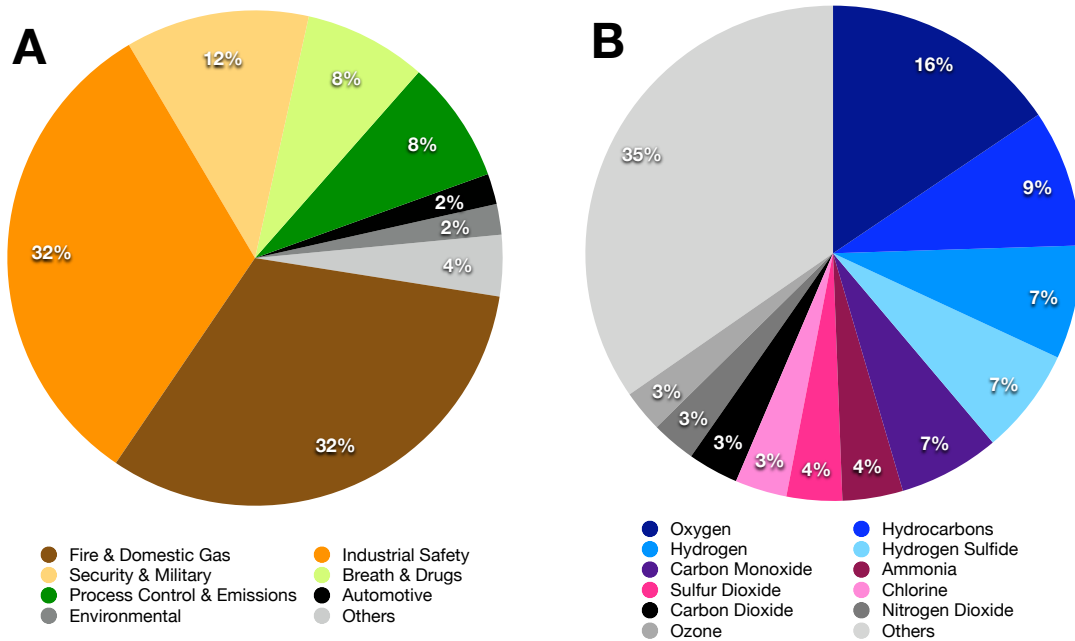
Figure 1.1: Market demand for gas sensors by application and analyte. (A) Market share by gas-sensing applications. (B) Number of available sensors by analyte. Data collected from [18] and [15].

sensors targeting safety and security[a] occupy 76% of the total gas-sensing market (*see* Figure 1.1A) [15].

The gas sensor market distributed by analyte is shown in Figure 1.1B. Data was collected from a global search engine for industrial products from the section 'Gases' in 'Sensors and Transducers' [18]. Only six different analytes account for 50%[b] of the total market, being, in order of importance, O_2, hydrocarbons, H_2, H_2S, CO and NH_3.

1.1.1 Current sensing technologies

Gas sensors vary in type depending on the analyte and the sensing mechanism. The vast majority of sensors use solid state technology or semiconductors because

---

[a]Comprises: fire and domestic, industrial safety and security, and military applications.

[b]The other species accounting for the remaining 50% are SO_2, Cl_2, CO_2, NO_2, O_3, represented in Figure 1.1 A, and AsH_3, Br_2, ClO_2, B_2H_6, F_2, GeH_4, HCl, HCN, HF, H_2Se, Hg, N_xO_x, PH_3, SiH_4, SF_6, and H_2O vapour as others. All data is shown in Table A.1 in the Appendix.

they are easy to fabricate and abundant in the market place. These devices detect changes in the semiconductor component as gas molecules are absorbed, thereby generating an electrical signal that is then converted to a concentration value; examples of these semiconductor components are transistors and capacitors [12,19]. Other technologies involve spectrophotometers, thermometers, potentiometers or electromechanical devices [12]. Table 1.1 shows a comparison of the technologies with the physical phenomena involved. These phenomena, or sensing mechanisms, have different sensing modes depending on the type of analyte-sensor interaction and, according to Yamazoe [12], can be classified as: 'Equilibrium', 'steady state', 'complete reaction' or 'accumulation'. Table 1.2 illustrates examples of physical processes and sensors for each type of sensing mode, together with commercial sensor examples. The 'accumulation' mode is not ideal since it requires the replacement of a sensor once it has been used. They often require special disposal or additional cleaning methodologies. The 'complete reaction' mode has the disadvantage of consuming or chemically modifying the analyte, and it is often not preferred for sensor designs. Regardless of the sensing mode, a generalized version of a sensor can be deduced from these classifications. A sensor configuration that applies to all types contains two elementary components: The recognition component (RC) and the transducer (T) are shown in Figure 1.2. The gaseous analyte (A) interacts with the sensor at the recognition component and generates a change. The nature of this change is known as the sensing mechanism (M) and it is governed by the analyte sensor interactions (I), and in combination, the change is interpreted by the transducer generating a measurable signal (S). Understanding these key factors is paramount for developing new sensors. Once an analyte is known to interact with a recognition component, the sensing platform can be designed, whose success depends on how specific the interactions are, and how strong they correlate with the sensing mechanism; the rest of the sensor construction is solely an engineering challenge. Therefore, designing new sensors relies mostly on understanding the sensing mode, the analyte interactions with the recognition component, and the change observed in the sensing mechanism. Since that is the scope of this work, particular attention will be paid to these factors and to the physical properties of the analytes and materials used in the sensor components.

Table 1.1: Examples of gas-sensing technologies and the sensing mechanisms involved.

Technology	Sensing Mechanism
Semiconductors	Changes in resistance
Piezo-electric crystals, surface resonators	Acoustic interference
UV-Visible-IR Spectrophotometers	Optical absorption
Cantilevers	Stress or mass changes
Electrochemical potentiometers	Electrochemical reactions
Thermometry	Energy of combustion or catalysis

Table 1.2: Sensing modes or analyte-sensor interactions, physical process examples and commercial sensor examples.

Sensing Mode	Physical process example	Commercial sensor example
Equilibrium	Absorption	Humidity
Steady state	Redox reactions	pH
Complete reaction	Combustion	Flammables
Accumulation	Strong binding	Toxics (disposables)
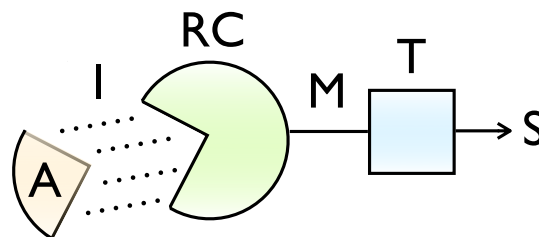
Figure 1.2: Sensor components. A: analyte, I: analyte-sensor interactions, RC: recognition component of the sensor, M: sensing mechanisms, T: transducer, S: readable signal.

1.1.2 A bio-approach to gas sensor design

Accurate technologies require the use of sophisticated and expensive signal processing equipment, electronics and, in some cases, a high degree of operator expertise. These technologies evolve as their components become more accurate, inexpensive or miniaturized, imposing limitations and constraining both innovative gas sensor design and the improvement of current sensors. Mass produced devices inhibit the introduction of new developments to compete in the market [20]. As suggested in reference [21], efforts should be directed at improving materials selection, affinity constants, sensor construction and the exploration of novel sensing mechanisms for the successful production of sensors.

New sensing mechanisms are not easy to discover, although the best examples are posed by nature. There is a wide range of naturally available recognition components selective for most natural molecules. Enzymes, antibodies, binding proteins, membrane receptors, porphyrins and aptamers, specifically bind to their counterpart analyte. This is why biomolecules are often included as recognition components in sensors. Some of these molecules can also be engineered to suit particular binding or sensing applications [22–24], whilst others have been synthetically conceived to mimic naturally occurring structures, or to simulate the spacial configuration and type of interactions present in natural binding structures [25–27]. Moreover, the sensing molecules can be incorporated into nano-scaled constructions, such as modified surfaces, nanowires, conductive polymers and nanoparticles to enhance the binding signals [28–34]. This insight on how molecules selectively bind in natural biochemical processes is also important for innovative gas sensor design. Intermolecular interactions in nature comprise reversible processes in equilibrium or steady state reactions driven by intermolecular forces, namely, coulombic, electrostatic, Van der Waals' and other apolar forces. The nature of the interactions should be taken into consideration to understand and improve the performance of gas sensors.

1.1.3 Target analytes and their detection

As discussed in §1.1, certain gaseous analytes represent key targets for gas sensor design and are commonly used in daily human activities. In general, as the

analytes become important for anthropogenic uses, the sensors that detect and monitor them become also important [35]. This work focuses primarily on three of the most important gaseous analytes: Oxygen, gaseous and volatile hydrocarbons, and ammonia.

1.1.3.1 Oxygen

Gaseous oxygen or dioxygen, O_2, is a reactive gas in its stable molecular from. It is frequently represented as two oxygen atoms bound by two bonds. Oxygen's reactivity as a basic oxidizing agent is related to its unpaired electrons associated with free radical reactions [7, 27]. Oxygen in the atmosphere, nevertheless, is essential to life on Earth and plays an essential role in processes such as respiration, photosynthesis, fermentations and combustion. It is also commonly used in pure or mixed form as a reactant in industrial processes, as a combustion enhancer, and for patient care in hospitals. Food quality, for instance, is ensured by packaging raw materials in low oxygen environments [36].

Oxygen is traditionally measured by redox reactions on electrode surfaces that consume it in the process and are, thus not ideal for some applications [37]. Other methods use fluorescence quenching with dyes, transition metal complexes or oxygen scavenging materials [27, 38–44]; these seem to be a suitable approach for reversibly binding oxygen. Scavenging is a reasonable option only if the analyte is in excess and can be consumed without interfering with the measurement. Metal complexes or dyes, on the other hand, require the use of synthetic molecules that are produced at small scale with complex chemical reactions [27]; moreover, incorporating these molecules into a sensor is challenging and the extraction of a readable signal will depend upon weak interactions. Fluorescent signals can be easily detected from this type of molecules; however, the use of sensitive dyes or fluorescent quenching molecules only works under specific light conditions and requires special fluorimetric instruments [45].

1.1.3.2 Hydrocarbons and volatile organic compounds

Hydrocarbon gases, widely used as combustibles, include alkanes, alkenes and alkynes with a maximum of five carbons in the aliphatic chain. Longer hydrocarbons are considered volatile liquids under atmospheric pressure and temperature.

Butane, propane and methane, for instance, are the main constituents of fuel gas for domestic uses or transportation. Structural isomers and derivatives of hydrocarbons such as alcohols, ketones and other VOCs are also used in many consumer products and are commonly released into the atmosphere. There is growing concern that these products may be imposing a risk to human health in indoor environments [13]. Therefore, measuring hydrocarbon gases and volatiles in the environment is becoming an important consideration for the design of sensors for the gas-sensing markets [19].

Current technologies for real time sensing of hydrocarbon gases and VOCs often classify them non-specifically as flammables or toxics [12]. Other, sensitive techniques, such as gas chromatography coupled with mass spectroscopy or flame ionization detectors, have been hampered by the need for expensive and sophisticated equipment, time and a high degree of operator expertise [46,47]. Although these technologies have proven applicability in many industrial processes, the need for real time sensors capable of distinguishing molecular differences in gases, locally and remotely, is as yet, unfilfilled.

1.1.3.3   Ammonia

Ammonia, NH_3, is a highly reactive gas and the most abundant alkaline constituent of the atmosphere. It is widely used for the production of explosives, fertilizers, resins, nylon and semiconductors, for waste-water treatment plants, and as a refrigerant for industrial processes [48]. Ammonia plays a major role in the soil and atmospheric chemistry, and, in its ionic form NH_4OH, neutralizes atmospheric acids and is a constituent of the aerosol responsible for water vapour nucleation and precipitation [49]. At high concentrations, ammonia may be toxic and caustic to the respiratory tract. Reported values for the Immediate Danger to Life Limit (IDLL) or fatal exposure dose are shown in Figure 1.3, which was assembled from different sources, and shows the limits and risks imposed by high ammonia concentrations [50–52]. The worldwide ammonia emission is estimated as more than 20Tg/year [52].

As in the case of oxygen detection, ammonia is usually measured with potentiometric electrodes that require the consumption or solubilization of the analytes or absorbent semiconductors [52]. Other more sophisticated devices include in-
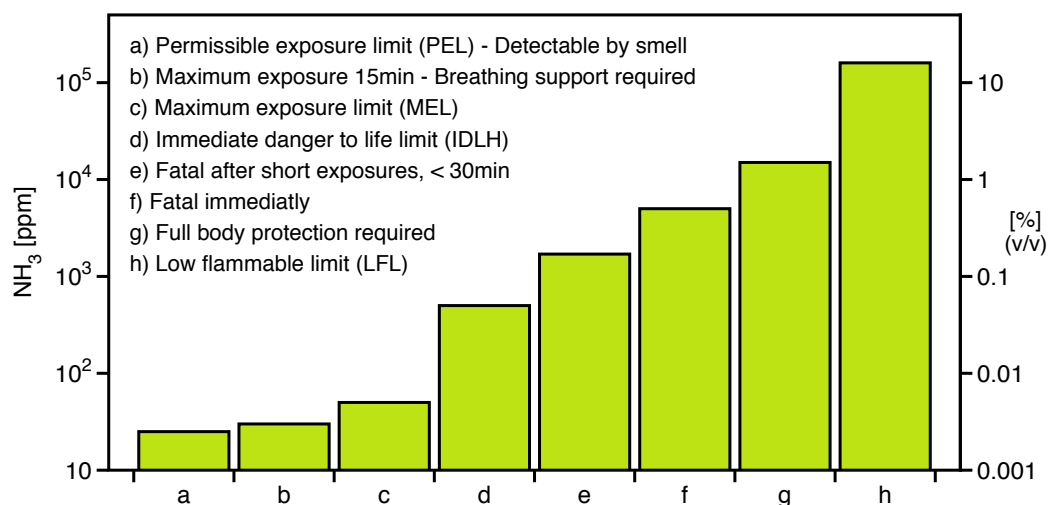
Figure 1.3: Ammonia concentrations in air by threshold limits [50].

frared gas analyzers, mass spectroscopy or gas chromatographs which offer more sensitivity at the cost of expensive and bulky equipment and require trained users to analyze and process the results [53,54]. Ammonia sensors are easily exhausted, requiring substitution after measuring large quantities of ammonia; furthermore, typical ammonia sensors cannot measure high concentrations of ammonia and exhibit a maximum detection limit of 100ppm [55]. Therefore, these sensors are not suitable for high concentration environments where special protection and fast continuous monitoring is required.

1.1.3.4 Other gases

There are other gas molecules that can be detected using most of the techniques mentioned above, although the challenges of producing a selective, sensitive and reversible sensor still remain. Therefore, as discussed in §1.1.2, not only are the intermolecular interactions important, but also their integration into a sensor device that can transform them into strong reliable signals, and their combination into a final product are essential ingredients of an effective gas sensor.

1.1.4 Optical techniques for detection of analyte-sensor interactions

Optical techniques are a popular and effective way of transducing sensor interactions into readable signals [56]. These techniques measure optical properties which include, but are not limited to, absorption spectra, reflectance spectra, luminescence intensity, evanescent waves, surface plasmon resonance and interferometry [56–62]. In order to detect changes in the sensor, optical methods rely on physical changes in the component materials. Such changes include index of refraction or dielectric constant, absorption coefficient, reflectivity, scatter coefficient, photon emission or photon transfer; all of which are caused by the interactions with the analytes.

Optical techniques are usually preferred over others because of their capacity for remote sensing. Although some techniques require proximity to the analyte in order to measure the changes, it is possible to detect optical changes from large distances [63]. Moreover, the visual display of the optical change can be easily observed with the naked eye as a change in coloration, intensity or opacity. There are many technological gadgets that emulate the human vision (*e.g.* digital cameras, photodiodes, spectrometers) and can be used in combination to take accurate readings of optical changes in sensor materials. If these readily available detectors were combined with inexpensive mass-fabricated sensors, the requirement for sophisticated apparatuses would not exist, representing a competitive advantage in the mass-produced electronic sensors market.

Optical gratings, in particular, have been used for gas detection. An optical grating gives colourful reflections visible to the naked eye and can be inexpensively fabricated. There are several examples in the literature that use gratings as sensor transducers: Self-assembly of colloidal crystals in hydrogels; fibre optics with recorded gratings; vapour deposition of layer-by-layer photonic crystals and other gratings produced by nano-fabrication methods [64–69]. The variety of fabrication techniques for optical gratings allows more materials to be used for sensing, thus expanding the sensing potential to several other analytes. However, each technique has its own limitations and new challenges appear: Durability and large scale manufacturing hurdles are yet to be overcome.

Photonic structures have been suggested for gas-sensing but are limited to

light absorption properties of gas molecules in the IR-Visible range of the spectrum [70, 71]. These constructions use the reflected wavelength and intensity of the multilayeres for modulating the signal rather than for sensing [72–74]. Holographic gratings have been used as sensors for analytes in solution but not for gaseous analytes, until now. This work reports the first attempt and successful production of holographic gas sensors.

1.2 Background on holography

The theoretical analysis of the holographic sensors couples physicochemical and optical phenomena. The physicochemical interactions will vary depending on the analyte-sensor types. However, the optical phenomena remain the same regardless of the chemical properties. Understanding the way holograms exhibit colourful reflections is important to exploit their use as sensors.

1.2.1 Light interference with matter

Light traveling through objects, its reflection and refraction, have been studied for centuries and the mathematical formulations describing that physical phenomena have also changed through the progress of Science. Foucault and Fizeau discovered in the 1850s that light waves travel with different frequencies in water [75]. Then, several other studies were conducted, and mathematical models developed, to understand the deviation of light's path when traveling through transparent media. This deviation is called refraction and different materials will give different degrees of deviation, or will have a distinctive index of refraction. From a Euclidean geometry point of view, when light interacts with a transparent medium it will experience linear deformations in its path: Consider a thin film as shown in Figure 1.4, and an incident ray of light ν_i which strikes the surface of the film at an angle θ_i, whence a portion of the light is reflected back and another portion travels through the medium experiencing a change in speed and direction. Some of this penetrating light is transmitted to the other side of the film and some is reflected back by the final film-air interface. Light waves that experience a change in velocity ν_r and angle θ_r when traveling through a medium are called 'refracted'. This refraction phenomena was first described by Snell who
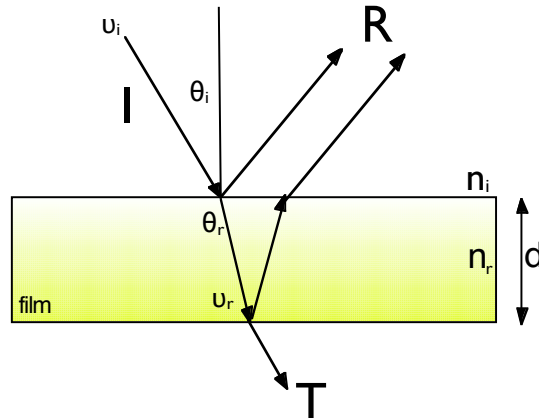
Figure 1.4: Refraction of light when traveling from a medium with refractive index n_i to a medium with refractive index n_r. Example of a thin film with thickness d; incident light is either reflected R or transmitted T.

determined a formula tho show that the ratios of velocity, index of refraction and sine of the angle of incidence are equal for light in two media[a].

When this refraction phenomenon occurs in structures with more than one layer the situation extrapolates, and, if the structure contains periodically ordered layers, an optical effect is observed. In 1887, Rayleigh first studied periodic structures containing alternating layers of material with varying refractive index, realizing that the reflected light is filtered, and only certain wavelengths are allowed to proceed from one layer to the next [76]. This filtering effect is observed only when the periodicity occurs at wavelength scales of hundreds of nanometers and it is referred to as the 'band gap'. This band gap is characteristic of stacks of layers with periodic order in one dimension, appearing to the naked eye as a bright monochromatic reflection. Contemporary to Rayleigh, Maxwell formulated the theory of electromagnetism and light as electromagnetic waves and this helped to understand the transformations of lightwaves when traveling through media. Maxwell used the concept of dielectric constant, related to the refractive index of the material[b], to describe the optical properties of the medium. Optics in periodic structures are well understood nowadays thanks to these formulations.

---

[a]Snell's equations: $n_i \sin \theta_i = n_r \sin \theta_r$, or, $\frac{\sin \theta_i}{\sin \theta_r} = \frac{\nu_i}{\nu_r}$. *see* Figure 1.4.

[b]The dielectric constant ϵ, used in the Maxwell's equations, is the square of the complex refractive index $\epsilon = N^2 = (n + ik)^2$.

The general phenomenon is known as optical interference and when it happens at optical wavelength scales it is termed 'photonic'. The study of these photonic structures has been generalized to include interference effects in 1, 2 or 3 dimensions, and as nanotechnology advances, it is now possible to fabricate complex structures that exhibit the same phenomena in 1D, 2D or 3D. These constructs are known as photonic crystals and exhibit one or more band gaps for different regions of the electromagnetic spectrum [77,78]. The importance of these studies is that the band gap can be calculated, for example, with the use of algorithms that compute solutions to Maxwell's equations for a given structure, thereby giving an accurate mathematical description of the phenomena [79,80].

1.2.2 The origin of holography and standard holographic recording techniques

Parallel to the study of optical interference, the contributions that made holography possible were also developed. 'Holography' is an invented word, conceived by Gabor in 1949 for what he initially called 'wavefront reconstruction' [81]. Gabor developed a theory and mathematical formulae to reconstruct objects, visually, in three dimensions, calling them 'holograms'. The theory explains how it is possible to store three-dimensional information from an object by recording reflected wavefronts.

The proposed theory required that the recorded wavefronts produced layers of varying index of refraction in the recording material. By using wavefronts reflected from an object it is possible to create a field of view recorded within the thin material, resulting in embedded layers separated by hundreds of nanometers. Holograms, in fact, are examples of stacks of ordered layers in one dimension, or 1D photonic crystals, also called Bragg mirrors or Distributed Bragg Reflectors (DBRs)[a] [82].

When the theory of holography was proposed, it was already possible to produce nanoscaled layers of particles with varying optical properties. Lippmann invented a method for recording light waves using silver halide photochemistry,

---

[a]Because at a certain angle the light incurs maximum reflectivity, this is an analogy for the so-called Bragg condition of X-ray diffraction in crystal latices, when waves reflected by different planes interfere constructively a peak in radiation is observed. Similarly, peak wavelengths are observed in holographic reflections (*see* §1.2.3).

further known as the colour photographic method [83–85]. The recording of holograms required, however, the use of monochromatic light for the wavefront reconstruction. Single wavelength light sources were not available at the time and it was only after Einstein's studies on the creation and conversion of light and the stimulated emission of radiation [86, 87], that it was possible to build the first monochromatic light source, the laser [88]. Shortly after this, the first real hologram was produced using Lippmann's silver halide photographic techniques [89, 90]; the result was a monochromatic three-dimensional reconstruction of the recorded objects. Optics for the holographic reflections, angles of reconstruction, the type of light sources and formulation of recording materials have been described theoretically [91]. The recording of holograms is not now limited to silver particle gratings made with silver halide emulsions, since other formulations and photosensitive materials have been subsequently developed.

Traditionally, holographic recording materials are fabricated with silver halide salts in hydrogels which, on exposure to laser light, are photo-reduced to produce metallic nanoparticles [89]. The silver halide salts are used in combination with photosensitizing compounds selected for the specific wavelength of the laser. Photosensitizing the material ensures an even reduction of the silver salts and homogeneous formation of silver grains. The optical set-up to record holograms consists of a laser pointing at a reflective object passing through a transparent recording film. The waves are reflected from the object's surface and interfere with the incident waves forming standing waves with nodes and anti-nodes, as illustrated in Figure 1.5. The total energy accumulated in the nodes and anti-nodes is different, higher energy being concentrated in the nodes than in the anti-nodes [89]. The energy differences in the standing waves are used to photo-reduce the silver salts differentially in the recording material, resulting in a film containing fringes of metallic particles. Although the fringes are spaced by the wavelength of the laser used, there is a smooth transition in the local concentration of metallic silver particles from one layer to the next. The resulting periodic structure produces a bright reflection of colour when illuminated with white light, characteristic of one-dimensional photonic structures.

Photo-reduction processes used in traditional holographic techniques are water based; aqueous solutions are also used to fix and stop the rest of the silver salts from further reduction [92]. Therefore, the hydrogel has to allow water
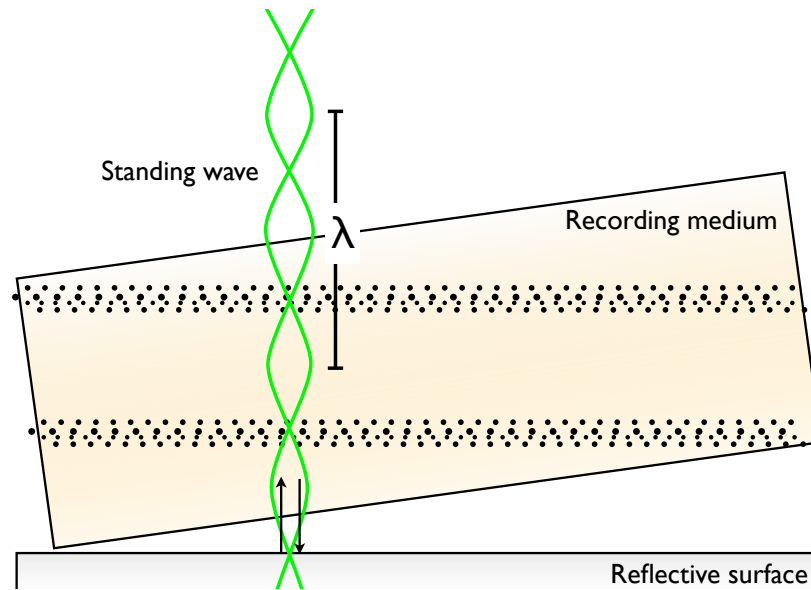
Figure 1.5: Sketch of a typical holographic recording set-up. A recording film is placed between a reflective surface and an incident laser beam, the laser beam is reflected from the reflective surface forming standing waves, the standing waves form nodes and anti-nodes that differentially photo-reduce silver salts, forming fringes of metallic particles. The film is placed at an angle so that the recorded fringes are not parallel to the surface. Drawing not to scale.

penetration at all times, be stable enough both to undergo such transformations, and hold the periodic structure of silver particles. Common holographic film supports are emulsions made with gelatin; however, there are a plethora of other hydrogel-like materials, polymers or plastics that can be used [93–95]. The silver salts that produce the layers are also chosen to suit the properties of the support material, although the production of layers is not limited to silver; metals such as gold, copper, iron, nickel, amongst others can be used to form fringes [96, p. 223] [97–99]. Furthermore, it is not only metals which can give a contrast in refractive index; the degree of cross-linking or polymerization in polymers can also provide this contrast. Other methods to produce a photonic effect that do not require photo-reduction use polymer beads and other nanoparticles [69, 100–102]. In this work, the exploration and use of non-hydrogel-like materials for the production of holograms and methods for the inclusion of silver nano-particles in them are reported.
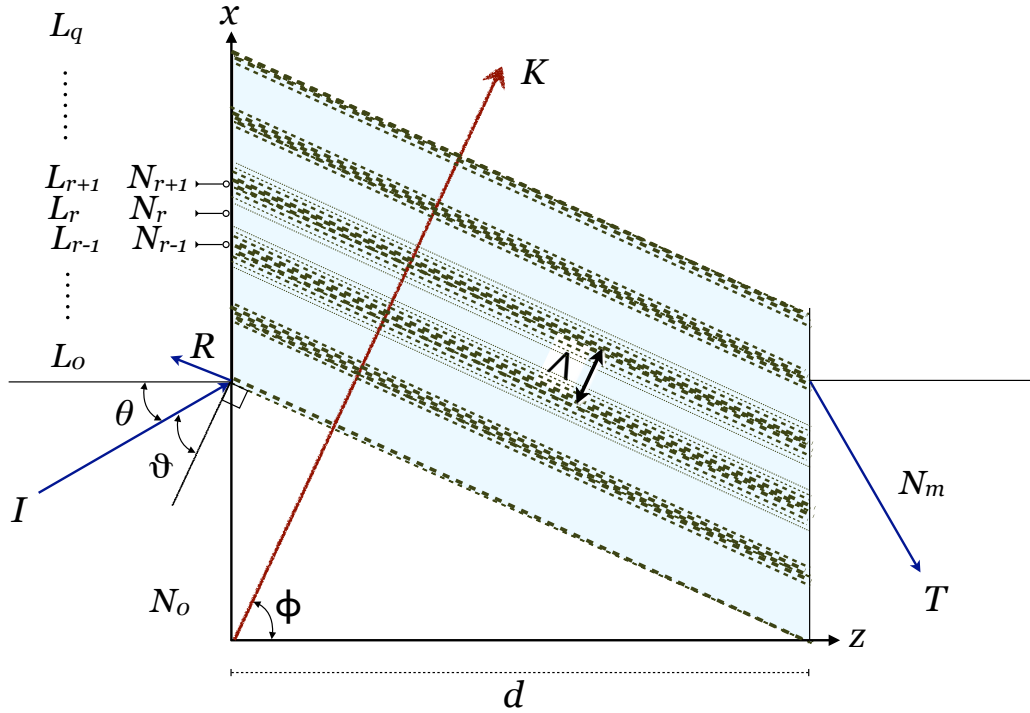
Figure 1.6: Model of a thick hologram grating as proposed by ref [103]. Where thickness is d containing angled fringes and notations for a stack of q layers L with N complex refractive indices, K the grating vector, R the reference wave, τ the emerging wave, Λ the fringe spacing, θ and ϕ are angles with $\vartheta = \phi - \theta$.

1.2.3 Mathematical models for light interference in periodic structures and holographic gratings

As discussed previously, it is possible to model the propagation of light waves through periodic structures and the underlying band gap phenomena caused by constructive interference of the reflecting waves.

Kogelnik [103] proposed the first theoretical analysis for thick hologram gratings using the scalar wave equation of the electric field. The study considers that only coupled waves I and τ are present in the grating as shown in Figure 1.6. As stated in the original paper, this theory is analogous to Phariseau's investigation of acoustic gratings [104] and Bragg's investigation of X-ray diffraction in crystals [103]. The theory utilizes the concept of 'Bragg angle' or 'Bragg condition' which is, in this case, the angle at which an incident wave incurs maximum

reflectivity[a]. Figure 1.6 shows the grating planes perpendicular to the grating periodicity vector K which is inclined at an angle ϕ with respect to the depth of the film d along the z axis. The incident wave I hits the surface at an angle ϑ with respect to the normal of the hologram's surface. The study defines a vector K of length

$$K = 2\pi/\Lambda \tag{1.1}$$

perpendicular to the fringe planes where Λ is the period of the grating or the distance between fringes. An average propagation constant β is introduced, for most wavelengths through the medium, and can be written as

$$\beta = 2\pi n/\lambda \tag{1.2}$$

where n is the average real refractive index and λ the wavelength. At the angle of incidence with maximum reflectivity θ_B, the propagation vectors for the waves equal the propagation constant, resulting in the following expression

$$\cos(\phi - \theta) = K/2\beta \tag{1.3}$$

where θ is, in this case, the Bragg angle θ_B and the difference $\phi - \theta_B = \vartheta_B$. From here, an expression that includes λ as a function of the hologram's intrinsic parameters n, Λ and ϕ can be deduced by combining equations 1.1 and 1.2 into 1.3:

$$\cos(\vartheta_B) = \frac{\lambda}{2n\Lambda} \tag{1.4}$$

or solving for λ,

$$\lambda = 2n\Lambda \cos \vartheta_B \tag{1.5}$$

This equation[b] is often used as a quick reference for the study of the reflected

---

[a]An optical grating is the assumed diffraction element, in analogy with Bragg's theory, and its behaviour is consistent with that of its X-ray counterpart [105].

[b]Sometimes confused with the Bragg's law of diffraction, however mathematically similar, they were deduced for different physical phenomena (*see* footnote a on page 13 and footnote a

wavelength in holographic gratings but has its limitations. Kogelnik's theory assumes fully uniform holographic gratings with sinusoidal fringe patterns; it is inadequate for explaining volume holograms with variations in fringe patterns or local refractive indices. The assumption that the refractive indices, the film surface and the fringe spacing do not change through the media is untrue in some practical cases and this limits its applicability, especially when holographic recording leads to shrinkage and swelling of the layers. The external refractive index on either side of the film is also not taken into consideration. However, this simple expression offers accurate estimates for reflected wavelengths in volume holograms and has been successfully applied in some studies [100]. There are mathematical models that provide extensions to Kogelnik's theory to include variations in the refractive index of the individual layers and outside media [106].

Similarly, there are simple expressions derived for the calculation of reflectivity from stratified media. An expression that calculates the reflection coefficient for wavelengths satisfying the Bragg condition[a] was deduced by Sheppard for a medium with m number of alternating refractive index layers [107]:

$$r_z = \frac{n_i n_2^{2m} - n_s n_1^{2m}}{n_i n_2^{2m} + n_s n_1^{2m}} \tag{1.6}$$

where r_z is the reflection coefficient, n_s the refractive index of the substrate or outermost medium, subindices 1 and 2 denote the values for the alternating layers of material. The refractive index values used in these formulas and from here onwards correspond to the average refractive index for visible wavelengths. Care should be taken when using this values indiscriminately for all types of materials because there is a strong refractive index dependance[b] to wavelength

---

on page 17).

[a]for a quarter of the wave thickness layers, as in the case of holograms.

[b] The refractive index dependance on wavelength can be estimated by the Sellmeier equation: $n(\lambda) = \sqrt{1 + \sum_j \frac{\alpha_j \lambda^2}{\lambda^2 - \beta_j}}$, where α_j and β_j are empirically determined coefficients for each type of material [82, 108]. The temperature dependent refractive index for non-magnetic media is given by $n(\overline{T}) \equiv \sqrt{\varepsilon(\overline{T})} = n_{T_0} + (\overline{T} - T_0)dn/d\overline{T}$, where $\varepsilon(\overline{T})$ is the permittivity of the medium, n_{T_0} is the refractive index of the material at temperature T_0 and $dn/d\overline{T}$ is the thermo-optic coefficient [109]. Mathematical expressions for the refractive index relationship on wavelength and temperature together are not generalized but have been proposed for different materials [110–114].

and temperature [108, 110–113].

The approximations for R and λ just mentioned always seek validation by comparing their results with more general and widely used methods for the analysis of periodic structures. These extended methods directly calculate the reflectance spectrum of multilayer systems by applying a matrix formalism approach to the Maxwell's equations. One of these theories is the matrix method proposed by McLeod [115]; it calculates wave propagation through assemblies of any number of films or layers. As illustrated in Figure 1.6, for a stack of q layers L with varying complex refractive index N and spaced apart by Λ, the electromagnetic wave traveling from the first layer to the q layer can be described by

$$
\begin{bmatrix} B \\ C \end{bmatrix} = \left\{ \prod_{r=1}^{q} \begin{bmatrix} \cos \delta_r & (i \sin \delta_r)/\eta_r \\ i\eta_r \sin \delta_r & \cos \delta_r \end{bmatrix} \right\} \begin{bmatrix} 1 \\ \eta_m \end{bmatrix} \tag{1.7}
$$

where

$$
\delta_r = \frac{2\pi N_r \Lambda_r \cos \vartheta_r}{\lambda} \tag{1.8}
$$

and

$$
\eta_r = \Upsilon N_r \cos \vartheta_r, \quad \eta_m = \Upsilon N_m \cos \vartheta_m \quad \text{(TE)} \tag{1.9}
$$

$$
\eta_r = \Upsilon N_r / \cos \vartheta_r, \quad \eta_m = \Upsilon N_m / \cos \vartheta_m \quad \text{(TM)} \tag{1.10}
$$

where N is the complex refractive index with imaginary part ik:

$$
N = n - ik \tag{1.11}
$$

and B is the normalised electric field amplitude of the wave, C the normalised magnetic field amplitude, Υ the optical admittance[a], $\vartheta = \phi - \theta$ the angle of incidence, the suffix r denotes the values at the layer number r, and m denotes the values at the emergent medium as denoted in the Figure. Equations 1.9 and 1.10 are employed for the transverse electric or s-polarised wave (TE) and the

---

[a]The optical admittance of free space is a constant, $\Upsilon = 1/Z_0 = (\varepsilon_0/\mu_0)^{1/2} = 2.6544 \times 10^{-3} ohms^{-1}$, where Z_0 is the impedance of free space in ohms, ε_0 the permittivity and μ_0 the relative permeability. The refractive index can also be defined in terms of ε and μ as $n = \sqrt{\varepsilon_r \mu_r}$, where ε_r is the permittivity of the medium and μ_r the relative permeability.

transverse magnetic or p-polarised wave (TM).

The total reflectance at the incidence point for a certain wavelength λ is calculated as the ratio of the reflected intensity to the incident intensity at the boundary layer L_0; it will depend upon the number of r layers q and it is defined as

$$R = \left(\frac{\eta_0 - \frac{C}{B}}{\eta_0 + \frac{C}{B}} \right) \left(\frac{\eta_0 - \frac{C}{B}}{\eta_0 + \frac{C}{B}} \right)^{*} \tag{1.12}$$

where the suffix 0 denotes the value at the incidence medium, which in this case can be assumed equal to the value at the emerging medium $\eta_0 = \eta_m$, and $*$ denotes a complex conjugate.

Another method that uses a matrix formalism is proposed in reference [116, p. 165] by Yeh; it models the light interaction using a periodic structure of alternating layers of material with different refractive indices. The layers have thickness a and b with refractive indices n_1 and n_2. Considering the geometry illustrated in Figure 1.6, a and b correspond to alternating layers L_r ($L_{r-2}, L_r, L_r, L_{r+2}, ...$ for a; $L_{r-1}, L_{r+1}, L_{r+3}, ...$ for b), and n_1 and n_2 correspond to alternating refractive indices n_r ($n_{r-2}, n_r, n_r, n_{r+2}, ...$ for n_1; $n_{r-1}, n_{r+1}, n_{r+3}, ...$ for n_2).

This method uses Maxwell's equations in the periodic form known as the Bloch theorem, to which exact solutions can be calculated. The equations written in matrix notation are

$$\begin{pmatrix} I \\ R \end{pmatrix} = \begin{pmatrix} W & X \\ Y & Z \end{pmatrix}^{q} \begin{pmatrix} \tau \\ 0 \end{pmatrix} \tag{1.13}$$

where q is the number of layers, I, R and τ are the amplitudes of the incident and reflected and transmitted waves respectively (*see* Figure 1.6), with

$$W = e^{ik_1 a} \left[\cos k_2 b + \frac{1}{2} i \left(\frac{k_2}{k_1} + \frac{k_1}{k_2} \right) \sin k_2 b \right] \tag{1.14}$$

$$X = e^{-ik_1 a} \left[\frac{1}{2} i \left(\frac{k_2}{k_1} - \frac{k_1}{k_2} \right) \sin k_2 b \right] \tag{1.15}$$

$$Y = e^{ik_1 a} \left[-\frac{1}{2} i \left(\frac{k_2}{k_1} - \frac{k_1}{k_2} \right) \sin k_2 b \right] \tag{1.16}$$

$$Z = e^{-ik_1 a} \left[\cos k_2 b - \frac{1}{2} i \left(\frac{k_2}{k_1} + \frac{k_1}{k_2} \right) \sin k_2 b \right] \tag{1.17}$$

for the transverse electric or s-polarised wave (TE) waves and

$$W_{TM} = e^{ik_1 a} \left[\cos k_2 b + \frac{1}{2} i \left(\frac{n_2^2 k_1}{n_1^2 k_2} + \frac{n_1^2 k_2}{n_2^2 k_1} \right) \sin k_2 b \right] \tag{1.18}$$

$$X_{TM} = e^{-ik_1 a} \left[\frac{1}{2} i \left(\frac{n_2^2 k_1}{n_1^2 k_2} - \frac{n_1^2 k_2}{n_2^2 k_1} \right) \sin k_2 b \right] \tag{1.19}$$

$$Y_{TM} = e^{ik_1 a} \left[-\frac{1}{2} i \left(\frac{n_2^2 k_1}{n_1^2 k_2} - \frac{n_1^2 k_2}{n_2^2 k_1} \right) \sin k_2 b \right] \tag{1.20}$$

$$Z_{TM} = e^{-ik_1 a} \left[\cos k_2 b - \frac{1}{2} i \left(\frac{n_2^2 k_1}{n_1^2 k_2} + \frac{n_1^2 k_2}{n_2^2 k_1} \right) \sin k_2 b \right] \tag{1.21}$$

for the transverse magnetic or p-polarised wave (TM) waves, where k_1 and k_2 are a function of the refractive index of each layer (n_1, n_2) and the resulting angle for each layer (θ_1, θ_2) [78, 116–118][a],

$$k_{1,2} = \left(\frac{n_{1,2} \omega}{c} \right) \cos \theta_{1,2} \tag{1.22}$$

where

$$nw/c = 2\pi/\lambda \tag{1.23}$$

ω is the angular frequency of the wave, and c the speed of light in vacuum $2.99 \times 10^8 \text{ms}^{-1}$. At the incident layer $n=1.00$, whence $\omega/c = 2\pi/\lambda$. θ_1 and θ_2 can be derived using Snell's equations (*see* footnote a on page 12), assuming the incident media to be air with $n = 1.00$,

$$\theta_1 = \sin^{-1} \left(\frac{\theta}{n_1} \right) \tag{1.24}$$

$$\theta_2 = \sin^{-1} \left(\frac{n_1 \sin \theta_1}{n_2} \right) \tag{1.25}$$

where θ is the angle of incidence as depicted in Figure 1.6.

The reflectivity can be calculated in terms of the coefficient of reflection r_q, defined as the ratio of the reflected wave amplitude R to the incident wave am-

---

[a]Yeh p.10, 166; Jackson p.385, 296; Joannopoulos p.31.

plitude I

$$r_q = \frac{R}{I} \tag{1.26}$$

Applying the solutions for the Bloch wave matrix equations above, the reflectivity formula becomes

$$|r_q|^2 = \frac{|Y|^2}{|Y|^2 + \left(\frac{\sin K\Lambda}{\sin qK\Lambda}\right)^2} \tag{1.27}$$

where

$$K\Lambda = cos^{-1}\left[\frac{W+Z}{2}\right] \tag{1.28}$$

as with the previous models, the reflection spectrum is a function of the refractive index pair n_1, n_2, the angle of incidence θ, the number of layers q, and the thicknesses of the layers a and b which in this case $a=b=\Lambda/2$.

Matrix methods have been applied successfully in several experimental studies [119]; however, these methods have important limitations, for example, assuming that the dimensions and the refractive indices of the layers are known. The methods also suggest a manual adjustment of these parameters in order to predict the experimental results. Hence, these assumptions can lead to idealistic situations that require accurate experimental designs for their proper use [79]. Nonetheless, with the correct experimental conditions in place, these methods can be successfully applied to volume holographic gratings.

There are other analytical methods that predict the reflectivity of light in periodic structures, such as fibre optics or waveguides [120, 121]. These methods are derived for those particular experimental designs, thus limiting their applicability. Other methods provide a more general solution for periodic structures in more than one dimension; for example, the one in reference [80] uses a 'quantum mechanics' approach and a vectorial algorithm to compute Maxwell's equations in three dimensions. This method works for arbitrary periodic dielectric structures and can be applied to the particular case of one dimensional photonic crystals[a].

---

[a]Solution available as software MIT Photonic Band Gaps at `http://ab-initio.mit.edu/mpb/`

Recapitulating from the different models above mentioned, the intensity and wavelength of the reflected light in periodic structures depend on three main factors: The geometry of the structure; the angle of observation; and the intrinsic material properties. The material properties give differences in refractive index n affecting the light path and speed and are affected by the chemical nature of the reactants used in fabrication: Metallic nano-particles and type of polymeric film support. The angle of observation, fringe dimensions and spacing Λ are determined by the fabrication methods and experimental set-ups; *i.e.* the wavelength of the recording laser and angle of recording.

1.3 Holographic sensors

A hologram integrates all the components required for a sensor to function. The analogous elements to Figure 1.2 (S, T, M & RC) in a holographic sensor are: λ or R as the signal; the periodic structure as the transducer; changes in Λ or n as the sensing mechanisms; and the film or particles as the recognition components.

Considering that a flat hologram reflects wavelengths (λ) at fixed angles of incidence and observation and this λ is a function of Λ and n (*i.e.* $\lambda = f(n, \Lambda)$). Then, changes in Λ and n will drive the sensor response. This is the sensing principle of a holographic sensor which has been harnessed to produce angle, position and fingerprint sensors by measuring the interference of mechanical forces with the objects [122–124].

Changes in Λ can be originated by expansion or contraction of the support material. This expansion and contraction is caused by the chemical interactions with the analytes. The fringes are made of metallic particles that are unlikely to swell or contract. However, changes in refractive index can be triggered by physicochemical modifications of the fringes or support materials. For instance, metallic particles can undergo chemical transformations that modulate their refractive index upon reduction or oxidation with chemical analytes [125]. The polymers or hydrogels of the support material can also change their optical properties upon interaction with chemical agents or analytes. In summary, the principle of holographic chemical sensing consists in transducing chemical interactions between analytes and hologram materials. The chemical changes ultimately cause

$$\lambda_1 = f(n_1, \Lambda_1, \theta_B)$$

$$\lambda_2 = f(n_2, \Lambda_2, \theta_B)$$
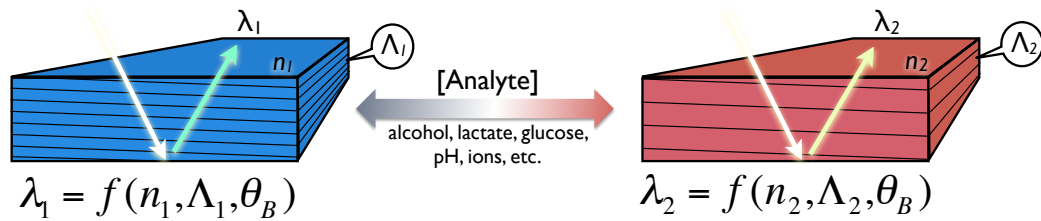
Figure 1.7: Holographic sensing principle. Changes in the optical properties of the materials and hologram geometry are caused by chemical interactions with the analytes or mechanical stimuli. Overall, a change in reflectivity R of the reflected wavelength λ is detected.

a change in the reflectivity or wavelength as illustrated in Figure 1.7. Because of this, the chemistry of the hologram materials plays a key role in the recognition chemical analytes.

Examples of holographic sensors are reported in literature. Holograms recorded in gelatin by traditional methods have been used for sensing proteases, water-solvent mixtures, alcohol content and humidity [94, 126–133]. Also, in aqueous solutions coupled with biomolecules, cells or organisms expand their capabilities and detection ranges [134–138]. Holograms produced in polymer hydrogels, such as acrylate, acrylamide and vinyl alcohol, have been used for holographic sensing of glucose, lactate, toluene, pH and different types of ions by introducing extra functional groups [25, 139–144]. Polymers in general have been explored as potential sensor components due to their flexibility in terms of chemical modifications. Including functional groups in the polymers is a way of enhancing the chemical and physical interactions with the analytes, thereby conferring improved sensitivity and selectivity [145].

The use of hydrogel holographic sensors is limited to aqueous solutions or aqueous environments due to the requirements of the holographic recording techniques. This work explores the fabrication of holograms in non-hydrogel materials for their use in non-aqueous environments or without interference from water.

Aims of the project

The work described in this dissertation aims to:

- Produce holographic sensors for gaseous analytes; preferably, for hydrocarbons, volatile organic compounds, oxygen and ammonia. Holographic gratings will be used as transducers of chemical interactions between hologram materials and gaseous analytes. The resulting changes in the bulk will provide a replay wavelength change readable as a colourful signal.

- Propose holographic recording methodologies for non-conventional holographic recording materials; such materials are polymers that will provide sensitivity to the targeted gas types. The current use of holographic sensors is limited to hydrogels in aqueous solutions or aqueous environments; therefore, the exploration and use of non-hydrogel materials for inclusion of silver nano-particles and recording of holograms will be investigated.

- Understand how changes at the molecular level caused by gas-polymer interactions affect the bulk properties of the holographic films. The concentration and type of gas will be correlated to the strength of the molecular interactions with the sensor components. The resulting changes in the holographic films will be translated to holographic reflection measurements of wavelength and intensity.

Materials and Methods

The sections below describe the materials and methods involved in the design, construction, and testing of the holographic gas sensors. All reactants used were of technical grade purchased from Sigma-Aldrich, UK unless otherwise specified.

3.1 PDMS films for holographic recording

Poly(dimethylsiloxane) (PDMS) films were prepared with the Dow Corning Sylgard 184 kit (from Farnell, UK), the instructions provided by the manufacturer were followed to form thin PDMS films on glass slides. A 10:1 (v/v) ratio of PDMS elastomer and curing agent solution were mixed thoroughly in a weighing boat using a glass rod. The mixture was then deposited onto clean microscope slides (75mm x 25mm) fixed on an even leveled surface. The glass slides were coated with the polymer mixture using a Mayer rod no. 14 to obtain $\sim 32\mu m$ thick films [146, 147]. Finally, the pre-formed unpolymerized films were cured in a preheated oven at 70°C for 2h. Optical microscopy in transverse sections was performed to corroborate thickness. Alternatively, 0.8mm thick PDMS films were prepared by depositing a volume of solution into a flat glass petri dish and cured as previously described. The thickness can be controlled by varying the volume of PDMS.

3.1.1 Nanoparticle formation in PDMS films

Conventional holographic recording techniques cannot be used to record holograms in PDMS because of its immiscibility in aqueous solutions. The silver salts need to be solubilized in hydrophobic solvents compatible with PDMS that cause as much swelling in the elastomer as water does in hydrogels. In this way the sil-

ver salts are transported into the film matrix by diffusion of the solvent solution. There are several solvents that cause the PDMS to swell; for example, xylene, chloroform, pentane, ether, hexane and tetrahydrofuran (THF), with THF causing the fastest swelling [148]. A silver salt that can be dissolved in THF is silver pentafluoropropionate (AgPFP) and a reducing agent that can be used in combination with AgPFP in THF is hydroquinone (HQ); this pair was selected to introduce silver particles into PDMS films. Unfortunately, this type of silver salt is not photosensitive enough and photosensitizing solutions for standard holography will not work for this hydrophobic construct. Therefore, the approach was to first produce the silver particles homogeneously distributed throughout the film, and then reduce their size in an ordered fashion using laser ablation. This was possible because of the high energy laser source available and because it has been demonstrated elsewhere that high energy laser radiation can reduce the size of large silver particles [149–152] (detailed in §3.3).

In situ formation of silver nanoparticles was accomplished as follows: 200μL solutions varying in concentration from 0.01M to 0.4M[a] AgPFP in THF were deposited on top of different cured PDMS slides together with 200μL of a 0.1M solution of reducing agent HQ in THF. The AgPFP and HQ solutions were simultaneously spread and mixed on the surface of the films with the help of a pipette tip. HQ reacts with AgPFP as the solutions diffuse through the film, leaving metallic silver that triggers the formation of metallic nanoparticles as shown in Figure 3.1[b]. Subsequently, the films were dried with a hot air flow at $\sim$50°C for 60s to remove the remnants of solvent. The films were rinsed thoroughly with deionized water and ethanol to remove excess particles on the surface and dried once again with an air flow. Additionally, a 4mm thick sample was prepared for studying the perfusion of the silver nanoparticles in the PDMS matrix; the sample was prepared by depositing 5mL of the elastomer and curing agent mixture into a flat 10mL glass petri dish and cured overnight, subsequently 0.2M AgPFP and 0.1M HQ were deposited on the surface to form nanoparticles as described above.

---

[a]concentrations used [M]: 0.01, 0.05, 0.1, 0.2, 0.3, 0.4
[b]the molecular weight of HQ=110.11 g/mol, of AgPFP=271.90 g/mol
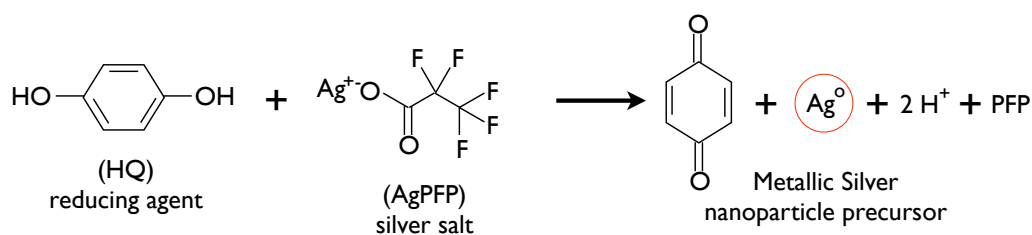
Figure 3.1: Reduction of silver penta-fluoropropionate (AgPFP) with hydroquinone (HQ) in a tetrahydrofuran solution (THF) yielding metallic silver nanoparticles.

3.2 Nafion membranes for holographic recording

Nafion (tetrafluoroethylene-persulphonic acid copolymer) membranes were purchased in sections of 15x15cm from AlfaAesar, UK. Two types with different cation exchange capacities[a] were used: N-117, 0.180mm thick with 0.9meq/g and NE-1035, 0.09mm thick with 1meq/g; designated, henceforth, as low exchange capacity and high exchange capacity respectively (the latter is discontinued from the fabricant).

3.2.1 Nanoparticle formation in Nafion membranes

The cation selective transport through the membrane allows only cations in solution to permeate into the pores. Therefore, it was necessary to develop a novel way of introducing the silver nanoparticles beneath the surface, specifically, for a holographic recording process as described below.

Segments of the membrane (8mm x 22mm approx.) were purified by submerging them into 50mL of constantly stirred concentrated HNO_3 ($\sim$68%) at 45°C for 18h. This step removes organic impurities existing during the manufacturing process [153]. After this, the membranes were washed in 50mL of stirred deionized water at 50°C for 25min. The purified and washed membranes were then transformed to the ionic form[b] Na^+ by soaking the membranes in a 0.25M NaOH

---

[a]CEC, measured in mili-equivalents of protons per gram of membrane (meq/g)

[b]Negative charges of sulphonic groups paired with positive Na^+ ions

Table 3.1: $AgNO_3$ concentration in 0.1M $NaNO_3$ and $[Na^+]:[Ag^+]$ molar ratio.

$AgNO_3$ [M]	0.001	0.004	0.007	0.01	0.025	0.05	0.06
$Na^+ : Ag^+$	1000:1	250:1	142:1	100:1	40:1	20:1	15.5:1
cont...	0.09	0.1	0.14	0.2	0.3	0.4	0.5
	11.1:1	10:1	7.1:1	5:1	3.3:1	2.5:1	2:1

solution for 24h. By transforming the membrane into its ionic form, the sulphonic groups interact in equilibrium with sodium cations and all the ionic clusters are occupied by them. Hence, silver cations can be loaded at a controlled rate by substituting the sodium cations because of their difference in electronegativity.

After being conditioned with NaOH, the membranes were washed in deionized water for 10min, then transformed to the Ag^+ form by immersing them in 0.1M $AgNO_3$ for 30 min. The loading of Ag^+ ions into the membrane is a diffusion mediated process that depends on the concentration gradient provided by silver ions in the surrounding solution and the loading time. It has been shown that a 30min incubation ensures 100% loading of Ag^+ ions (*i.e.* equilibrium) for concentrations higher than 0.02M $AgNO_3$ [154].

To control the Ag^+ content in the membranes from 0% to 100%, it is possible to either change the concentration of $AgNO_3$ for a given time, or to change the contact time with the $AgNO_3$ solution for a given concentration. If the process does not reach equilibrium, the distance that the silver diffuses into the membrane might be different for the given conditions, thus affecting the holographic recording process. In order to reach controlled loading, $AgNO_3$ solutions of various concentrations were equilibrated with a 1.0M $NaNO_3$ solution prior to the Ag^+ loading step. This yielded different concentration ratios of Ag^+ and Na^+ ions as shown in Table 3.1, and helped to find the optimal concentration required for the formation of holographic gratings.

Once the Ag^+ ions were loaded in the membrane, it was necessary to reduce them to metallic silver Ag^0. The cation selective membrane with nano-metric pore sizes cannot be reduced using customary holographic reducing solutions, imposing a challenge for the nanoparticle formation process. Silver can spontaneously photo-reduce after long periods of exposure to light but not in the membrane form Nafion-Ag^+. To accelerate the process, a 0.1M solution of sodium

borohydride $NaBH_4$ was used; the strong reducing properties of $NaBH_4$ reduce Ag^+ ions to Ag^0 forming a layer of BH_4^- ions on the surface that prevents the leakage of Ag^+ ions from inside the membrane [155]. This process allows some $NaBH_4$ to enter the membrane reducing silver beneath the surface to a distance up to $15\mu m$ [155]; this distance is enough to contain a few grating layers of a hologram. The membranes were submerged in the $NaBH_4$ solution and gently agitated to avoid saturation of particles on the surface, then washed with deionized water and wiped with a wet tissue. After the nanoparticle formation the membranes were kept hydrated in deionized water. In addition, it has been shown that the presence of nanoparticles in Nafion membranes does not affect their cation transport properties, the sulphonic groups remain functional to provide ionic exchange and sensing capabilities in the holographic sensor [155].

3.3   Optical grating formation by laser ablation

Contrary to typical holographic recording protocols the previously formed silver particles were ablated to produce a holographic grating using a frequency doubled Nd:YAG (Nd-Yttrium-Aluminum-Garnet) pulsed laser (Quantel, France). It has been proven that high energy laser radiation can reduce the size of metallic particles to nano-metric scales [149–152, 156]. The laser energy output was 300mJ with a 532nm wavelength and a 258 μs Q-switch delay (*i.e.* max. power). The set-up for the recording is shown in Figure 3.2, the nodes of the standing waves provide concentrated energy to ablate the preformed silver particles. In this set-up, the laser beam from the source (A) is diverted using dichroic mirrors (B, C, E) and a spreader lens (D) to finally strike the recording material (H). In order to form the fringes at an observable angle, the recording material was placed at a 7° inclination from a mirror-like surface (G) with the help of a supporting rod (F). The small angle is fixed to a known value for the corresponding angle ϕ shown in Figure 1.6; this allowed a different angle for the reflection of the incident light and the holographic reflections satisfying the Bragg angle ϑ_B. The laser spot was fixed to 1cm in diameter and the assembly of recording material (H), mirror (G) and support (F) were displaced accordingly to ablate the whole surface of the recording material.
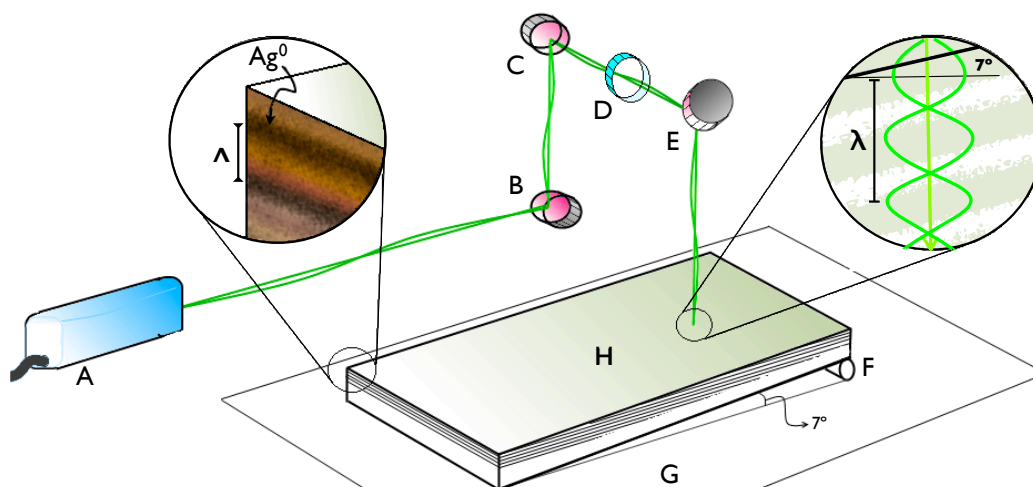
Figure 3.2: Set-up for holographic recording by ablation. A Nd:YAG pulsed laser 'A' produces a laser beam deviated by dichroic mirrors 'B', 'C' and 'E' and a spreader lens 'D'. The beam is reflected by a mirror-like surface 'G' through the recording material 'H' inclined at an angle given by the support 'F'. The nodes of the standing waves concentrate enough energy to ablate the preformed silver particles as sketched; drawings not to scale.

PDMS films containing nanoparticles are flat after being cured on glass slides and were shot twice with the laser at its maximum power immediately after the nanoparticle formation. Nafion membranes on the other hand, present undulated surfaces and are not completely flat with a tendency to curl in free form. The holographic recording process requires the membranes to be flattened down onto a transparent surface for exposure to laser radiation. In order to achieve that, the membranes were dried with a hot air flow ($\sim 50°$C) for 2min and then submerged in an index-matching liquid[a] that facilitates the laser light transmission through the material avoiding reflections that diminish the quality of the recording. The samples were washed with ethanol to remove the index-matching substance and the edges of the membranes were fixed to microscope slides using clear tape (Scotch®, 3M). The use of transparent layers of material during the holographic recording process introduces refractive index differences that affect the path and wavelength of the light, thus altering the final outcome. Once fixed and flattened, the Nafion membranes were also shot twice at the same laser power output. The

---

[a]decalin (decahydronaphthalene) n=1.47-1.48 or mineral spirit n=1.41-1.44

distance from node to node of the standing waves corresponds to half of the wavelength of the laser radiation used, and dictates the distance of the grating period Λ. Contrary to standard holographic techniques the bright fringes were formed where the laser energy is concentrated and the particles ablated; the dark fringes, or the fringes containing particles, were formed in the anti-nodes as depicted in Figure 3.2.

3.3.1 Optimization of Nafion hologram recordings

In further experiments, the recording methodology described in §3.2.1 was optimized for brighter and more responsive holograms by modifying the following steps: Low exchange capacity membranes (Nafion-117) were exposed to 9:1 (v/v) ethanol-water solutions of $AgNO_3$ for 3s and to 1:1 ethanol-water solutions of $NaBH_4$ for 2min; using ethanol increases the swelling and penetration of the solutions [157]. One side of the membrane was blocked by attaching it onto an impermeable surface of tape or ethyl-cyanoacrylate resin prior to the loading of Ag^+ ions; having particles on both sides makes the recording process less effective and surface reflection artifacts might appear due to local reflections between the interfaces when exposed to the laser radiation. The laser spot size was also changed to determine the optimal exposure area that yielded brighter holograms with fewer surface effects. In view of the fact that the heating and cooling systems of the laser were variable, it was more reliable to keep the Q-switch delay constant for a maximum power output fixing it to 258ms. The laser spot changed according to Table 3.2; as shown in Figure 3.3D, the spot was not completely circular due to the angle of the mirrors and lenses; its dimensions are reported in Table 3.2 together with the conditions and orientations used during the recording (Figure 3.3 A-C). The configuration shown in Figure 3.3C is the only one that does not contain boundary layers between the standing waves reflected on the hologram surface and was, therefore, preferred.
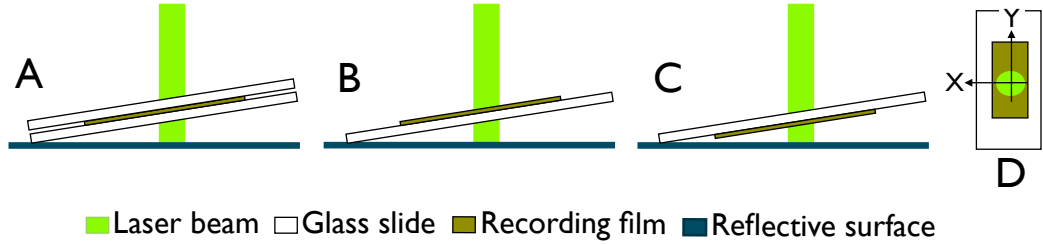
Figure 3.3: Different ablation set-ups and spot size variation. (A) Lateral view of recording film clamped between two glass slides for flatness with silver layer facing laser beam. (B) Lateral view showing the side of the film containing the silver particles facing the laser beam, (C) Lateral view showing the side of the film containing the silver particles facing the reflective surface. (D) Frontal view of the slide and hologram showing the dimensions of the resulting laser spot.

Table 3.2: Spot size variation for Nafion holographic recordings.

Sample	1	2	3	4	5	6	7	8	9	10	11
Index matching	Yes	Yes	Yes	Yes	Yes	Yes	Yes	Yes	Air	Air	Air
No. of shots	1	2	1	1	2	2	2	1	1	2	5+
Configuration	A	A	C	C	C	C	C	C	B	B	C
Y[cm]=	1.2	1.2	1.7	1.8	1.8	2.0	1.7	1.2	1.2	1.2	1.2
X[cm]=	1.4	1.4	1.9	1.9	1.9	2.5	1.9	1.4	1.4	1.4	1.4

*conditions described in §3.3 and configurations A, B, C in Figure 3.3.

3.4 Analytical techniques for understanding grating formation by laser ablation

3.4.1 Refractive index measurements

The refractive index of the films was measured using an ATAGO 4T Abbé refractometer. The samples were placed between two glass windows of the instrument. After calibration, the windows were firmly closed to compress the samples to ensure full contact between the interfaces. An oil-based refractive index matching liquid of n=1.62 (Rayner, UK) was used to ensure there were no air interfaces between the instrument glass and samples; the index of the matching liquid was required to be higher than the sample. Readings were taken using an optical scale with accuracy of ±0.001. The temperature variation was accounted as ±0.003 refractive index units per degree Celsius. The temperature recorded on the refactometer thermocouple was 25.4°C during all measurements.

3.4.2 Absorption spectrometry of ablated and non-ablated membranes

The PDMS and Nafion membranes loaded with nanoparticles were analyzed by UV-visible spectrometry using a Perkin-Elmer Lambda 35 spectrophotometer. Segments of the hologram were fitted in a 1cm cuvette fixed perpendicularly to the spectrophotometer beam path. The cuvette was filled with water to reduce beam mismatch between the interfaces. Absorption spectra were recorded at 240nm/min for wavelengths in the range of 300nm-900nm with a slit aperture of 2nm. The membrane samples were analyzed before and after ablation.

3.4.3 Microscopy

The resulting images were analyzed using image analysis software Fiji[a] [158]. The Fiji software allows to automatically set the scale of the image and measure distances, angles, areas, etc. It also contains scripts for particle size and colour value analysis.

---

[a]a distribution of ImageJ available at `http://fiji.sc`

3.4.3.1   Optical microscopy

Optical microscopy photographs were recorded with a Nikon Digital Sight DS-2MV CCD detector mounted on a Nikon microscope. Surface photographs were taken by placing holograms on the slide holder of the microscope. Transverse sections of the hologram were analyzed by placing the slides or sections of thick holograms at a 90° angle with respect to the microscope slide holder. Slanted view photographs were taken by placing an inclining support under the microscope slide to give a final angle of inclination of 45°.

3.4.3.2   Electron microscopy

Transmission Electron Microscopy (TEM) was performed on a 200kV JEOL 200CX and a FEI Philips CM100 microscopes. The PDMS and Nafion samples were mounted on epoxy resin to produce ~100nm cross sections, and mounted on Cu clip grids for the TEM sample holder. Since the metallic nanoparticles should produce enough contrast on their own, no contrast agents were used on the samples; thin and thick samples were analyzed.

Scanning Electron Microscopy (SEM) of PDMS samples was performed using a JEOL 5800LV SEM equipped with a UTW X-ray detector and back scatter diffraction camera. Segments of the samples (3mm x 0.6mm) were mounted sidewise on an aluminum support and coated with a thin layer of Pt (~100nm) using a electro-sputter; the coating ensures the reflection of electrons from the sample into the back scatter detector. Also, a Zeiss X-beam Focused Ion Beam (FIB) /SEM was used to further analyze the samples; a section of the sample was mounted on a silicon disc on a stainless steel support and coated with a thin layer of gold (~100nm). Milling of the sample with the FIB was executed at low ion current at 50pA in an area of 30μm x 10μm, and observed with 2.0kV electron density. The Fiji software was used for particle size measurements and particle counts.

3.4.3.3   Atomic force microscopy

The PDMS samples were also analyzed using a NanoScope Atomic Force Microscope (AFM) (Digital Instruments, Inc). The samples were used as formed on

the microscope slides, whence the resulting holograms were washed with concentrated ethanol, dried with Nitrogen gas, kept upside down in dust free containers to avoid contact with particles, and finally placed on the AFM sample holder for analysis in scanning mode.

3.5 Holographic signal measurement

The holographic signal measurements were carried out in a dark room with specially designed movable fume extractors. All spectrophotometric measurements were performed in the dark under the fume extractor flow. The results standard error indicated by error bars for the sections below corresponds to the standard deviation (1σ).

3.5.1 Sample preparation for exposure to analytes

For gaseous analytes, the PDMS holograms recorded on to glass slides were sectioned with a diamond pen in 8mm x 25mm portions and fixed inside a 3mL glass cuvette sealed with a flow-through cap. The cap was attached with polyacrylate resin. Nafion holograms were fixed flat onto glass slides during the recording process and the resulting holograms were enclosed in a flow-through chamber specifically designed for flattened samples. The flow-through chamber designs for containing the samples are shown in Figure 3.4; both chambers were tested for leaks before exposure to gaseous analytes by using a continuous air flow.

For liquid analytes, the flow-through cap of the cuvette was removed for testing the interaction of PDMS holograms with liquid substances. In the case of Nafion holograms, it was preferable to fix them on transparent polystyrene 55mm x 14mm petri dishes where the liquids were deposited on top of the samples.

3.5.2 Replay wavelength: Experimental setup

The flow-through cuvette for PDMS samples was mounted in a temperature controlled cuvette holder; the holder allows for the adjustment of the front angle of the hologram to capture the holographic reflection. A lens-terminated torch (E10x12 lamp, 3.7V, 300mA, RS - UK) was used as the white incident light and
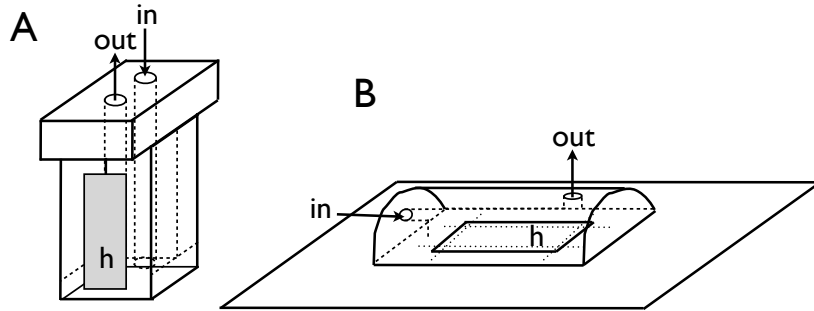
Figure 3.4: Flow-through chamber designs. (A) Vertical configuration in glass cuvette. (B) Horizontal configuration on flat glass. Dashed lines represent internal chambers represented, dotted lines fixing tape and 'h' represents the hologram surface.

a Oriel CCD reflectometer as the collector of changes in reflected wavelength; Figure 3.5A shows the geometry of the set-up. Andor MCD software provided with the spectrophotometer was configured to capture the percentage of holographic reflectance. The spectrophotometer program code was modified to pick the maximum reflectivity peaks for wavelengths in the visible range. Calibration of the instrument was performed by subtracting the background signal with the torch switched off in the dark; a reference signal was acquired with the torch switched on over a hologram surface at a non-satisfying angle (*i.e.* no holographic reflections); finally, the light source and detector were fixed at a $\sim25°$ angle with respect to the normal (ϑ). The Bragg angle was found by adjusting the angles in the cuvette holder. The holographic response of PDMS holograms was measured as a function of time for as long as it took to reach a stable maximum response (*i.e.* equilibrium). The cuvette holder was connected to an automated water bath to regulate or maintain the temperature for the temperature dependence experiments.

The flow-through chamber for Nafion samples was positioned and fixed on a flat-bed fibre optic spectrophotometer Avaspec-ULS2048-SLIT-25-VC (Avantes, UK) with a halogen white light source Avalight-Hal-S (Avantes, UK) shown in Figure 3.5B. The setup was connected to a computer via a USB using spectrum analyzing software AvaSoft 7.2 in reflectance mode and configured to record the peak reflectivity for wavelengths, also in the visible range. The calibration was performed by subtracting the signal over a hologram surface at a non-satisfying

angle, the 'blank'; then, the fibre optic directing the light source was placed at a ~25° angle and adjusted to find the holographic reflections. Since the sample holder does not offer a variable angle, the reflections satisfying the Bragg condition were found by changing the fibre optic positions. The holographic response of Nafion holograms was also measured as a function of time long enough to detect a maximum response at equilibrium.

For both cases PDMS and Nafion, a change in R and λ was expected upon exposure to the analytes as the Bragg angle was kept fixed during the experiments. The molecular analyte-hologram interactions are expected to generate a change in the local Λ and n affecting R and λ values that are measured over time by the spectrophotometer. The peak intensity values and their corresponding wavelength were extracted and plotted against the analyte concentration or physical parameter tested. In the case of a linear dependance, the data was fitted to a linear model for which the correlation coefficient was given by $r_{xy}{}^{a}$.

3.5.3 Proof of concept: Holographic response to stimuli

The holographic signal was recorded from PDMS and Nafion holograms responding to known external stimuli as a positive control and proof of the holographic sensing principles; both types of hologram were tested to prove that it is actually possible to detect a reflected colour change when fringe spacing or refractive indices are changed.

Nafion samples in petri dishes were exposed to deionized water 30s after obtaining a baseline since the refractive index of water differs from that of air and the holographic materials (*i.e.* polysulphonic acid copolymer and metallic silver nanoparticles). Therefore, a change in reflected wavelength and light intensity were expected. This experiment required extra precautions, as changes in the local environmental humidity and temperature could affect the performance of the sensor due to its hydrophilicity. A relative humidity and temperature monitor (Ebro, EBI20-TH, ±0.5°C, ±3%RH) was used to monitor the drying of a pre-wetted hologram: The hologram was wetted with deionized water and wiped-dry with a tissue, then fixed in the monitoring chamber and exposed to a constant

---

[a]The Pearson's correlation coefficient equals $\frac{N\sum x_i y_i - \sum x_i \sum y_i}{\sqrt{N\sum x_i^2 - (\sum x_i)^2}\sqrt{N\sum y_i^2 - (\sum y_i)^2}}$
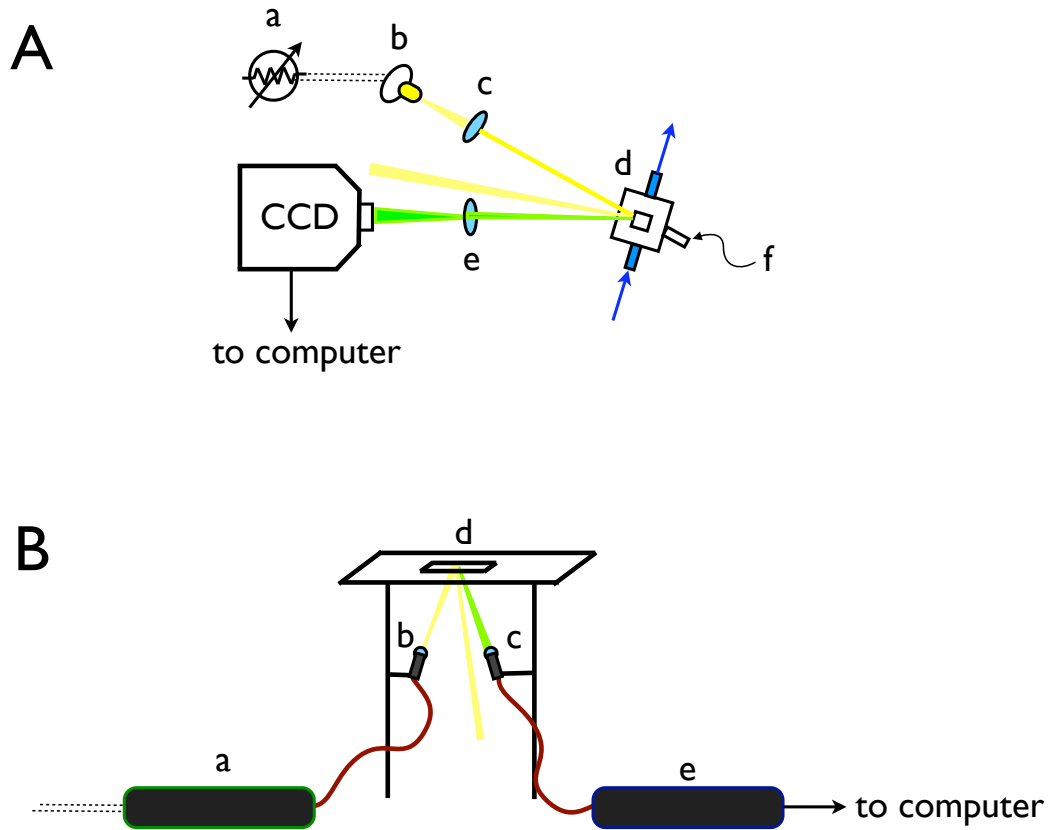
Figure 3.5: Hologram interrogation setup. (A) Top view of vertical cuvette holder setup for PDMS holograms: The variable resistance 'a' controls the light intensity produced by the lens-terminated torch 'b', the light is focused with 'c' on the frontal surface of the hologram inside the cuvette holder 'd', the horizontal and vertical angles are positioned with 'f' to deviate the holographic reflections to the CCD detector through a spreader lens 'e'. (B) Frontal view of horizontal flat-bed setup for Nafion holograms: The halogen light source 'a' directs the light through a lens-terminated fibre optic 'b' to the hologram surface on the flat-bed 'd', the fibre optic heads are adjusted to capture the holographic reflections with 'c' which are detected by the spectrophotometer unit 'e'.

flow of N_2 and O_2 gas for 1min (30mL/s) while recording the temperature and relative humidity at the outlet. The room under climate control was also monitored for 24h to understand possible variations in the local humidity; the temperature and humidity data logger was placed in the centre of the room 3m away from the air conditioning unit.

PDMS, contrary to Nafion, is a hydrophobic elastomeric material; thus, changes in the internal geometry of the contained hologram can be caused by simply stretching or compressing the films. To prove this concept, a large 60mmx80mm PDMS hologram was prepared without Mayer bar coating, the final measured thickness was set to 0.76±0.04mm by pouring a certain volume over a rectangular surface. The hologram was interrogated by stretching and compressing it using the fibre optic AvaSpec spectrophotometer in a vertical position, the fibre optics were separated by a $\sim 20°$ angle and adjusted to match the Bragg angle. The force and pressure applied to the hologram were calculated by using known weights as shown in the force diagrams of Figure 3.6. The hologram was stretched evenly by clamping its extremes to a support and weights respectively, the effective stretched area was 60.1mm x 22.2mm. Additionally, the hologram on a flat bed configuration was compressed by adding different weights over a circular area of 1cm in diameter Φ. Knowing that $F = \bar{m}g$ where F is the applied force, $\bar{m}$ the mass of the weights used and g the gravity constant $9.81 m/s^2$; the changes in reflectivity were related to changes in the geometry caused by the stretching force. Similarly, $P = F/A$ where P is the pressure, F the calculated force and A the area on which that force was applied $A = \pi(\Phi/2)^2$; therefore, changes in reflectivity, in this case, were related to changes in the geometry caused by the compression of the hologram.

3.5.4 Exposure of PDMS holograms to gaseous analytes

High purity n-butane, 1-butene, 1-butyne, iso-butane, propane, propene, propyne, ethane, ethene and ammonia gases used in this work were purchased in lecture bottles (97%-99.5%) from CK-Gases, UK and Intergas Ltd, UK. High purity ethyne ($\geq 99\%$) and stabilized propyne in propadiene (48% propyne, 23% propadiene, 27% propene (v/v)) were obtained from a welding gas kit from MacKay, Camb. UK. Oxygen, nitrogen and carbon dioxide were purchased from BOC
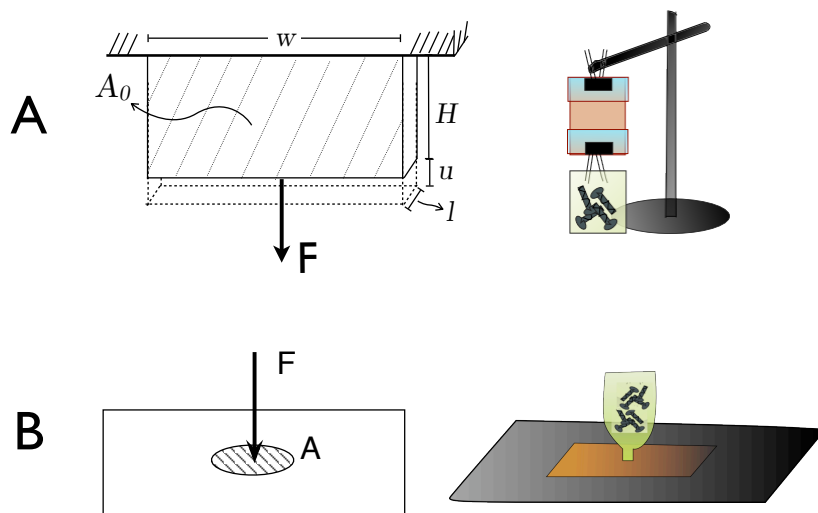
Figure 3.6: Force diagrams and schematic representation of stretched and compressed holograms. (A) Large hologram clamped on its edges evenly stretched in the direction of the force F. (B) The hologram mounted on a transparent support and compressed in the direction of the force F over an area A of 1cm diameter.

Ltd, UK in high purity cylinders ($\geq$99.99%). The concentrations displayed in the results chapters below were volume percentages from the known values of gas in the lecture bottles and atmospheric air, unless otherwise specified.

For testing the performance of PDMS holographic sensors, the gases were pumped into the sealed cuvettes using a 60mL plastic syringe. The gases were collected into a syringe from the lecture bottles using a pressure regulator (4bar) and a valve; the syringe fabricant specifies that for a taken volume V, there is an error of $1\pm0.015V$% [159]. For the following experiments, and given the maximum volume taken of 60mL, an error of $\sim$2% prevails. After establishing a constant baseline for 5s the gases were pumped in the cuvette at 12mL/s for 5s; the signal was collected every second for 30s for the different hydrocarbons. In a similar way, a flow of 6mL/s was pumped into the cuvette and stopped after 10s when the signal reached equilibrium to measure the signal decay, whence, one of the cuvette orifices was opened to the atmosphere removing the syringe connections. Data for the decay signal measurement was collected every 3s for 17 min while the gas diffused out.

For testing the concentration dependence, different hydrocarbon gases were

mixed with air at different volume percentages directly from the lecture bottles. The mixture was pumped in from the containing syringes into the sealed cuvette at 10mL/s until a maximum response was reached, and then, washed with a vigorous airflow. O_2, N_2, CO_2, water vapour and air were measured in the same manner as negative controls; the measurements were repeated for different gas concentrations and a baseline was recorded for 5s prior to exposure.

For proving the repeatability and reversibility of the measurements, the gases were pumped in at 10mL/s and an air flow of the same magnitude was used to clear the gas from the chamber after reaching equilibrium. All the exposure measurements were carried out at 40°C, 22°C and 4°C ($\pm$0.5°C) for each gas and concentration using the self-controlled water bath connected to the metallic cuvette holder with plastic tubing. The water bath flow was left on for 30min to reach equilibrium before the experiments started; the temperature at the hologram surface was measured by inserting a thermometer into the cuvette holder while the reflectance data was recorded.

3.5.5 Exposure of Nafion holograms to gaseous analytes

High exchange capacity Nafion membranes were removed from the deionized water flasks, blotted dry, and mounted on the air-tight chamber for gas exposure. N_2, CO_2 and O_2 (99.9%) were pumped into the chamber after a baseline was recorded for 60s, a flow of 60mL/min (0.5bar relative to atmospheric pressure) was used for 60s. In a second experiment for oxygen gas, the membranes were exposed to the same gas flow for 45s in 4 intervals; after the signal recovered its initial position the cycle was repeated to show the reversibility of the sensor response. The response to ammonia was also tested; the holograms were exposed to 10mL/min flow after a baseline was recorded for 60s; then, the recovery of the response was recorded for 48h until a stable baseline appeared and repeated.

Unfortunately, the high exchange capacity membranes (NE-1035) were no longer supplied by the fabricant, and thus low exchange capacity membranes (N-117) were used for the following experiments. N_2 (99.99%) , NO (99.9%) , CO_2 (99.99%), O_2 (99.99%), a mixture of hydrocarbons (65:35, butane-propane), and 0.19% (v/v) NH_3 were tested on the low exchange capacity membranes under the same conditions detailed for the high exchange capacity membranes above. The

Table 3.3: Blot-dried membranes pre-exposed to a gas flow for testing oxygen dilutions in different gases.

Sample	pre-exposed to	O_2 dilutions
1	water	in Air
2	Air	in Air
3	Air	in N_2
4	N_2	in N_2
5	O_2	in N_2

repeatability for N-117 membranes was tested by exposing them to a 60mL/min gas flow in repeated cycles after obtaining a stable baseline for 20min. These experiments were performed on the flat-bed configuration spectrophotometer at room temperature (23.5±0.5°C). These set of experiments included membranes recorded by the non-optimized method only (*see* end of §3.3.1).

The holograms recorded using the optimized method, also sensitive to water, were exposed to O_2 gas under different controlled conditions: The holograms were blotted dry before fixing them into the air-tight chamber, the holograms were pre-exposed to either water, a flow of air and then left to equilibrate for 72h, a flow of O_2 or a flow of N_2 for 10min, the dilutions of oxygen were made either with atmospheric air or with N_2. Since Nafion membranes are sensitive to humidity, it is necessary to extract the real response to O_2 by discarding a possible false response caused by the gas flow drying the water in the hologram. One sample was wetted with deionized water, the others were pre-exposed to air, oxygen or nitrogen as shown in the Table 3.3. After a baseline was recorded for 60s each sample was exposed to different oxygen concentrations in air or nitrogen as noted in the table. The gaseous mixtures were injected at 1mL/s gas flow during 1min, in completion the flow was stopped and the signal was continuously recorded while a constant maximum signal was reached, indicating equilibrium. This process was repeated three times for the construction of the calibration curves. The integration time in the spectrophotometer for these experiments was 100ms.

These improved Nafion holograms were also exposed to different concentrations of gaseous NH_3 up to 18% (v/v) in air using a 20mL/min flow. The samples were exposed to the gas for 3min while measuring light intensity and wavelength,

the recording was stopped after a maximum response was registered. All the samples exposed to NH_3 were blotted dry and let to rest under room conditions for 18h (23.5°C and 40% RH). To prove the repeatability and reversibility of the sensor response, holographic signals were continuously measured in cycles. Each cycle consisted of: 1min recording of a baseline, 1 min of a 1mL/s flow of 0.19% (v/v) NH_3, and 20 min of the chamber open to the atmosphere. The cycle was repeated four times, continuously recording light intensity and peak wavelengths.

3.5.6 Exposure of PDMS and Nafion holograms to liquid analytes

Exposure of PDMS holograms in liquid substances, such as water, volatile organic compounds or solvents, was performed in the same cuvette configuration. The hologram surface was covered with liquid filling the cuvette cell after the cap was removed; after a 5s baseline was recorded, the signal was continuously measured in 1s intervals until equilibrium was reached.

Nafion samples exposed to liquids were placed in the centre of flat and transparent petri dishes. First, the holograms were fully covered with 5mL deionized water until the signal reached equilibrium; then a baseline was recorded for 60s. Salt solutions of 1.0M NaCl, 0.5M NH_4Cl and 1M NH_4OH were tested by injecting 1mL into the deionized water using an accurate glass syringe ($\pm 10\mu L$). The signal recovery time varied for the three different salts. When the signal was stable, another milliliter was added to the solution; this was repeated 6 times or until no change was detected. In addition, a control experiment consisted on injecting 1mL of water to the initial 5mL and continuously recording.

3.5.7 Temperature dependence

The temperature on the surface of the PDMS holograms was controlled with an automatic water bath connected to the cuvette holder. A thermometer was inserted to acquire the temperature values at the hologram's surface. The cuvette was cooled and heated in repeated cycles for temperature ranges from 12°C to 63°C. In the case of Nafion holograms, the flat-bed spectrophotometer was heated up using a hot air flow. The temperature was measured by attaching a

thermometer to the top surface of the hologram from 24°C to 90°C.

3.6 Molecular modeling

As mentioned earlier, the interaction between sensor components and analytes can be indirectly measured by quantifying the holographic reflections. There are limited experimental techniques to measure intermolecular forces directly, and thus there is a motivation for simulating them at a molecular level. Atomistic simulation of Molecular Dynamics (MD) helps to comprehend the influence of the molecular structure properties in the bulk polymer. MD models have been successfully applied and validated for solvent mixtures in PDMS membranes, for hybrid polymer membranes containing inorganic compounds or nanoparticles and for structural analysis of persulphonic acid membranes in fuel cells [160–164]. In this work, MD simulations were used for the reconstruction of polymer molecular structures in the holographic films. The simulations were carried on using 'Materials Studio' software, Newton energy minimization methods [165] and COMPASS[a] force fields [166].

PDMS membrane simulations required building a cubic cell of the cross-linked PDMS matrix as follows: First, prepolymer and cross linker chains consisting of 17 $[-Si(CH_3)_2 - O-]$ units were built atom by atom (*see* §4.1.1); then, one cross-linker was attached to 4 evenly separated prepolymer units and mixed with 10 free prepolymer units; the resulting cross-linked PDMS chains were packed into a cubic cell of $(47\text{Å})^3$; finally, molecular dynamics were applied to the atomistic model with a 5000-step energy minimization and cut-off distances of 9.5Å. The PDMS cell was used to calculate the sorption of different gas molecules; this simulation used 45000 equilibration steps. In order to find the sorption sites for the analytes in the PDMS matrix, the calculation included electrostatic and Van der Waals' potential energies.

---

[a]Condensed-phase Optimized Molecular Potentials for Atomistic Simulation Studies

Holographic Sensors for Hydrocarbons and VOCs

4.1 Materials selection

Hydrocarbons and VOCs have aliphatic chains that interact with themselves via hydrophobic interactions. These interactions are known as Van der Waals' or London dispersion forces and are caused by differences in electronegativity of the neighbouring atoms in the carbon chains [167]. These differences generate induced dipoles that attract the molecules together. Hydrophobic interactions are ideal to trigger sensing mechanisms because they are reversible and governed by equilibrium processes. Thus, the design of holographic sensors for VOCs and hydrocarbons focused on using these interactions.

The recognition component of the sensor had to be able to form reversible hydrophobic interactions with the analytes, *i.e.* it also has to be hydrophobic. This material not only had to be compatible with the analyte but also comply with the holographic recording process. In other words, the material had to be hydrophobic, optically transparent and light sensitive for recording the laser wavefronts.

There are several hydrophobic transparent materials, most of which are plastics [168]. However, not all of them remain unmodified upon interaction with VOCs. For example, in a test experiment, dissolution or deformation occurred with polystyrene and prolypropylene. A cross-linked and elastic material that does not dissolve or deform was a preferred matrix. A readily available material that complied with these characteristics is poly(dimethylsiloxane) (PDMS). This silicon elastomer is optically transparent and hydrophobic, and therefore ideal for the construction of holographic sensors [146].

4.1.1 Poly(dimethylsiloxane) (PDMS)

The polymer formulation consisted of a prepolymer and a cross-linker solution containing a platinum-based catalyst. The prepolymer and cross linker reacts to form entangled polymer chains, as depicted in Figure 4.1. The PDMS formulation used was Sylgrad 184 with molecular weight of $55000g/mol$, viscosity of $5150cp$, 16-18 monomer[a] units for the prepolymer, and 8-9 for the cross linker [146, 169–171]. Taking into consideration the molecular weight of the monomer, the mass of a single strand was calculated to be $1119.6g/mol$. Cross-linked PDMS is optically transparent, inert, thermally stable, has low permeability to water, and high permeability to atmospheric gases [146, 171]. These properties, combined with the fact that it is a hydrophobic material, make it an ideal construction material for hydrocarbon-VOCs sensors. PDMS is, however, not sensitive to laser radiation, and thus light sensitivity has to be introduced with external agents. Traditionally, light sensitivity is introduced in hydrogels by soaking them in solutions of silver salts. However, aqueous solutions do not interact or mix with hydrophobic materials; hence, an alternative method was needed. The process of introducing light sensitivity was engineered for hydrophobic environments as described in §3.1.1 and the results are in §4.2.

4.2 Film formation and nanoparticle perfusion in PDMS films for holographic recording

First, it was necessary to form flat films on glass slides with a uniform thickness. The Mayer bar used for coating the samples on glass slides yielded thickness of $\sim23.7\pm0.6\mu m$ and not the nominal thickness $32\mu m$; this due, perhaps to the viscosity of PDMS or the cross-linking. However, the thickness was maintained homogeneous as confirmed by optical microscopy in transverse sections of 4 samples. Figure 4.2A shows a transverse cross cut of the sample showing the glass slide, the polymer layer and the air interface. Figure 4.2B shows the measured thickness; it was obtained using the Fiji image analysis software by measuring the distance with contrast in grey values.

---

[a]$-Si(CH_3)_2O-$
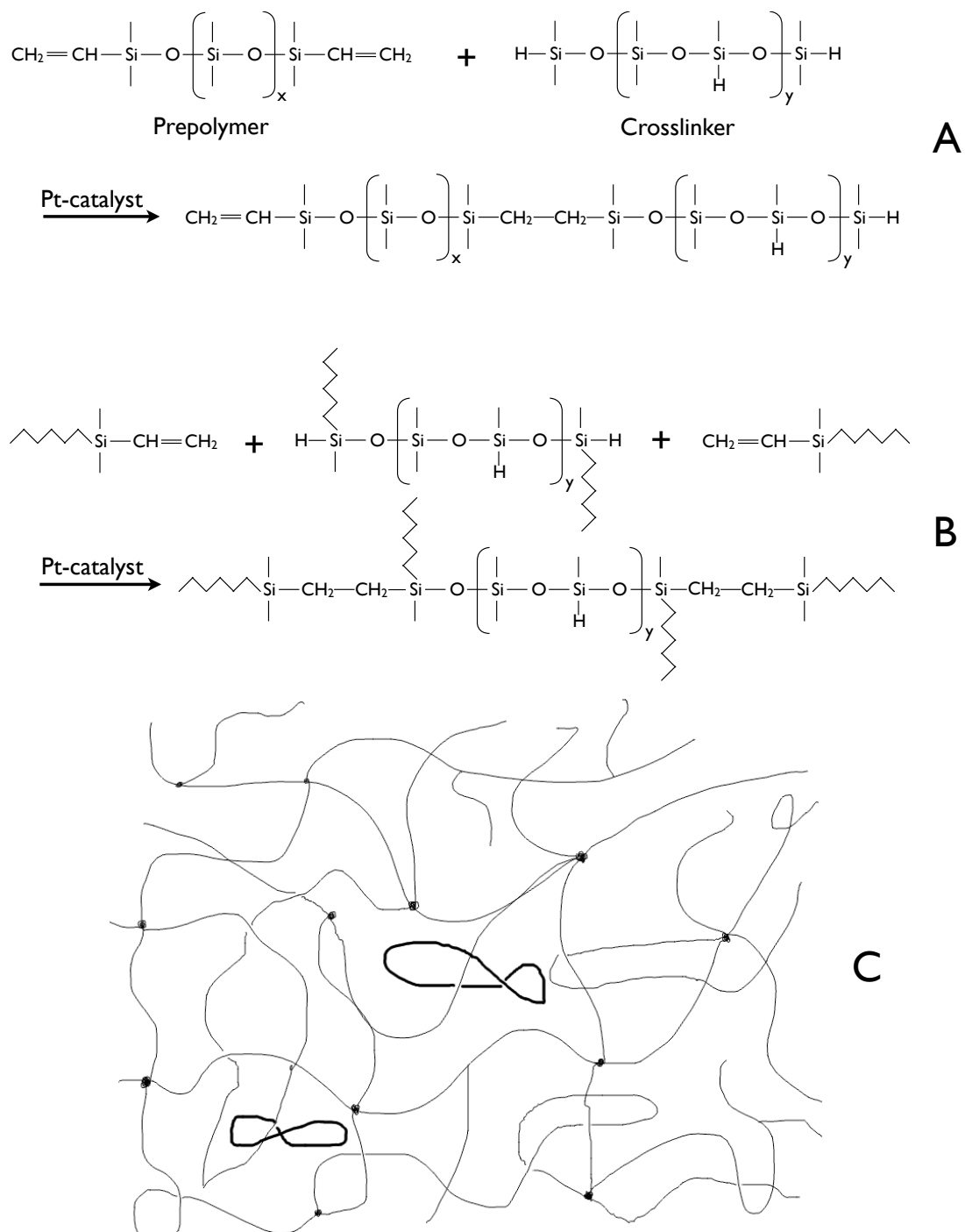
Figure 4.1: PDMS cross-linking reaction and resulting polymer matrix of entangled chains. (A) Primary reaction $x = 16 - 18$, $y = 8 - 9$. (B) Subsequent reactions. (C) Sketch of entangled chains from multiple cross-linking [169, 170]

.
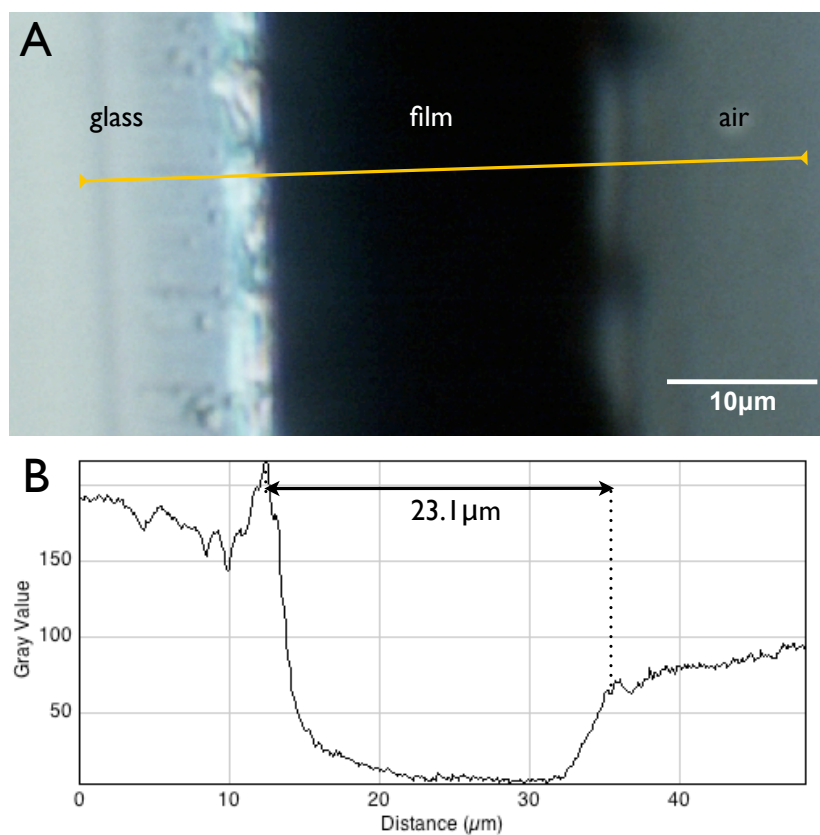
Figure 4.2: Holographic thickness measurement. (A) Optical microscopy image of a transverse section of a PDMS film on glass slide; the yellow line indicates the position of the measurement in B. (B) Thickness measurement using grey scale contrast values; the graph was generated by the image analysis software and the distance was taken from the peaks of the grey value changes.

THF was used for preparation of the silver salt and reducing agent solutions. This solvent is known to cause significant swelling in PDMS membranes which is necessary for improved perfusion [148]. By spreading the solutions on the surface of the films, the silver salt and the reducing agent react as they perfuse in. The solutions travelled through the films reacting and forming silver nanoparticles; it is known that this process commences with the formation of nucleation sites around which the nanoparticles grow [172]. After the solvent evaporated completely, the diffusion of the nanoparticles in formation, and the swelling of the polymer ceased. After washing the films to remove excess silver, they appeared as brown or green semi-translucent films. This coloration is indicative of the formation of metallic silver nanoparticles (<100nm in diameter) [173].

The diffusion process limits the homogeneity of the concentration of particles through the film. There is a gradient concentration that decreases with increasing distance beneath the surface. Figure 4.3 shows a micrograph of a thick film used to study this particular limitation. As noticed, there is a higher concentration of particles near the surface than deeper inside the polymer. However, there is a region near the surface where the concentration remains more or less constant for a depth of $\sim 20\mu$ (*see* Figure 4.3B). The 24μm thick films used for the recording of holograms are within this reasonably uniform region.

4.3 Grating formation in PDMS films by ablation

It was found that concentrations between 0.1M and 0.2M AgPFP were suitable for holographic recordings. The 0.1M AgPFP solution yielded a hologram not as bright as the one of the 0.2M AgPFP solution. Concentrations lower than 0.1M produced fewer nanoparticles, and hence the contrast in refractive indices was insufficient to produce a hologram. On the other hand, concentrations higher than 0.2M were too concentrated to permit the laser light to pass trough and form the fringes. Therefore, the optimum concentration chosen for the subsequent recordings was 0.2M AgPFP.

Figure 4.4 shows a PDMS hologram after ablation. The typical holographic green reflection can be seen when placed at the correct angle of incidence. Af-
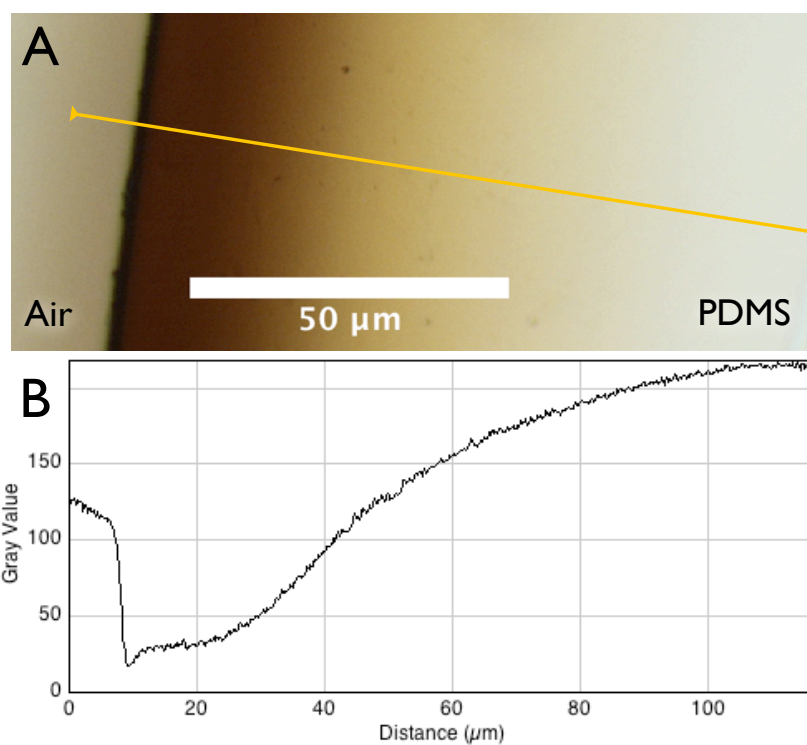
Figure 4.3: Micrograph of a thick PDMS film after *in situ* formation of silver nanoparticles. (A) Transverse cut of the film showing the distribution of silver particles as a gradient which appears homogeneous ∼20μm beneath the surface; yellow line indicates the position of the measurement in B. (B) Grey values showing the diffusion profile of the silver salts through the film.
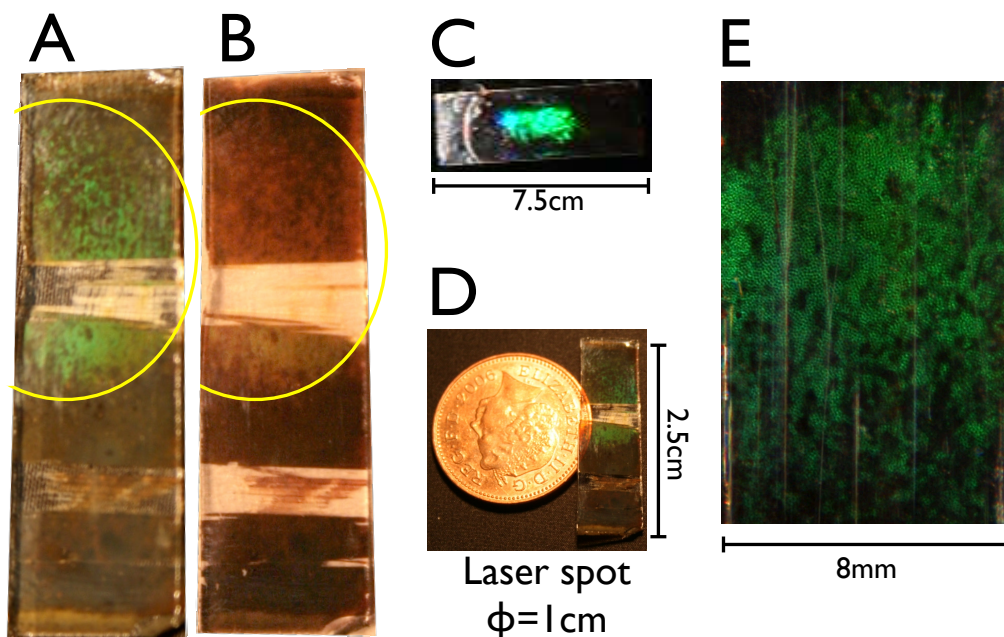
Figure 4.4: Photographs of holographic reflections and ablation spot area. (A) Portion of a hologram showing the ablation area at the Bragg angle of incidence. (B) Same hologram as A at a non-satisfying angle. (C) Full slide before sectioning; only a spot reflection is seen because the illumination source was a spot-light. (D) Size comparison of the ablation spot. (E) Magnification of the hologram's surface showing the ablated region and holographic reflection; $\lambda \approx 540$nm.

ter ablation, the translucency of the samples increased and showed patches of the randomly ablated particles. This uneven ablation pattern is perhaps caused by a broad distribution of particle sizes; suggesting that only certain particle sizes were ablated. Another plausible explanation is that the polymer film was substantially cross-linked in those areas, and thus there were restrictions on the growth or nucleation of the nanoparticles. Only a few nanoseconds of laser exposure were required to form a bright grating. Therefore, the possibility of rapid mass-producible holographic sensors is a significant advantage for holographic sensors of this type.

It was observed that the films comprising a homogeneous flat surface formed brighter holograms, since a flat surface generates less random reflection and refraction, and therefore increases the uniformity and definition of the fringes. Well defined fringes are paramount for the brightness and quality of holograms [174].

Nevertheless, the final outcome of the laser recording also depends on the optical set up, the laser quality, the efficiency of lenses and mirrors, and the efficiency of the ablation process *per se*. The ablation of particles inside the holographic film changes the homogeneity of the nanoparticles, and therefore determines its quality and brightness [175]. All the factors mentioned above impose limitations on the hologram quality, and thus the use of laser-based holography might not be the optimum procedure for recording photonic gratings. Other grating fabrication techniques such as controlled layer-by-layer assemblies or deposition could help to optimize the brightness [176, 177]. Notwithstanding these issues, the holographic fabrication by ablation gives sufficient brightness to produce sensors.

In contrast to traditional holography, the fringes in the ablated holograms were generated in the nodes of the standing waves. However, this geometry might not be the one expected for a given laser wavelength. As light travels through the material, it experiences transformations in the path due to differences in refractive index. During the recording process the wavelength, direction and matching of the standing waves are affected by the refractive index of the PDMS films and silver nanoparticles. These changes are taken into account in the equations given in §1.2.3.

The ablation of particles with high energy pulsed lasers has been applied for the first time to silver nanoparticles in PDMS films. Therefore, comparable refractive index data is scarce. However, it is possible to estimate the content of silver per PDMS slide knowing the salt concentrations, the density of metallic silver (10.49g/mL) and the final volume of PDMS per slide (56μL). The stoichiometry of the silver reduction reaction is shown in Figure 3.1; HQ is the limiting reactant (0.1M) and AgPFP (0.2M) is in excess. Assuming that the reaction is 100% complete for the limiting reactant, the maximum amount of metallic silver is 5.43mg per slide. This mass corresponds to 0.009% in volume of silver nanoparticles in the PDMS polymer. However, considering that the reaction is unlikely to be 100% complete, that not all the reduced silver formed nanoparticles, and that most of the silver was cleared from the surface, then the fraction of silver that is retained could be orders of magnitude lower. Thus, one of the limitations of this hologram making methodology is the limited amount of silver available to form fringes. Fringes with a few particles have a lower refractive index contrast, and therefore limited brightness.

Commercially available emulsions for the brightest high-resolution holograms contain 20-30g/L of silver [178]. Optimum concentrations of 1.1 g/m^2 in 10μm thick films have been reported [178]; these values comprise 10.48mL/L or 0.01% (v/v). Therefore, if most of the silver is transformed and retained in the PDMS, and the particles are homogeneously sized and distributed, then PDMS holograms by ablation can be as bright as the optimized commercial ones.

4.4 Analytical techniques for studying of PDMS holographic films

In order to understand the fringe formation process, cross sections of the samples were analyzed using different microscopy techniques. Image analysis of the film micrographs also provided fruitful insights into the fringes.

4.4.1 Transmission electron microscopy

TEM imaging with the PDMS films is problematic. PDMS is a soft elastic material that can be easily deformed due to local degrees of cross-linking. The microscope electron beam can break these bonds and thereby degrade the polymer. After processing the samples for TEM, it was found that the polymer with nanoparticles absorbed electrons from the electron beam: The polymer became 'charged' and showed signs of degradation; thus, it was not possible to observe a definitive structure.

Figure 4.5 shows different samples before and after ablation. Thin 200nm cross sections were cut and embedded in epoxy resin. The thin samples curled and bent because of the PDMS elasticity and electron beam power. The epoxy resin also contains solvents that could have made the PDMS films swell and deform. In consequence, it was difficult to observe fringes, although the nanoparticles were detected and measured in several regions of the films. One solution to the charging and degradation issues could be to reduce the voltage of the electron beam. It has been shown that polymer samples can be imaged in detail at low voltage in ultra-thin samples [179]. However, the elasticity of the PDMS film does not allow thin samples to maintain their shape. Therefore, the preparation of a
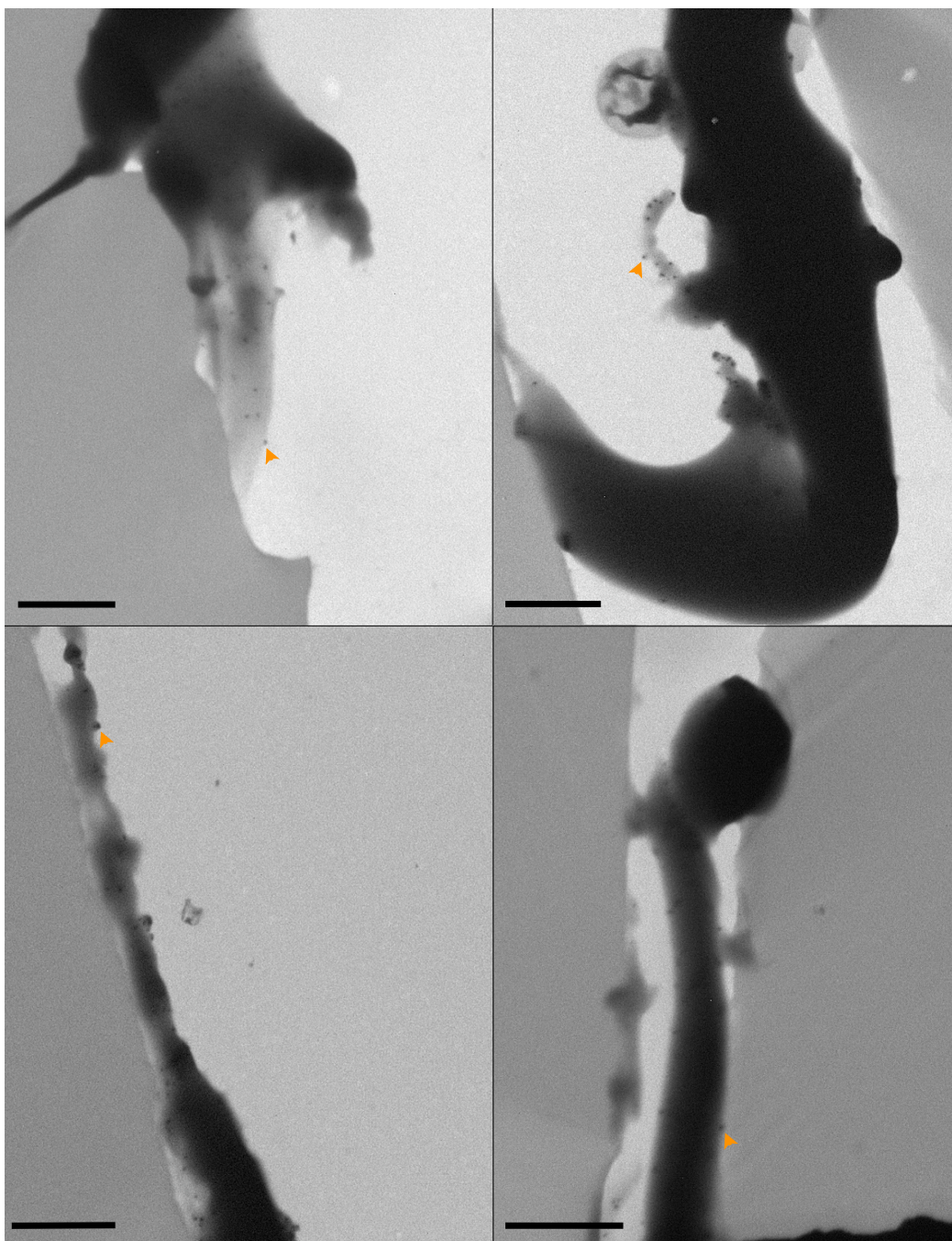
Figure 4.5: Transmission electron microscopy images of PDMS films with nanoparticles. The thin samples curled and bent because of the PDMS elasticity and electron beam power. Images were taken in the Philips TEM at 80kV for 700X direct magnification, the scale bar measures 2 μm for all samples, and arrows highlight the Ag nanoparticles.
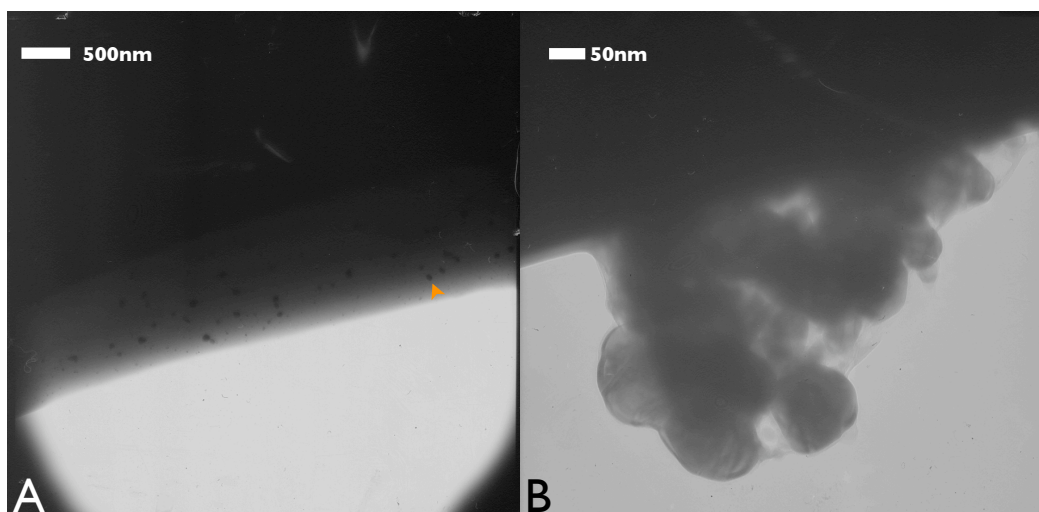
Figure 4.6: Bright field transmission microscopy image of PDMS films with nanoparticles. (A) 15000X direct magnification; large particles were observed through the thick film edge. (B) 100000X magnification; the high voltage destroyed the films but conglomerates of particles showed individual amorphous silver crystals. Images taken with the JEOL TEM at 200kV.

thick sample seemed to be the only alternative to image the fringes with TEM: A sample 20μm thick was prepared for this purpose. The sample was held in place in the TEM chamber with clips on copper grids. Once again, the samples showed 'charging' due to the attraction of electrons making difficult the observation and causing the polymer chains to degrade. The film thickness did not allow the beam to pass through the sample. Therefore, only images of the edges were collected and shown in Figure 4.6. The individual nanoparticles can be seen, counted, and measured in the images; however, no fringes were identifiable. Figure 4.6B is a magnification of a conglomerate of particles after the surrounding polymer was etched away by the electron beam. The shape of the particles was not perfectly spherical and showed random irregularities on the surface.

It was possible to record the diffraction patterns for the silver particles in these samples using the selected area of diffraction mode of the JEOL TEM. The recorded pattern was not conclusive about the crystal structure, although it is similar to silver patterns reported in the literature [180, 181]. Its irregularity suggests that there is a non-uniform array of the crystal planes [181, 182]. Figure 4.7 shows a comparison between the diffraction pattern of the particles in the
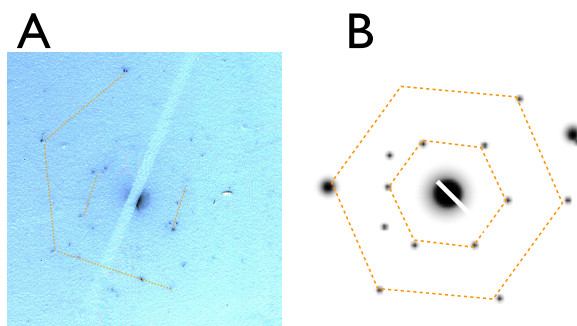
Figure 4.7: Dark field selected area of diffraction pattern of silver nanoparticles in PDMS. (A) Diffraction pattern of the amorphous crystals showing characteristic pattern for silver particles. Image taken with JEOL TEM dark field, digitalized from a negative. (B) Sketch of a typical non-spherical silver particles selected area of diffraction pattern [180, 181].

hologram with a typical silver diffraction pattern of irregular nanoparticles.

4.4.2 Scanning electron microscopy

In another attempt to image the holographic fringes, a transverse section of a 2mm thick hologram was analyzed by SEM. The aim was to image the fringes on a side view looking for protuberances of particles on the cut, and also to determine the distribution of silver beneath the surface using X-ray scattering. To avoid electron absorption, the sample was fixed to an aluminum holder with conductive tape, however it was not possible to identify a fringe pattern. Figure 4.8 shows the SEM sample preparation and results highlighting the position of particle protuberances. The silver diffusion gradient can be observed near the surface (Figure 4.8B), whilst a close magnification of this area is shown in Figure 4.8D. The lines visible along the surface were caused by the cutting blade.

X-ray scatter detection corroborated that, indeed, there were silver particles embedded in the PDMS matrix. Figure 4.9 shows the energy distribution of the back-scattered counts and the corresponding chemical element. The figure shows peaks corresponding to C, O and Si from PDMS, Al from the support and Pt from the coating layer. Most importantly, the peaks corresponding to the Ag particles were also detected.
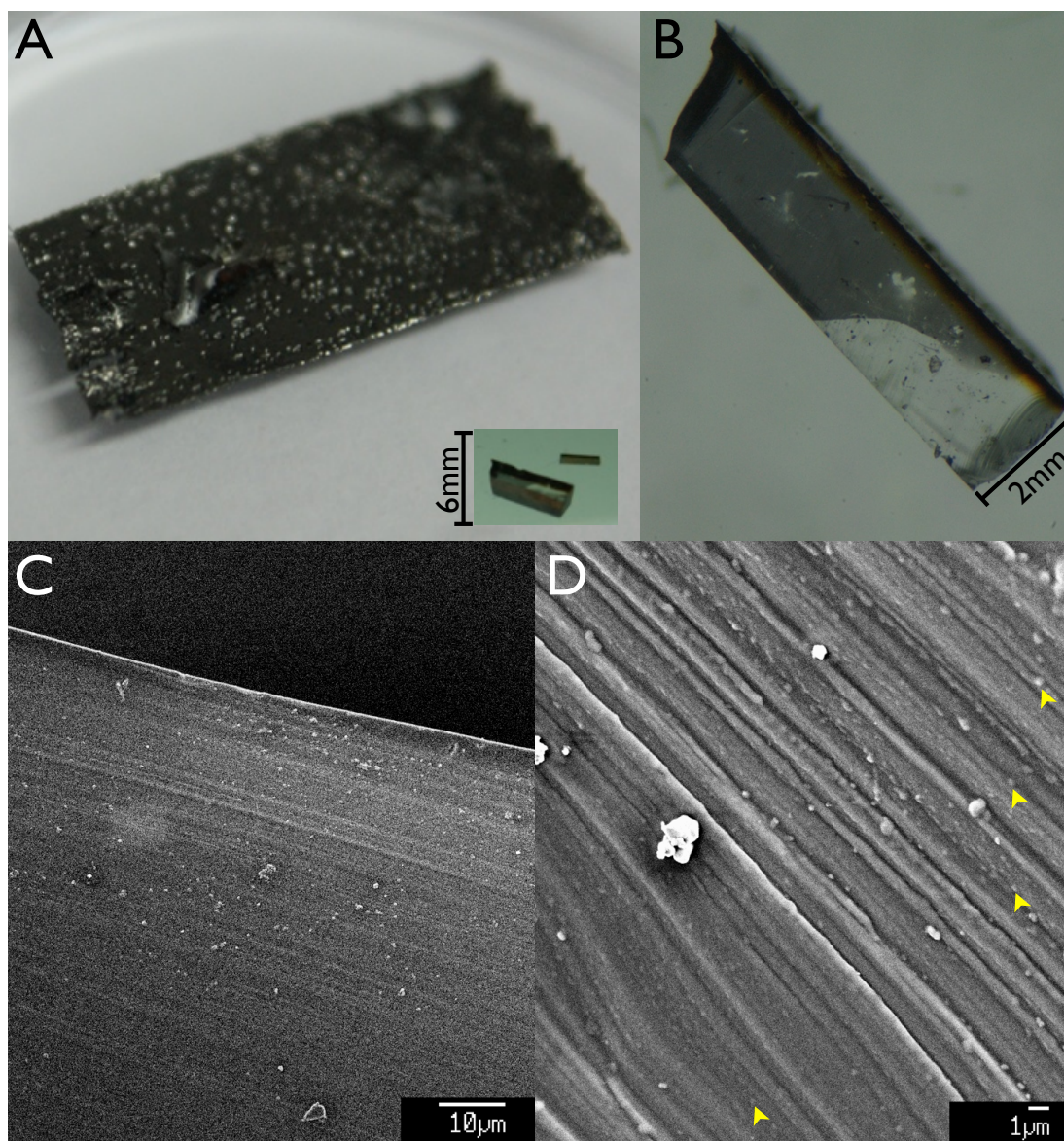
Figure 4.8: Scanning electron microscopy of PDMS holograms. (A) Sample preparation attached with conductive tape to avoid electron absorption; top image shows the platinum covered tape and sample, the insert corresponds to the sample alone showing the scale. (B) Micrograph of sputtered sample with a thin layer of platinum covering a portion of the transparent film, and the silver diffusion gradient in amber color running in the top-rigth to bottom-left direction. (C) Low magnification of the edge of the sample containing the nanoparticle gradient. (D) High magnification of the sample in C; protuberances highlighted by arrows may correspond to the silver particles.
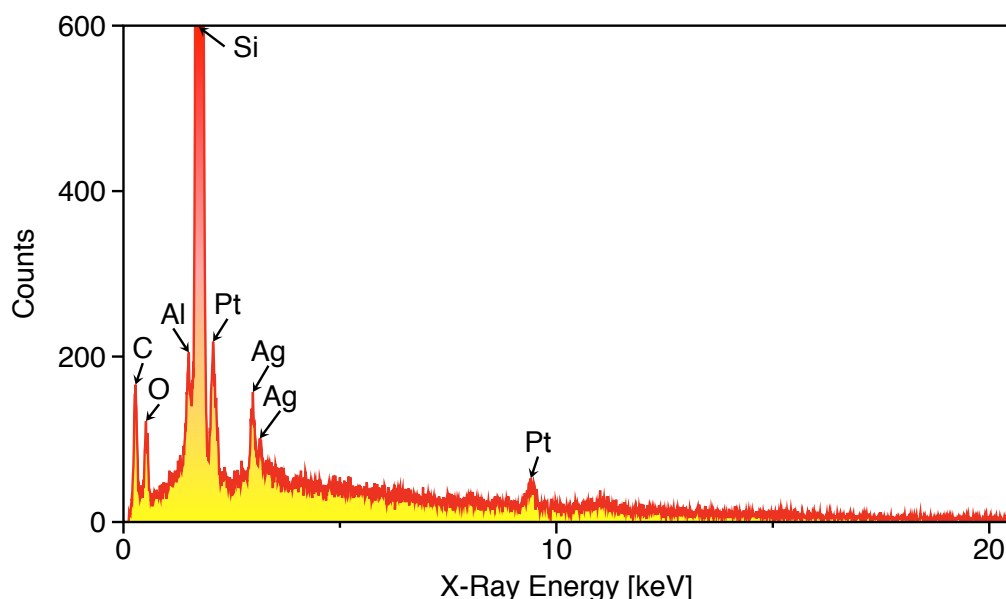
Figure 4.9: SEM X-ray back-scatter detector counts from JEOL SEM. The element peaks are indicated at their corresponding energy distributions in keV.

4.4.3 Scanning electron microscopy with focused ion beam

SEM allowed to observe a cross-section cut of the holograms, however the surface showed features corresponding to the blade and not necessarily the silver particles. Focused ion beam was an alternative preparation method and produced a flat surface on a transverse cut. It allowed to image individual nanoparticles on an etched cross-section under SEM, as shown in Figure 4.10. The sample was mounted on a silicon disc and coated with a thin layer of gold; it was carved in the middle from the top surface to expose a transverse view. The SEM showed a flat surface and nanoparticle protuberances; however, no fringes were detected because of the particles spatial distribution. At low magnifications the particles could not be observed and at high magnifications it is not possible to see their distribution on the fringes. Nevertheless, it was possible to count and measure the individual particles on the edged cross-sections.
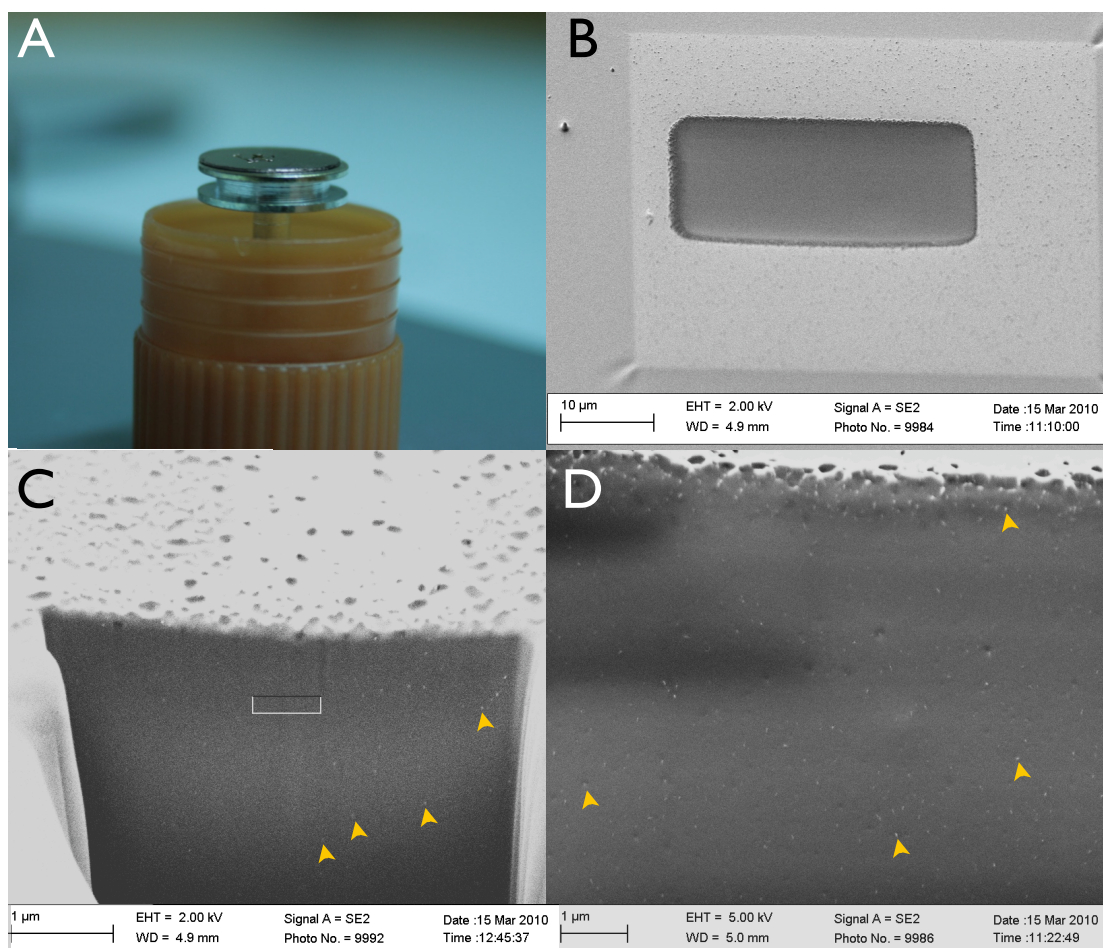
Figure 4.10: Focused Ion Beam etching SEM of PDMS hologram. (A) Sample preparation mounted on a silicon disc and coated with a thin layer of gold. (B) Beginning of the etching process with FIB; light areas are caused by the electron beam; the dark rectangle exposes the PDMS under the surface. (C) 45° angle view of the edged surface. (D) Magnification of the side view, scale bar provided. Features that give contrast to the image under SEM correspond to metals, thus the nanoparticles should correspond to the features highlighted with arrows.

4.4.4 Particle size distribution from electron microscopy

.

The image analysis software allowed the counting and measuring of large numbers of particles from the different electron microscopy images. The PDMS holograms showed a broad distribution of particle sizes after ablation with an average diameter of 19.2nm: The results are summarized in Figure 4.11. The particle counts are relatively small compared to other experimental work because of the difficulties in imaging the PDMS films. It is probable that particles in a certain range of sizes are ablated whilst others are not. The plots in Figure 4.11 correspond to counts after ablation and show that there is a region with lower particle counts around 50nm in diameter. Since a normal distribution was expected, it can be hypothesized that particles of ∼50nm in diameter were more susceptible to ablation. The size could also be limited by the reduction reactions; larger nanoparticles appear more often because of the low particle counts or the magnification at which they were imaged. It was not possible to draw a final conclusion from these results. It can be hypothesized that particles in the 50nm range are more susceptible to ablation since an even distribution of sizes was expected before ablation.

4.4.5 Atomic force microscopy

Another attempt at imaging the particles was using AFM for scanning the surface exposing the embedded nanoparticles, either from the front surface or a cross-section. AFM can resolve not only the presence of protuberances that may correspond to the particles, but also the dimensions of said particles down to the atomic level [183]. It was thought that the nanoparticle fringes could be noticeable as bulges projecting off the front surface of the film. The results corroborated that there were observable features on the surface. However, there was no ordered profile from the suspected nanoparticles and the presence of dust interfered with the observation; dust particles are easily attracted to the surface of PDMS, not cross-linked bonds on the surface may cause the strong attraction of dust particles or debris. After scanning different areas of the surface, it was not possible to measure a difference in the particle arrangement along the sample; whence, the
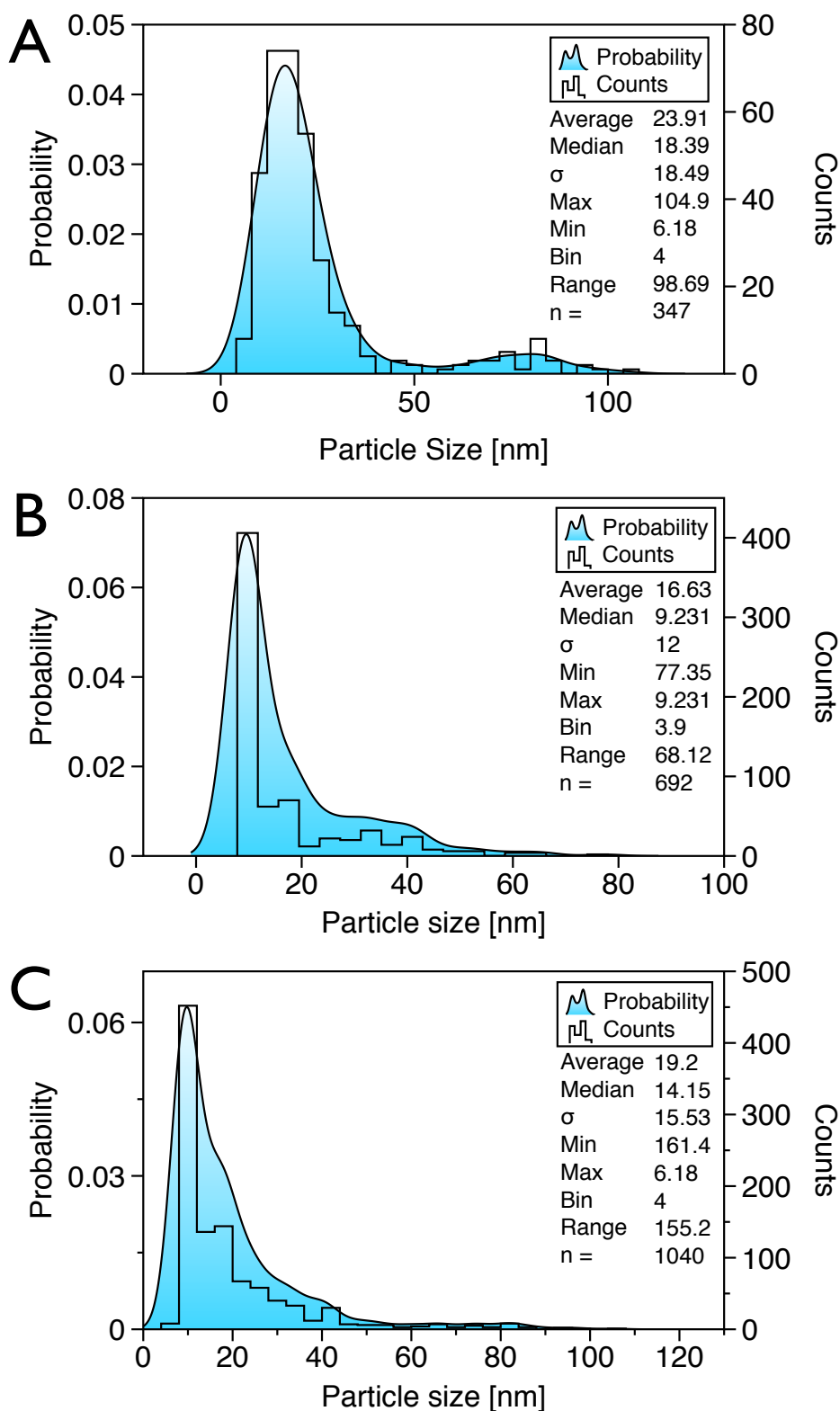
Figure 4.11: Particle counts from TEM and SEM experiments for samples after ablation. (A) TEM. (B) SEM-FIB. (C) The area of observation differs in both techniques, some particles may not be visible by one of the techniques. To obtain an average size distribution the both counts A & B were treated together giving 19.2nm average diameter.

fringes could not be defined with this method. Figure 4.12 and Figure 4.13 show the AFM results and the 3D reconstruction.

4.4.6 Optical microscopy

To date, it has not proven possible to extract information relating to the fringe formation in PDMS holograms using TEM, SEM or AFM techniques. This might be explained by the low distribution of particles through the film: A cross-cut only gives access to a thin section of the whole thickness. In consequence, the particles appear randomly distributed and highly spaced across the cut making it difficult to distinguish the fringes. An alternative method for imaging the fringes is optical microscopy. However, there is a resolution limit when using optical methods to image small objects. Two objects that are separated by a distance below the diffraction limit cannot be distinguished as separate objects [184]. The diffraction limit can be calculated for most optical microscopes as:

$$d_l = \frac{\lambda}{2n \sin \alpha} = \frac{\lambda}{2NA} \tag{4.1}$$

where $n \sin \alpha$ is the numerical aperture NA. Depending on the optical set up the limit is usually around 200nm. For the microscope used in the following experiments it was possible to calculate the diffraction limit using Equation 4.1.The values of α and n were provided by the fabricant as 1.5 and 65° respectively [185]. For the calculations, an average wavelength of 550nm was used, giving NA=2.72 and d_l=202.3nm. Without considering the effect of refractive index, the separation of the standing waves should give fringes separated by ∼266nm. Therefore it is theoretically possible to image the fringes optically. However, the sample has to be cut in a way that the light travels through the fringe planes without interference; which was not possible in this case.

Looking at the geometry of the hologram in Figure 4.14, the separation between the fringes on the surface of the hologram h must be visible. Since $\sin \Phi = \Lambda/h$, Λ=266nm and Φ=7°; then h=2.28μm and should be visible with the microscope.

In order to image the fringes, the sample was placed at an angle for the light to travel through the edge showing the separation. Figure 4.15 shows photographs of
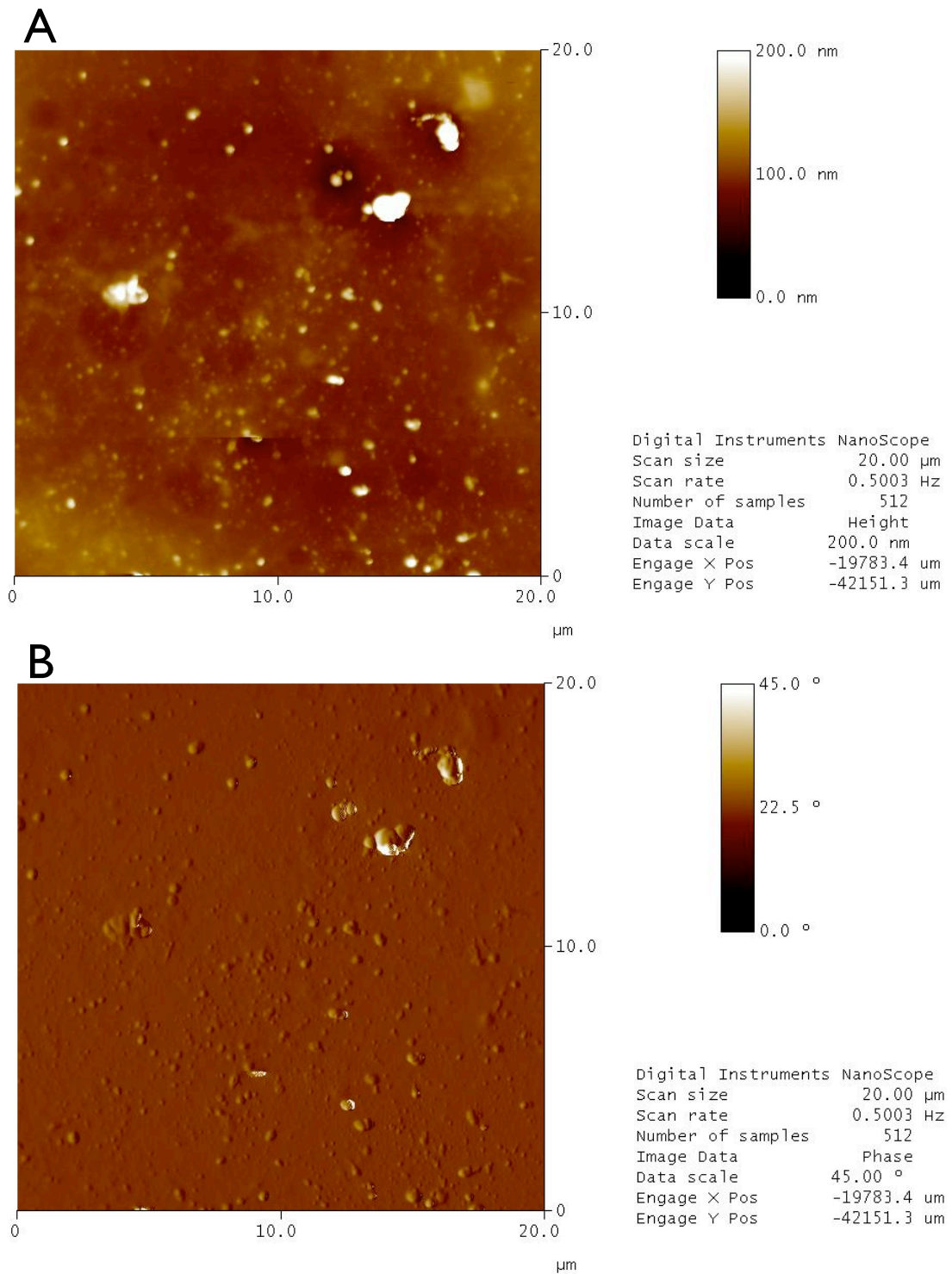
Figure 4.12: AFM scan of a PDMS hologram surface. (A) Height measurements. (B) Phase measurements.
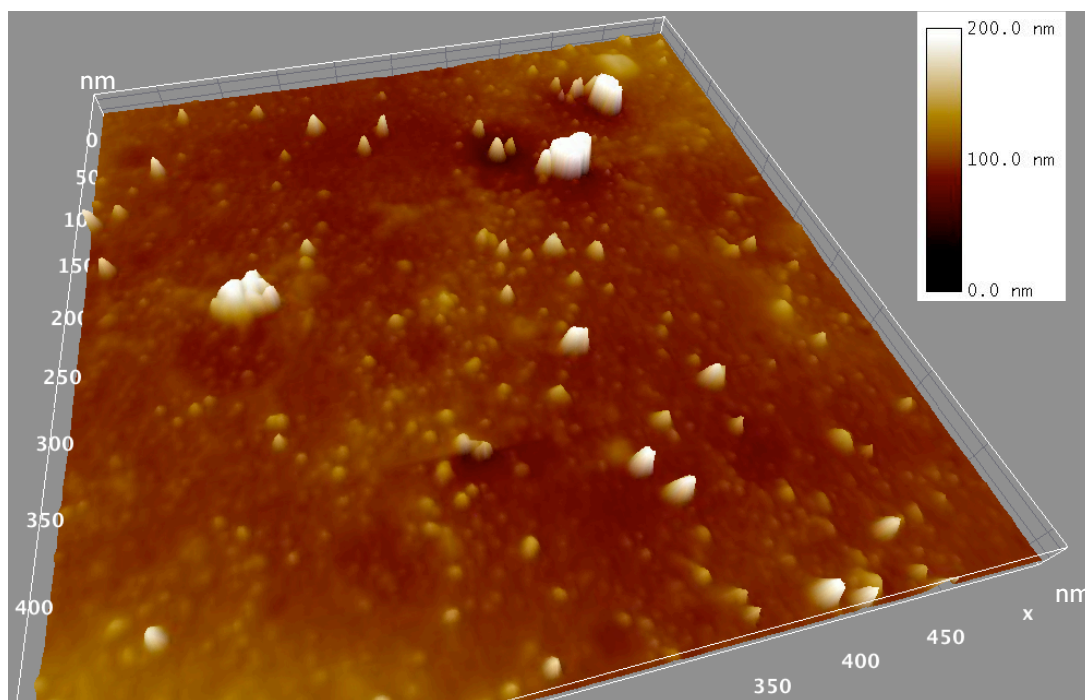
Figure 4.13: AFM scan of the surface of a PDMS hologram in perspective.
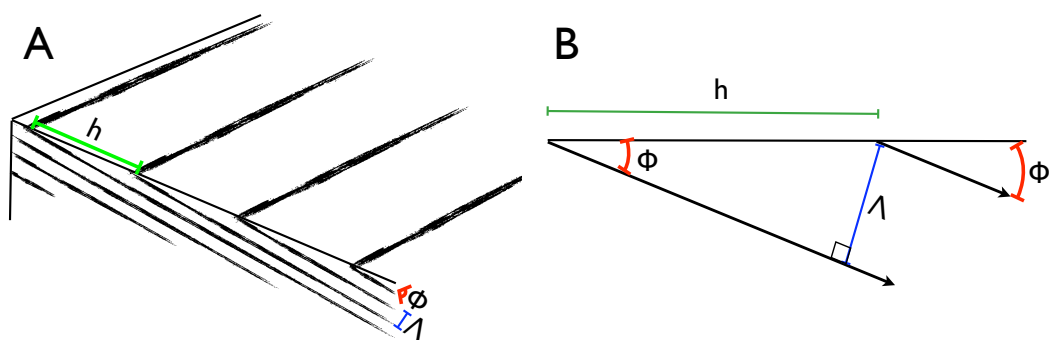
Figure 4.14: Sketch of the fringe geometry. (A) Fringe separation on the surface is larger due to angled planes. The centre of the dark fringe is represented as a line for illustration of the geometry. (B) Planar geometry of the fringe planes used for calculations.

the edge of the hologram and the fringes. The focal plane was not perfectly aligned with the fringes. However, it can be seen that the lines are evenly separated along the edge. A raw image shown on Figure 4.15A shows the position of the fringes at the edge; the same image was digitally enhanced in Figure 4.15B to highlight the dark fringes.

The image dimensions and position of the fringes were measured with the image processing software. Figure 4.16A shows the fringes highlighted with dashed lines and the lines where the measurement was taken. Figure 4.16B shows the grey values profile measured and the distance in micrometers. The separation between the fringes was $3.07 \pm 0.16 \mu$m for a fringe spacing Λ of 374nm and fringe thicknesses a and b of 187nm. This measurement was within 25.7% of the calculated value. However, whilst indicative, it was not conclusive for determining the fringe separation because there was a large variation in the angle of measurement and the angle of the cut which were difficult to control[a]. Furthermore, the presence of silver particles is likely to affect the local refractive index of the film, and, fringe formation by ablation can generate portions of the film with different refractive indices. Overall, these local refractive index variations may have changed not only the average refractive indices, but also affected the amplitude of the wavelength of the laser [186, 187]; thus, the fringe patter could have also changed dimensions.

4.4.7 Absorption spectroscopy

Absorption spectroscopy has often been used for characterization of nanoparticle formation [188]. Thus, it could give additional information about the ablation process. It has been shown that the surface plasmon resonance of silver nanoparticles changes for different particle sizes and spatial distribution in the polymer films [188, 189]. The typical Surface Plasmon Resonance (SPR) absorption of silver nanoparticles shows a peak value near 410nm [190–193]. In this work, a colour change was observed after particle formation and ablation. Figure 4.17 shows the characteristic absorption spectra. Interestingly, the peak shifted from 410nm to near 400nm after ablation. Comparing these results with the absorption profiles of commercially available nanoparticles reported elsewhere [194], the peak posi-

---

[a]correcting for a cut angle of 50.6° the perpendicular distance in the image is 2.37μm.
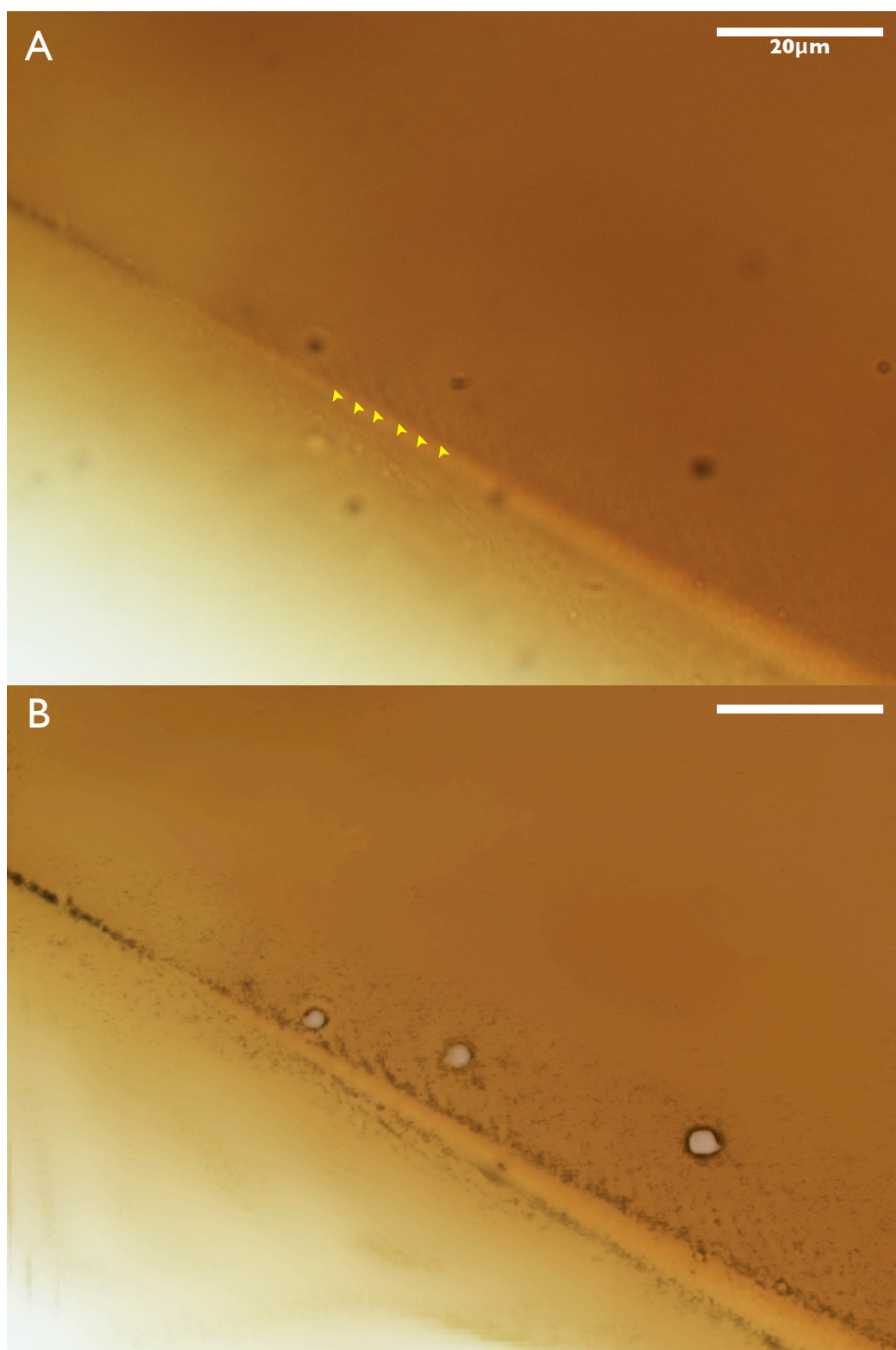
Figure 4.15: Optical imaging of PDMS hologram indicating the presence of fringes. (A) Raw image indicating the presence of fringes at the edge of the cut highlighted by the arrows. (B) Same as A with an superposition of an enhanced contrast image to highlight the dark fringes. The large dark particles are optical artifacts from the microscope lens. Scale bars are 20μm.
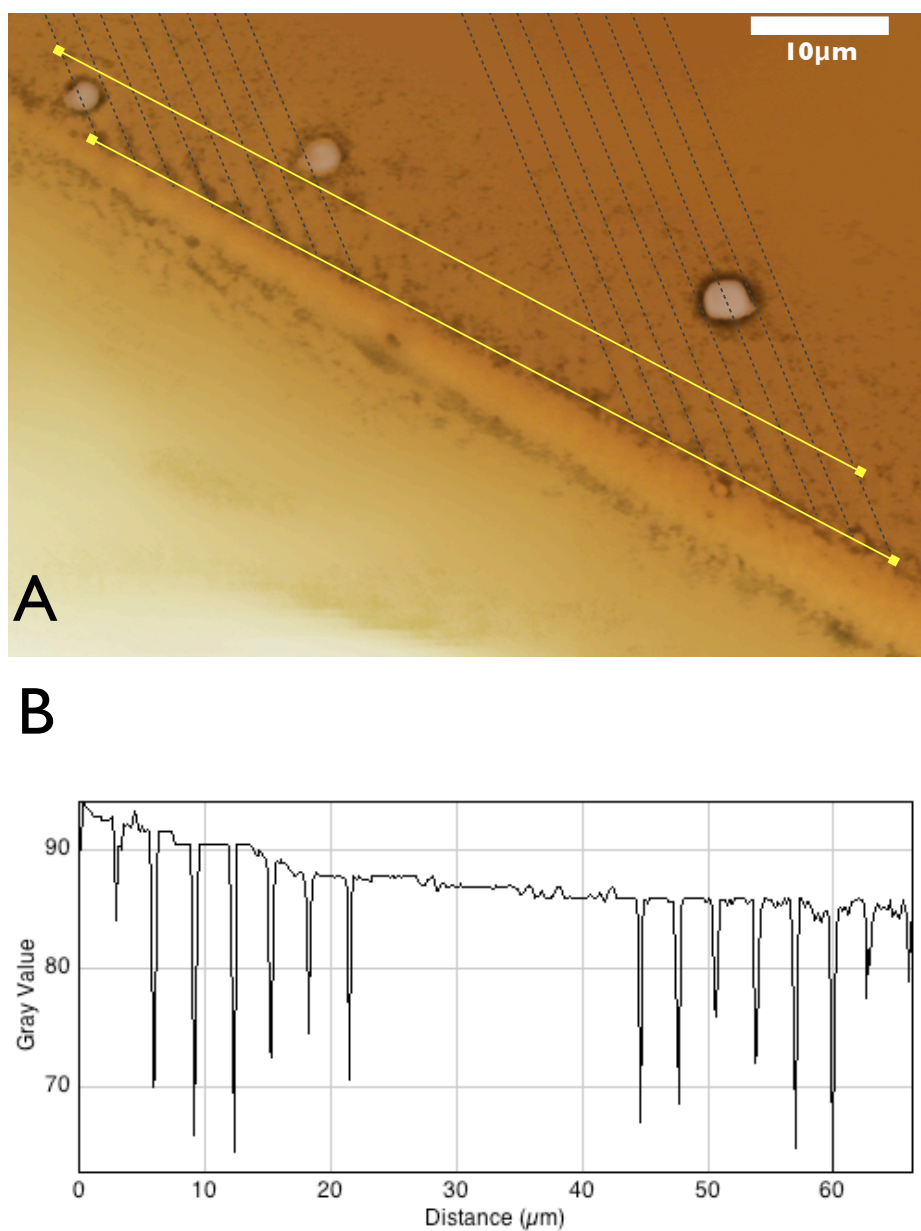
Figure 4.16: Measurement of the fringe spacing in PDMS holograms by optical microscopy. (A) Enhanced contrast image of the fringes with dashed lines used for defining the geometry. (B) Measured grey values in the direction of the yellow lines for determination of the fringe spacing; the sharp peaks correspond to the inserted dashed lines and the image features in the background. Images taken with the mounted digital camera on the Nikon microscope.
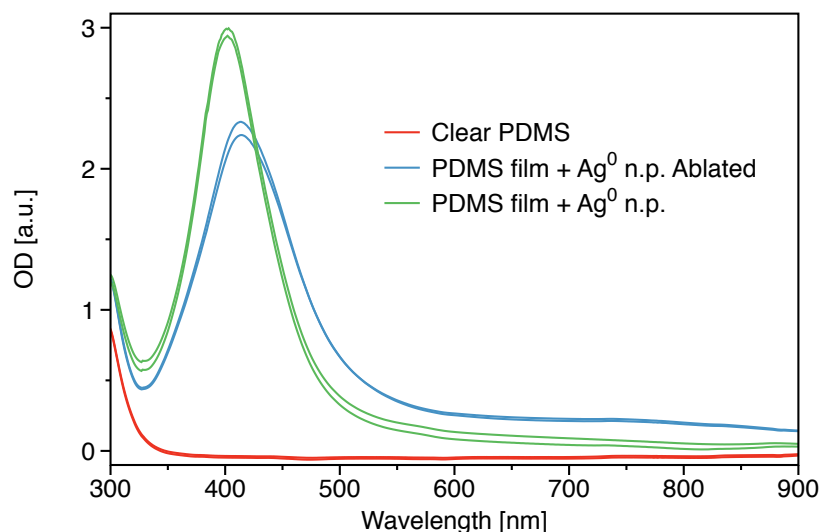
Figure 4.17: Absorption spectrometry of a PDMS film containing silver nanoparticles before and after ablation. The typical absorption peak due to the surface plasmon resonance of silver nanoparticles was shifted after ablation. The graph shows plots for two samples. Ag^0 *n.p.* stands for metallic silver nanoparicles.

tion after ablation corresponds to a reduction of size from 35nm to 15nm, similar to what was inferred based on Figure 4.11.

There are factors that affect the absorption profiles of nanoparticles in polymer films: The space between the particles, their shape, and their sizes affect the absorption peak profiles [188, 189, 194]. Nevertheless, it was clear that for the PDMS holograms a change in the absorption profile occurred before and after ablation. Surface plasmon resonance and related light absorption phenomena are important to consider for the holographic signal reading. The light interference or absorption with the particles in the gratings may cause the holographic signal to change. Although, the change can be very small to be considered if compared wit the large intensity values of the holographic reflections.

SEM, TEM, AFM and optical imaging techniques used for understanding the physical nature of the PDMS holograms encountered problems defining the fringe pattern or the presence, sizes, or the spatial distribution of the silver nanoparticles. Optical imaging of an edge of the hologram proved to be able to show the presence of fringe-like features on the surface, which dimensions correspond to the ones expected for the holographic fringes. Nevertheless, further studies are
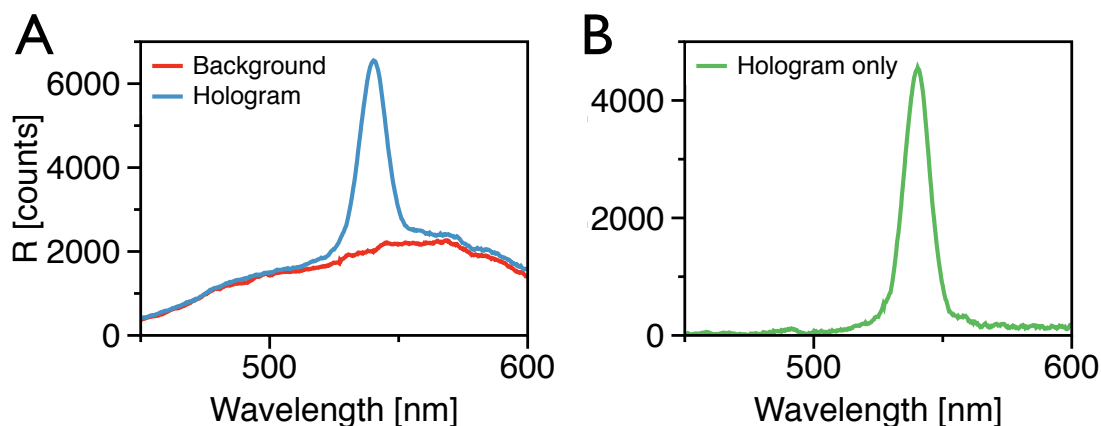
Figure 4.18: Signal measurement and background correction for PDMS holograms. (A) Hologram reflection and background light raw spectra. (B) Extracted hologram peak only.

recommended to fully understand the fringe formation in PDMS. Imaging the fringes in other materials could be an alternative (*see* §5.3)

4.5 Holographic signal measurements

The holographic signal was taken as the peak wavelength of the reflected light from the holograms. The reflections were recorded with a spectrophotometer as photon counts in the visible range. The wavelength at which the count was the highest corresponds to the holographic signal. The spectrophotometer measurements are described in §3.5. The signal measured after holographic recording showed characteristic peaks near the wavelength of the recording laser of ~532nm. The recorded spectra are shown in Figure 4.18A, which also includes the background reflections from the incident light on the cuvette surface. Subtracting this background signal from the total holographic reflection leaves a corrected holographic signal shown in 4.18B. This calibration procedure was repeated for all subsequent experiments and model fitting.

4.5.1 Mathematical models for reflection spectra

The wavelength of the characteristic reflection peak of the PDMS holograms was near that of the recording laser. This was expected, on the assumption that the value of the product $n \cos \vartheta_B \approx 1$ and that the value of Λ is $\sim \lambda_0/2$ from the standing waves, in which case, Equation 1.5 can be simplified to $\lambda = 2\Lambda$, whence, $\lambda \approx \lambda_0$. This approximation, however useful, is too simplistic and does not give more information about the peak position and intensity[a]. An extended mathematical model that predicts intensity for the whole spectrum has been introduced in §1.2.3. This model requires knowledge of the refractive indices of the layers, their number, and spacing in order to predict the holographic reflections for any given angle of observation.

The fringes generated by ablation do not have uniform refractive indices; in fact, it is difficult to draw the boundary between the dark fringes and light fringes. The dark fringes have a higher refractive index in the centre, whereas the light fringes have a lower refractive index. The transition between the two is a gradient rather than a fixed value due to the nature of the standing waves (*see* Figure 1.6). Therefore, in order to use the models effectively, average refractive indices were assumed for the geometry in Figure 1.6.

According to some publications, transparent PDMS should give a refractive index of 1.44 for the curing times used in this study [186]. Others have calculated that the refractive index of composite polymer films loaded with silver nanoparticles increases up to 2.0, depending on the shape and size of the particles [187]. For the concentration of 0.01% used in this work, a value of 1.5 is expected for wavelengths in the visible range [187]. In consequence, the resulting average refractive index of the ablated fringes should lie below this value. It has been reported elsewhere that the refractive index of silver particles dispersed in a polymer matrix increases by 0.1 unit for every 10nm reduction in diameter [195]. Assuming that the ablated nanoparticles were reduced to 30nm in diameter, as suggested by the electron microscopy and absorption spectroscopy results (§4.4.4 and §4.4.7); then, the refractive index for the ablated region should be 1.47. This

---

[a]The assumption that $n \cos \vartheta_B \approx 1$ is not necessarily valid for all cases; for $n \in [1.33, ..., 1.50]$ and $\vartheta_B \in [5°, ..., 45°]$ the product $n \cos \vartheta_B \in [0.94, ..., 1.49]$. The assumption is completely valid for traditional gelatine holography where: n=1.538 and ϑ_B=45 [96, p239].

refractive index contrast is necessary for the photonic effect to occur. Another way of estimating this value is averaging the average refractive indices of the polymer composite and cured PDMS; the result also gives a refractive index of 1.47.

In order to corroborate the estimated and reported values, the refractive indices of the films were measured using an Abbe refractometer. The refractive index of clear PDMS was 1.438 and the film with nanoparticles was measured as 1.502; both values are consistent with those reported in literature [186, 187]. However, there are no reported values for the ablated regions, nor was it possible to measure them directly. A possible solution could be to ablate the films a second time in the position of the dark fringes to ensure a uniform ablation throughout the film. This would leave a film with no optical grating and in order for this to happen the position of the film should be controlled nanometrically. If this movement was performed at random, the ablated particles could be ablated again and affect the overall measurement.

Calculated and estimated values were input in Equation 1.13 to model the photonic effect mathematically. The model also required knowledge of the number of fringes which were estimated from the microscopy results. It was determined that up to a depth of 27.3μm beneath the surface of the holograms, a total of 150 effective fringe layers contributed to the reflection.

The final values included in the mathematical models were: 150 fringe layers; 1.50 refractive index of dark fringes; 1.47 refractive index of light fringes; 20° and 25° angles of observation for the different experiments; and 187nm fringe thickness. The photonic model prediction proposed by Yeh[a] described in §1.2.3 [116], and the experimental data for a non-exposed PDMS hologram are plotted in Figure 4.19. The maximum photon counts of R were normalized to match $|r_q|^2$. Variations in the sharpness of the peak in Figure 4.19 may be due to the normalization, the calibration with the light source, or lower brightness of the PDMS holograms compared to other grating systems.
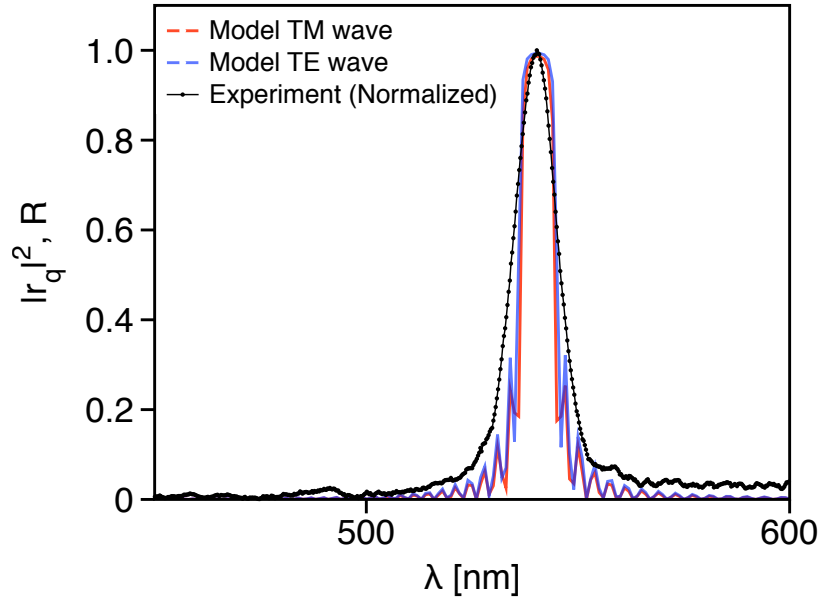
Figure 4.19: Experimental data compared to mathematical model of holographic reflection spectra in PDMS holograms.

4.5.1.1 Photonic model implementation and sensitivity

In order to test the sensitivity of the model, different input parameters were tested to compare the final outcome. Figure 4.20 shows the results of these trials; the initial values for the input were $n_1=1.45$, $n_2=1.49$, $L=50$, $\Lambda/2=150$nm and $\theta=25°$. Then, higher and lower values for n_2, L, $\Lambda/2$ and θ were respectively inserted into the model without changing the other initial values.

The model was noticeably sensitive to variations in the input parameters: For example, a change of 0.2 units in the refractive difference index produced a $\sim$5nm and $\sim$50% change in λ and $|r_q|^2$ respectively; removing 25 layers halved the intensity but did not affect the peak position; a change of 5° in the angle of observation resulted in a $\sim$10nm wavelength shift; and a change of 15nm in the layer's thickness shifted the peak position by $\sim$30nm. The effect of these changes is shown in Figure 4.20.

For the actual experimental data, the number of layers and the angle of ob-

---

[a]Equation 1.27 using a Mathematica® snippet [196]. The computing code is given in Program A.3 in the Appendix.
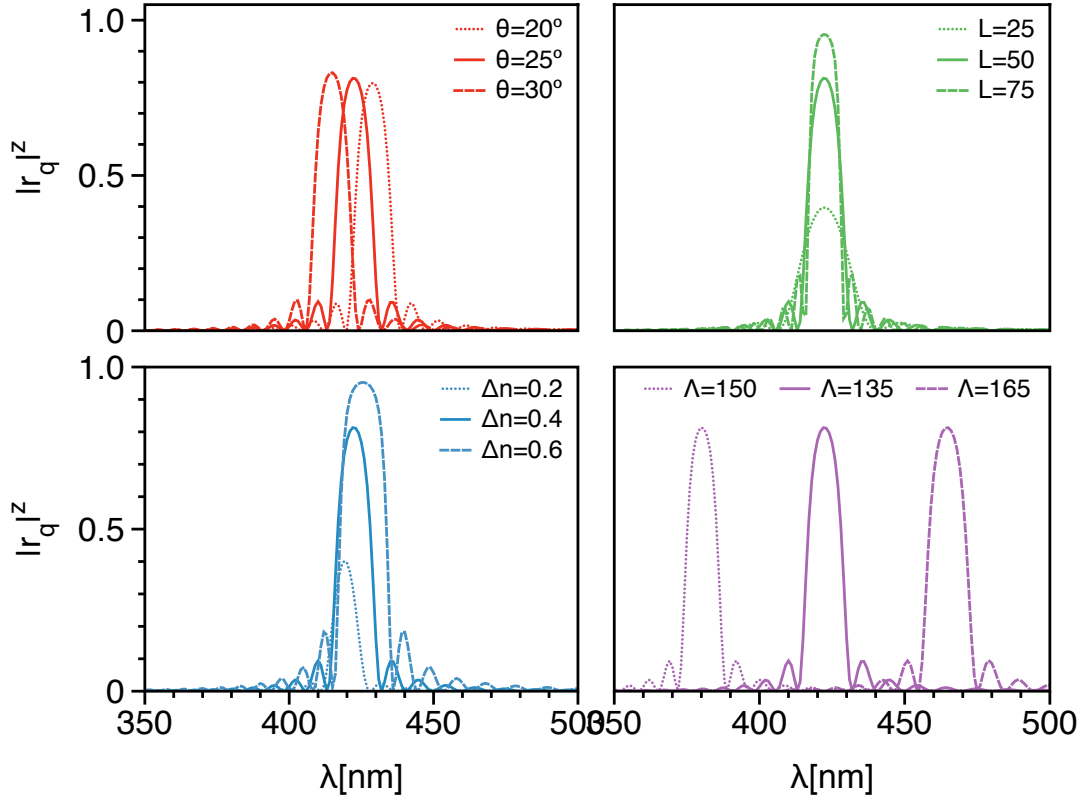
Figure 4.20: Sensitivity of the mathematical model to variations in the input parameters. The plots show variations in angle θ, number of layers L, difference in refractive indices $|n_1 - n_2|$ and fringe thickness $\Lambda/2$. Solid lines represent the same values for all different colours: n_1=1.45, n_2=1.49, L=50, $\Lambda/2$=150nm and θ=25°. The dashed and dotted lines correspond to variations in the values of the parameters indicated by the legend. Curves are plotted for the TE wave only; TM waves were roughly in the same position.

servation were fixed. Therefore, changes in wavelength were mainly caused by changes in fringe thickness, and changes in reflection intensity by the refractive index differences. The model predicted the peak wavelength position of the TM and TE waves roughly at the same position with respect to the experimental values. The model fit deviated by <1nm from the experimental data.

One of the disadvantage of the model is that it does not consider the quality of reflection in the fringes, which in this case, is given by the amount of silver particles referred to as the reflection efficiency. For this reason, the model could not account for changes in reflection intensity that were not caused by changes in refractive index. When stretching the holograms, for example, the space between the silver particles also changes, thus reducing the quality of the interfaces and the reflection efficiency[a]. Nevertheless, a conclusion can be drawn from these results: The mathematical model agreed with the peak position in the experimental data as seen in the plot of Figure 4.19.

4.5.2   Proof of concept: Response to mechanical stimuli

The expected response of the holographic gratings when exposed to gaseous analytes would be a change in λ caused by a change in Λ or n as predicted by the model. In the case of PDMS holograms, VOCs are partitioning into the film as chemical reactions with the metallic nanoparticles are not be expected a change in the refractive index of the particles would also be unlikely. The presence of the VOC may, however, change the refractive index value of the polymer. This change if present would be insignificant compared to the change caused by the swelling of the polymer. In order to confirm that the reflected wavelength can be altered by changing the spacing of the fringes, a thick hologram was stretched and compressed while recording the holographic signal. These external stimuli caused a bulk deformation which, in turn, resulted in a change in the fringe spacing.

Figure 4.21 shows the reflection spectra of a PDMS hologram as it was compressed, including the background signal. The wavelength and intensity decreased as the hologram was compressed by applying pressures up to 671 kPa. The experiment was repeated adding and removing pressure; Figure 4.22 shows a plot of

---

[a]The space between the particles increases and the fuzzy line between the dark fringe and light fringe is less distinguishable. Thus, there is more transmittance in the direction of the vector K and, as a result, less incoming light is reflected reducing the reflection efficiency.
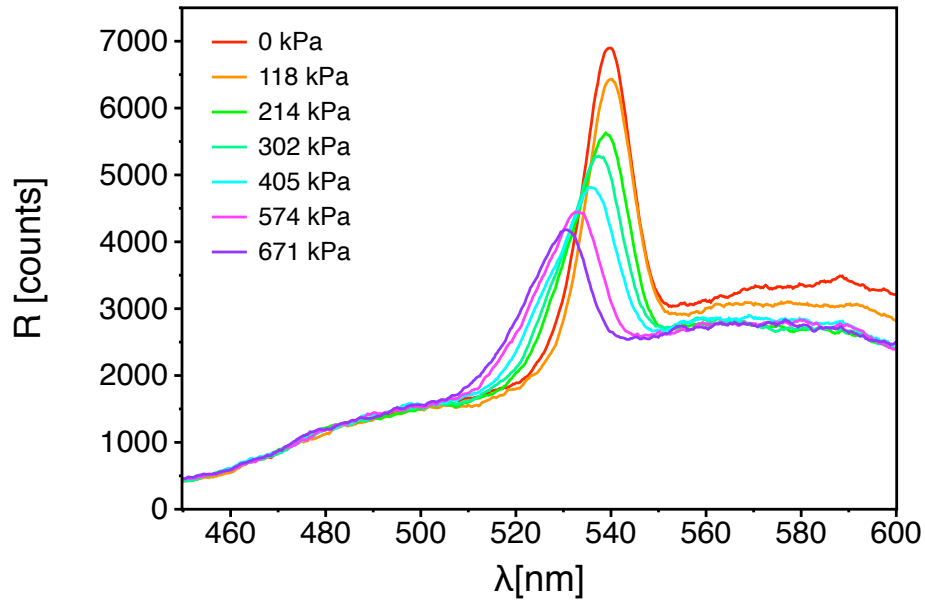
Figure 4.21: PDMS hologram response to compression. Raw spectra recorded for applied pressures in the range of 0-671 kPa. The pressures were calculated knowing the mass applied over a 1cm diameter circular area.
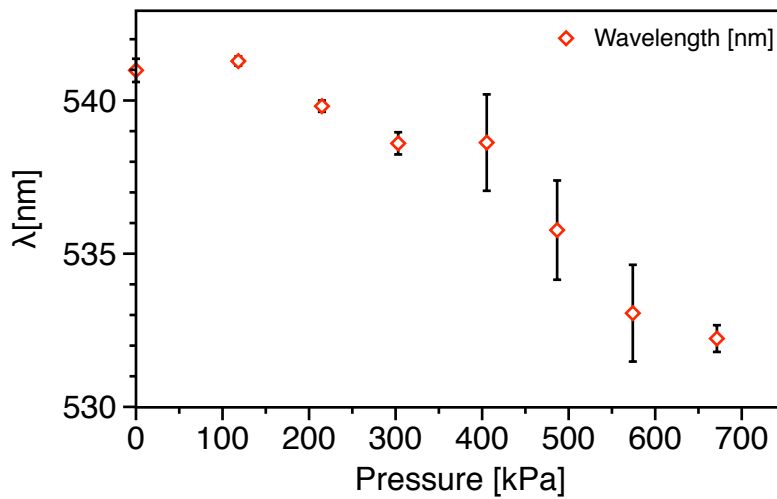

Figure 4.22: Correlation of peak wavelength and applied pressure for a PDMS hologram. The values correspond to the peak wavelengths of raw spectra as in Figure4.21. Pronounced error bars (standard deviation, 1σ) are caused by hysteresis due to compressing and decompressing.
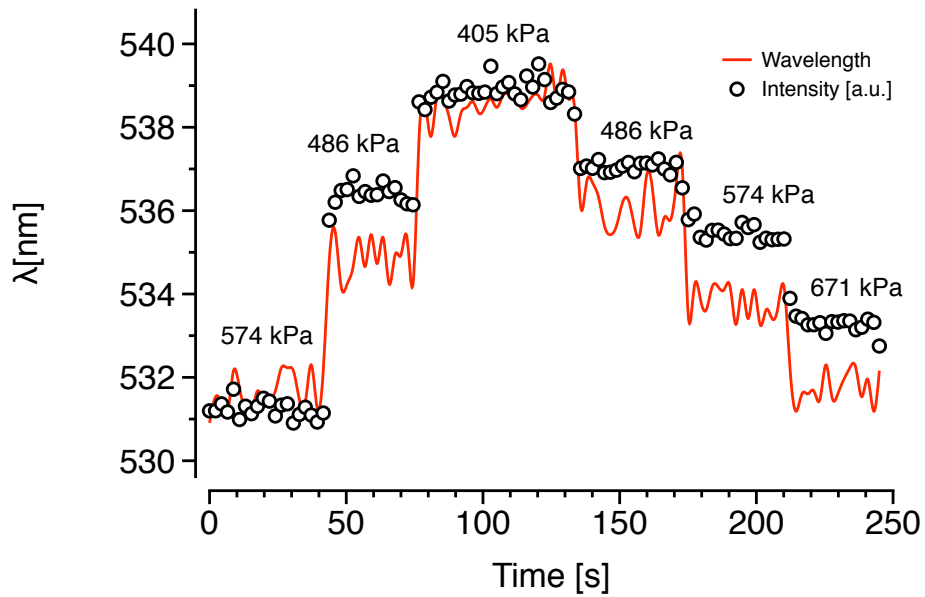
Figure 4.23: Continuous recording of the peak wavelength during a compression-decompression experiment. The changes were reversible over longer periods of time but not for the short duration of the experiment.
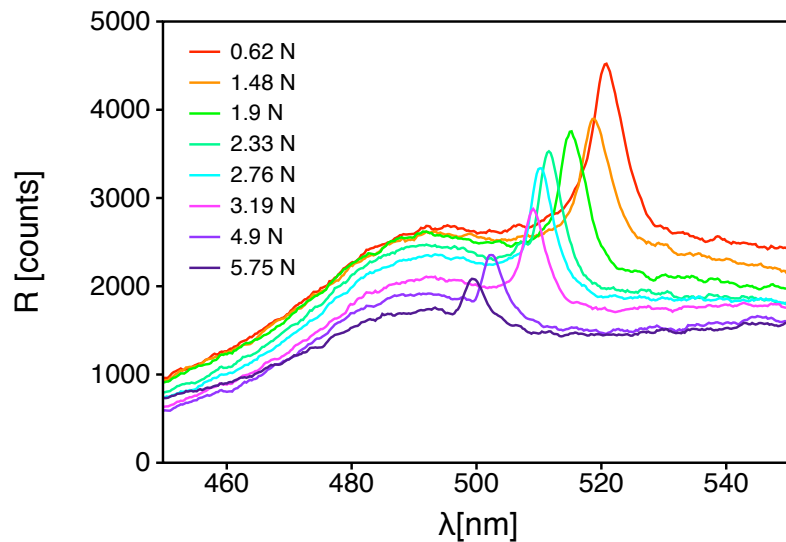
Figure 4.24: Response to stretching of a PDMS hologram. Raw spectra recorded for stretching forces in the range 0.62N to the maximum available load of 5.75N. The forces were calculated by knowing the mass applied in the direction of the stretching (*see* methodology).
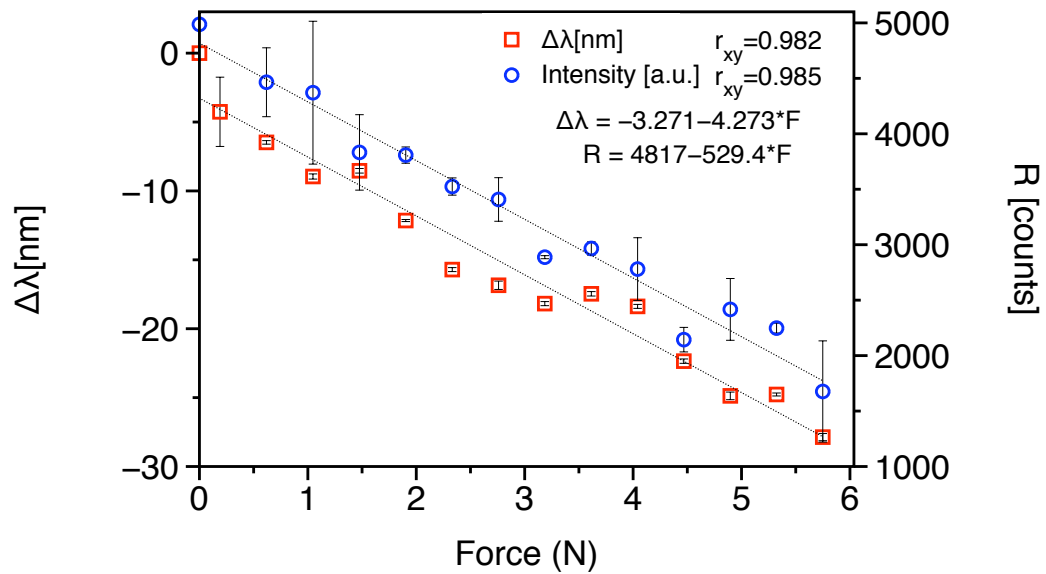
Figure 4.25: Correlation between peak wavelength, intensity, and applied force for a PDMS hologram. The values correspond to the peak wavelengths of raw spectra as in Figure 4.24. There was no noticeable hysteresis in this case.

replay wavelength versus pressure. This result was highly influenced by the elastic properties of the PDMS film; for example, there was high variability for certain values because of the hysteresis caused by the slow relaxation of the polymer. The response changed at a rate of 58kPa per nanometer but it did not return to the initial λ value immediately after relaxing the compressed films. Figure 4.23 shows a countinous measurement increasing and decreasing pressure showing hysteresis.

Figure 4.24 shows the reflection spectra of a stretched PDMS hologram. There was a reduction of the peak intensity and wavelength as the stretching force increased to 5.75N. There was no noticeable hysteresis within this force range. The linear correlation of force against wavelength change and intensity is shown in Figure 4.25. The total change was 27nm with a rate of 5nm/N and $\sim$60% reduction of intensity.

The hologram dimensions were measured before and after stretching to compare the results with the mathematical model. H, w, l and V are the height, width, thickness, and volume of the hologram respectively (*see* Figure 3.6). The initial dimensions were 22.10mm x 60.10mm x 0.76mm and 24.69mm x 60.08mm

x 0.68mm when stretched at 5.75N. Assuming that the total volume does not change, the distance between the fringes can be calculated using the relation: $V_1 = V_2$ or $H_1 w_1 l_1 = H_2 w_2 l_2$. Substituting the measured values, the ratio l_1/l_2 was 1.11. Assuming the geometry of the fringes, the thickness of the layers in the hologram will change accordingly, and thus for Λ_1=187nm, Λ_2=168nm. These values were used in the model to compare with the experimental data; the results are shown in Figure 4.26. The value of $\Delta\lambda$ predicted by the model was 20nm larger than expected.

Stretching the hologram contracts the fringes in one dimension but expands them in another one. This resulted in a reduction of the fringe spacing but an increase in the spatial separation of particles within the fringes. In other words, there are fewer particles per unit area on the fringe planes. This could cause changes in the local refractive indices which could account for the 20nm offset shown in the model. Furthermore, the Bragg angle and the light spot are in different positions after stretching. Even though small changes in the angle of the fringes are negligible, the intensity and wavelength of the peak could have changed. Nevertheless, the model predicts the same type of shift towards shorter wavelengths. Stretching and compressing the hologram proved to affect directly the fringe spacing and, therefore, the reflectivity and wavelength.

In an attempt to link the elastic properties of the hologram to the reflection results, the measurements of the dimensions were combined with a strain-stress model. This made it possible to link the mechanical properties to the photonic effect, such that a change could be predicted when the hologram was mechanically stimulated, in other words, to predict a colour change for a given stretching or compressing force. The elastic properties of the hologram are defined in terms of the stress and strain which are given by $\varepsilon = u/H$ and $\sigma = E\varepsilon$ respectively. These values are related to the applied force by $F = A_0\sigma$, where ε is the tension or strain, σ is the stress, E is the Young's modulus, u is the length gained after stretching $H_2 - H_1$ and A_0 is the area of the film before stretching (*see* Figure 3.6). For these experiments E=36.9kPa, which is lower than the reported values for this formulation[a]. This discrepancy could arise because of the presence of silver particles in the film or the solvent treatment during the perfusion of the silver

---

[a]E for Sylgard 184 with 10:1 mixing ratio is 1.84MPa at 23°C; *see* references [197, 198].
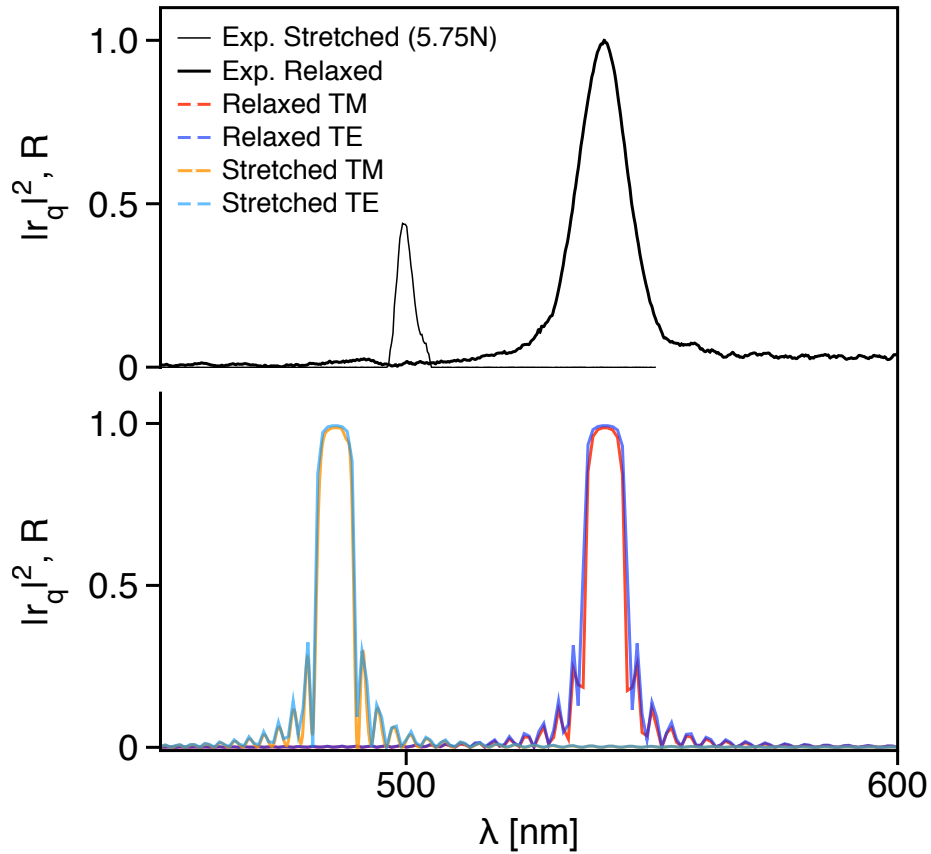
Figure 4.26: Mathematical prediction and experimental values of holographic response to stretching in PDMS holograms. The experimental data is normalized and corresponds to the hologram with 0 load and stretched with a 5.75N force as indicated in the legend. The model predicted a larger shift.

or the curing times and temperatures used or, most likely, the breakage of linked polymer chains during the ablation process. It has been shown that, despite its optical transparency, PDMS can be completely ablated using high energy lasers [199,200]. Despite the difference in the elastic properties, the mathematical model can be used as a predictor of the behavior of the sensor, at least for predicting the direction of the shift. The aim of these set of experiments was to prove that a change can be inflicted in the holographic reflection by applying external stimuli, and thus prove holographic sensing principle, as it was shown.

4.5.3 Proof of concept: Response to thermal stimuli

In order to prove that the expansion of the polymer matrix can also give a change in the holographic signal, energy was given to the system in the form of heat. As the temperature raised, a change in the molecular conformations of the PDMS chains is expected due to thermal expansion of the polymer. Figure 4.27A shows the wavelength changes for temperature increments over time. The temperature of the surface was kept constant while recording each data point with variations no higher than $\pm 0.5°C$.

There were no significant variations for small temperature changes; the temperature change affected the hologram by 0.25nm/°C (Figure 4.27B), which is not significant compared to the analytical signal (§4.6.1). It was also noted that there was no hysteresis, this is important to consider for the rest of the experiments with this system. The response to thermal stimuli confirms again the holographic sensing principle for the expansion of the fringes. A change in refractive index may also affect the overall wavelength shift, since refractive index is dependent of temperature, however this change would not be enough to affect the shift caused by change in the fringe spacing.

4.6 Holographic sensing of hydrocarbons and VOCs

A holographic sensor uses the molecular interactions with analytes to generate a change in either Λ or n. Hydrocarbons and VOCs do not cause chemical
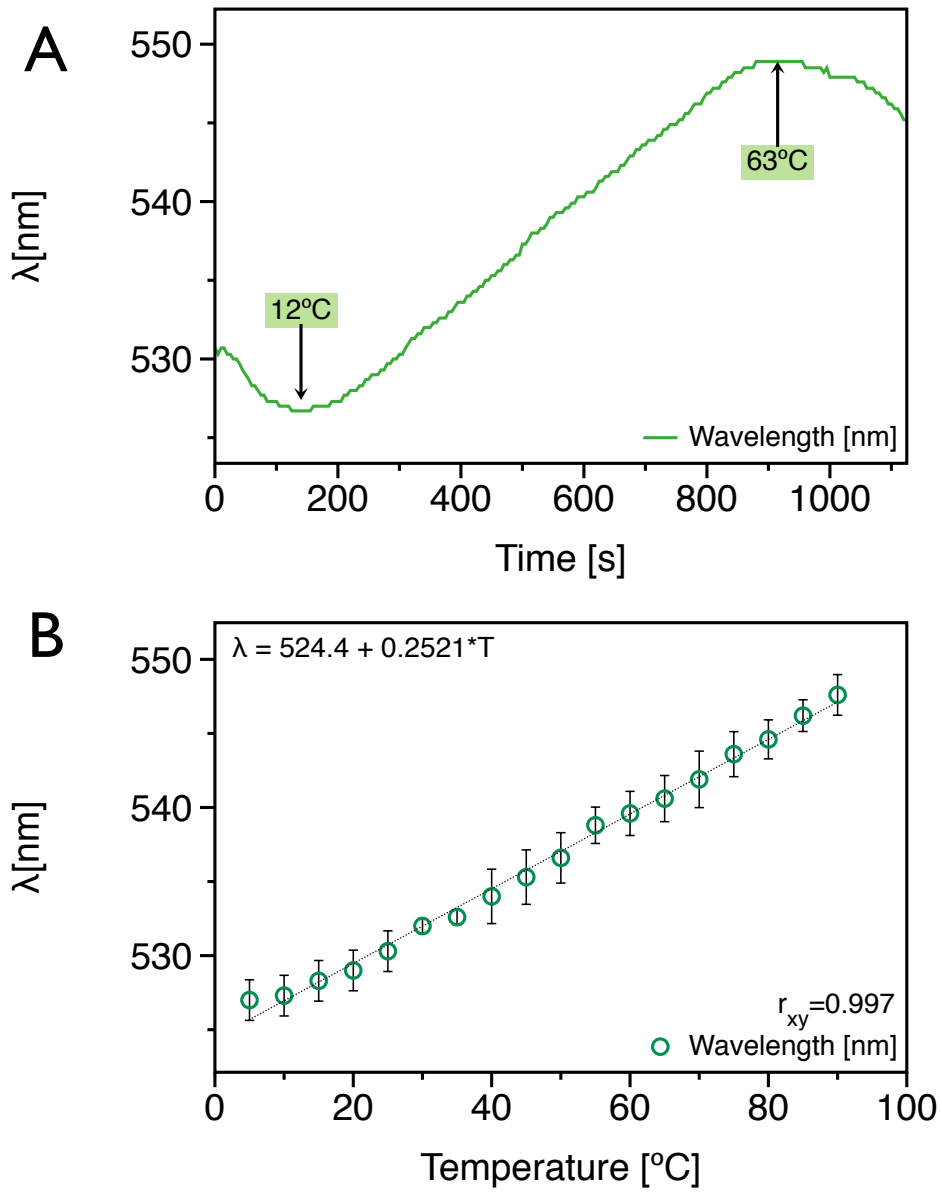
Figure 4.27: Holographic response to thermal stimuli in PDMS holograms. (A) Peak wavelength over time as the system was heated and cooled. (B) Linear correlation between peak wavelength and temperature with a change rate of 0.25nm/°C.

changes in the silver particles when in contact with them. Furthermore, there is no evidence of chemical reactions between the silver particles and hydrocarbons which could change their refractive index. Therefore, hydrocarbons and volatile compounds will only cause changes in the fringe spacing because of polymer swelling or concentration. These substances are usually gaseous but some can be found in the liquid state under ambient conditions. Results for gases and liquids are reported separately in the sections below.

4.6.1 Gases

The PMDS holograms were placed in the test cuvettes with the spectrophotometer configurations described in the Materials and Methods. The experiments were designed to test the sensing capabilities of the films, such as repeatability, reversibility, sensitivity, detection limits and hysteresis. The results showed that for all holograms fabricated in PDMS films the signal change was, in fact, repeatable, reversible and continuously recordable. For example, Figure 4.28 shows the response to 99.5% (v/v) iso-butane followed by purging with air. The gas was injected, as indicated by the arrows in the Figure, and then flushed out of the chamber after reaching a maximum response. This cycle was repeated continuously at least three times without affecting the level or response.

In order to prove the usability of the holograms as sensors, different concentrations of the hydrocarbon gas were injected into the cuvette to measure the holographic response. Figure 4.29A shows the response to different concentrations % (v/v) of n-butane. The gas was continuously added and purged with air allowing the hologram to recover its initial state. The peak position shifted to a different wavelength for each concentration tested. Plotting the wavelength against concentration gives a linear correlation; as shown in Figure 4.29B. Similar results were obtained for all the other gaseous hydrocarbons. These results indicate that a holographic grating in PDMS can effectively be used for the sensing of hydrocarbons.

The hologram was not only operated in continuous cycles of exposure, but also displayed no hysteresis. Figure 4.30A shows how different concentrations can be tested in repeated cycles for n-butane and Figure 4.30B shows a concentration cycles from high to low and low to high for 1-butene. It was difficult
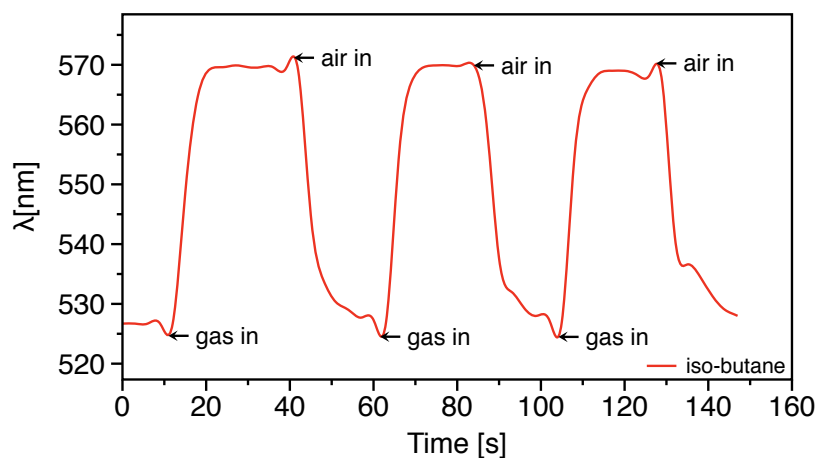
Figure 4.28: Holographic response to 99.5% (v/v) iso-butane gas. The gas inlet is indicated by the arrows; air was used to flush the gas out of the cuvette after a maximum value was reached.

to detect wavelength changes below 5% due to the relatively small changes in the fringe spacing and the sensitivity of the spectrophotometer; this value corresponds to a 1.5nm wavelength shift. The sensitivity of the hologram depends principally on the intensity of the reflected wavelength and the detection limits of the spectrophotometer. The Oriel spectrophotometer used in these experiments can resolve down to 0.3nm, equivalent to a sensitivity of 1% (v/v) in concentration. The sensitivity, thus, depends primarily on the quality of the holographic reflections, which in turn is given by the sharpness of the wavelength peak and the reflectivity in combination. Nevertheless, the detection range that can be measured extends from 5% up to 100% (v/v), which is advantageous for some industrial applications and is still significantly broader than the commercially available sensors with fixed concentration limit (*i.e. for limits within regulations, non-variable*) [12].

The wavelength shift for some of the gases resulted in an obvious change in colour that could be potentially read by 'eye'. Figure 4.31 shows photographs of the hologram when exposed to different concentrations of 1-butyne. A colour change can be seen from 0 to 98%; however, the colour transition at intermediate concentrations may not be discernible by the human eye (*see* §4.9 for further explanation and analysis of the colour change in these images).
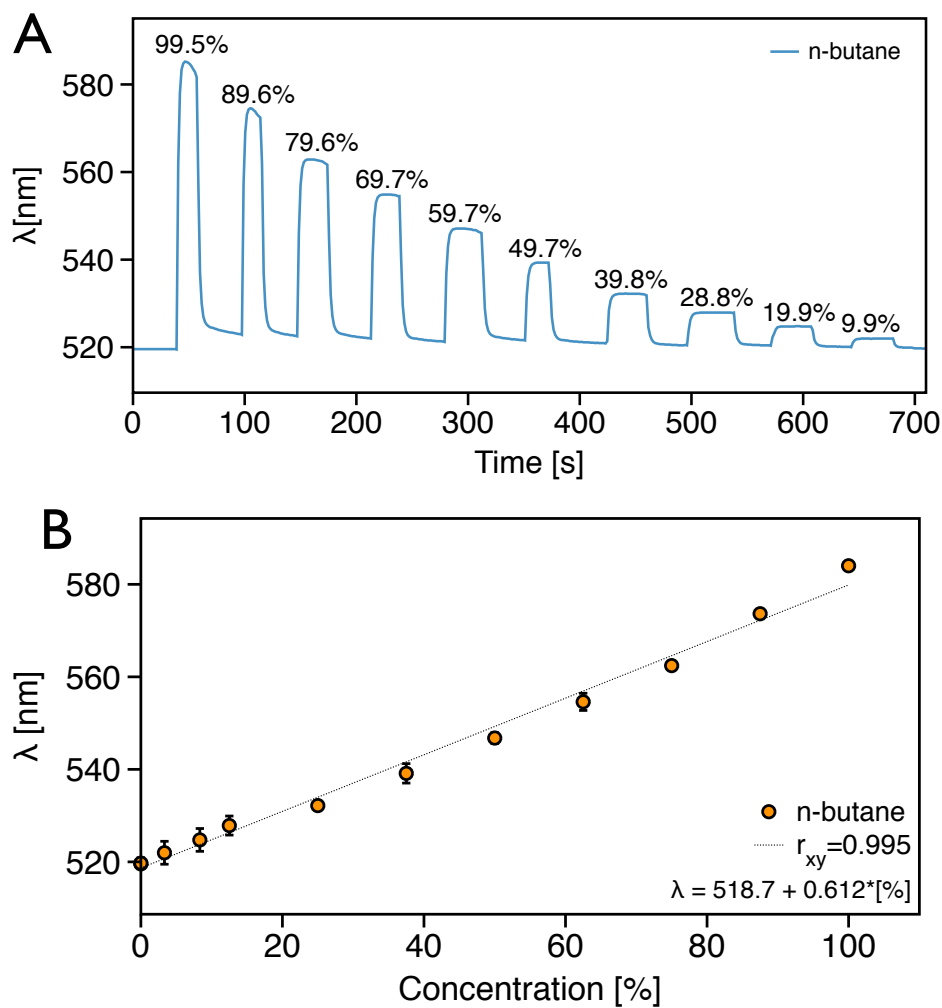
Figure 4.29: Holographic response to different concentrations of n-butane. (A) Continuous recording of the response cycles for air-gas injections of different concentrations. (B) Linear correlation of maximum wavelength values and n-butane gas concentration in % (v/v).
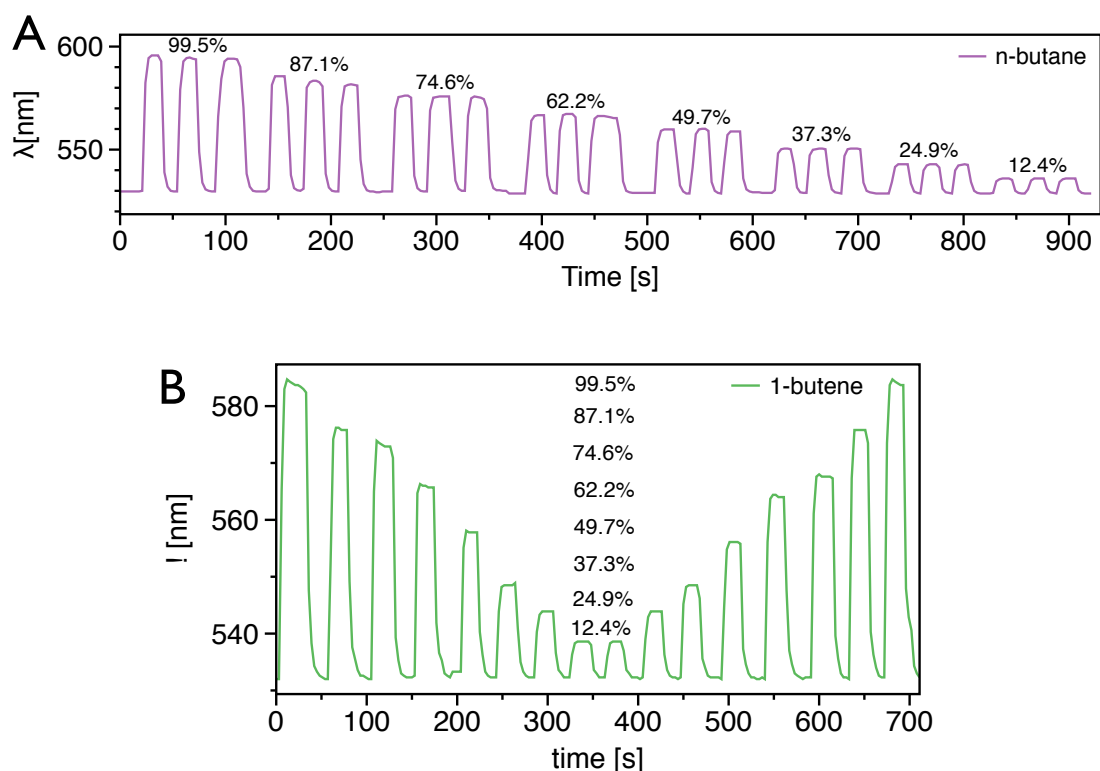
Figure 4.30: Repeatability and reversibility of the holographic response to hydrocarbon gas concentrations. (A) Cycles of exposure to concentrations of n-butane and repetitions. (B) Cycles of exposure from high concentration to low concentration and vice-versa for 1-butene.
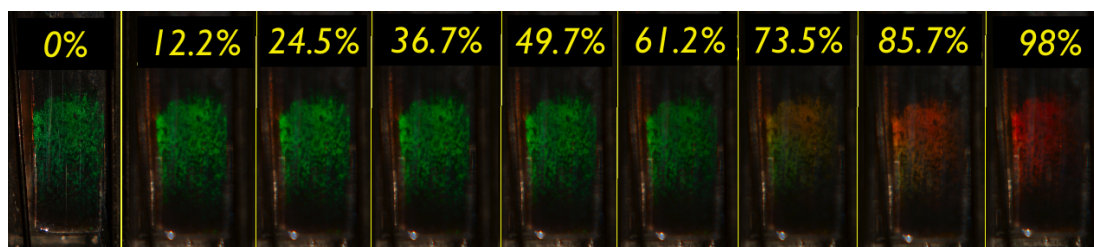
Figure 4.31: Photographs of the hologram reflection when exposed to 1-butyne. Green colour at 0% (v/v) and red colour at 98% (v/v). Digital images were taken with an SLR camera with a CMOS sensor; colour transition may not be obvious due to color perception, digital image processing and printing (*see* §4.9).
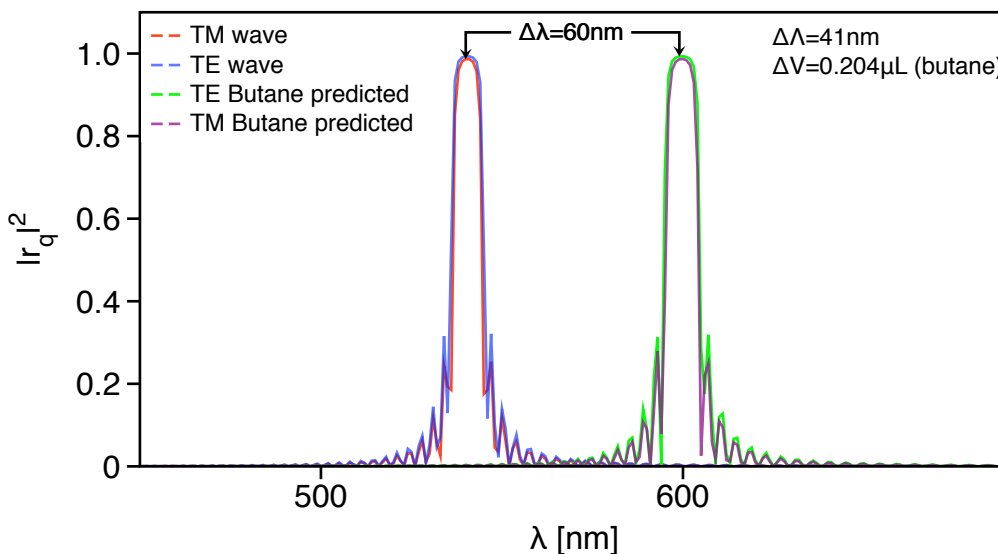
Figure 4.32: Mathematical prediction of holographic reflection peaks for exposure to n-butane. The model was adjusted to a 60nm wavelength shift to calculate the fringe swelling $\Delta\Lambda$.

The mathematical model was used to estimate the swelling of the polymer based on the wavelength shift $\Delta\lambda$. Assuming that n_1 and n_2 do not change, the contribution $\Delta\lambda$ is related to a change in $\Delta\Lambda$ only. Figure 4.32 shows the fit of the experimental parameters with the the wavelength allowed to vary for the 60nm shift for 99.5% (v/v) n-butane. The model showed that for this shift, a change of 20.5nm in thickness for the a and b layers ($\Lambda/2$) was required; this gives a total $\Delta\Lambda$ of 41nm. Considering the original dimensions of the films and fringes, the hologram gained $0.204\mu L$ in volume according to the model[a]. This volume should, in principle, be occupied by the total amount of gas held by the hologram at that given point. Thus, assuming that the absorption contributes to the swelling of the polymer so that the total volume of gas is preserved, and that it behaves as an ideal gas; $8.5x10^{-9}$mol of butane would be retained in that volume[b] equaling

---

[a]Initial dimensions were 8mm x 25mm x 0.0237mm with 187nm fringe spacing, *see* §4.2. The number of fringes across the slide was calculated to be 147 from the total thickness of $27.3\mu m$ and vertical spacing of 187nm(cos 7°); this gives a thickness of 147x20.5=3015nm. The final volume is then 8mm x 25mm x 0.0237+0.003mm.

[b]Volume per mol of ideal gas is $V_m = RT/p$, where the measured temperature T=23°C, atmospheric pressure p=101kPa and the universal constant R=8.314 $J/molK$, giving V_m =24.3L/mol [201].

3.7% (v/v) of n-butane in the film matrix. Only a portion of the molecules in the gas flow diffused into the film to interact with the polymer chains, and, according to the results, this amount is expected to vary with concentration.

A summary of the response of the sensor to all gases and concentrations is shown in Figure 4.33 and Figure 4.34; the results are expressed as a change in wavelength ($\Delta\lambda$) for the corresponding dilution from the lecture bottles. The figures include the results for different temperatures: 8°C, 22°C and 40°C, and even though the holographic response *per se* is not significantly affected by temperature, the interaction of the gases with the film may be. In fact, the response is at least 2-fold greater when the temperature is decreased by 14°C for all the hydrocarbons tested. The hologram being colder than the gas effluent might have helped to increase the interaction time and swelling.

Figure 4.35 includes the correlations between the holographic response and gas concentration for the three different temperatures tested. The plots show an obvious increase in $\Delta\lambda$ at colder temperatures and a decrease at higher temperatures. It is also important to notice that there is a linear correlation between concentration and holographic response; all correlation coefficients for the linear fits were >0.95 except 1-butyne. The graph for 8°C (Figure 4.35A) shows that n-butane and 1-butyne followed an exponential increase for higher concentrations (>60%) and not the linear trend observed for lower concentrations. The value corresponding to 100 % (v/v) n-butyne exceeded the detection range of the spectrophotometer, and at that temperature and concentration the butyne gas condensed on the hologram surface causing an apparent exponential increase in the signal[a]. The liquid form of the gas might have interacted considerably more with the polymer causing extra swelling. Unsaturated hydrocarbons also exhibited higher responses than their saturated counterparts at lower temperatures; similarly, higher molecular weight hydrocarbons exhibited greater responses than lower molecular weight ones. Thus, the holographic response is closely related to the molecular structure of the test molecules.

Figure 4.36 shows a more detailed view of the kinetic processes including the decay of the holographic signal when the gas was diffused out of the test chamber. In these experiments, the cuvette chamber with the hologram was left open to

---

[a]1-Butyne boiling point is 8.08°C [202]; just above the experimental temperature.
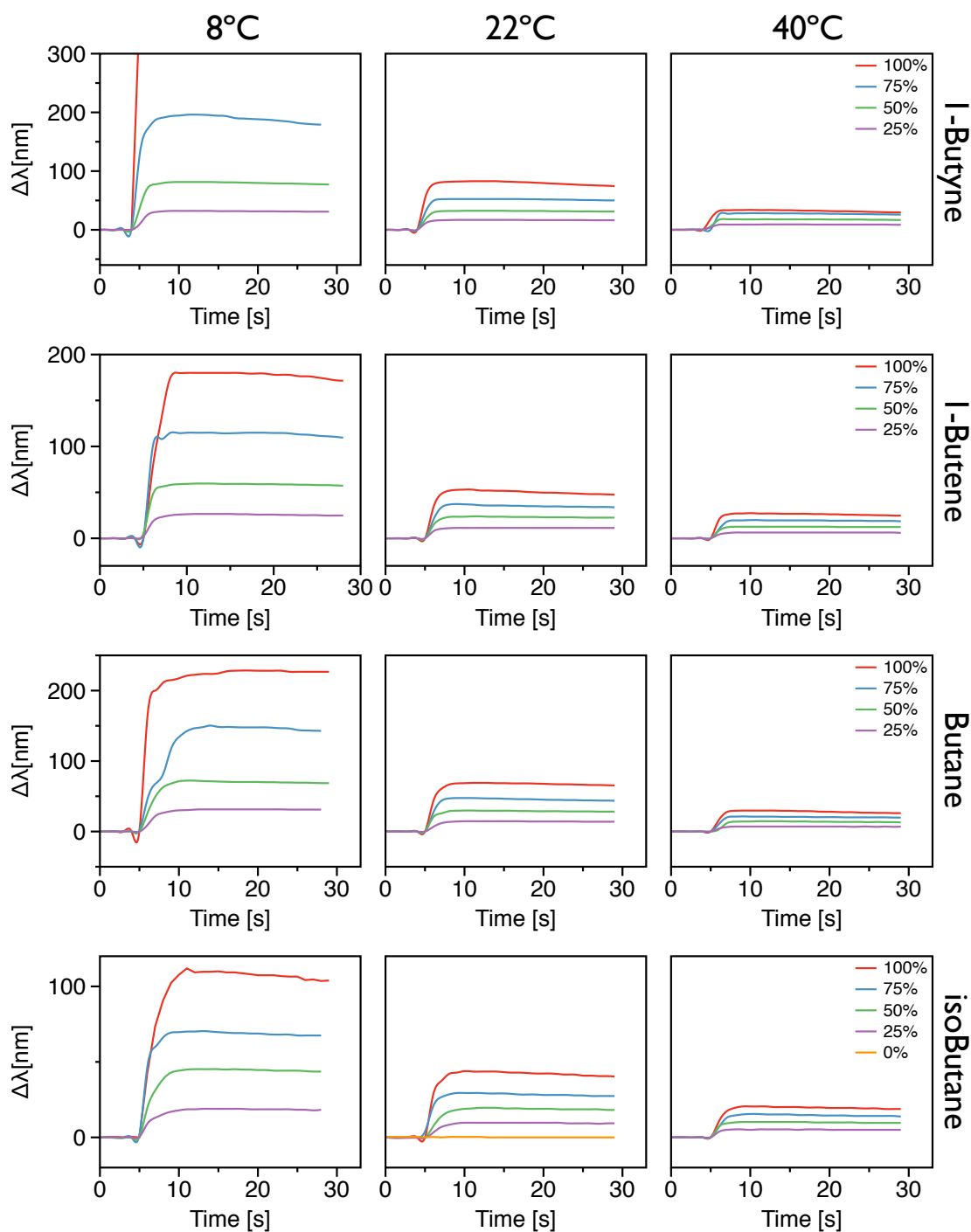
Figure 4.33: Holographic signal response to 1-butyne, 1-butene, n-butane and iso-butane at different temperatures and concentrations. Graphs grouped by analyte and temperature in rows and columns respectively. The signal reached equilibrium in no more than 5s of exposure for all concentrations, gas types and temperatures.
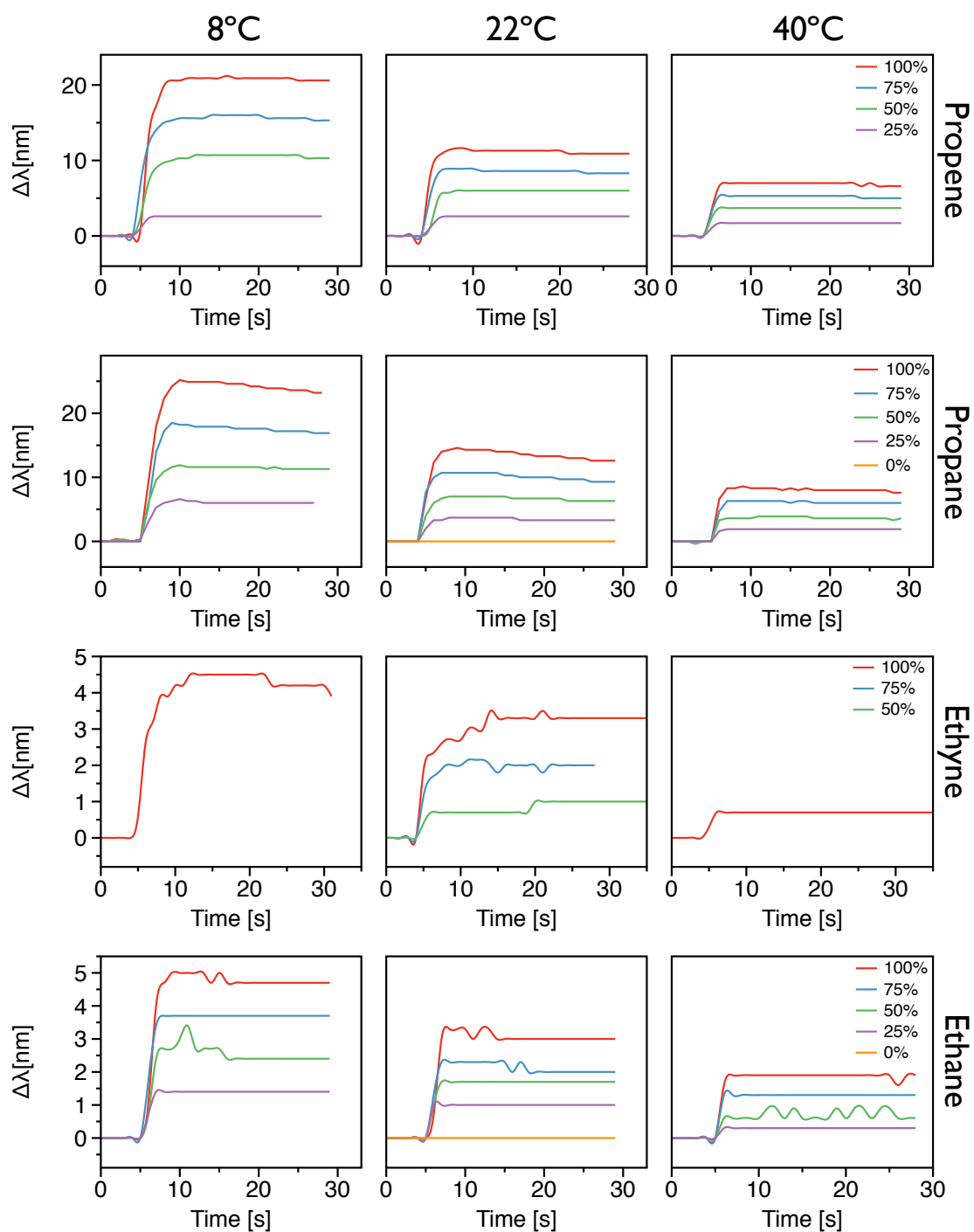
Figure 4.34: Holographic signal response to propane, propene, ethane and ethene at different temperatures and concentrations. Graphs grouped by analyte and temperature in rows and columns respectively. The signal reached equilibrium in no more than 5s of exposure for all concentrations, gas types and temperatures. Ethyne was scarce and only measured at the concentrations and temperatures shown.
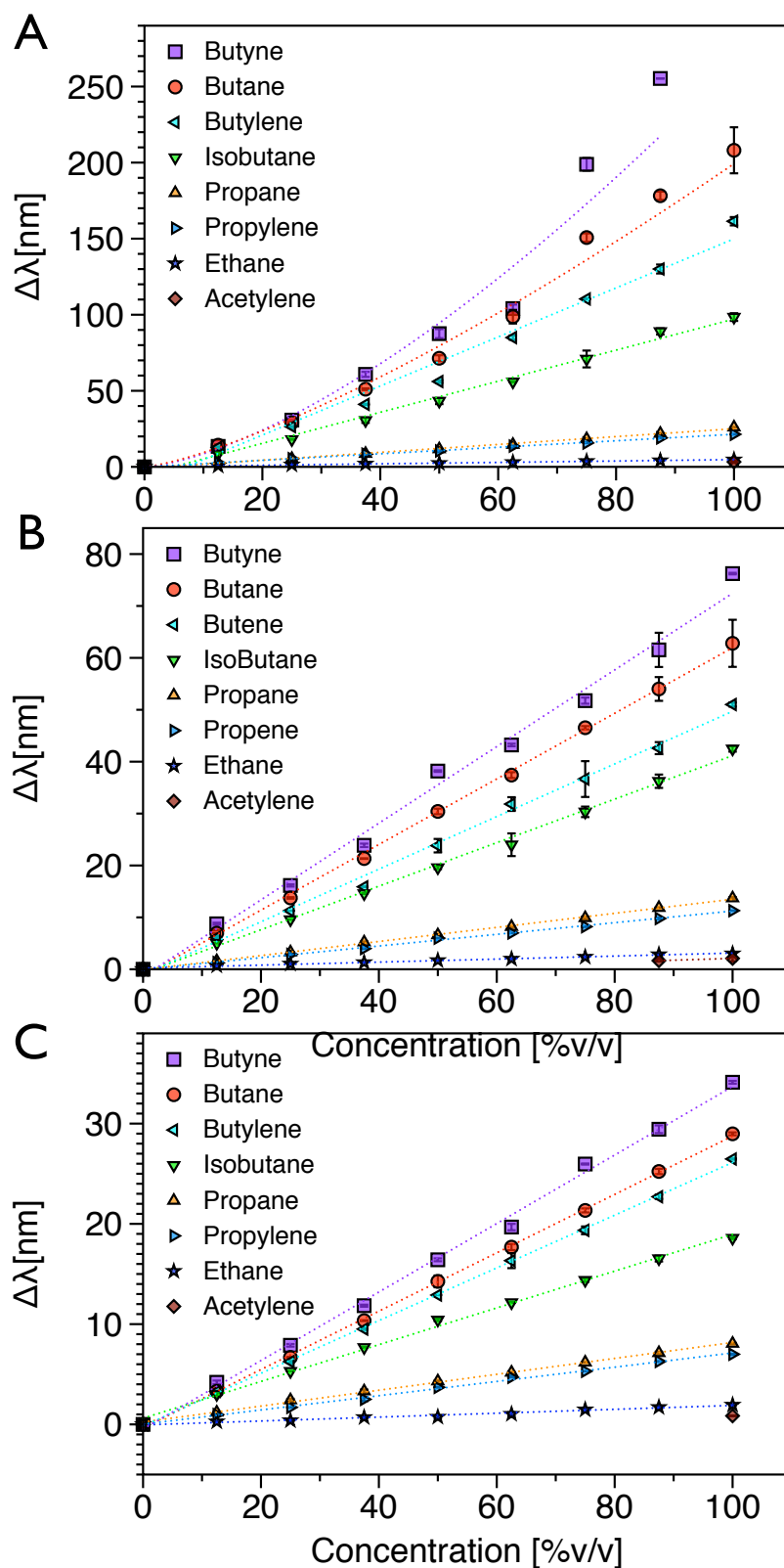
Figure 4.35: Correlation of holographic response to hydrocarbon gas concentrations at different temperatures. Concentrations tested in the range of 0-100% (v/v) for: (A) 8°C, (B) 22°C and (C) 40°C. The linear correlation coefficient for all plots except 1-butyne is $r_{xy} > 0.95$.
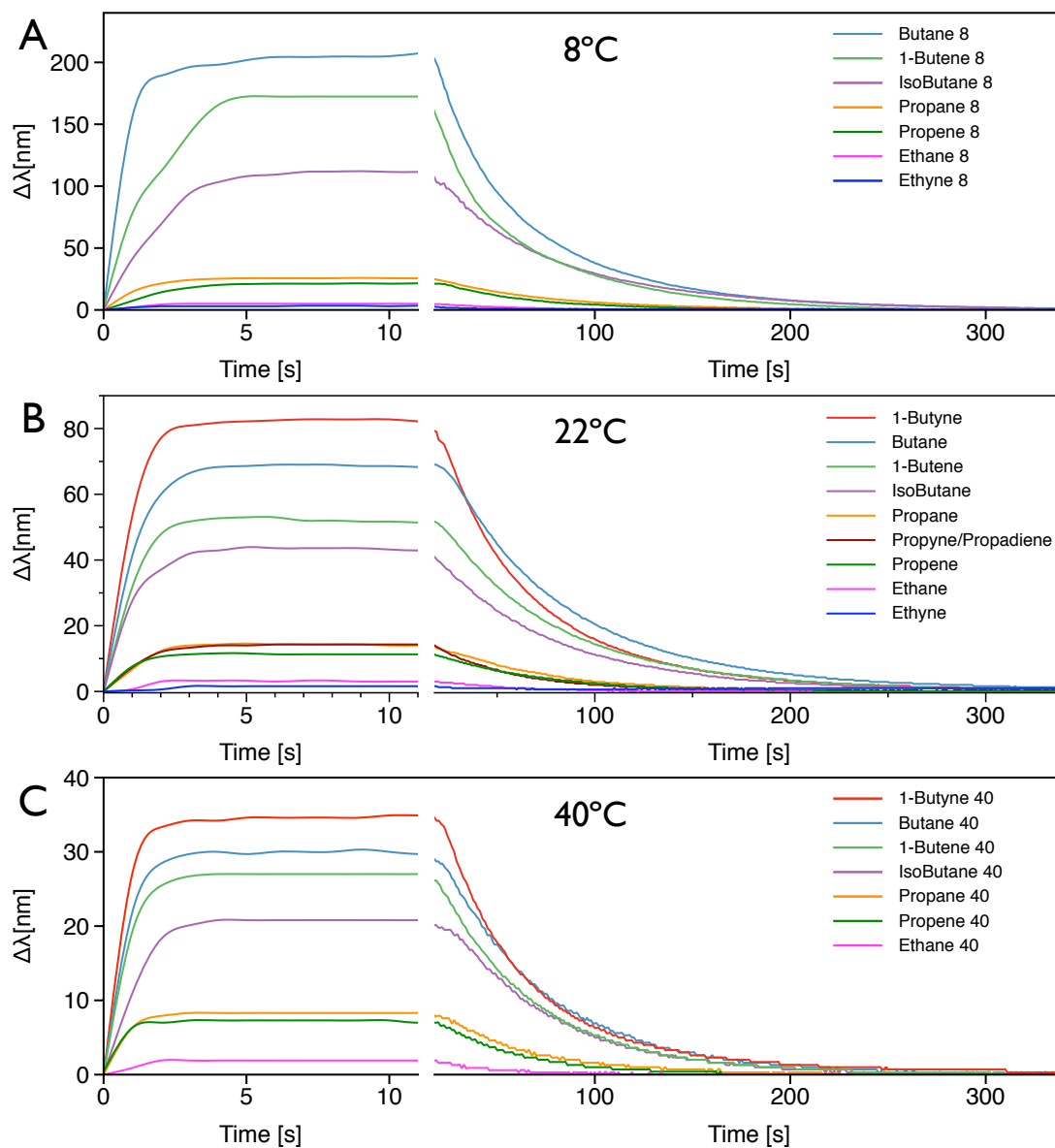
Figure 4.36: Holographic signal decay at different temperatures. (A) 8°C; (B) 22°C; and (C) 40°C. The release kinetics were monitored without external air flow perturbations. All plots corresponded to the maximum concentration of gas (> 99.5% (v/v)).
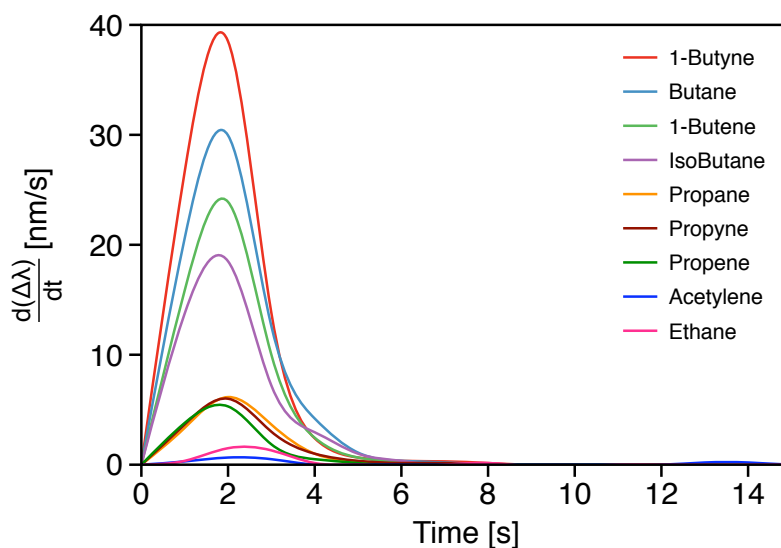
Figure 4.37: Holographic sensor response rate and equilibrium for gaseous hydrocarbons for maximum concentration at 22°C. Numerical differentiation by centered finite differences shows equilibrium: $d\Delta\lambda/dt = 0$, after 6s of exposure for all species.

the atmosphere after exposure to the gas; the gas was allowed to diffuse naturally out of the cuvette. The maximum response was reached in no more than 5s of exposure to the gas, and the signal stayed constant thereafter. Likewise, the wavelength returned to its original position in <300s. All types of gases reached maximum response at similar times: $\sim$2s for 40°C, $\sim$3s for 22°C and $\sim$5s for 8°C. Notwithstanding, smaller molecules took less time to diffuse out, and unsaturated hydrocarbons displayed a faster initial decay in wavelength. For higher temperatures there was a steep decay compared to that of lower temperatures, which was mainly noticeable for higher molecular weight hydrocarbons.

The holographic signal kinetics show response and decay profiles characteristic of absorption, desorption or diffusion processes [203–211]. This data could be coupled to models for those phenomena in further research to obtain information about the relation of the analytes with the physical properties of the materials.

Figure 4.37 shows the rate of response to hydrocarbon gases for the maximum concentration (> 99.5% (v/v)) at 22°C. The plot was acquired applying a finite central-difference derivative approximation to the values in Figure 4.36. The response rate varied for different types of hydrocarbons showing a general tendency
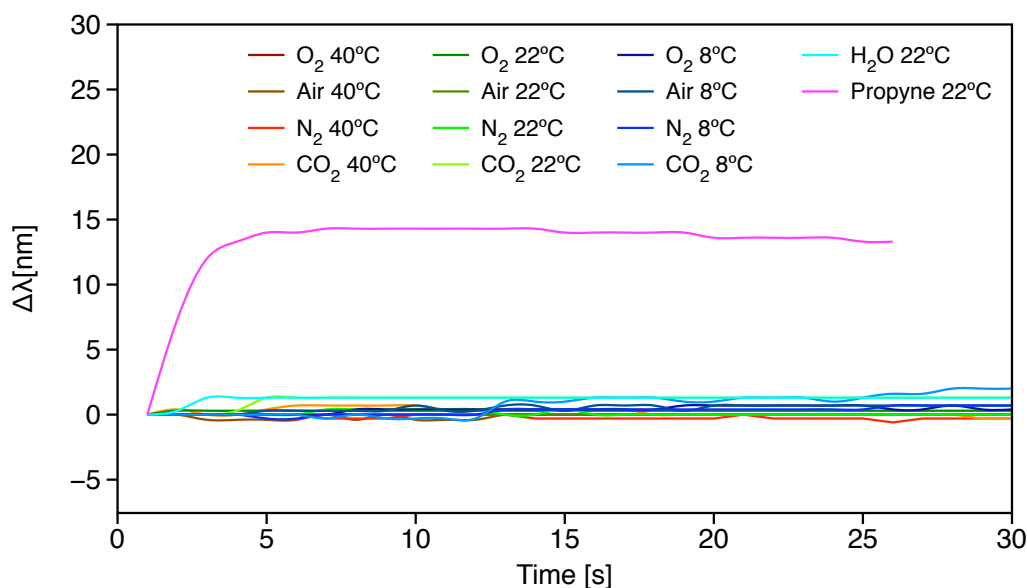
Figure 4.38: Holographic response to atmospheric gases at different temperatures. No significant responses were observed for O_2, N_2, CO_2, air and water at 8°C, 22°C nor 40°C. Response to propyne is included for comparison.

to increase for high molecular weight hydrocarbons or unsaturated gases. An important observation to emerge from the data comparison was that all hydrocarbons reached equilibrium (*i.e.* $d\Delta\lambda/dt = 0$) in <6s. This response rate is at least two orders of magnitude faster than other holographic sensors and as fast as commercially available gas sensors [134, 212]. These direct measurements can be taken in real-time for all concentrations and types of hydrocarbons. However, it was faster for higher temperatures and slower for lower temperatures.

The holographic sensors were neither responsive to common atmospheric gases (O_2, N_2, CO_2) nor to water. Figure 4.38 shows the response to the control gases and water for different temperatures; small variations for water were observed due to the refractive index differences at the interfaces. However, variations of less than 2nm are not significant compared to those caused by the hydrocarbon gases. Since the sensor is unresponsive to water, it becomes evidently suitable to operate in humid environments or aqueous solutions. Therefore, it can be coupled with biomedical devices for breath or other biological fluids, industrial processes or gas-enriched atmospheres.
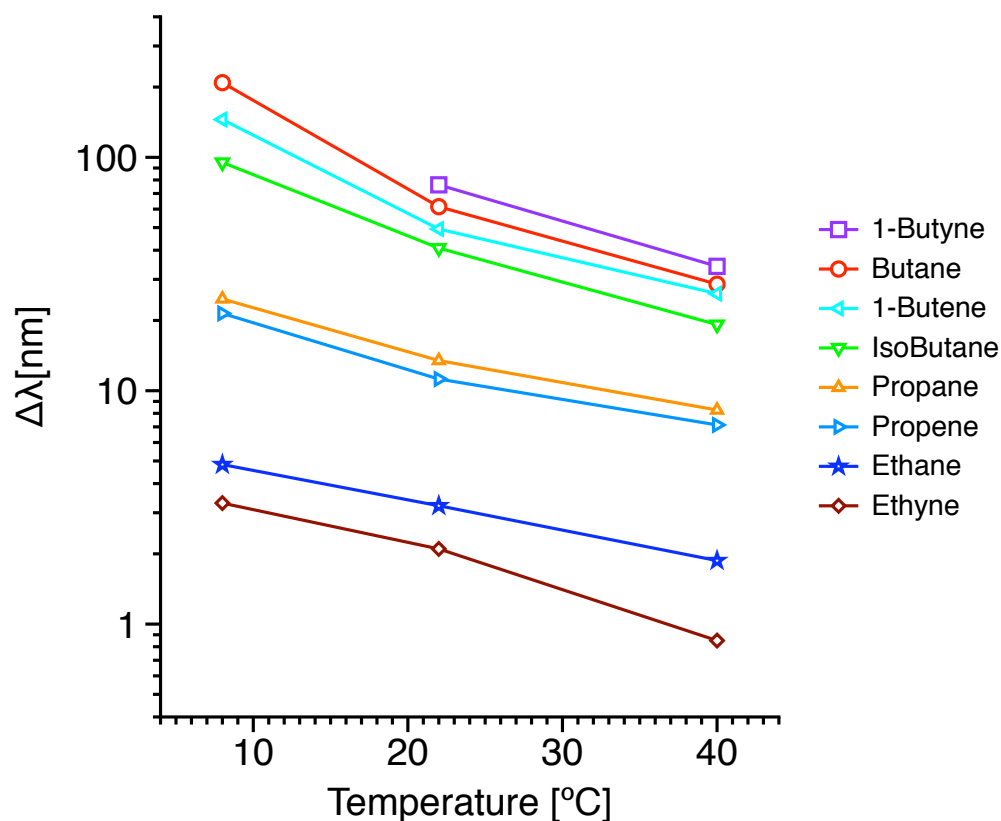
Figure 4.39: Holographic response versus temperature for all gaseous hydrocarbons. All plots correspond to the maximum concentration of gas ($> 99.5\%$ (v/v)). 1-Butyne at $8°C$ exceeded the spectrophotometer detection range.

Figure 4.39 summarizes the holographic response at different temperatures. It is apparent that the differences between hydrocarbon types, their number of carbons, or double or triple bonds generated different holographic responses. There is a trend in the increase of $\Delta\lambda$ with respect to a decrease in temperature.

Since larger molecules and low temperatures caused greater shift in replay wavelength ($\Delta\lambda$), it is likely that the sensor response is related to the thermodynamics of the gases in contact with the hologram's matrix. The boiling point is a physical property that can be related to the thermodynamics of the system for each type of molecule. Figure 4.40A shows the correlation for wavelength shift ($\Delta\lambda$) and boiling points at standard temperature and pressure[a]; there is an

---

[a]Values from RSC chemical database [213].
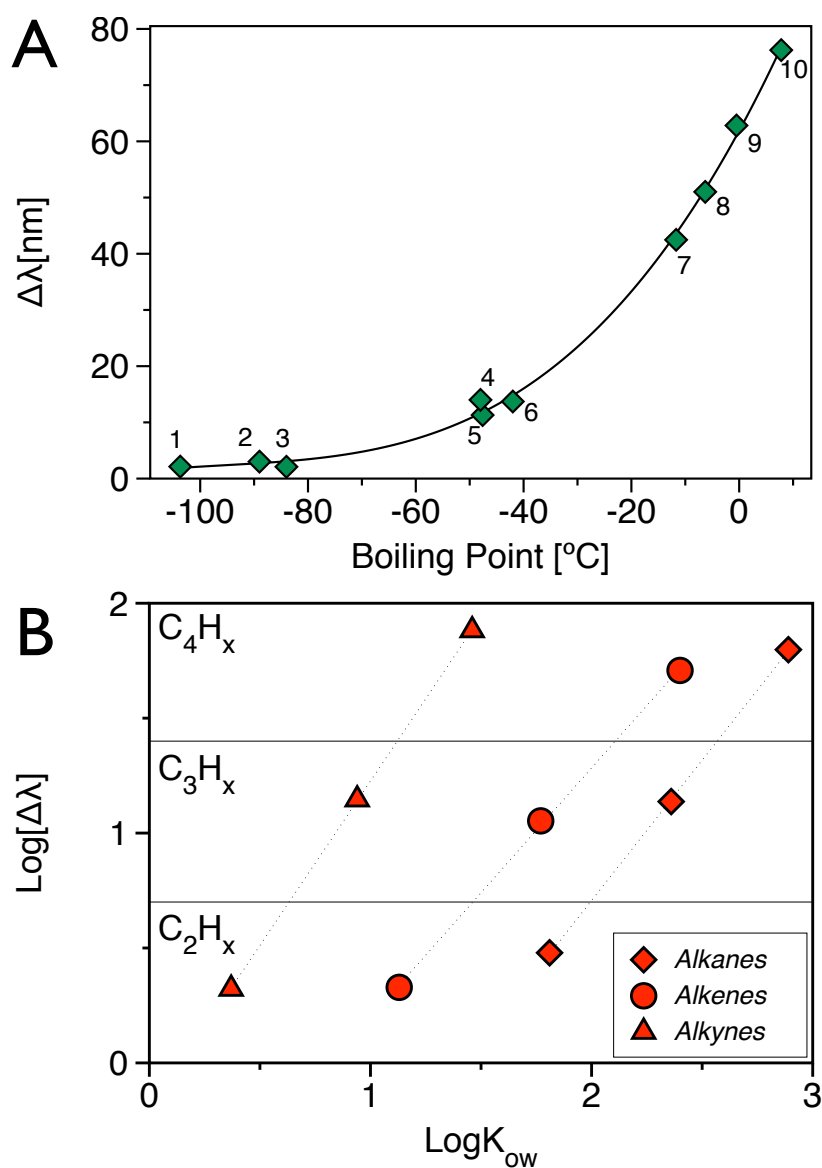
Figure 4.40: Correlation of the holographic response to the boiling point and octanol-water partition coefficient (K_{ow}) for each analyte. (A) Replay wavelength shift $\Delta\lambda$ versus boiling points: 1, ethyne; 2, ethene; 3, ethane; 4, propyne; 5, propene; 6, propane; 7, isobutante; 8, 1-butene; 9, butane; 10, 1-butyne. The fitted curve corresponds to $\Delta\lambda = 62e^{0.035BP}$ with 0.99 correlation coefficient. (B) $\log_{10}(\Delta\lambda)$ versus $\log K_{ow}$. The response is grouped for three homologous series of saturated and unsaturated hydrocarbon gases. All data points correspond to the maximum measured concentration at $22°$C.

exponential increase in wavelength shift as the boiling point decreases. Three groups of data points can be distinguished in the figure and correspond to gases with 2, 3 and 4 carbon atoms in their aliphatic chains.

Hydrocarbons form hydrophobic interactions with the surrounding molecules due to differences in polarity. The larger the molecule, the larger the volume and surface area to form interactions. Thus, the correlation with size and volume is more a correlation with the number of hydrophobic interactions that transfer the information of the gas type and concentration to the polymer. A physical property used to estimate the hydrophobicity of molecules is the octanol-water partition coefficient, K_{ow}. Partition coefficients relate to the polarity of the molecules according to their partition between two immiscible solvents with different polarities, in this case, octanol and water [213]. Figure 4.40B shows the sensor response as a function of K_{ow}. Not surprisingly $\Delta\lambda$ increased as the number of carbons in the hydrocarbons increased, and was distinct for the homologous series of alkanes, alkenes and alkynes. Therefore, the holographic response is related to the molecular structure of the analytes and their hydrophobicity. Although, this relationship applies to the hydrocarbon gases, it is not always valid for other volatile organic compounds in the liquid state (*see* §4.6.2 and Table A.2); thus, the relationship with the thermodynamics of the system should include other parameters or a more direct measurement of the interactions.

4.6.2 Liquids

The holographic sensor was able to detect a plethora of VOCs and distinguish between their molecular differences. Figure 4.41 shows the level of response to liquid analytes: Branched and unbranched alcohols, $-OH$; polyols, $(-OH)_x$; molecules with carbonyl groups >C=O; and controls. Different types of molecules showed different levels and rates of response, as expected due to their molecular differences. In this case, there was no direct correlation between the molecular size, boiling point, or K_{ow}, and the wavelength shift. The introduction of functional groups affected the response in an ordered fashion: For example, primary alcohols increased the response with the number of carbons in the aliphatic chain up to three, and then decreased. Molecules with more than one $-OH$ group showed no response at all, presumably because when the apolar surface of the molecule is

surrounded by polar moieties, hydrophobic interactions are reduced. Tertiary and secondary alcohols, however, conserve their hydrophobicity when the $-OH$ group is near the aliphatic chains and showed an increase in the holographic response; the same applied to cyclic alcohols.

High molecular weight ketones, alcohols and hydrocarbons in the liquid state such as n-pentane, 1-pentene, 1-pentyne, hexane, heptane, octane, decane, 4-methyl-2-pentanone, heptanone, hexanol, heptanol, iso-amyl alcohol and tert-amyl alcohol were also detected by the sensor. However, the replay wavelength response expanded rapidly beyond the visual range into the infrared and the signal lost intensity; thus, the maximum shift could not be detected under the selected test conditions. The detection range for high degrees of swelling could be improved using a different support material, increasing the cross-linking of PDMS to reduce its swelling or the holographic grating could be recorded at 266nm for the swelling to fall within the visual range.

VOCs in the liquid form had longer interaction times with the hologram's surface, which resulted in increased diffusion into the polymer film than was the case with the hydrocarbon gases. It should be noted that for most of the molecules with alkyl and alcohol groups, the holographic replay wavelength increased, whilst for molecules with more than four carbon atoms in the aliphatic chain it decreased. However, the correlation seems to be not only affected by size, volume or available surface area, but also by the nature of the interactions.

Oxygen, hydrogen and carbon have different electronegativities when they form covalent bonds. These differences result in a net polarity differentially distributed across the surface of the molecules. These differences in charges on the surface are called electrostatic potentials and it has been shown that the hydrophobic free energy, which causes the hydrophobic interactions, is strongly correlated to them [214]. Since hydrophobic interactions cause the PDMS chains to swell, then surface electrostatic potentials generate the holographic response. In other words, not only the volume and geometry of the molecule affect the response, but also the type of atoms in the molecules. Therefore, the sensor should be able to identify differences in the molecular structure of the analytes when in the pure form.

In terms of the response kinetics, liquid analytes were slower than the gaseous analytes. For most VOCs, the response reached 90% of the maximum after 120s of
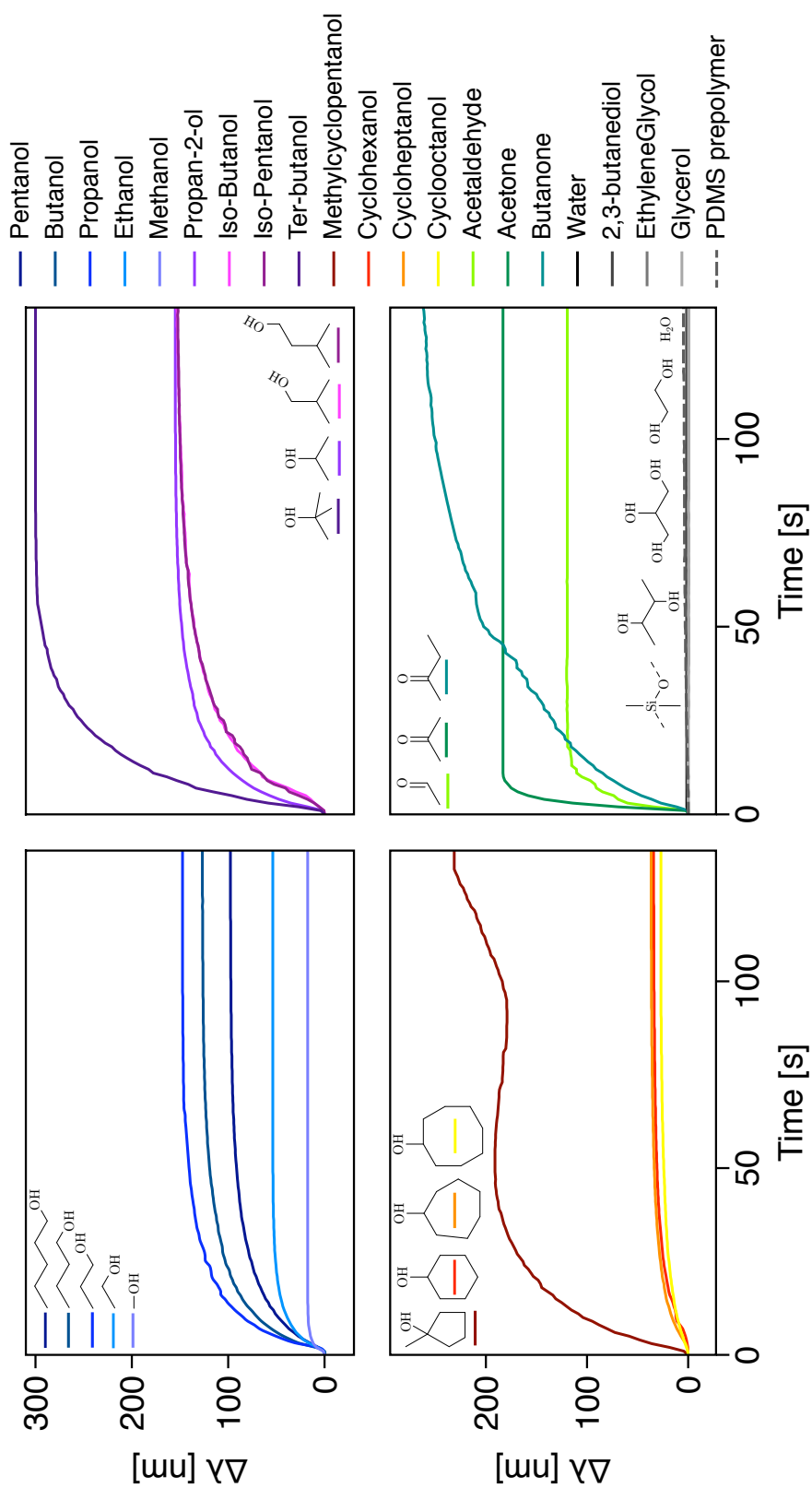
Figure 4.41: Holographic response to volatile organic compounds and liquid controls. The plots in the figure are grouped by analyte type: top-left, unbranched alcohols: pentanol, butanol, propanol, ethanol, methanol; top-right, branched alcohols: tert-butanol, propan-2-ol, iso-butanol, iso-pentanol; bottom-left, cyclic alcohols: methyl-cyclopentanol, cyclo-hexanol, cyclo-heptanol, cyclo-octanol; bottom-right, carbonyl groups, polyols and controls: ethanal, propanone, butanone, dimethylene glycol, ethylene glycol, water and non-crosslinked PDMS. The corresponding molecular structures are included in each plot for reference.
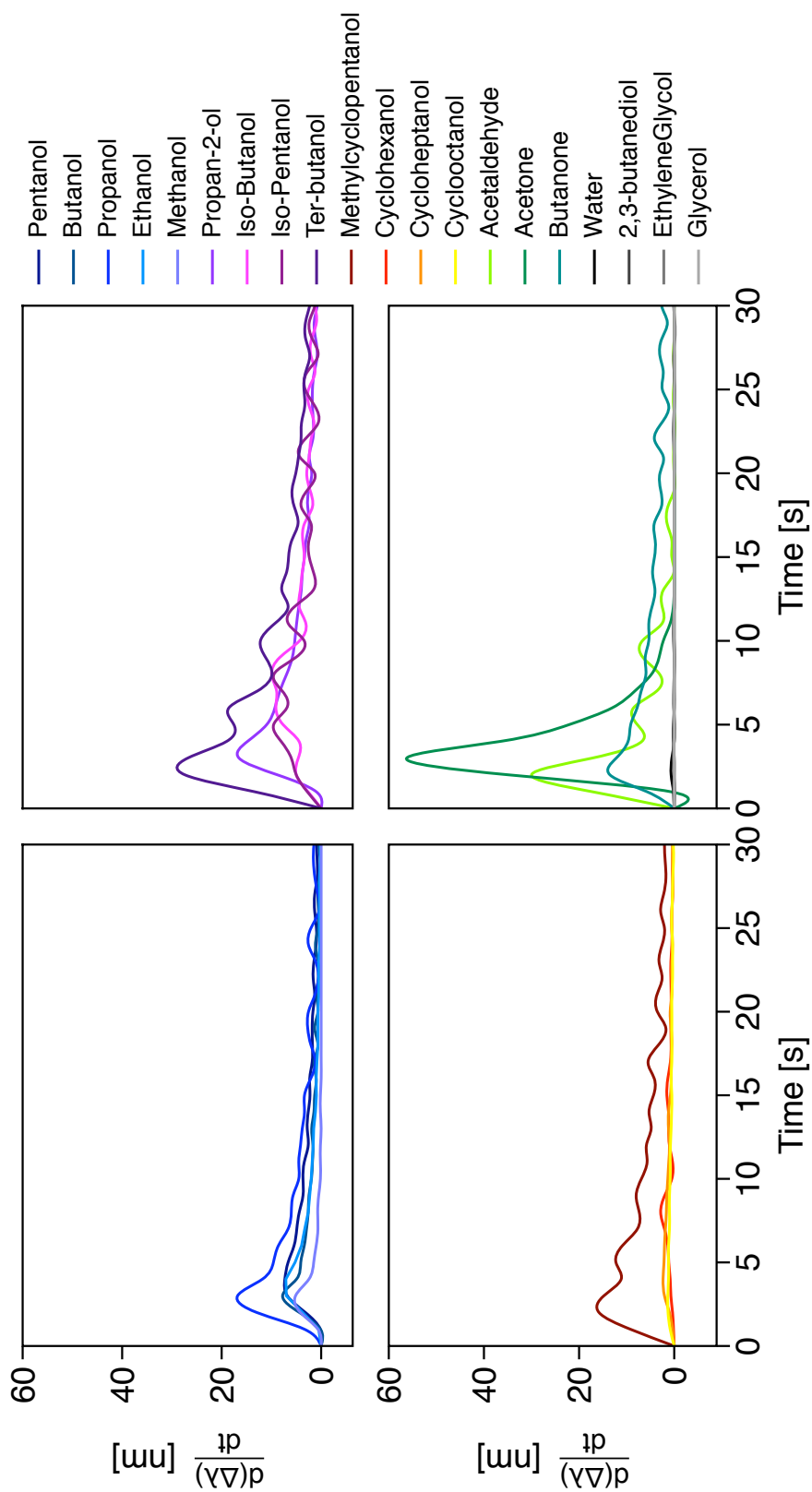
Figure 4.42: Holographic sensor response rate and equilibrium to VOCs. Numerical differentiation by centered finite differences shows equilibrium ($d\Delta\lambda/dt = 0$) after 120s of exposure for most types. Figure shows detail up to 30s.
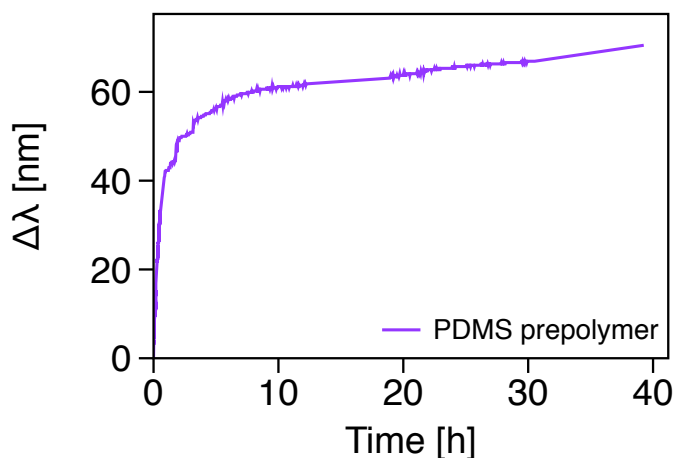
Figure 4.43: PDMS holograms response to PDMS prepolymer.

exposure. The rate of response was different for each VOC, with higher responses ($\Delta\lambda$) showing faster initial rates. A plot of the rates of response for all VOCs in Figure 4.41 is included in Figure 4.42. Larger molecules took longer to reach the maximum response compared to the smaller ones.

Figure 4.43 shows the response to PDMS prepolymer with the response continuing to increase at a slower rate for over 40h. This response was slower than all the other compounds, perhaps because the size of the prepolymer chains was larger and the analytes took longer to diffuse in. Expansion of the PDMS films and, therefore, the grating spacing, is a complex process that depends on the porosity of PDMS, the diffusion rate of the analytes; the absorption of the analytes on the polymer matrix, and the swelling of the polymer chains after absorption. Once the molecules travel into the film matrix, the polymer chains absorb them momentarily via Van der Waals' forces, particularly London dispersion forces. These forces transmit kinetic energy from the analytes when mixed with the polymer, making the chains swell as it will be explained in §4.7. Polymer swelling could contribute to the expansion of the intermolecular spaces, thereby assisting the diffusion and absorption of the analytes. These three phenomena, absorption, diffusion and swelling, in combination, form the basis for the holographic sensing of hydrocarbons and VOCs. Cyclopentanol, for example, showed a two-step swelling behaviour that might be caused by a combination of these phenomena;

however, further investigation is required to confirm this.

A PDMS holographic sensor is thus capable of detecting, not only different concentrations of hydrocarbon gases, but also different types of VOCs. The sensor response depends on the type of molecule and type of interactions between the PDMS polymer chains and the analytes. These interactions cause the polymer chains to swell, and the swelling causes the holographic replay wavelength to change. Therefore, it is important to understand the mechanisms of polymer swelling to correlate the sensor response with the interaction of the analytes.

The results presented in this section must be interpreted with caution because the analytes were tested separately and not as part of a mixture. Even though it is relatively easy to distinguish between two components in isolation (*see* §4.8), it might not be the same for a complex mixture including different types and concentrations of analytes. There are various ways for distinguishing between different species in complex mixtures, some reported in literature include neural networks for sensor arrays, or Principal Component Analysis (PCA) algorithms to discriminate between the sets of kinetic data [215, 216]. An attempt of the latter is included in §A.1 in the Appendix.

4.7   Mechanisms of polymer swelling

There is substantial 'empty' space between the polymer molecules that can be temporarily occupied by smaller analyte molecules. During this momentary permeation, the molecules interact with the polymer chains via electrostatic interactions and the mixture behaves collectively as a different material for as long as the interactions are present [217]. These interactions result in swelling or contraction in the bulk caused by changes in the local molecular conformations.

In the case of holograms, this change affects the grating dimensions, resulting in different wavelengths being reflected by the photonic structure. Therefore, the photonic effect can be related to the phenomena of polymer swelling by looking at the thermodynamics of the polymer-analyte mixing process.

4.7.1 Thermodynamics of PDMS-analyte interactions

To understand the thermodynamics of polymer-analyte interactions, it is necessary to understand first the thermodynamics of the single molecules, particularly the polymers. Single covalent bonds that link the atoms in the molecules are flexible, can rotate and rearrange in numerous spatial conformations [218]. Polymers, in particular, have long chains of bonded atoms which increase the possible number of conformations; thus, probabilistic approaches may be applied to estimate a final arrangement of polymer chains in space [218]. Although in theory all conformations are possible, the thermodynamics of the system may limit their number. Boltzmann described matter using 'statistical mechanics' to incorporate the mechanical properties of molecules and atoms [219]. He suggested that the entropy of a system is related to the probability of the system having certain arrangements or conformations: $S = \kappa \ln \Omega$, S is the total entropy, κ the Boltzmann's constant $(1.38 \times 10^{-23} \mathrm{JK}^{-1})$ and Ω the total number of ways of arranging the system [218].

When two or more molecules come close together and there are significant attractive forces between them, an interaction or a change will occur. In the case of polymer-analyte interactions, the polymer chains experience a change in conformation when mixed with the analytes. This change can be understood as a change in entropy, also called the 'entropy of mixing':

$$\Delta S_m = \kappa \ln \Omega \tag{4.2}$$

In this case, Ω is the total number of spatial conformations for the mixture of polymer and analyte. Flory and Huggins developed a theory to calculate the polymer conformations by arranging the polymer chains in grid lattices [218]. They defined the total number of molecules N_t as the sum of the number of polymer molecules and the analyte molecules N_2 and N_1 respectively. The Flory-Huggins solution theory was formulated for solvents and polymer mixtures; in this work, the 'solvents' are also the analytes. The permutations of the possible arrangements in the lattice can be calculated as: $\Omega = N!/(N_1!N_2!)$ [218]. This calculation can be performed for segments of the polymer or per molecule.

During the mixing process, not all the analyte molecules will interact with the

polymer segments; polymer-polymer interactions and analyte-analyte interactions are also present. The energy of the mixing process is only influenced by the polymer-analyte interactions; this energy is expressed as the enthalpy of mixing. Flory and Huggins proposed a expression for the enthalpy of mixing based on their lattice model:

$$\Delta H_m = \kappa \overline{T} \chi_{12} N_1 \upsilon_2 \qquad (4.3)$$

where υ_2 is the volume fraction of the polymer in the mixture, $\overline{T}$ is the temperature and χ_{12} is an energy parameter called the Flory interaction parameter. χ_{12} characterizes the rearrangement of the polymer chains due to the polymer-solvent interactions and is related to the energy per solvent molecule. It is also inversely proportional to temperature [218].

There should be free energy from the mixing process to allow the polymer to swell. This free energy of mixing (ΔG_m) is given by

$$\Delta G_m = \Delta H_m - \overline{T} \Delta S_m \qquad (4.4)$$

The cross-linking of the polymer in the PDMS chains reduces the molecular motility and leaves a porous material in which the intermolecular spaces can be in-filled with analyte molecules. When a cross-linked polymer is mixed with a solvent, the molecules tend to distribute homogeneously within the total volume. This results in the film expanding and filling itself with solvent molecules, in this case with the analytes. The distance that is gained between the molecules is the product of the forces pushing and pulling the polymer chains away from their original positions. This mechanical work occurs because there is 'free energy' available. Substituting Equations 4.2 and 4.3 in Equation 4.4 gives the Gibbs free energy of mixing ΔG_m in terms of the polymer-analyte interaction parameter χ_{12}:

$$\Delta G_m = \kappa \overline{T} \left(\chi_{12} N_1 \upsilon_2 - \ln \Omega \right) \qquad (4.5)$$

According to this equation, the main contributions to the free energy for swelling are temperature, volume fraction and the interaction parameter. This relationship strongly agrees with the experimental results presented in this work: Temperature, concentration and type of molecule were the main factors affecting the holographic response.

In the Flory-Huggins theory, a positive ΔG_m indicates that dissolution will not occur, whereas a negative ΔG_m indicates that dissolution will occur and there will be available energy for swelling [218]. For a given concentration and temperature, the only term that affects ΔG_m is χ_{12}. Larger values of χ_{12} will decrease the total free energy for swelling, and smaller values will favour it. In summary, the swelling of the polymer, therefore the holographic response, depends primarily on the value of χ_{12}.

One question that needs to be asked, however, is whether it is possible to measure the molecular interactions to calculate χ_{12} for each polymer-analyte pair. The answer is no; measuring forces at the molecular scale for all the possible polymer-solvent combinations is practically impossible. However, it is possible to calculate them indirectly. Let E^c be the sum of all the individual intermolecular forces that keep molecules together. The strength of these attractive forces can be determined inversely by measuring the total energy required to separate the molecules completely. This means, to put all the molecules in an 'ideal gas' state with no contacts or interactions between them. In other words, the energy required to break all interactions should be proportional to the total number of interactions and their strength. This energy is defined as the molar energy of vaporization and can be calculated experimentally for each molecule via the heat of vaporization ΔH_v. ΔH_v is related to the cohesive energy density E^c by $E^c = (\Delta H_v - RT)/V_m$; where V_m is the molar volume. Furthermore, Scatchard and Hildebrand proposed an equation for ΔH_v in terms of E^c by defining the solubility parameter of a substance δ as the square root of the cohesive energy density:

$$\delta = \sqrt{E^c} = \sqrt{\frac{\Delta H_v - RT}{V_m}} \tag{4.6}$$

the equation is:

$$\Delta H_m = V_t(\delta_1 - \delta_2)^2 \upsilon_1 \upsilon_2 \tag{4.7}$$

where V_t is the volume of the mixture, δ_1, δ_2, υ_1 and υ_2 the solubility parameters and volume fractions for the solvent and polymer respectively [218, 220, 221].

By equating the equations for ΔH_v, it is possible to relate χ_{12} to E^c

$$\chi_{12} = \frac{V_t}{RT}(\delta_1 - \delta_2)^2 \tag{4.8}$$

where δ_1 and δ_2 are defined as the solubility parameters for analyte and polymer respectively.

There are theories that allow the calculation of δ using information from the molecular structure of the mixing components [218]. Different chemical groups in a molecule have different molar attractions that can be added up to calculate δ^a. Knowing δ for both polymer and analytes should give an accurate prediction of the level of interaction and, thereby, the holographic response of the sensor.

As discussed previously, for a fixed temperature and concentration, the only contribution to the free energy of swelling is χ_{12}. χ_{12} depends mostly on the difference between δ_1 and δ_1 values for the analyte and PDMS. Hence, by substituting Equation 4.8 in 4.5 with constant concentration, temperature and number of conformations, the free energy of swelling is a function of the difference in solubility parameters $(\delta_1 - \delta_2)$. Since the solubility parameter of the polymer δ_2 will not change, the free energy for swelling is mainly dependent on δ_1 which is renamed as δ for simplicity. Then, $\Delta G_m = f(\delta)$.

Since the relationship between the intermolecular forces and the polymer swelling has been established, the only relationship to be found is the one between $\Delta\lambda$ and δ. Thus, an empirical approach was used to link the experimental data to the thermodynamics of swelling. Values of δ for all the analytes were calculated or collected from different sources, as specified in Table A.2 in the Appendix.

Figure 4.44 shows a plot of the holographic response $(\Delta\lambda)$ against the solubility parameters (δ). The figure includes the molecular structures of the analytes, in order to relate to previous discussions on molecular interactions and molecular geometry. The figure also includes different values of δ found for PDMS prepolymer with an average of 16.2 MPa$^{1/2}$ [146, 222, 223].

The experimental data strongly agrees with the thermodynamic theory for polymer swelling. Thus, it is facile to establish a correlation between the holographic response and intermolecular interactions. The following relations were found: $\delta = 10.81\Delta\lambda^{0.05484}$ for most gaseous hydrocarbons and $\delta = 43.63\Delta\lambda^{-0.1358}$ for all liquid VOCs. Molecules with similar values of δ to those of PDMS exhibited higher responses. Likewise, substances with dissimilar values of δ, such as

---

^{a}for example $-CH_3$, $-CH_2-$ and $= CH-$ have different molar attraction values F_i that affect the value of δ as $\delta = \sum_{i=1} F_i/V_m$.

Figure 4.44: Holographic sensor response $\Delta\lambda$ versus solubility parameters δ for hydrocarbon gases and volatile organic compounds. The chemical formulae of the molecules are shown in the legend: 1, ethyne; 2, ethene; 3, ethane; 4, propene; 5, propane; 6, iso-butane; 7, 1-butene; 8, butane; 9, tert-butanol; 10, butanone; 11, propanone; 12, iso-butanol; 13, propan-2-ol; 14, iso-pentanol; 15, propan-1-ol; 16, butan-1-ol; 17, ethanal; 18, pentan-1-ol; 19, 1-butyne; 20, ethanol; 21, methanol; 22, propyne/propadiene; 23, ethylene glycol; 24, glycerol; 25, water. δ for PDMS has been reported to have different values within the range 14.9-7.5 MPa$^{1/2}$, depending on the cross linking, chain length, etc. Fitting equations and absolute values of correlation coefficients are included adjacent to the fitting curves.

water or glycerol, displayed limited or no holographic response.

In conclusion, there is a strong correlation between the holographic response and the solubility parameters. Thus, these parameters can be used to predict the sensor response to any organic molecule with relatively good accuracy by interpolating them in the plot of Figure 4.44.

4.7.2 Molecular dynamics simulations

The solubility parameters are an indirect measurement of the intermolecular interactions which depend on the surface electrostatic potentials of the molecules. The electrostatic potential is determined by the differences in electronegativity in the atoms or radical groups in a molecule. These differences are caused by charge perturbations by the electrons in the atoms and bonds that can be modeled using molecular dynamics simulations. Moreover, there is extensive research work on how to calculate or estimate cohesive energy densities based on molecular dynamic simulations [224].

Molecular dynamics simulations allow the capture of a snapshot of the molecules at equilibrium. Molecules are in constant movement, always occupying the empty intermolecular spaces. Inter-molecular force fields pull the molecules together while their relative velocities keep them apart; these two factors preserve the distance between the molecules in equilibrium. The result of molecular dynamics simulations is a visualization of the spatial arrangement of the molecules and their intermolecular spaces.

Figure 4.45 shows the results for different visualizations of a single 18 unit poly(diemethylsiloxane) chain: Figure 4.45A is the randomly arranged 18 unit chain; Figure 4.45B shows the same chain after energy minimization for finding the best conformation; Figure 4.45C shows the atoms as spheres with Van der Waals' radii; and Figure 4.45D shows the Van der Waals' surface in solid colour and the solvent accessible surface dotted. The Van der Waals' surface separates the Van der Waals' spheres from the outer space and the 'solvent accessible surface', also known as the Connolly surface, represents the points at which a solvent sphere can touch the Van der Waals' surface[a]. The latter was used for the simu-

---

[a]A solvent probe with a fixed radius of 1.4Å is used to surround the Van der Waals' surface and draw the solvent accessible surface A_{SAS} [225].
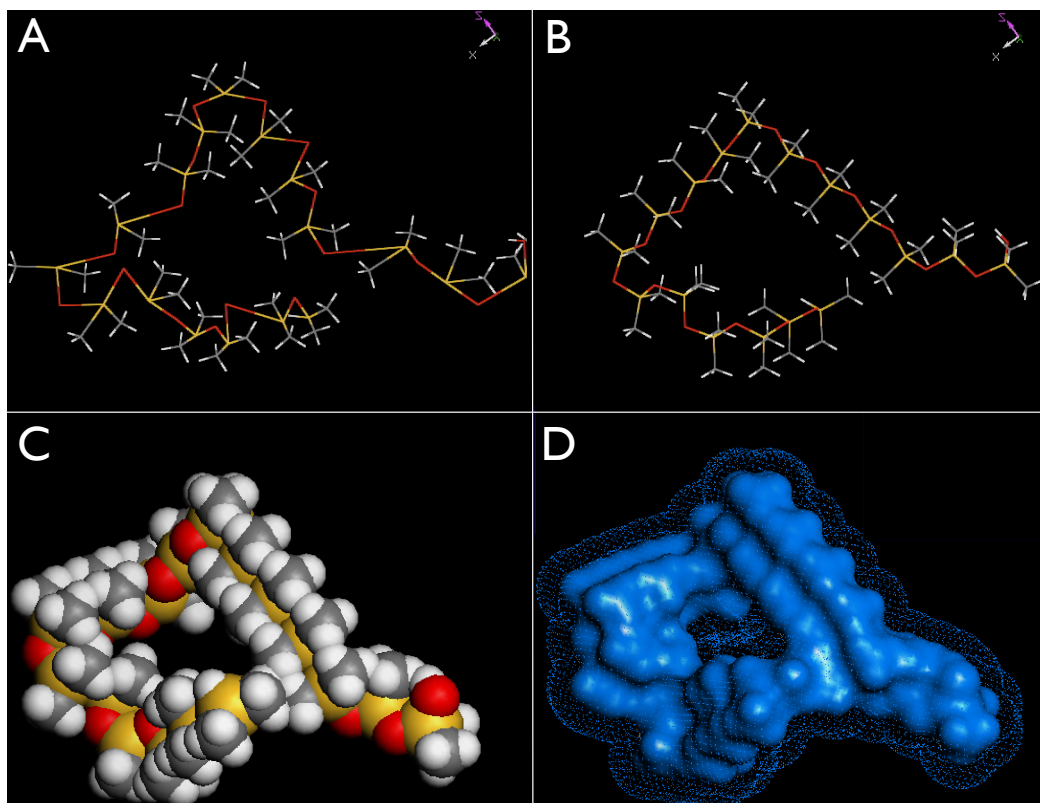
Figure 4.45: Visualizations of a single 18 unit PDMS chain. Si atoms in yellow, O atoms in red, C atoms in grey, and H atoms in white. (A) Randomly arranged chain. (B) Best conformation with bond lengths and orientations corrected after energy minimization. (C) Atoms as spheres with Van der Waals' radii. (D) Van der Waals' surface in solid colour and solvent accessible surface in dots.

lation of interactions between the PDMS polymer matrix and the analytes.

The PDMS polymer chains were assembled to produce an atomistic model of the cross linked PDMS films as described in the methodology (§3.6). The number of chains and lengths used matched the ones reported in the literature [146, 169–171]. The prepolymer and cross-linker chains were built separately and then linked randomly at a 10:1 ratio using the defined attachment points. Figure 4.46 shows the different steps taken and the final cross-linked PDMS chains.

In order to create a more realistic simulation, the cross-linked PDMS unit from Figure 4.47A was packed into a 4.7nm side cube shown in Figure 4.47B. The cube contained 10 cross-linked units displayed in Figure 4.47C with a total of 8530 atoms of the 7 types used. Figure 4.47D shows the atoms as Van der Waals' spheres and their respective surface. The resulting lattice conformation was optimized by applying a 5000 iteration energy minimization. The final result was a PDMS cell of cross-linked polymer shown in Figure 4.47E. The PDMS cell can also be visualized as a solvent accessible surface shown in Figure 4.47F. The surface area was calculated to be 13122Å^2 with a 80861Å^3 occupied volume and 23239Å^3 free volume. The free volume on the outer side of the surface is the one available for the analytes to fill in the polymer film and interact with the polymer chains.

Once the polymer matrix was constructed, simulations were carried out to obtain information about the interactions with the analytes. Analyte molecules were loaded into the cross-linked PDMS cell; the model takes into account the interaction parameters of the analytes and calculates the sorption sites in the cubic cell. This results in a subsequent rearrangement of the polymer matrix. Figure 4.48 and Figure 4.49 show the final results for loading molecules with 5000 steps of energy minimization. Butane, butanol and butanone were chosen for these simulations; the figures show the changes when loading one molecule and the maximum number of molecules allowed per cell. The maximum number that was loaded depended on various parameters: The strength of the interactions or absorption with the polymer chains; the polarity of the molecule; the kinetic energies of the molecules; etc. The number of molecules loaded is included in the Figure captions. There was a direct correlation between the number of molecules absorbed and an decrease in free volume. This volume change is the one that affects the bulk swelling of the polymer which is responsible for fringe expansion,
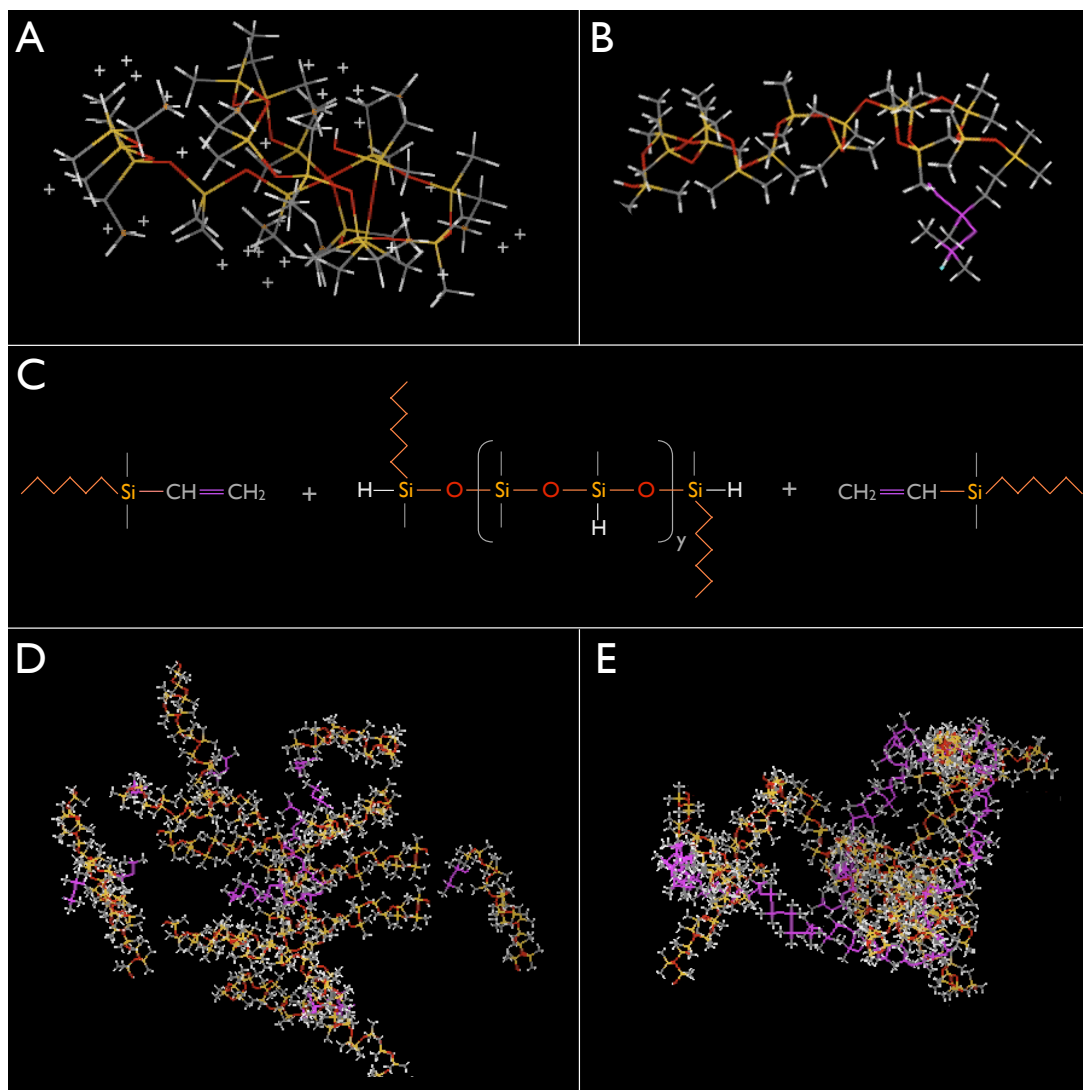
Figure 4.46: Molecular modeling of a PDMS cross-linked chain. (A) Cross-linker chain and attachment points in purple. (B) Prepolymer with cross-linking reaction sites in purple. (C) The cross-linking reaction with colour coded atoms [169]. (D) 10:1 ratio of prepolymer to cross-linker molecules with cross-linking sites in purple. (E) Final cross-linked PDMS chain with the backbone highlighted in purple.
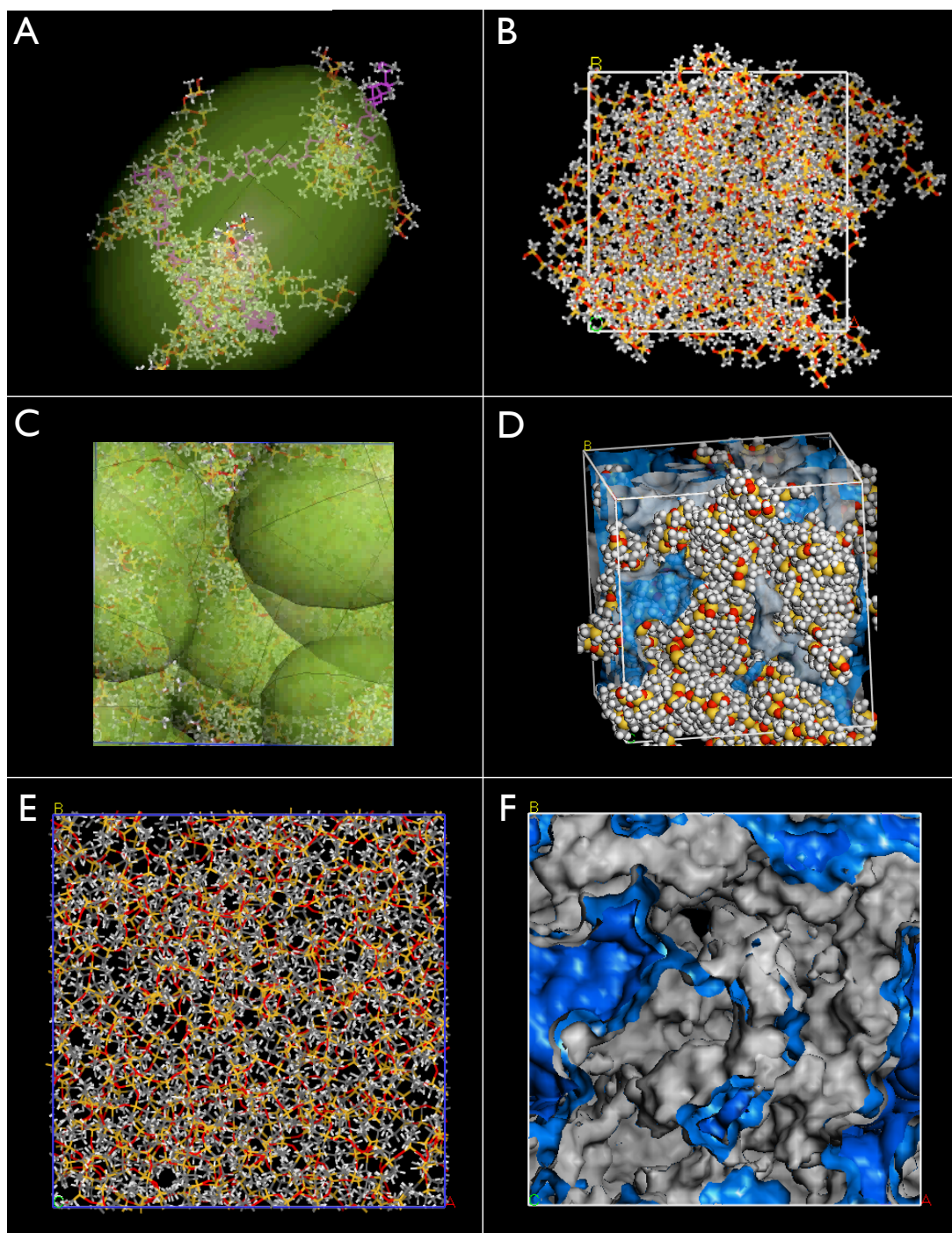
Figure 4.47: Packing of PDMS cross-linked units into a $\sim$104nm^3 cell. (A) Cross-linked PDMS unit used for the packing highlighted with a green ellipsoid. (B) 4.7nm side cube packed with the cross-linked units. (C) The trimmed cube allowed 10 cross-linked units to be packed, shown as green ellipsoids. (D) Atoms represented as Van der Waals' spheres with the Van der Waals' surface. (E) Cubic lattice after energy minimization; atoms and bonds represented as sticks. (F) Cubic lattice showing Van der Waals' and solvent accessible surfaces; inner surface in grey and outer surface in blue.

Table 4.1: Geometry results for the molecular simulations of solvent accessible surface, occupied volume and free volume. Values for the PMDS cell without molecules are: 13122Å^2 for surface area, 80861Å^3 for inner volume and 23239Å^3 for free volume.

Solvent accessible surface	Butane +1	Butanol +1	Butanone +1
Area [Å^2]	4048	4037	4018
Free Volume [Å^3]	3392	3381	3381
Inner Volume [Å^3]	100708	100517.57	100718
	Butane +41	Butanol +35	Butanone +34
Area [Å^2]	572	520	727
Free Volume [Å^3]	259	229	335
Inner Volume [Å^3]	104841	103870	103764
	Butane only	Butanol only	Butanone only
Area [Å^2]	249	265	250
Inner Volume [Å^3]	324	354	332

and therefore the change in reflected wavelength of the hologram. Table 4.1 summarizes the results for the calculated surface area, occupied volume and free volume after loading butane, butan-1-ol and butanone; it also includes the values for the individual molecules.

It was possible to estimate the number of molecules per unit cell from the holographic response using the previously calculated volume gain from the experimental data. For 99.5% (v/v) n-butane the volume gained per slide was $0.204\mu\text{L}$, corresponding to 3.7% (v/v); this corresponds to 10 molecules of butane in the cubic cell. This value is obviously lower than the maximum possible load because the absorption of butane molecules depends, not only on the concentration of butane, but also on the rate of diffusion into the film, the swelling and the absorption. A further study with more focus on these physical phenomena and their relation with the holographic response kinetics is, therefore, suggested.

4.8 VOC sensing applications

Since the sensing capabilities of a PDMS hologram for hydrocarbons and VOCs have been demonstrated, it is possible to use the sensor in an appropriate application. A common problem with VOCs is their presence in water as pollutants [226]; in fact, some VOCs are highly toxic and cause severe environmental
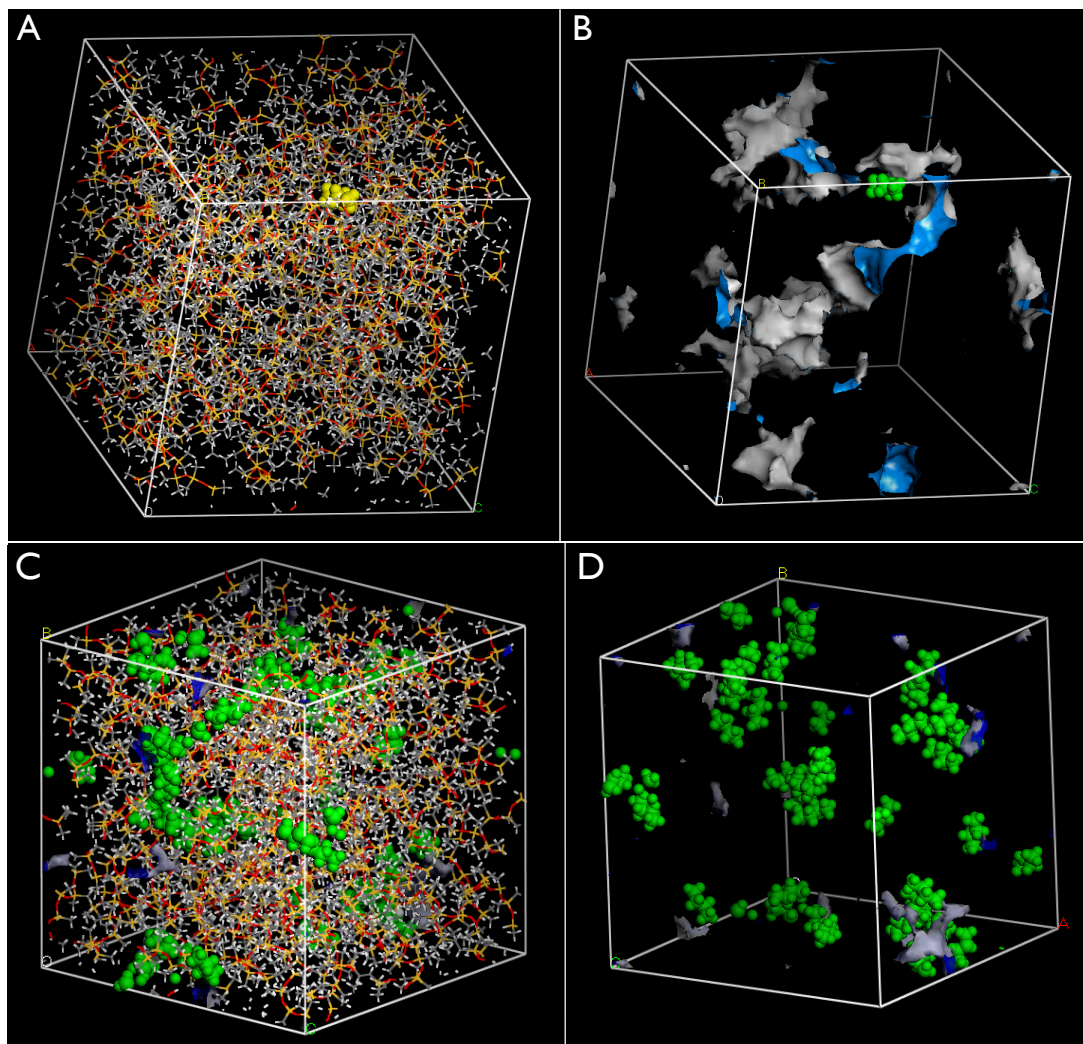
Figure 4.48: Molecular simulation of loading butane molecules into the PDMS polymer matrix. (A) Loading of a single butane molecule per cubic cell, in yellow. (B) Solvent accessible surface for the loading of one butane molecule, in green. (C) Loading of 99 butane molecules to the calculation yielded a maximum of 41 per unit cell. (D) Solvent accessible surface for the maximum load of butane molecules.
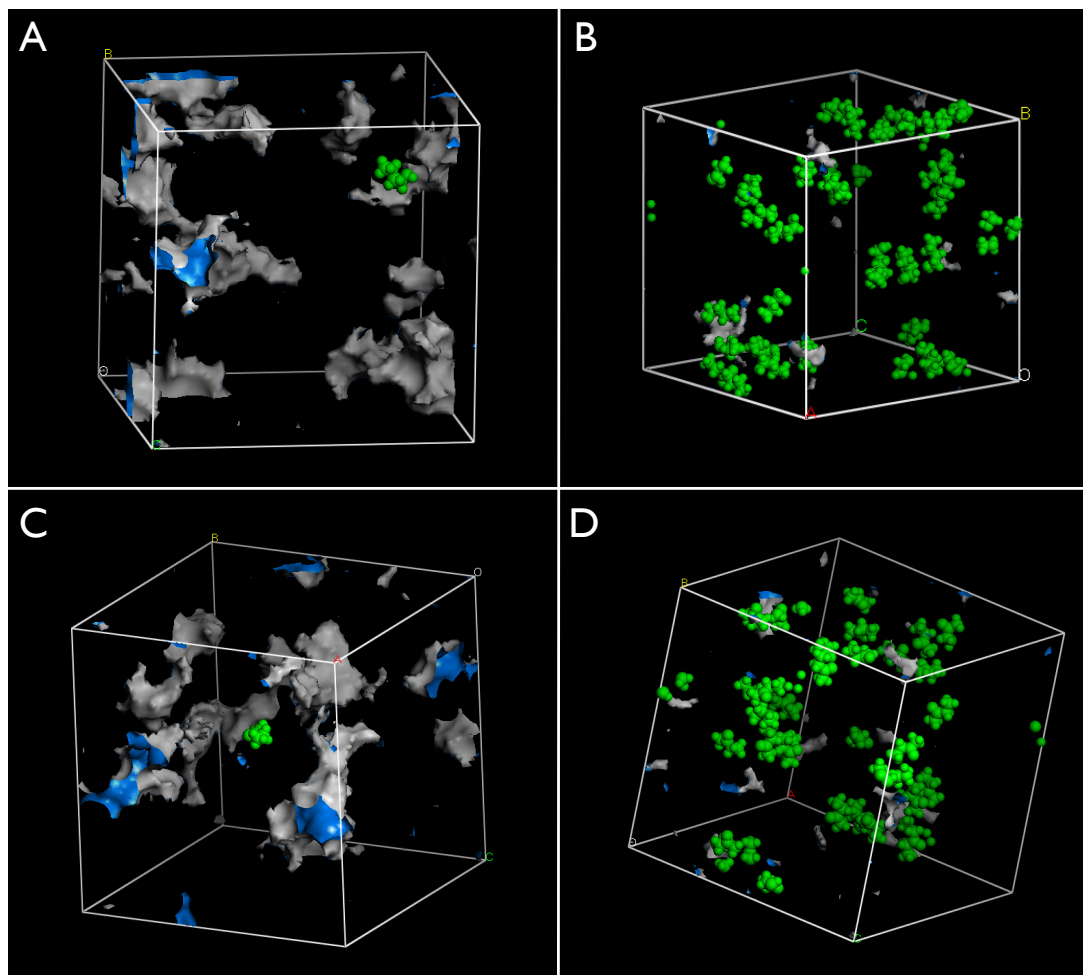
Figure 4.49: Molecular simulation of loading butanol and butanone molecules into the PDMS polymer matrix. (A) Solvent accessible surface for the loading of a single butanol molecule, in green. (B) Loading of 99 butanol molecules to the calculation yielded a maximum of 35 per unit cell. (C) Loading of one butanone molecule. (D) Loading of 99 butanone molecules to the calculation yielded a maximum of 34 per unit cell.
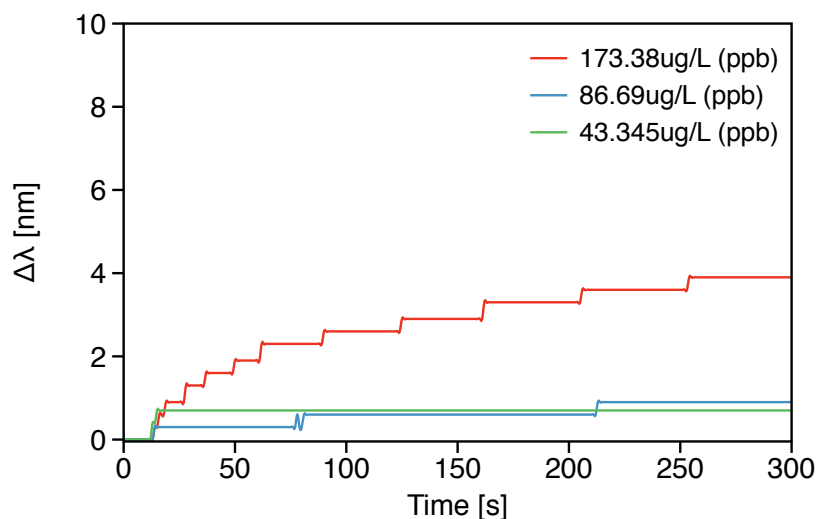
Figure 4.50: Holographic detection of toluene in water at *ppb* concentrations. The stepped plot is due to the minimum detection of the spectrophotometer of 0.3nm.

damage. PDMS is inert to water and it has been shown that it can be used to separate VOCs from aqueous samples in a process known as pervaporation, in which minor components of a liquid mixture are preferentially transported by partial vaporization into permselective membranes [160, 227]. The same principle can be applied to sense VOCs using PDMS holograms.

A typical water contaminant is the organic compound toluene, which imposes several risks to human health and aquatic life if found in excessive concentrations. The maximum limit of concentration in water proposed by the UK environment agency is 74μg/L and the one established by the US environmental protection agency is 1mg/L [228, 229]. Toluene was selected to test the efficacy of the PDMS holographic sensor in an aqueous mixture. Figure 4.50 shows that the sensor was able to detect toluene below the concentrations proposed by both the UK and US agencies. Although accurate concentration readings took more than 300s to give a maximum response, the presence of the contaminant was detected within 10s of exposure to the hologram. These results are encouraging for using the sensor in the detection of VOC contaminants in water.

Mixtures of analytes could also be tested for particular applications. For example, to detect differences in fuels, volatiles in furnishing materials or the detection of contaminants in transport pipes for gases or liquids. However, the

selectivity should be improved, such that the concentrations of a complex mixture in which all species interact, can also be measured. Turning the sensor into a more selective and sensitive system could be achieved by incorporating specific ligands, adding plasticizers, increasing the level of cross-linking, including reacting compounds in the PDMS chains, or modifying the silver particles in the fringes to make them chemically selective. Interactions with the Ag^0 particles would appear as a change in refractive index and, consequently, a change in diffraction efficiency. Nevertheless, a way of improving selectivity or sensitivity could be to include triple bonded ligands on the silver metal surface, red-ox reactions or covalently attaching metal-organic compounds to the particles.

4.9 Holographic signal measurement by RGB colour image analysis

The ultimate goal and principal advantage of using a holographic sensor is that an end user could read the sensor signal by 'eye'. Human vision and perception could, of course, introduce subjectivity in the analysis of the results. However, there are inexpensive daily-use devices that emulate human vision and can be used instead. Nowadays, there are several devices that integrate light detectors in their functions, such as digital cameras and mobile phones, which have inbuilt light sensors for recording images. These devices process photons as red, green and blue colours to produce digital images. Expensive spectrophotometers and software can, therefore, be replaced by these mobile devices. An application may be written to read the holographic sensor response by taking a photograph of its surface and thereby improving the analytical collection of data from the user. This section shows the results for extracting gas concentration information from digital images. The holographic reflections were analyzed by extracting the pixel counts for the three digital colour channels.

As reported in §4.6.1, it was possible to measure a direct real-time response of the hologram to varying concentrations of hydrocarbon gases. Furthermore, the response can be seen as a colour change in the holographic reflection. This change is, however, neither obvious to the human eye, nor to digital image processing. Thanks to the invention of CCD and CMOS sensors, which are the elements

that process the light in digital cameras and spectrophotometers, it is possible to collect colour or wavelength information digitally.

Wavelength and colour, if well correlated with each other, are not complete synonyms; a good explanation of these phenomena can be found in reference [230, §4.3]. The naked eye processes light radiation into neural signals that the brain interprets as colours. The wavelengths perceived as green include a broader part of the electromagnetic spectrum than the ones perceived as yellow or red, for example. The human ability to discern between colours is limited to the abundance of light-sensitive cells in the eyes. Likewise, electronic light sensors are limited in their efficiency by their size and the semiconductor materials used in their construction. Both, human eyes and electronic sensors have better absorption efficiency at wavelengths that corresponds to green ($\sim$490nm-580nm). Thus, it is easier for human eyes to perceive green than other colours. Figure A.4 in the Appendix shows the absorption spectra for the rods and cones of the eye and the quantum efficiency spectra for two types of camera sensors.

The images of the hologram collected by the camera showed the slight differences in colour which could be seen by 'eye', or from a computer screen, or on a printed page. Therefore, the data in the digital image was collected as an array of pixels with three colour channels: Red (R), green (G) and blue (B). The sensor of the digital SLR camera uses a CMOS sensor which is more efficient in capturing colour than common CCDs, although it is less effective than the special CCDs found in spectrophotometers [231]. A spectrophotometer uses a light splitting grating for counting the photons at high resolution, *i.e.* the equivalent of having thousands of colour channels.

The total count for each channel was plotted separately for each concentration measured; the results are shown in Figure 4.51. Rows A, B and C show the histograms for the red, green and blue channels respectively; row E shows the RGB values in three dimensions where the x, y and z axes are red, green and blue respectively; row D shows the average values which were used to correlate the concentration of the tested gas with the RGB data. In this particular case, a difference in colouration appears obvious to the naked eye only after a 50 nm wavelength shift due to the processing of the wavelengths to colours. However, it was possible to detect the subtle differences in green from 12.2% to 61.2% with the RGB analysis. The tested gas was 1-butyne and the concentrations
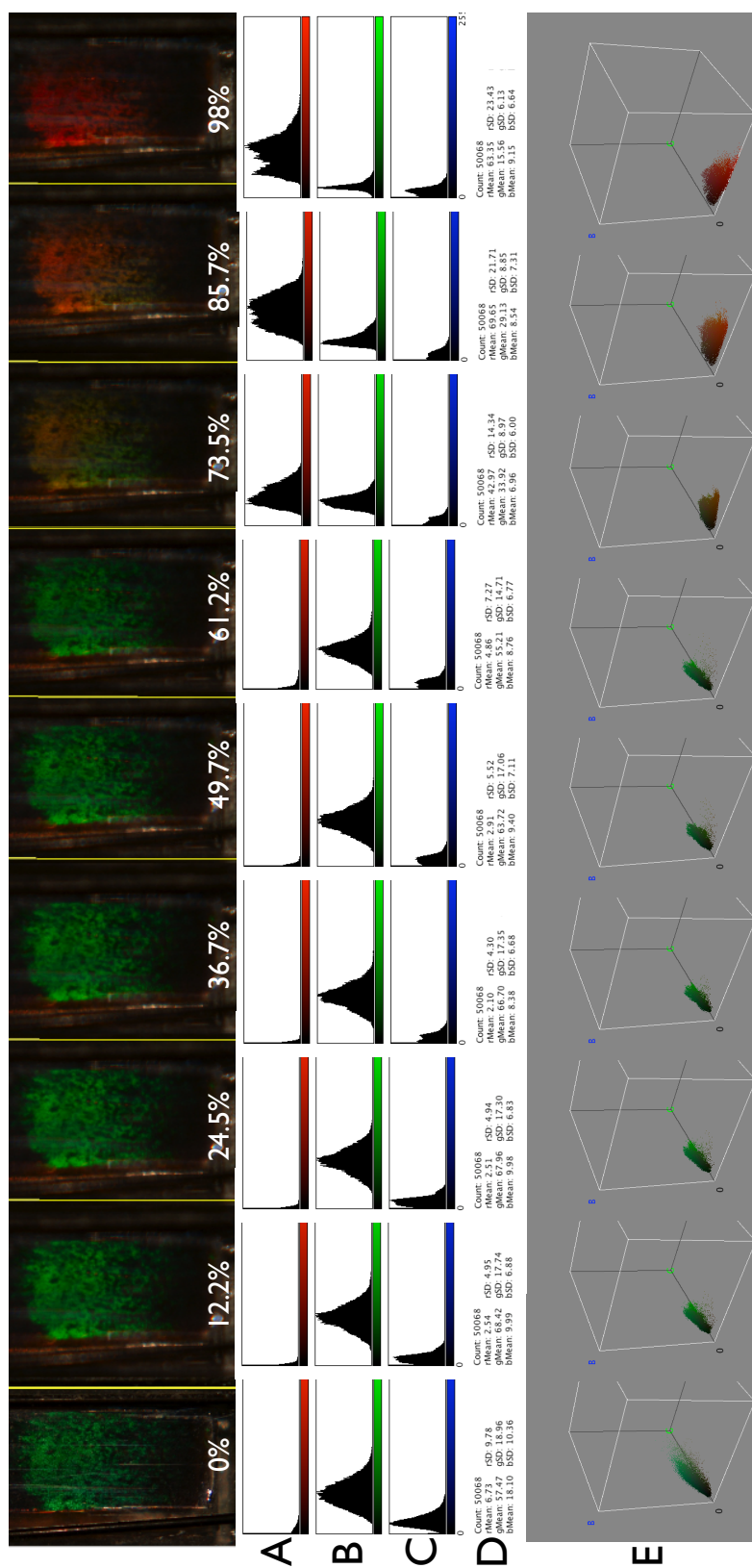
Figure 4.51: RGB image analysis of holographic reflection response to 1-butyne. (A), (B) and (C) are the RGB values respectively, corresponding to the images above each column. (D) Average RGB values. (E) 3D plots for all channels and concentrations.
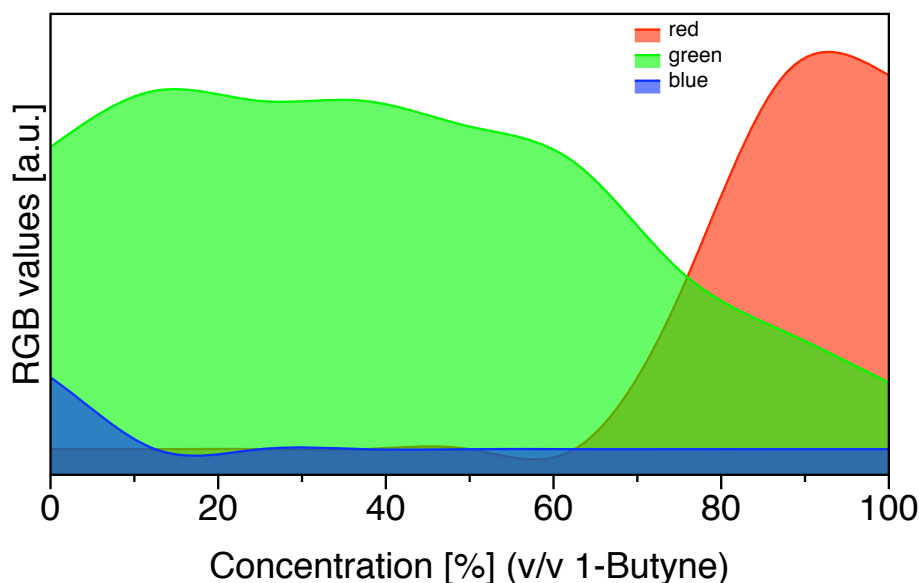
Figure 4.52: Determination of 1-butyne gas concentration with RGB values from a digital camera. The light detected by the sensor in the camera is split into three channels: Red, green and blue; the difference at the edge of each channel separation result more obvious than in the middle of it, as it can be seen for the green channel.

were in % (v/v). The average values between 36.7% and 49.7% do not show an obvious difference when observing only at the green channel; however, a difference is apparent when viewing the blue and red channels. Therefore, comparing the values of the three channels can give a reading of the holographic signal.

An advantage of using digital photographs is that the response can be collected from large distances depending on the lenses. This eliminates the need for wiring or placing electronics at the source of the measurements. In other words, the sensor can also operate in a process that requires remote sensing or real-time monitoring. Furthermore, both holograms and digital cameras are relatively inexpensive.

4.10 Summary

Holographic sensors fabricated in PDMS have been shown to address the need for a real-time sensor capable of distinguishing concentrations and, in some cases,

molecular differences, in hydrocarbons and VOCs. The sensor can be read continuously and remotely without great interference from temperature, moisture, or the presence of other atmospheric gases, thus satisfying the needs for many industrial and biomedical sensing applications.

Consideration of the nature of the intermolecular interactions has assisted in the understanding of the nature of the holographic sensor response at the molecular level. The integration of those interactions as readable signals in a holographic sensor was successfully achieved. However, the challenges of producing a more selective and sensitive sensor still remain.

Holographic gratings were successfully used as transducers for quantifying chemical concentrations: The signals were produced by transforming the swelling or contraction of the polymer matrix into a difference in reflected wavelength. These changes were read by a spectrophotometer or a digital camera for determining the concentration of the analytes.

Furthermore, it was shown that the light reflection of the hologram can be predicted mathematically with good agreement by knowing the grating parameters Λ, n, ϑ_b and L. Changes in Λ appeared to be the only contribution to the holographic signal change in this case, and were caused by the swelling or contraction of the polymer chains in the PDMS films.

The polymer-analyte interactions were affected by the diffusion and absorption of the analytes into the films, and the consequent swelling of the polymer chains. This swelling was empirically predicted using the experimental data and the thermodynamics of polymer-analyte mixing: The free energy for swelling ΔG_m depends on the interaction parameter χ_{12}, which is defined by the differences in cohesive energies E^c. The relationship between the molecular interaction parameters and the swelling of the polymer could also be predicted mathematically and can be compared with the empirical model to predict the sensor response $\Delta\lambda$.

In conclusion, there was a strong correlation between the holographic response and the strength of the intermolecular interactions. Moreover, merging the photonic and thermodynamic models, the sensor response to any analyte could be entirely predicted mathematically.

Holographic Sensors for Ammonia and Oxygen

5.1   Materials selection

Keeping in mind that the holographic sensor response is a function of the grating spacing Λ and the refractive index n, a material sensitive to oxygen or ammonia should produce conformational changes that affect Λ or chemical changes that affect n. Furthermore, the selected material has to be transparent and able to form flat films for the holographic recording process.

The unpaired electrons in the oxygen molecule confer a partial negative charge to form weak dipole interactions, and hence with its capacity to form hydrogen bonds [7]. Similarly, ammonia has an induced dipole and forms ions in solution which produce coulombic interactions. Both, ammonia and oxygen can also form covalent bonds upon interaction with nearby molecules due to these partial charge changes [52, 232]. Thus, a sensor aiming to exploit the nature of the molecular interactions in O_2 and NH_3 should investigate the charges in the molecules. There are several examples of ammonia and oxygen sensors that use charge related chemical properties at an electronic level to generate readable signals [9, 52, 233]. These sensors often face the same challenges, *i.e.* those related to the reactivity of the gases.

The high reactivity of oxygen is often problematic for sensor design because most of its reactions are irreversible or form new compounds that inhibit the sensing [234]. It has been demonstrated that, in Nature, reversible oxygen-binding reactions are mediated by enzymes with metallic cores, and most likely, Nature possesses the optimum conditions for reversible oxygen binding [27, 41, 232]. These reversible reactions have been studied in molecules that partially accept electrons,

usually fluorescent molecules or porphyrins with metallic cores [38–40, 42, 43]. Oxygen sensors often seek to mimic these types of interactions. The key problem is that these interactions are weak and that conformational or optical changes occur at the molecular level and are difficult to scale to the bulk. Furthermore, polymeric materials with metal-core porphyrins or oxygen-binding fluorescent cores are not yet available as flat films for holographic recording.

Ammonia on the other hand is more reactive than oxygen. Ammonia sensors are commonly made with dye molecules which change colour upon binding to catalytic metal capacitors, or chemisortive metal oxides [52]. Similar problems might be expected to arise when trying to apply these types of interactions to holographic sensors because the changes are small and only detectable at the molecular level.

Hence, a sensor material for oxygen and ammonia should selectively accept charged or partially charged molecules and generate molecular changes that affect the bulk properties, such as refractive index, swelling or contraction. A careful review of the literature pointed to ion-exchange membranes; these membranes are flat, transparent, and selectively interact with charged or partially charged molecules. Thus, they are suitable for holographic recordings. Proton Exchange Membranes (PEMs) for H^+ ions are nowadays common, particularly for their use in H_2 fuel-cells as alternatives to fossil fuels [235]. A popular material for PEMs is tetrafluoroethylene persulphonic acid copolymer (Nafion). This material is commercially available as membranes that are known to experience swelling or changes in optical properties when in contact with oxygen and ammonia [232, 236–239]. Therefore, this material maybe considered to be the ideal candidate for the construction of holographic oxygen and ammonia sensors.

5.1.1 Tetrafluoroethylene-Perfluorosulphonic acid copolymer

Nafion® is the commercial name of persulphonic acid derivates of tetrafluoroethylene which is also known as Teflon® (Dupont, Inc). The molecular structure of Nafion co-polymer is shown in Figure 5.1A; the teflon copolymer length y has 5-12 units of tetrafluoroethylene monomers and the persulphonic acid length x is usually 1 unit [157, 240]. Several studies have showed that the sulphonic acid

functional groups aggregate in continuous regions of ion clusters or cavities inside the membrane as shown in Figure 5.1B [157,240,241]. These regions are hydrated upon exposure to humidity, whilst protons dissociate from the SO_3^- counter ion allowing the transport of cations through the membrane [240].

Nafion membranes contain a network of inter-connected channels with cavities; some models in the literature based on X-ray scattering have proposed a geometry as shown in Figure 5.2. Their findings based on X-ray scattering and crystallography suggest that the core of the cavities is separated by 9nm, their diameters are ∼4nm, and the channels connecting them are 1nm thick [155, 232, 241–244]. These features are important because their geometry will dictate the amount and size of silver particles that can be loaded into the membrane. Studies that have achieved nanoparticle formation in the ionic clusters conclude that particles can grow to 2-40nm in size depending on the type of membrane [155]. It has also been suggested that the size is not affected by the amount of metal ions in the solutions but by the geometry of ionic clusters and channels [155]. Nafion 117, for example, showed nanoparticle mean sizes of 15±3nm in one study, and 13.4±2.2nm in another [154, 155]. It has also been shown that the cavities are flexible enough to accommodate larger silver particles in the range of 10-18nm in diameter [244]. The presence of particles also affects the optical properties of the membrane which are important for hologram formation. The reported refractive index of clear Nafion-117 without particles is ∼1.38 [245,246]; however, depending on the stress conditions and relative humidity the refractive index may increase in value up to 1.41 [247]. Membranes with nanoparticles show refractive indices around 1.42 [248].

5.2 Nanoparticle formation and ablation in Nafion membranes

The Nafion membranes were purchased as films and had to be flattened for the holographic recording process. The main challenge, however, was to produce a homogeneous distribution of silver particles beneath the surface. This had to be accomplished under the constraints of the cation permselectivity of the membranes. The process described in detail in the methodology included the
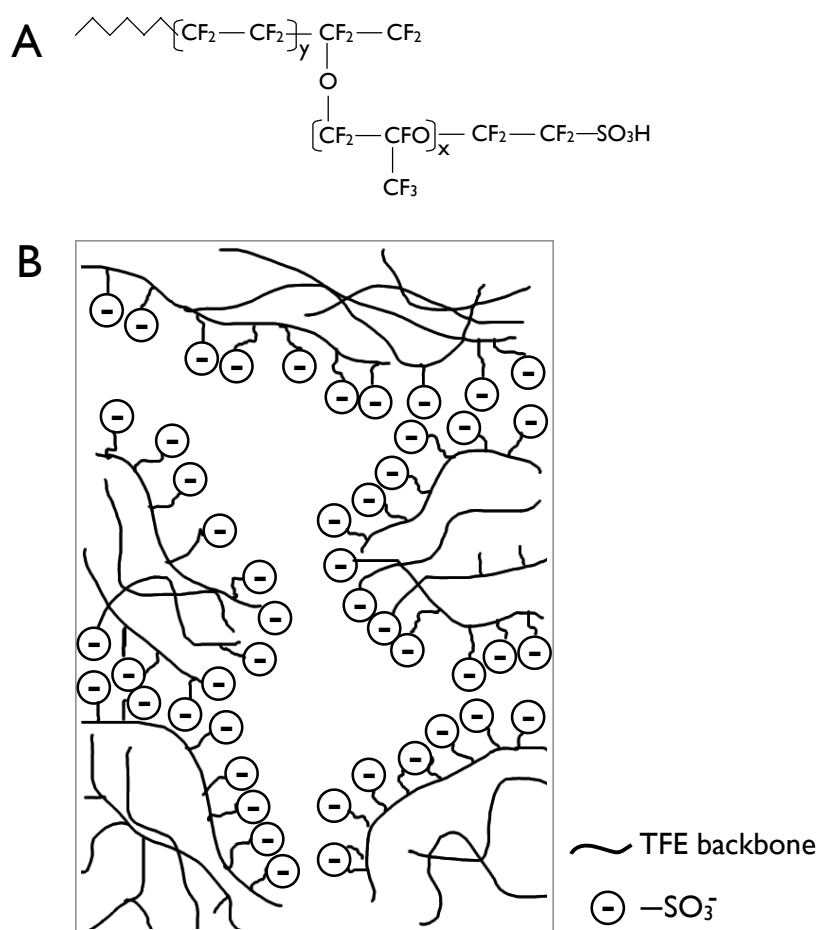
Figure 5.1: Molecular structure of Nafion and sketch of its porous matrix showing the exposed sulphonate acid charges. (A) Tetrafluoroethylene(TFE)-perfluorosulphonic acid copolymer molecular structure, $y =$5-10, $x = 1$. (B) Sketch of entangled matrix with negative charges oriented towards the pores. Teflon backbone towards the entangled matrix [240, 241].
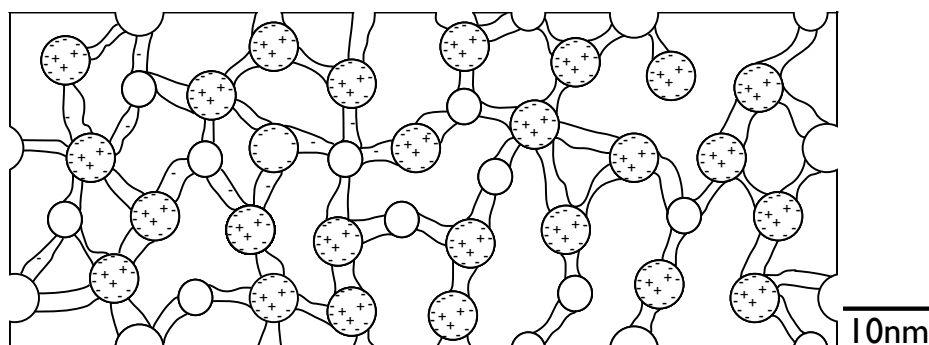
Figure 5.2: Model of the geometry of ion-exchange cavities in Nafion [242–244].
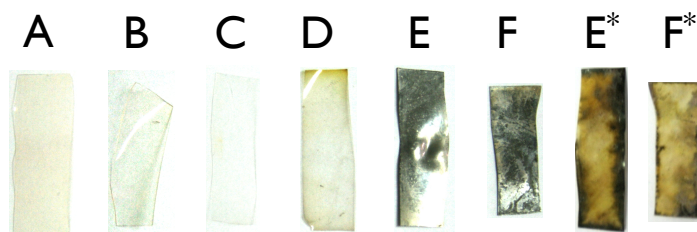
Figure 5.3: Nafion membrane transformation from purification to ablation. (A) Membrane as provided by the fabricant. (B) Purified membrane. (C) Na^+ form. (D) Ag^+ form. (E) Ag^0 formation with 0.1M Ag^+. (F) Ag^0 formation with 0.02M Ag^+. An asterisk denotes the same membranes after ablation.

following steps: First, the membranes were purified in concentrated HNO_3; then, transformed to the Na^+ form; then, to the Ag^+ form; and finally, Ag^+ cations were reduced to Ag^0 with the concentrated reducing agent $NaBH_4$ (*see* §3.2.1). The membranes were then flattened between glass slides and shot with the laser. Photographs of the membranes during the transformation steps from purification to ablation are included in Figure 5.3.

The membranes in Figure 5.3 were analyzed by absorption spectrometry. Figure 5.4 shows the shift of the peak from 400nm to near 410nm; the typical SPR of silver nanoparticles in solution is ∼410nm [190–193]. The figure includes spectra for different steps of the membrane transformation process. Similar to what occurred with PDMS membranes, the typical absorption peak of silver nanoparticles shifted to higher wavelengths after ablation. It has been shown that the characteristic SPR can be tuned for different particle sizes and spatial distribu-
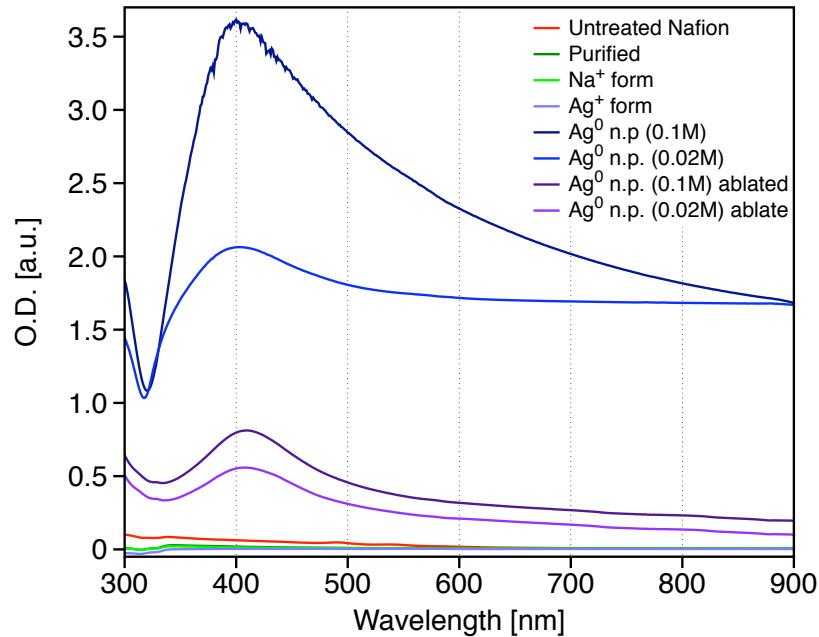
Figure 5.4: Absorption spectra of Nafion membranes during the nanoparticle formation process.

tion in polymer films [188, 189]. The ablation process appears, thus, to affect the sizes or distribution of the particles in the films.

The loading of silver particles in Nafion depends on the permeation of the charged particles and their transport through the hydrophilic network of channels. Large conglomerates of particles were formed on the surface where the channels begin. Microscopy images of the surface before and after ablation are shown in Figure A.5 in the Appendix.

Membranes E* and F* in Figure 5.3 did not show holographic reflections. The concentration of silver was too high to allow the laser light to reflect back from the mirror surface and form standing waves. These results only show that the methodology for loading silver nanoparticles into the membrane was successful. The next step was to optimize the required concentration of silver to produce bright holographic reflections. Table 5.1 summarizes the results of this optimization. Figure 5.5 includes photographs of the different concentrations and a subjective evaluation of the holographic reflections, together with absorption spectra before and after ablation for the low concentrations.

Table 5.1: Optimization of AgNO$_3$ concentration in 0.1M NaNO$_3$ for holographic recording in Nafion membranes (*see* Figure 5.5).

AgNO$_3$ [M]	0.001	0.004	0.007	0.01	0.025	0.05	0.06
Na$^+$: Ag$^+$	1000:1	250:1	142:1	100:1	40:1	20:1	15.5:1
Hologram*	-	-	-	-	-	+	++
AgNO$_3$ [M]	0.09	0.1	0.14	0.2	0.3	0.4	0.5
Na$^+$: Ag$^+$	11.1:1	10:1	7.1:1	5:1	3.3:1	2.5:1	2:1
Hologram*	+++	++	++	+	+	+	-

* - absence; + faint reflections; ++ acceptable reflections; +++ bright reflections.

It was found that solutions between 0.06M and 0.14M of AgNO$_3$ provided sufficient amount of silver for bright holograms with 0.09M as the optimum value. It was also noticed that after loading the silver ions and reducing with NaBH$_4$, the coloration of the membranes changed to amber. This change in colouration is indicative of nanoparticle formation [154,155]. Also, the characteristic absorption peaks for metallic silver appeared in the absorption spectra of all the concentrations tested and shifted after ablation. Thus, Ag^0 nanoparticles are likely to be present in the membranes and this is confirmed by the SPR peak shift.

5.2.1 Optimization of holographic recording by ablation for low-exchange and high-exchange Nafion membranes

The ablation process encountered several problems when applied to the Nafion membranes. One major issue was the flatness of the membranes: In order to record an interference pattern with the standing waves, the membranes had to be flattened on the glass slides. Several ways of ensuring that the membranes were flat were tried: Compressing the membranes between two slides, attaching them permanently to the slides with cyanoacrylate resin, and sticking the edges to the glass slide and spreading refractive index matching solution on both sides. Using extra glass slides or glue layers adds interferences in the laser path, thereby increasing scatter and reducing the recording efficiency; this did not produce encouraging results. The next major issue was to determine the right laser energy to ablate the particles homogeneously. Table 5.2 summarizes the result of the
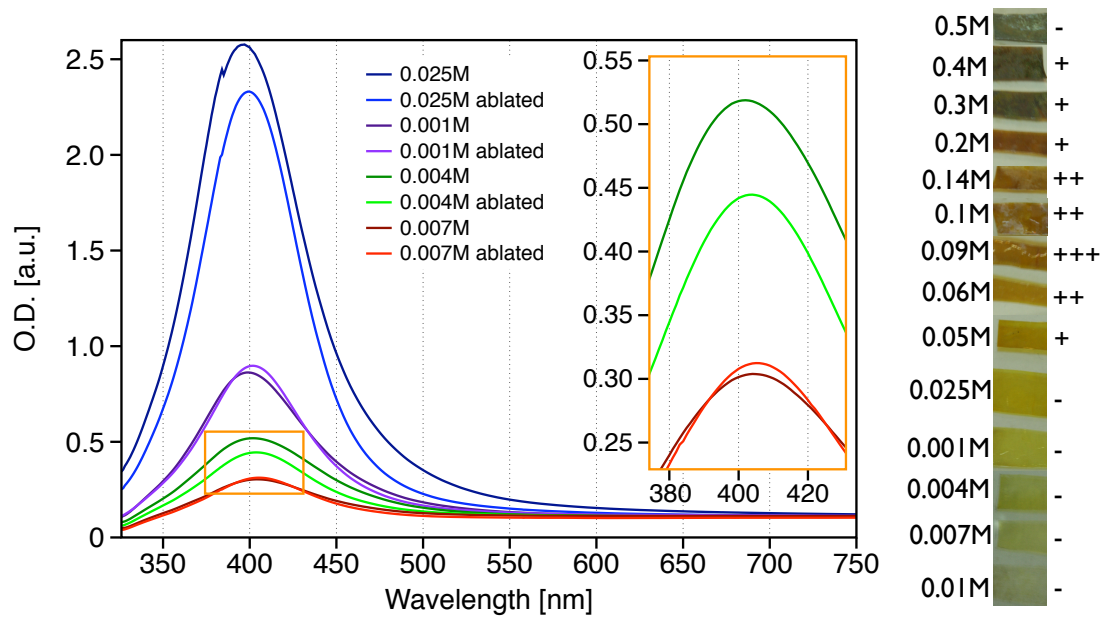
Figure 5.5: Absorption spectroscopy of Nafion membranes for the various $AgNO_3$ concentrations during the optimization process and photographs of the results. The absorption spectrophotometer was set to detect the lower concentration; a shift in the absorption peaks was detected after ablation.

Table 5.2: Results for the optimization of the ablation parameters in Nafion holographic recordings (*see* Table 3.2 and Figure 3.3).

Sample	1	2	3	4	5	6	7	8	9	10	11
Area[cm^2]	1.3	1.3	2.5	2.7	2.7	3.9	2.5	1.3	1.3	1.3	1.3
Hologram	-	-	+	++	++	++	++	-	-	-	-
Surface	+++	+++	++	+	-	-	+	++	++	++	++
Intensity	+++	+++	+	++	++	+	+	+	+	+	+
Index m.	Yes	Yes	Yes	Yes	Yes	Yes	Yes	Yes	Air	Air	Air
No. shots	1	2	1	1	2	2	2	1	1	2	5+
Config.	A	A	C	C	C	C	C	C	B	B	C
Y[cm]=	1.2	1.2	1.7	1.8	1.8	2.0	1.7	1.2	1.2	1.2	1.2
X[cm]=	1.4	1.4	1.9	1.9	1.9	2.5	1.9	1.4	1.4	1.4	1.4

* 'Hologram' corresponds to the monochromatic reflections: - absence, + very faint, ++ faint, +++ abundant; 'Surface' corresponds to multicolor reflections from the surface: - absence, + very faint, ++ faint, +++ abundant; 'Intensity' corresponds to the intensity of the reflected light: : +++ intense, ++ weak, + very weak; and 'Index-m.' to the use of index-matching liquid; and configurations A, B, C correspond to the arrangements in Figure 3.3. The elliptic areas were calculated as $A = \pi Y X/4$, where X and Y are the measured axes.

recording optimization.

The laser was operated at the maximum energy output; its radiation was deflected by the lenses to a final spot size of approximately 1cm in diameter. Assuming that all the laser energy is focused on that spot, the 300mJ per pulse would be concentrated in that area. In order to find the optimum ablation conditions, the spot size was changed for different recording set-ups as shown in Table 5.2.

Ablation in Nafion membranes generated 'surface effects', or undesired multicolour reflections, caused perhaps by the excess of particles on the surface. These surface perturbations are surface gratings and not layered structures because they can be seen at different angles of observation. The brightness of these undesired reflections may overcome the brightness of the holographic grating making the hologram unusable as sensor. PDMS for example is more elastic and was resistant to surface ablation; on the contrary, Nafion is stiff and was significantly affected. Table 5.2 includes evaluation of these surface reflections for different ablation configurations.

The number of shots seemed not to influence the recording quality if the films

were kept static between shots, although a second shot decreased the surface effects. The configuration at which the silver particle faced the standing waves produced better holograms and was used for all subsequent experimental work, *i.e.* column 5 in Table 5.2.

The same result might be obtained by reducing the power output increasing the Q-switch delay. However, the laser cooling and heating showed substantial variability and it was unreliable for changes in the power output. Thus, the maximum delay value was selected and the optimization performed by changing the area of exposure. The power uniformity distributed over a large area of exposure yielded better holograms. Thus far, it can be said that the ablation required: Homogenous distribution of particles inside the membrane and beneath the surface; no interfaces between the membranes and other transparent materials in the laser path; and membranes as flat as possible.

5.3   Transmission Electron Microscopy

The stiffness of Nafion membranes was advantageous for the analysis of thin sections of the holograms with TEM. Figure 5.6 shows images of the membranes before and after exposure to the laser. The effects of ablation on the distribution of particles can be seen as lighter areas. The contrast of the images is different; however, a region with a high concentration of nanoparticles can be observed beneath the surface, and fringes appeared in the ablated sample. At low magnification, conjuncts of particles emerge as dark areas and particles cannot be distinguished separately.

The nanoparticles were near spherical and homogeneous in size. Higher magnifications of the particles before ablation are shown in Figure 5.7. The contrast given by the particles varied for some particles, lines corresponding to crystallographic planes were observed [181]. The silver in the ablated particles might not be entirely metallic silver, but silver oxide; however, this has yet to be tested.

The fringes that appeared to correspond to the ablated particles showed no difference in particle sizes, only in the number of them. This may be due to the ablation into smaller particles that could not be resolved at those magnifications. Figure 5.8 shows a magnification of the interfaces for one of these observed fringes;
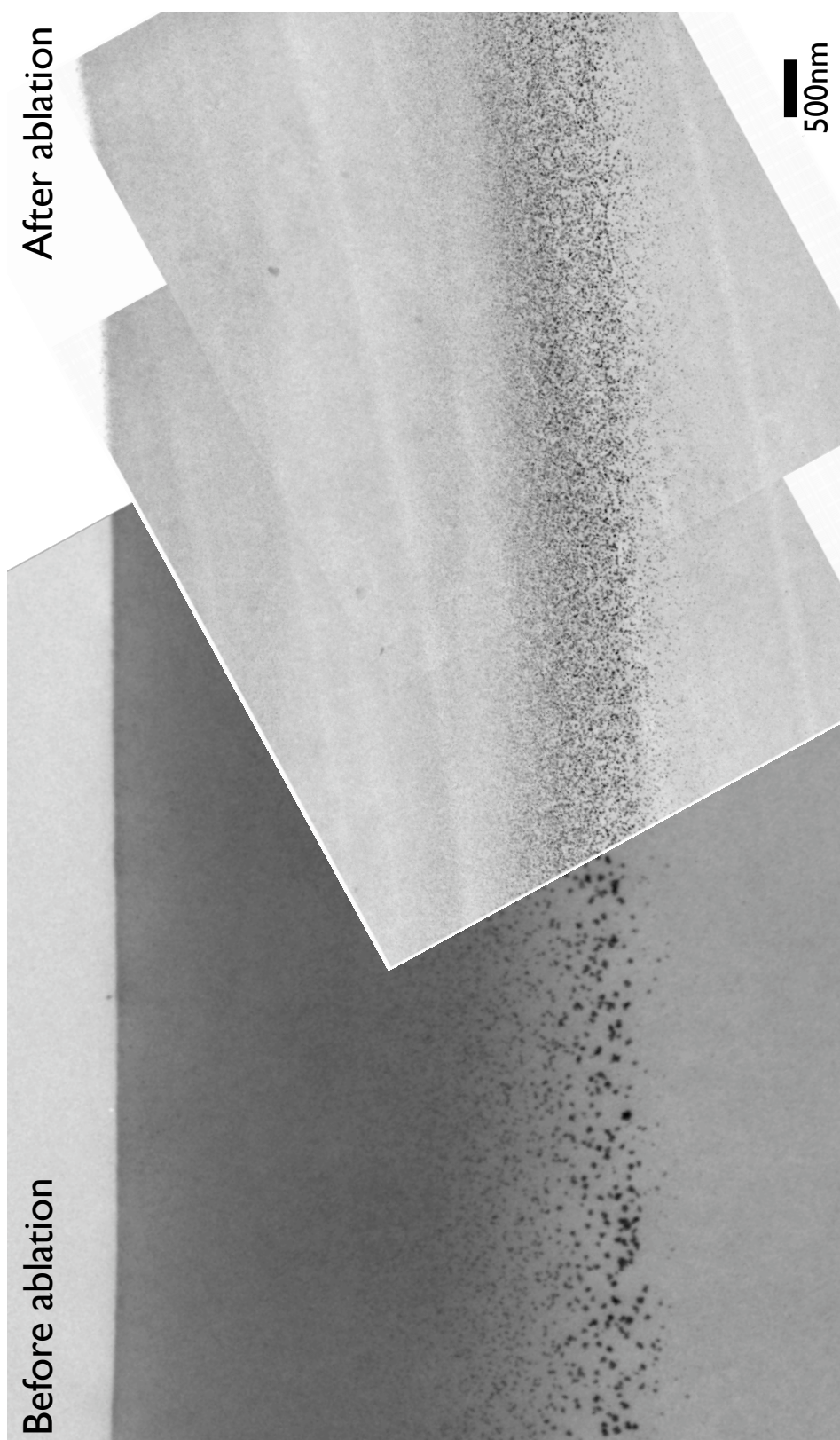
Figure 5.6: TEM images of Nafion membranes with nanoparticles before and after ablation. Overlapped images with different contrast were scaled to the scale bar shown. Image before ablation was taken at 2500x direct magnification and image after ablation at 5000x direct magnification. All images taken with a Philips TEM at 120kV.
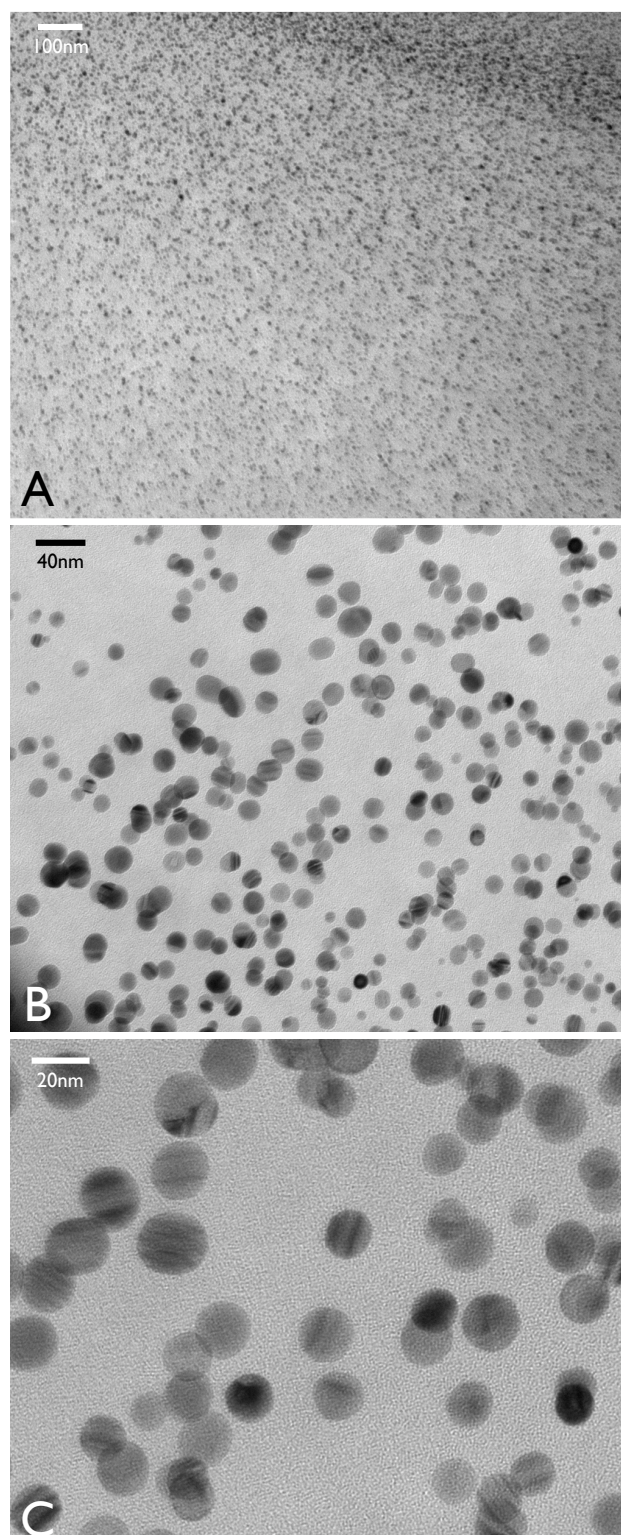
Figure 5.7: TEM images of silver particles in Nafion before ablation at different magnifications. (A) 19000x direct magnification. (B) 62000x direct magnification. (C) 150000x direct magnification. All images taken with a Philips TEM at 120kV. The particles appear spherical and show lines corresponding to different crystallographic planes [181].

133
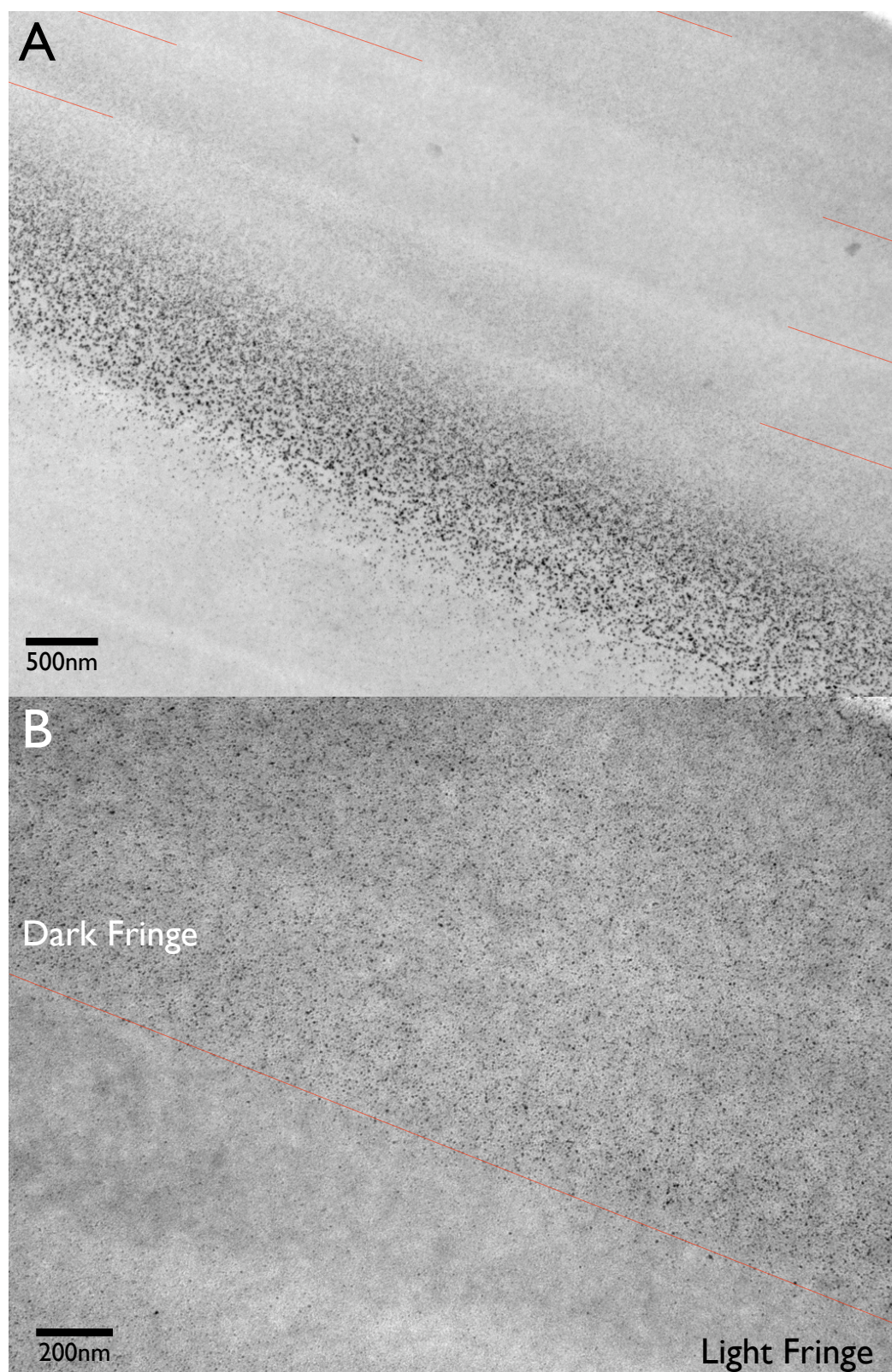
Figure 5.8: TEM of holographic fringes in Nafion membranes. (A) 5000x direct magnification after ablation; fringes highlighted with red lines at 8.83° from the surface, spaced by ∼650nm. (B) 14500x direct magnification; the light fringe shows a lower density of particles. Both images taken with a Philips TEM at 120kV.

the edges are highlighted with yellow lines. It is known that after ablation the particles decrease in size [149]; therefore, it can be assumed that the particles became too small to be detected as individual particles at those magnifications.

Information about the geometry of the fringes for the mathematical model was gathered from these TEM images. The region containing silver particles extended to approximately 4.5μm beneath the surface. The angle of the apparent fringes was 8.83°, slightly larger than the fixed angle used in the experiments. The fringe spacing manually measured from the TEM images at different positions varied significantly with an average of 650nm, which is nearly double the expected value of $\lambda_0/2$. A possible explanation for these discrepancies is that the material was sliced at an angle not perpendicular to the surface resulting in a slanted cut that cause the space and angles to appear larger. Alternatively, it could be that not all the ablated fringes can be distinguished at those magnifications, or that the laser power was somehow reduced. Nevertheless, the distance between the fringes could not be determined with certainty. Further research in finding an appropriate technique for measuring the geometry of these photonic gratings is recommended for future experimentalists.

The most important finding from the TEM image analysis was the determination of particle size distributions. As noted previously, the size of the cavities is $\sim$4nm in diameter [242–244]; therefore, the size of the particles is expected to be near the size of the cavities. However, the results of this work show particle sizes of $\sim$20nm, not surprising since other studies of nanoparticle formation have also found them to be larger [244]. Figure 5.9 shows plots for the particle size distribution before and after ablation. The fluoropolymer matrix flexibility is small, but allows for the particles to grow further, as shown elsewhere [244]. Furthermore, swelling occurs in the presence of water which increases the available space for the nanoparticles to form. This observation suggests that the cavities are substantially larger than anticipated and expand after nanoparticle formation.

Figure 5.9 also shows the reduction on nanoparticle sizes; it is apparent that nanoparticles of $\sim$30nm in diameter were removed or reduced in size, and only particles under 20nm were preserved after ablation. This result should be interpreted with caution because the particle count was substantially lower for the ablated regions. It is possible that the ablated nanoparticles are too small to be detected or gave no contrast for the TEM.
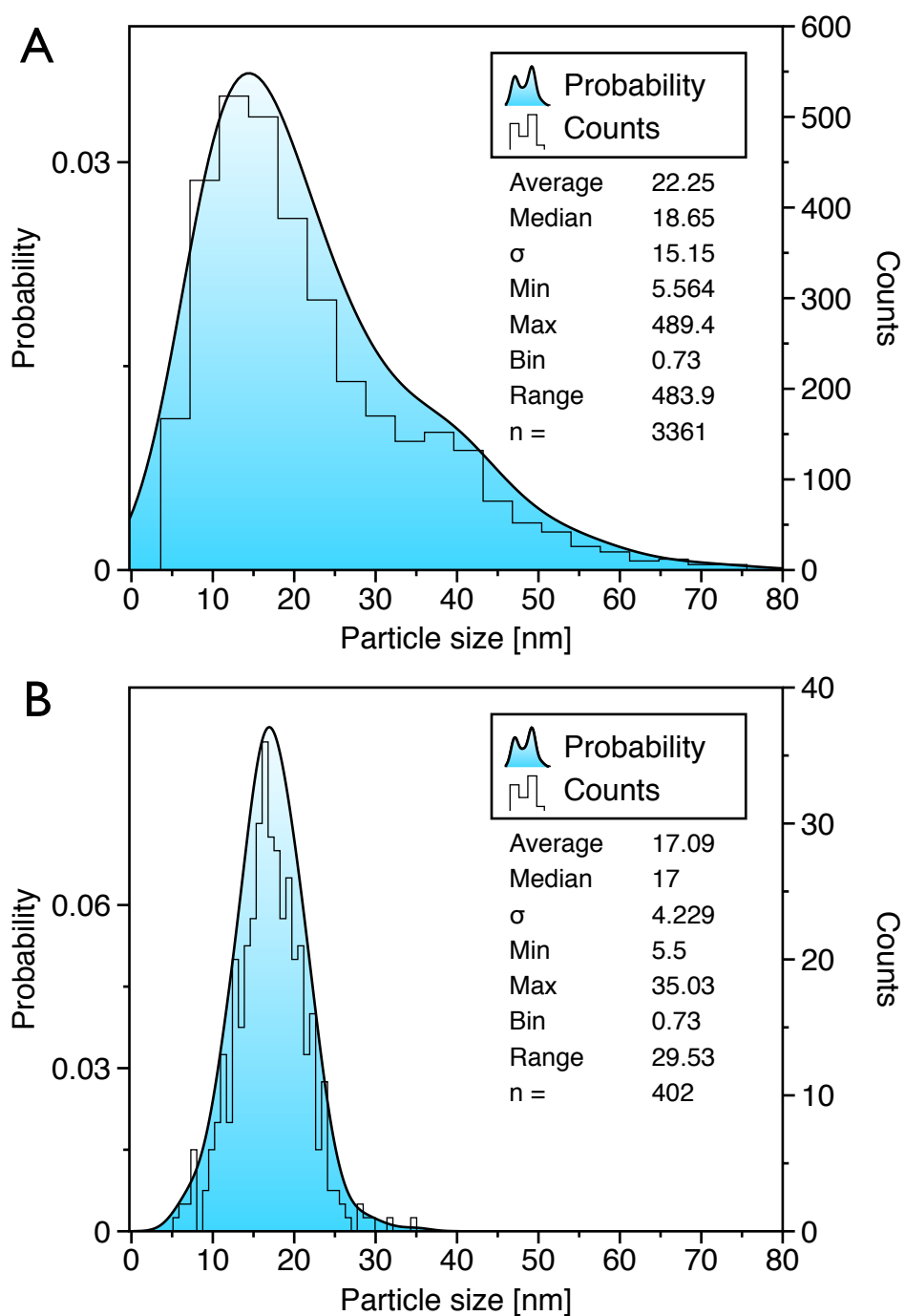
Figure 5.9: Particle counts from TEM of Nafion holograms before and after ablation. (A) Counts before ablation. (B) Counts after ablation in the light fringes (*see* Figure 5.8).
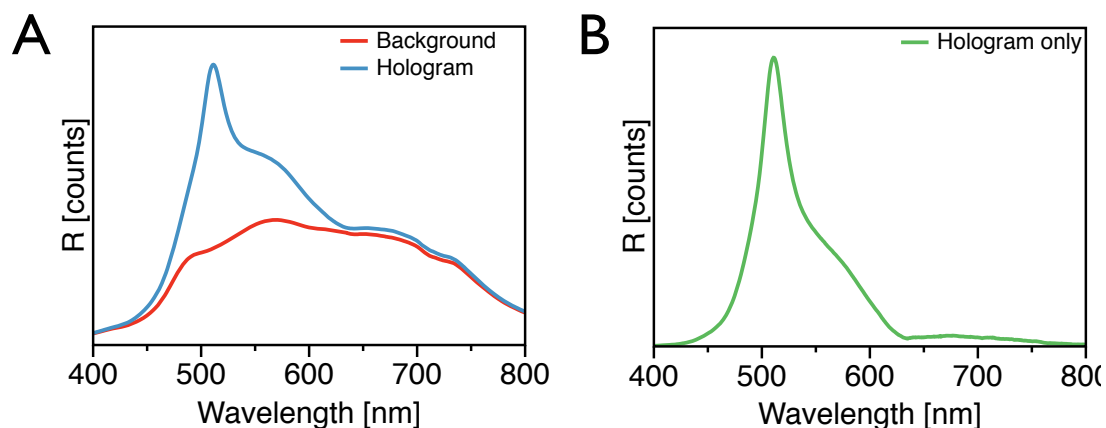
Figure 5.10: Holographic signal measurement and background correction for Nafion holograms. (A) Raw spectra of holographic reflection and background light. (B) Isolated hologram peak after subtracting the background.

5.4   Holographic signal measurements

Preliminary results with the high-exchange membranes showed that, in fact, the membranes contained a holographic grating bright enough to be seen under a white light halogen lamp. Figure 5.10 shows the holographic reflection peak of a Nafion hologram before and after subtracting the background reflection. The holographic reflection shows a second peak near the maximum of the background reflection. It is likely that this corresponds to enhanced background reflections or faint surface effects that were not completely subtracted from the background correction.

5.4.1   Mathematical models for reflection spectra

The photonic model described in §1.2.3 was used to fit the experimental data of Nafion holograms. As in the case of PDMS holograms, the refractive index values of the layers had to be estimated. It has been reported elsewhere that Nafion membranes increase[a] their refractive index when loaded with nanoparticles [249–251], and thus it was expected that the refractive index also increased for

---

[a]CdS, Fe_2O_3 and SiO_2 particles have been reported; for example, CdS and Fe_2O_3 increased the refractive index from 1.38 to 1.6 and 1.75 respectively.

metallic silver particles. The logic applied for PDMS membranes was also used in this case: For a 0.01% (w/w) concentration of silver in a polymer, an increase in refractive index of $\sim$0.06 units is expected; and for every 10nm reduction in particle size, a 0.01 units decrease [187, 195]. Therefore, for clear Nafion of n=1.38, the estimated values for the Ag^0-Nafion composite corresponding to the non-ablated region would be 1.44 and for the ablated region 1.42, considering a 20nm reduction in diameter. These numbers agree with previously reported values for Nafion membranes with nanoparticles [248].

The model also required to know the thickness of the alternating fringes and total number of layers. The effective distance beneath the surface containing nanoparticles obtained from the TEM results was $\sim$4.5μm. Since it was not possible to measure the fringe thickness in the case of Nafion, and considering that the refractive indices are similar to those of PDMS, the value of 187nm was taken as the layer thickness. Thus, the total number of fringes would be 24. The final input parameters for the mathematical model were: 24 layers, layer thicknesses a, b=$\Lambda/2$=187nm, n_1=1.44, n_2=1.42, and angle of observation from the experimental set up θ=25°. The results of the modeling are coupled with the experimental results in Figure 5.11.

The experimental peak was broader than the peak predicted by the model; this could be due perhaps to deficiencies in the background correction or the intensity of the illumination source. This same background correction was performed for the rest of the experiments in the following sections.

5.4.2   Proof of concept: response to water

The holographic sensing principle had to be proven for Nafion holograms; a change in n or Λ should cause a change in λ or R. Nafion is not an elastic material[a], therefore, a stretching and compression experiment would tear the membranes apart. In this case, the swelling properties of Nafion to imbibing water are used to prove that the holographic signal changes in response to expansion [253]. The use of Nafion membranes for holographic sensors attempts to exploit the interactions with partially charged gaseous molecules, such as oxygen or ammonia, that may or may not cause swelling. Water was chosen because it also induces changes in

---

[a]The Young's modulus of Nafion is $\sim$0.25MPa which makes it a soft non-elastic plastic [252].
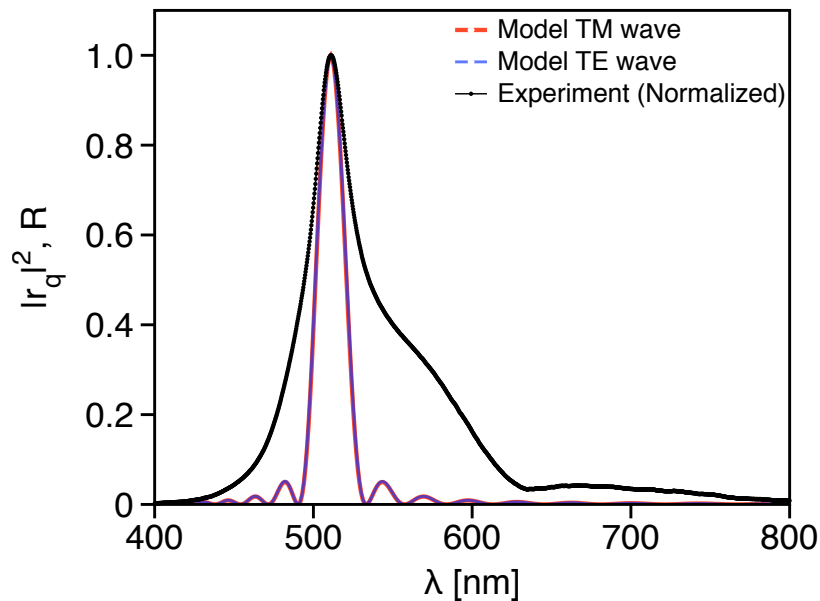
Figure 5.11: Experimental data and mathematical model of the holographic reflection spectrum of a Nafion hologram. The model TE and TM waves are shown in colours and the normalized experimental data as a black line.

refractive index [247, 254].

The interconnecting channels in Nafion are surrounded by hydrophilic sulphonic acid groups with negative charges. Its pK_a has been calculated to be -6 and experimentally determined as -3.09 [255, 256]. It was expected that molecules with a partial negative charge would cause swelling, while molecules with positive charges would cause contraction. In this case, the charged gaseous molecules have extra reactivity that could cause other type of changes, *e.g.* in refractive index. Therefore, the holographic response could react, not only to swelling and contraction, but also to refractive index variations (§1.2.3).

The experiments in the following sections aim to provide an insight into the nature of the dual changes. When dry Nafion membranes are exposed to water, the water molecules first associate with the hydrophilic sulphonic acid groups [257, 258]. The water in the ionic channels forms clusters around the previously associated molecules via hydrogen bonds [257–259], and once the water content is high enough, the activity of the water molecules no longer holds the clusters together and begins to coalesce, causing enhanced swelling [258–260].

Since the nanoparticle presence does not affect the ionic properties of the membrane, the swelling behaviour should also be exhibited in membranes with holographic gratings.

Figure 5.12 shows plots of the holographic signal peak wavelength and intensity for the water exposure experiments. The wavelength increased and the reflection intensity decreased as the Nafion membrane absorbed water. This causes a separation of the silver particles in space, reducing the reflection efficiency of the layers. It is important to consider here that the refractive index of water is similar to that of Nafion, and when the membrane is filled with water, the average refractive indices of the dark and light fringes will change. It has been reported elsewhere[a] that when the membranes are hydrated, the total refractive index decreases by 0.01 unit.

Since the refractive index of both layers is changed in the presence of water, the refractive index difference is expected not to change because after subtracting 0.01 units, the refractive indices were 1.43 and 1.41 for dark and light fringes, respectively. This change should not alter the reflectivity; this can be verified by imputing the values in Equation 1.6 or the other mathematical models described in §1.2.3. It can also be verified that a change of 0.01 units would not cause the ~50% reduction in intensity observed in the experiments. The reflectivity change is, then, mostly attributable to expansion of the fringes, which thereby reduce the reflection efficiency. However, the models considered in this work do not account for a reduction in reflection efficiency.

Figure 5.13 shows the kinetics of the holographic response to ingress of water; the wavelength increases as the intensity decreases until a maximum change is recorded. This not only proves that Nafion membranes swell in the presence of water, but also that the gratings swell as a consequence of this. The colour change in the reflected wavelength was also noticeable by eye as a change from green to red. Figure 5.14 shows photographs of a flattened hologram under different light conditions for exposure to water at a non-satisfying angle of incidence and at the Bragg angle.

It was not possible to measure the dimensions of the holograms after swelling. Therefore, the mathematical model was applied in reverse: For a given wavelength

---

[a]Lies and Pantelic report average refractive index of Nafion of 1.35 when dry and 1.34 when hydrated, [247, 254].
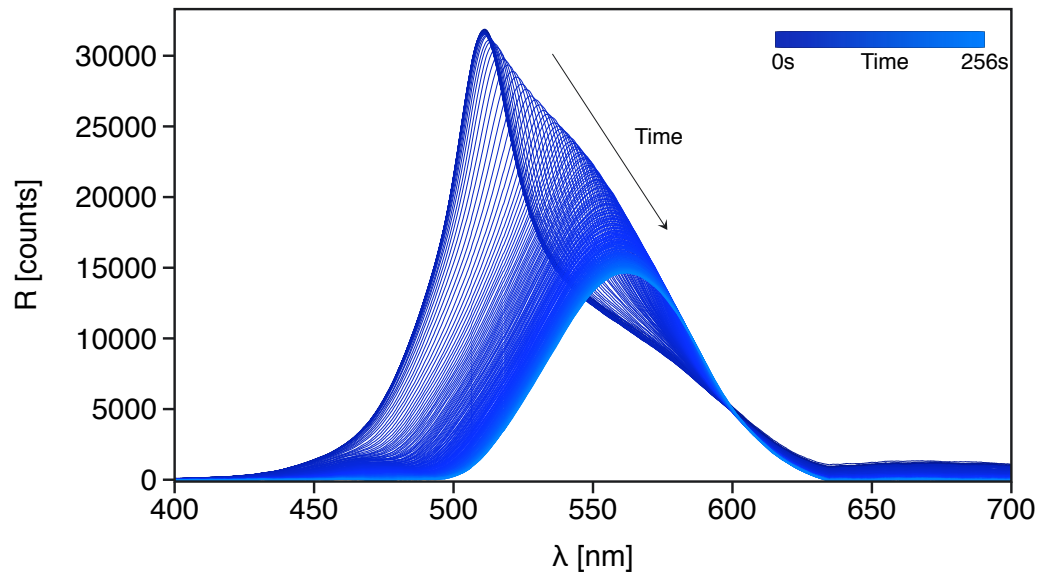
Figure 5.12: Holographic response to water in Nafion holograms. The spectra were collected every 3s for 4min; the colour of the curves indicates the time shown in the colour bar.
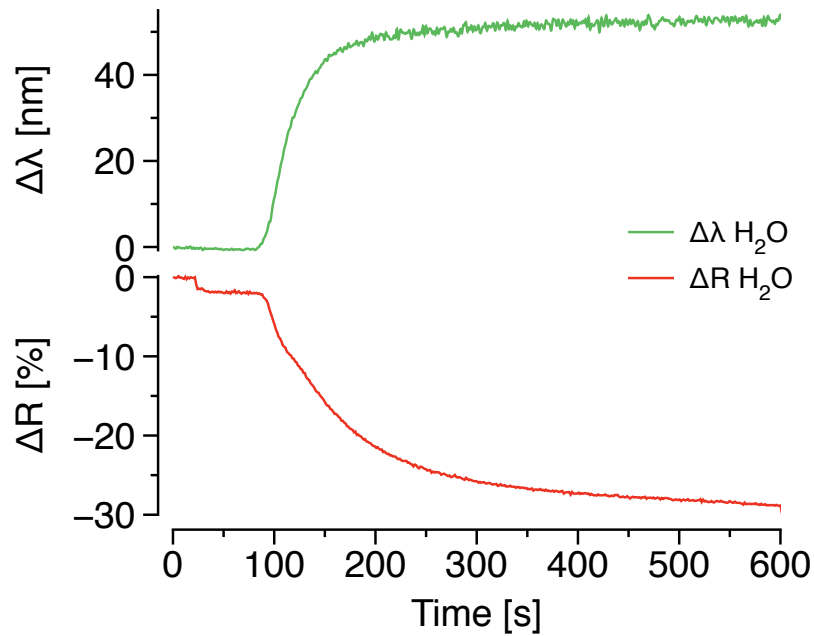
Figure 5.13: Holographic response kinetics of Nafion holograms to water. $\Delta R \approx 45\%$ and $\Delta\lambda \approx 30$nm.
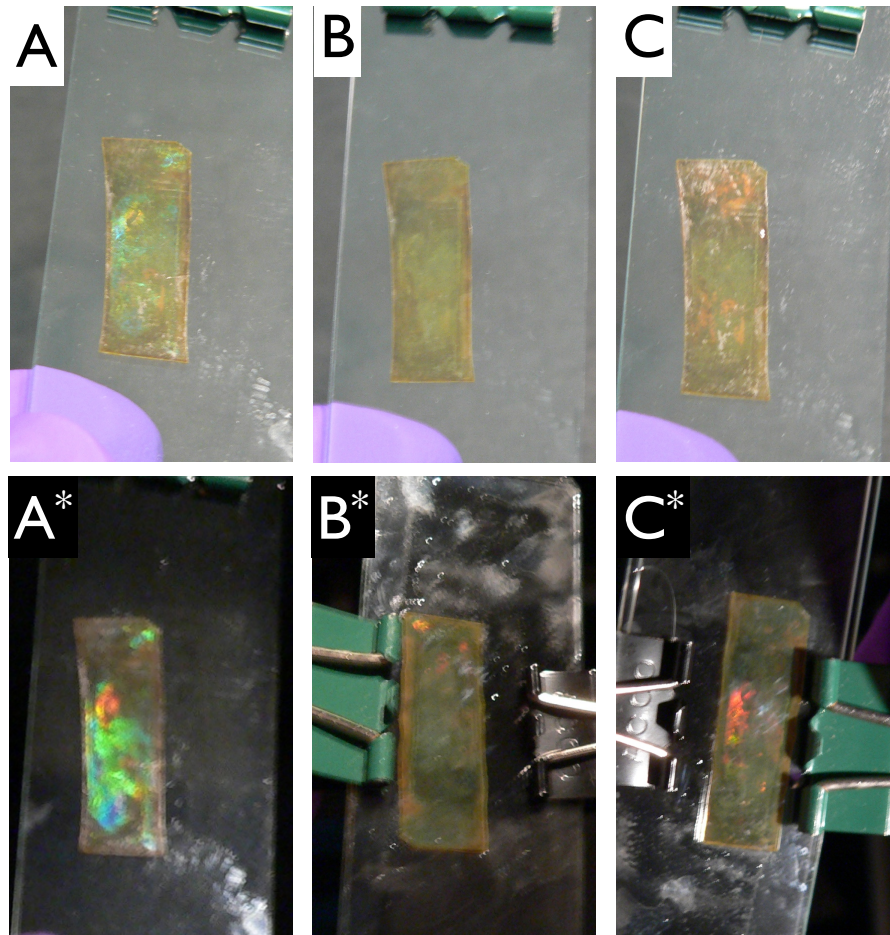
Figure 5.14: Holographic reflections in Nafion holograms under different light conditions. Top images taken under illumination with a diffuse white halogen lamp and bottom images under a tungsten filament spot light. (A) Holographic reflections approximately at the Bragg angle of maximum reflectivity. (B) Holograms at a non-Bragg angle. (C) Reflections at the Bragg angle in response to liquid water. The asterisks denote different illumination. The red spot in A* corresponds to a protuberance, thus giving different angles.
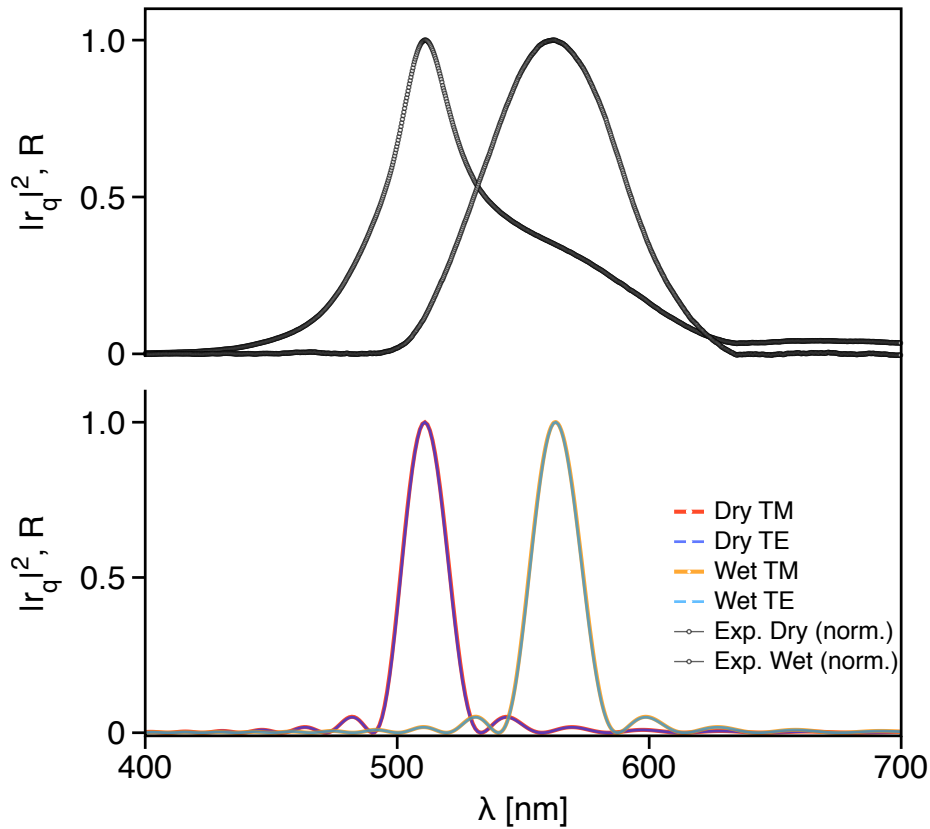
Figure 5.15: Mathematical model and experimental values of holographic response to water in Nafion holograms. The experimental data was normalized to unity at the peaks.

shift and fixed refractive index values, the increase in fringe spacing was predicted. For the observed 51nm wavelength shift, the model fits to a change in 15nm fringe thickness. Figure 5.15 shows the experimental data and the model fits. The experimental peaks appeared broader than the model predictions, perhaps because the model does not consider reflection from the light source on the first layer.

Similar to the colour analysis of PDMS holograms in §4.9, the holographic reflections of Nafion membranes were measured as RGB values with the image analysis software. However, it was not possible to obtain individual photographs for varying concentrations of humidity in the membranes. It was only possible to measure changes with and without water; the RGB plots for the images in Figure

5.14 are included in Figure A.6 in the Appendix.

5.4.3 Proof of concept: response to thermal stimuli

Temperature is known to affect the physical properties of Nafion, particularly the refractive index [261, 262]. Nafion is not elastic, and therefore expansion would be minimal. In general, an increase in temperature means an decrease in the refractive index values (*see* footnote *b* on page 18 §1.2.3). The refractive index variation of metallic silver is also dependent on temperature but Nafion is subjected to a larger change than silver because its thermo-optical coefficient is higher [263–266]. As temperature increases, the refractive index difference between Nafion and silver should decrease, and as a consequence, the reflection intensity will be reduced. This can be verified by Equation 1.6, or by looking at the sensitivity of the photonic model in §4.5.1.1.

As expected, there was a reduction in the reflection intensity when the surface of the hologram was heated. Figure 5.16 shows the wavelength ($\Delta\lambda$) and reflection changes (ΔR) as the temperature increased and decreased over time. There seemed to be a linear dependence of the reflection intensity change (ΔR) with temperature, which was affected by hysteresis. A small increase in wavelength was also detected due to the limited thermal expansion of the fringes, or generated by more substantive differences in refractive index (*see* Figure 4.20).

In conclusion, the wavelength change in response to swelling and the refractive index change in response to temperature confirm the holographic sensing principle is operational in Nafion holograms.

5.5 Preliminary results

5.5.1 High-exchange membranes

The holograms made in high-exchange Nafion membranes (NE-1035) were exposed to hydrocarbon gases, N_2, NO, CO_2 and O_2. Nitrogen gas and hydrocarbons are inert molecules with no charge dipoles; therefore, no response was expected from them. Nitric oxide is associated with free radical reactions which give a holographic response change [267, 268]. Carbon dioxide forms carbonic acid
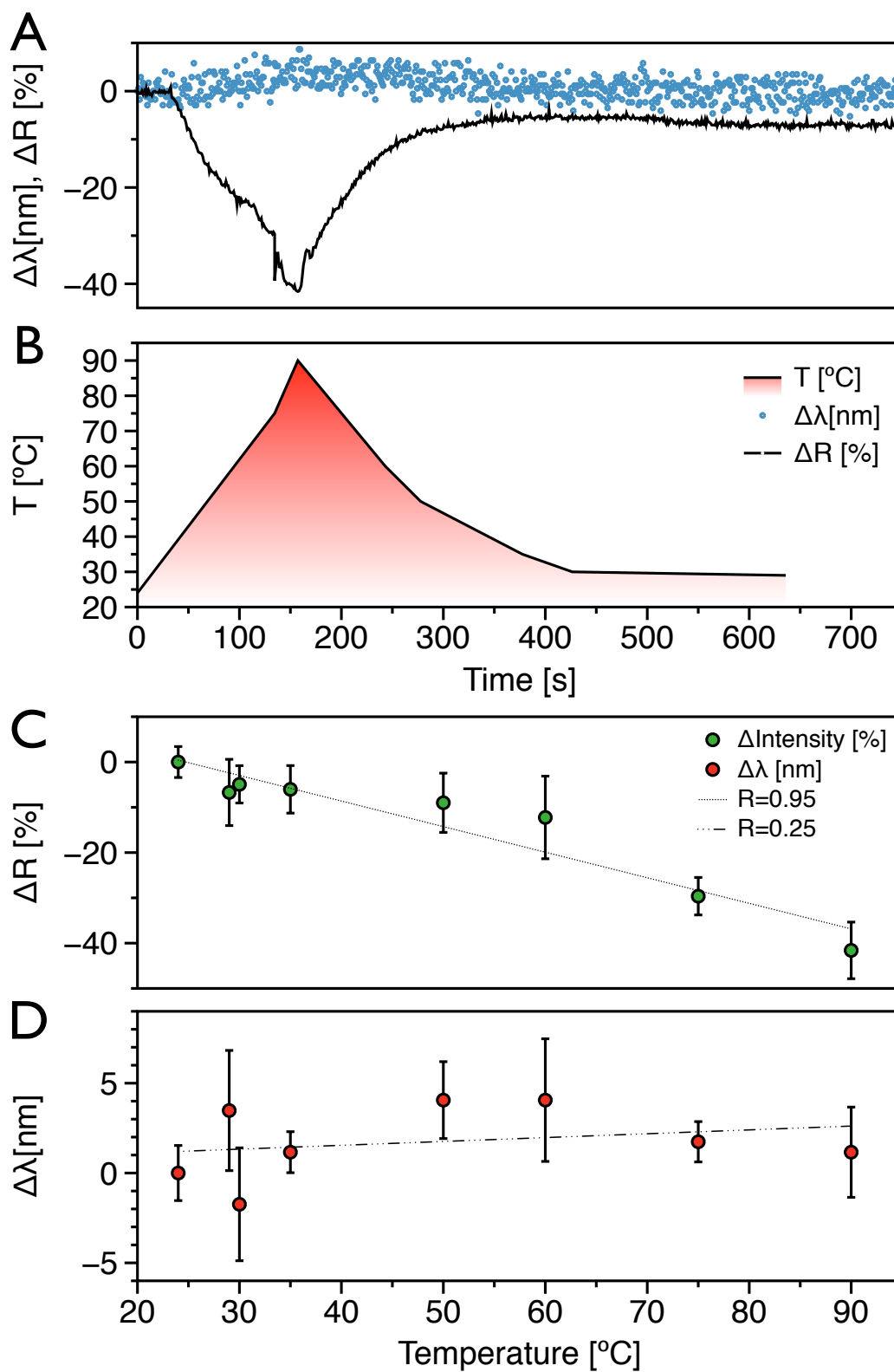
Figure 5.16: Holographic response to temperature of Nafion holograms. (A) Wavelength and intensity changes vs time for a 60°C increase and decrease. (B) Surface temperature. (C) Temperature vs intensity correlation. (D) Temperature vs wavelength correlation.
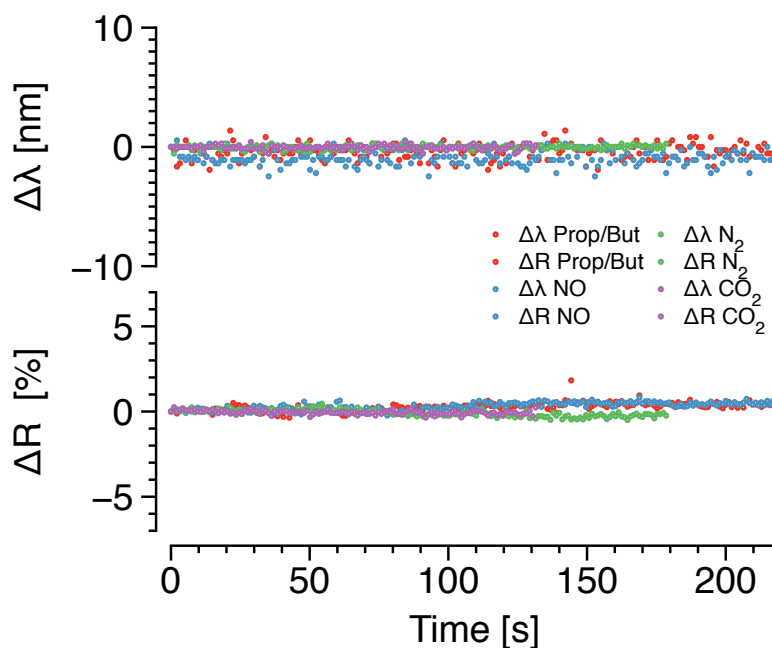
Figure 5.17: Holographic response to control gases in high-exchange Nafion holograms. Nitric oxide, nitrogen, carbon monoxide and a mixture of hydrocarbons, butane-propane (30:70 (v/v)), showed no response. Oxygen data is shown in Figure 5.18. The concentrations correspond to the concentrations of the lecture bottles, $\geq 99.0\%$ (v/v).

in the presence of water and the charged carbonate group might also have an effect in the holographic response [269]. Similarly, dioxygen was expected to give a change due to its reactivity and unpaired electrons. Of the reactants investigated, only dioxygen showed a response (Figures 5.17 and 5.18). The membranes were completely dried using an absorbent tissue and a hot air flow to remove as much water as possible. The membranes were then left to cool down in the air-tight analyzing chamber. The drying was performed because it was also found that dried gases caused the hydrated membranes to give a response regardless of the gas specie due to drying. Therefore, to avoid false positives, the experiments in this section correspond to dried membranes only. The drying method does not ensure 100% removal of water from the membranes because of the strong interactions with the sulphonate groups. However, this was sufficient to avoid the drying effect in the holographic response.

The holographic response to oxygen gas exposure is shown in Figure 5.18.
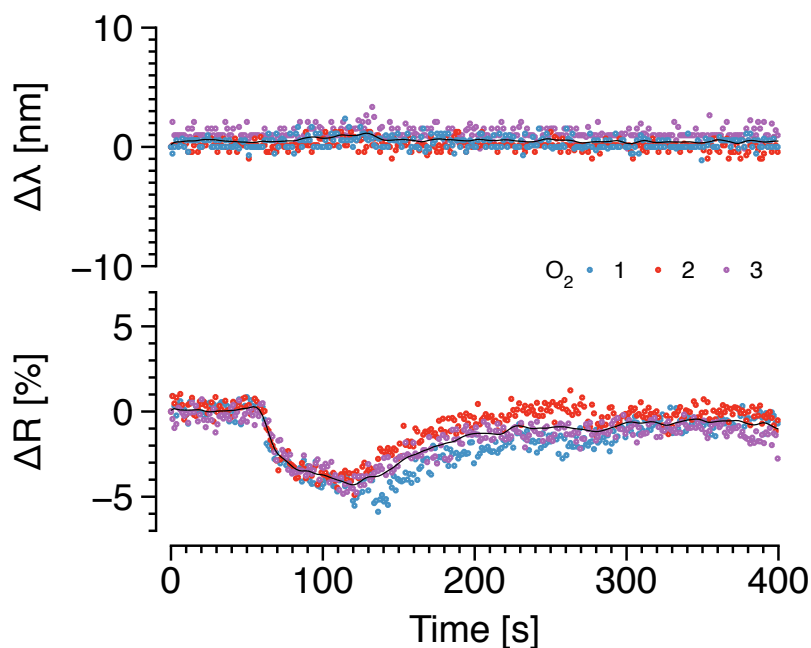
Figure 5.18: Holographic response to oxygen gas in high-exchange Nafion holograms. The concentration of oxygen gas was 99.99% (v/v) taken straight from the lecture bottle. The black line corresponds to the average response and the different colors (1, 2, 3) to different runs.

There was no change in reflected wavelength but a negative change in reflection intensity was recorded. Furthermore, the signal was completely reversible and could be collected continuously as shown in Figure 5.19. The noise level of the response to pure O_2 was high and did not permit lower concentrations of oxygen to be measured. In addition, the mechanisms of refractive index change with O_2, and the effect of drying, were difficult to deconvolute. A negative change in intensity is related to a decrease in the refractive index contrast of the fringes. However, it is not yet clear why the interaction with oxygen caused this change. Several plausible hypothesis may be proposed, for example:

1. Any remaining water molecules strongly bound to the sulphonate groups were displaced by oxygen causing a refractive index change. It has been reported that structured water has a higher refractive index when in close proximity to Nafion [241, 270].

2. The singlet oxygen modifies the surface of the nanoparticles, changing their

147

refractive index. It has been found that in oxidizing atmospheres the outer most layer of silver nanoparticles could have variable refractive indices due to the oxygen interaction with the metallic surface [271].

3. The refractive index of gaseous oxygen inside the membrane will contribute to the total average refractive index of the fringes with and without ablation and will reduce the reflection efficiency. The refractive index of oxygen is ~ 1.0 and therefore a global reduction of refractive index is expected [272]. It is known that gas-polymer interfaces in foam micro-structures cause scatter which will affect the refraction and reflection [273].

4. Oxygen molecules with partial negative charges momentarily push the sulphonate groups apart, increasing the space between the cavities and changing the refractive index. Hydrophilic sulphonate groups could repel oxygen that appears to be hydrophobic when in hydrated Nafion membranes [274, 275].

The first hypothesis is discarded because the water content after drying was low, and, if water in the membrane cavities reduces the refractive index, the difference n_1-n_2 should increase, thereby giving a higher reflectivity, not a lower reflectivity.

The second hypothesis seems feasible; however, there was no response to oxygen in PDMS holograms containing metallic silver particles. The presence of sulphonic acid charges favoured the oxygen diffusion into the membrane, forcing the oxygen to form silver oxide on the nanoparticles. Even if there was silver oxide (Ag_2O) present on the surface, its refractive index would not contribute greatly to that one of metallic silver and a change would not be noticeable [276].

The third hypothesis is also feasible; however, it needs to be shown that gaseous oxygen flows freely through the PEMs cavities. In Nafion, dioxygen coordinates with water and the volume occupied by dioxygen decreases as the water content increases [274]. Since the membranes are dried, it is likely that oxygen diffuses in the gaseous form. Polymer-gas interfaces increase scattering, and thus the reflection efficiency and the holographic reflection intensity will decrease [273]. This third hypothesis is the most feasible explanation because it is the only way to justify changes in reflectivity when there is no change in refractive index, at least from the model perspective which does not account for
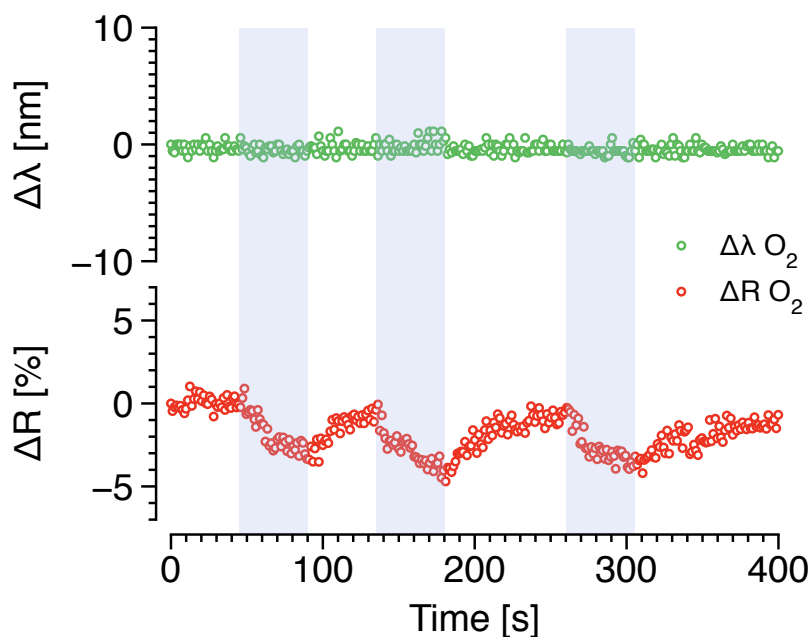
Figure 5.19: Holographic response to oxygen gas in high-exchange Nafion holograms. The shadowed areas indicate the period of gas exposure. The concentration was 99.99% (v/v).

reflection efficiency reduction by scattering.

The last hypothesis suggests that not only the refractive index changes, but also the fringe spacing. This behaviour would be similar to the water response in which both n and Λ changed and is also feasible.

These hypotheses should be interpreted with care because the response level to oxygen is very low; the reason for this might be due to the hologram efficiency more than the oxygen-Nafion interactions. Furthermore, it could be a combination of several phenomena that are causing the change. Thus, more than one hypothesis can be valid. In conclusion, further investigation is needed to establish the mechanisms of refractive index change in Nafion membranes exposed to O_2. Nevertheless, Nafion holograms were able to detect oxygen gas at 99.99% (v/v) repeatedly and reversibly.
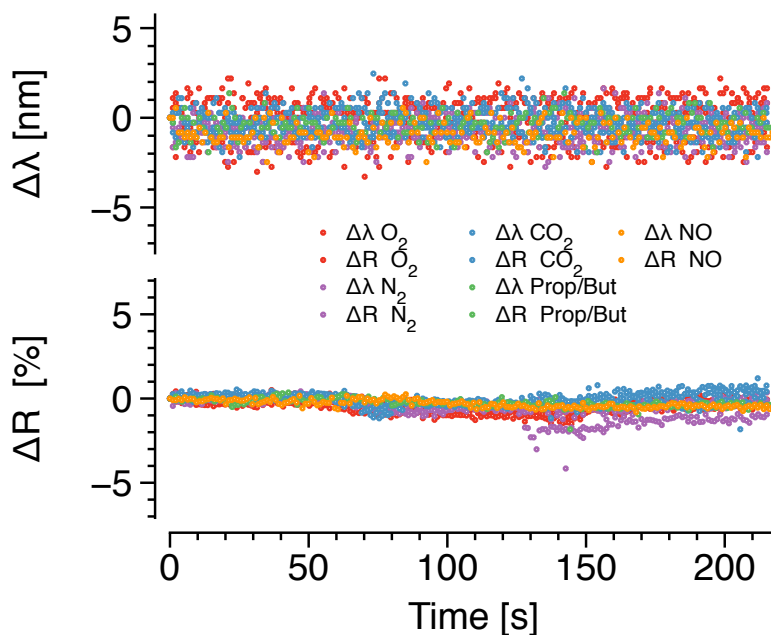
Figure 5.20: Holographic response to oxygen, nitric oxide, nitrogen, carbon monoxide and a mixture of hydrocarbons, butane-propane (30:70 (v/v)), for high-exchange Nafion holograms. None of these gases showed a response. The concentrations corresponded to the concentration in the lectures bottles $\geq 99\%$ (v/v).

5.5.2 Low-exchange membranes

Holograms made in low-exchange membranes (N-117) were also exposed to hydrocarbon gases, N_2, NO, CO_2, NH_3 and O_2. The tests were also performed for dried membranes; only ammonia showed a significant response. The results for all the gases except ammonia are shown in Figure 5.20, and the response to ammonia shown in Figure 5.21. Gaseous ammonia was only tested at concentrations of 0.19% (v/v) in air. There was no significant change in wavelength, only in reflection intensity.

As discussed in previous sections, a reflectivity change would be caused by a change in refractive index or in the quality of the fringes. The hypotheses for the different mechanisms in which ammonia can change the refractive index are similar to those for oxygen:

1. The fringes are contracted by the attraction of positive charges in ammonia

and negative charges in the sulphonate groups. The particles in the fringes come close together, increasing the reflection efficiency and the brightness.

2. The refractive index of ammonia is different from Nafion and silver particles which experience a global average change upon interaction[a].

3. Ammonia may displace any remaining water molecules coordinated with the sulphonate groups or formed ammonium ions NH_4^+, which caused changes in the refractive index [279]. Ammonia is not known to react with metallic silver; therefore no change in the silver particles is expected.

None of these hypotheses explain the increase in brightness except the contraction of the fringes caused by the difference in charges. However, this should also affect the reflected wavelength. Figure 5.21 shows a small change in wavelength that would support this hypothesis. Further efforts to understand this effect may include the optimization of the recording process to improve the brightness of the hologram and testing the response under different humidity conditions.

5.5.3 Further optimization for low-exchange Nafion membranes

A comparision of the response to 0.19% (v/v) NH_3 gas for low-exchange and high-exchange membranes is shown in Figure 5.22. Holograms in high-exchange capacity membranes took longer time to reach a maximum response and recover their original position. In fact, the high-exchange capacity membranes took a thousand times longer to reach a maximum response or recover their original state. Thus, low-exchange membranes were preferred for fast response; however, only high-exchange membranes showed a response to O_2, 2-fold higher than the response to ammonia.

At this point the NE-1035 high-exchange membranes were no longer available and low-exchange N-117 membranes were used for all subsequent experiments. Further optimization of the methodology was required to increase the sensitivity of the low-exchange membranes in order to sense interactions with O_2. The

---

[a]The refractive index of liquid ammonia is 1.325 and ∼1.0 for the gaseous state [272,277,278].
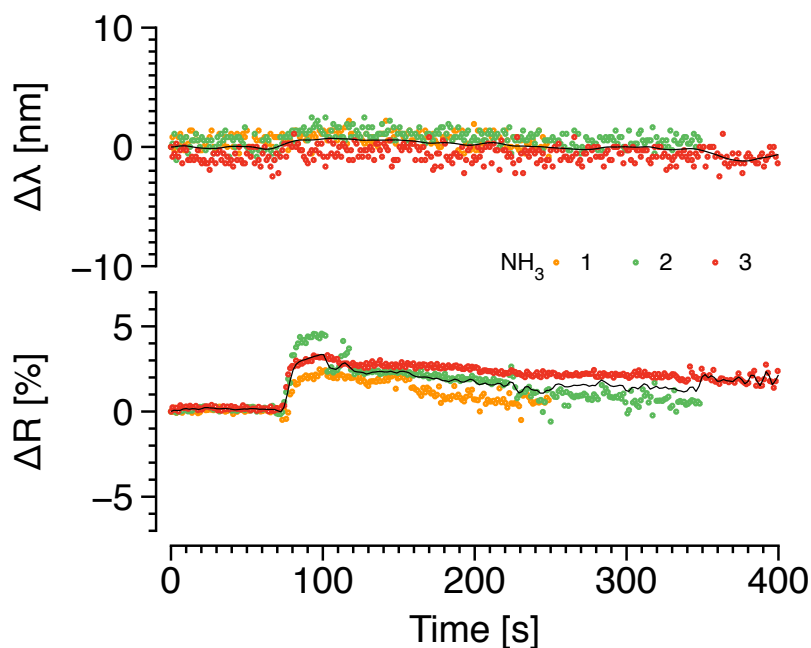
Figure 5.21: Holographic response to ammonia in low-exchange Nafion holograms. All plots correspond to 0.19% (v/v) in air. The black line represents the average response and the different colours (1, 2, 3) different runs.

optimization studies targeted an increase in brightness aiming to enhance detection of small changes in the signal. The improvements listed below apply to the methodologies described in §3.2.1 and §3.3.1.

Thus, commencing with the ablation process, one side of the membrane was blocked with synthetic sticky rubber to avoid deposition of particles on both sides, whilst to improve the nanoparticle loading times, the membranes were exposed to silver ions without purifying or equilibrating with sodium ions. However, a potential disadvantage of doing this is that the membranes could carry impurities, although the presence of impurities did not appear to influence the brightness of the resulting holograms. Furthermore, discarding the purification and equilibration steps substantially reduced the fabrication times.

The final concentration of silver particles in the membranes was initially controlled by the concentration of the equilibrating solutions. The metallic silver content was controlled by allowing enough time for the membranes to equilibrate with the silver ions, whilst to optimize the nanoparticle-formation times even
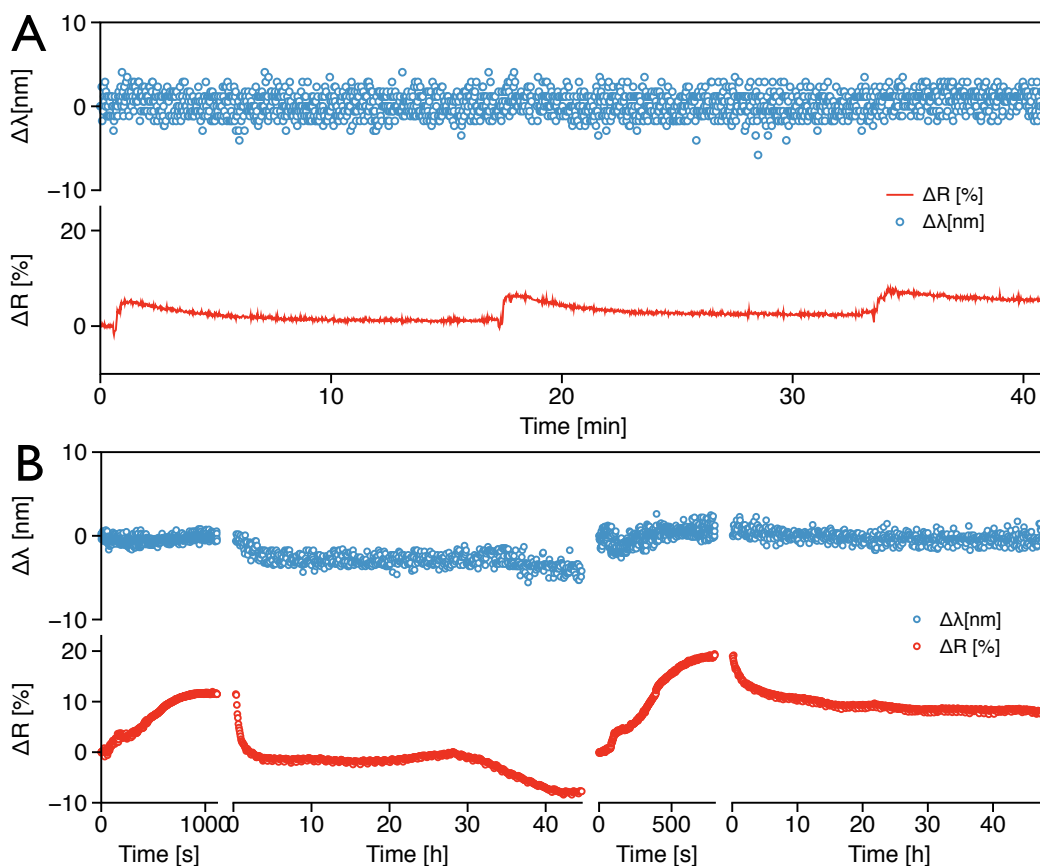
Figure 5.22: Comparision of holographic response to 1.9%(v/v) NH_3 for low-exchange and high-exchange Nafion holograms. (A) Low-exchange capacity membranes. (B) High-exchange membranes.

further, the concentrations were changed and the exposure times reduced. The silver loading process might be limited by the permeability of the membranes to the solvent, in this case water, and thus the solutions were prepared in a mixture of water and ethanol. The ethanol in the solution caused the membrane to swell, allowing a faster diffusion of the silver and reducing ions into the membranes. The total time was reduced to 3s for 0.1M $AgNO_3$ in a 9:1 (v/v) ethanol:water solution at room temperature.

After exposure to the silver solutions for 3s, the membranes were immediately transferred to a beaker containing deionized water and stirred vigorously for 10s, in order to prevent the silver from accumulating on the surface and causing undesirable surface reflections. The surface was wiped with dry tissue and

the membranes transferred to a 0.1M NaBH$_4$ 1:1 (v/v) ethanol:water solution for 2min. The final outcome was ready-to-shot membranes with the optimum concentration of silver for the production of bright holograms. After ablation, the membranes were transformed into bright holograms observable under diffused halogen white light and spot lights (as in Figure 5.14, §5.4).

5.5.4 Effect of environment humidity and temperature on the holographic response

As shown in Figure 5.16, a change of $\sim$0.5nm in the replay wavelength was recorded for every 1°C change in temperature on the surface of the hologram. In other words, small environmental temperature variations appeared not to cause a significant change in the holographic response. However, water content substantially affected the membrane, as shown in the water exposure experiments. Therefore, it was necessary to demonstrate that the environmental temperature and humidity remained constant during the experiments. The temperature and relative humidity in the spectrophotometer room and the rest of the laboratory are controlled by an air conditioning unit, which recycles the air in the room; in this process, water from the incoming air is temporary removed by condensation [280]. The room was monitored for 24h to verify that the temperature and relative humidity were constant[a]. Figure 5.23 shows the recorded values which were 42% and 23.9°C on average with $\pm$7% and $\pm$8.5°C variations respectively. Thus, any recorded temperature changes were unlikely to affect the holographic response although humidity variations could affect it. All subsequent experiments were carried out during short periods of time to avoid significant variations in relative humidity.

Temperature and humidity were also measured at the outlet of the air-tight chamber to test the effects of flushing a dry gas on the holographic response. Figure 5.24 shows that flushing O$_2$ and N$_2$ directly from the lecture bottles led to a decrease in the local relative humidity as the experiment progressed, whilst the temperature showed a continuous increase. All gases in the lecture bottles were free of moisture and thus caused the local atmosphere proximal to the holograms to change. Dry gases not only affected the local relative humidity, but could

---

[a]Set to values of 23° and 40%.
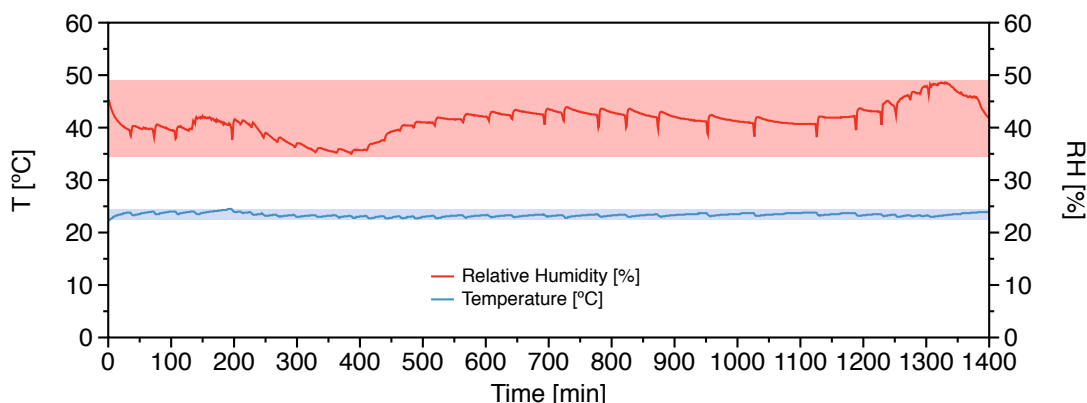
Figure 5.23: Monitoring relative humidity and temperature in spectrophotometer room. Relative humidity, in red, oscillated from 35% to 49% with an average value of 42%. Temperature values changed from 23.1°C to 24.8°C with an average of 23.9°C. The time axis zero value corresponds to 20:00h.

also result in false positives because of a drying effect. This has to be factored in to avoid confusion of the holographic response to the gaseous molecules with desiccation of the membrane.

5.6   Holographic sensing of O_2

The concentration of O_2 in atmospheric air was asumed to be 20.9%. The test gases were free of moisture and dilutions with atmospheric air thus exhibited variations in humidity content. The initial humidity in the membranes could not be controlled or measured during the experiments; it was only possible to perform experiments for water-saturated, dry, or atmospheric humidity-equilibrated membranes. Preliminary studies showed that dry low-exchange membranes produced no response to oxygen. However, the low-exchange Nafion holograms were exposed to oxygen concentrations under different conditions as follows: pre-wetted by soaking in deionized water, equilibrated with atmospheric humidity for 72h, or dried under a gas flow of either N_2 or O_2. The oxygen concentrations were obtained with dilutions made in atmospheric air or N_2 to consider the effect of variable moisture content in the inlet. Table 5.3 summarizes the different conditions tested for which results are plotted in the figures, as indicated in the table.
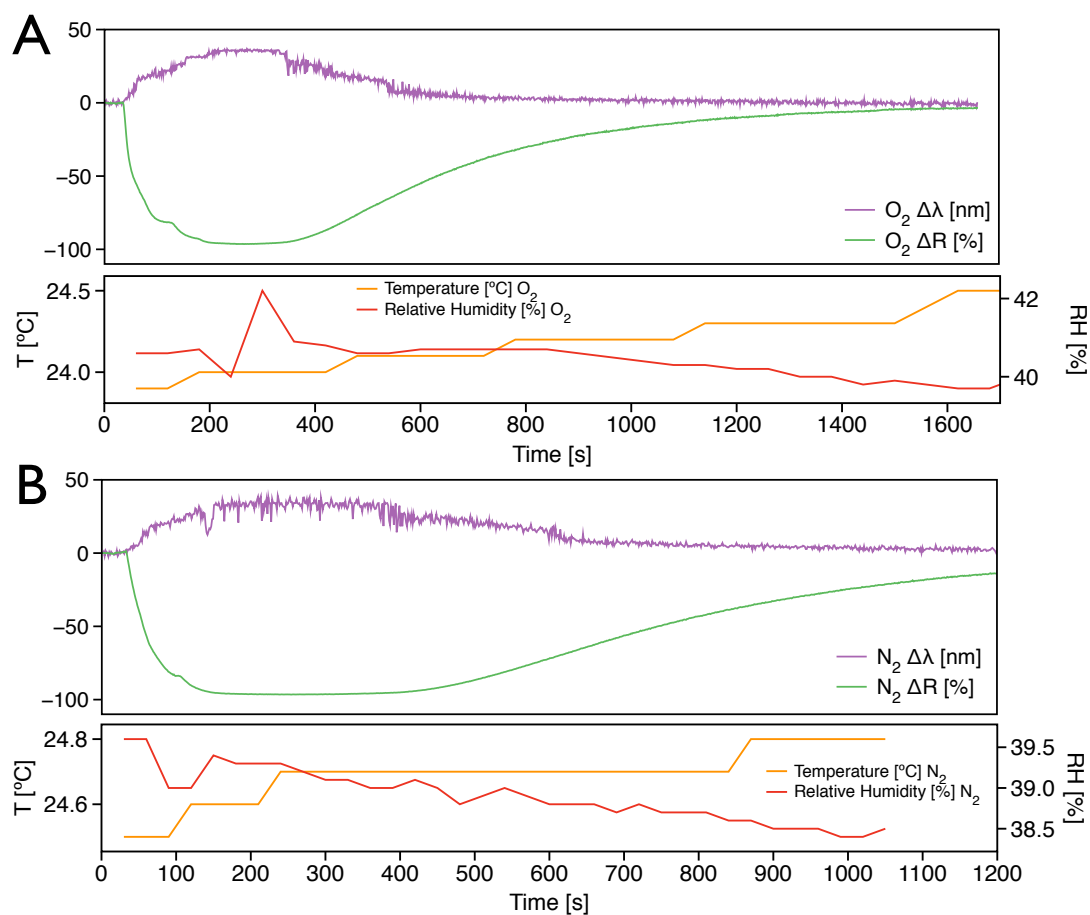
Figure 5.24: Holographic response of pre-wetted holograms to moisture-free gases. The gases were pumped in after recording a baseline for 30s. The purple line represents the wavelength shift, the green line the change in reflection intensity, the red line the relative humidity, and the orange line the temperature. (A) Experiment under O_2 flow. (B) Experiment under N_2 flow.

Table 5.3: Experimental conditions for O_2 sensitivity tests in Nafion holograms. Included: Figure containing the plots; wavelength peak at the beginning of the experiment (λ_0); intensity peak at the beginning of the experiment (I_0); dilutions of O_2 in air or N_2; and the pre-treatment of the membranes: wetted, equilibrated with atmosphere, or dried with a gas flow.

Figure	λ_0 [nm]	I_0 [counts]x10^{-3}	O_2 in	Pre-treatment
5.25	545	60	Air	wet
5.26	569	50	Air	atmospheric
5.27	567	50	N_2	atmospheric
5.28	561	30	N_2	N_2 flow
5.29	562	47	N_2	O_2 flow

Holograms made by the optimized method were also insensitive to NO, CO_2, and hydrocarbons.

Figure 5.25 shows the response to O_2 dilutions in air for a wet hologram. In this experiment, the relative humidity in the inlet changed for the different O_2 concentrations from 0% for the pure O_2 to 40% for atmospheric air. There was also O_2 in the air which appeared to give a response. However, all the experiments were accompanied by the effect of drying the hologram. There seems to be a good correlation with changes in λ and the O_2 concentration but this is obfuscated by the differences in humidity.

Figure 5.26 shows the response to the same conditions as Figure 5.25, but in this case the hologram was left to equilibrate with atmospheric humidity for 72h. It was expected that changes caused by the drying effect would not be present when exposed to air, or were reduced for the presence of air in the dilutions with dry O_2. The same humidity variations from 0% to 40% were present in this experiment. Comparing the response to that shown in Figure 5.25, there was a reduction in the large responses due to wetting. The decrease in wavelength observed for the wet holograms was also present in this case. Similarly, a positive wavelength shift for low O_2 concentrations and negative shift for high O_2 concentrations were recorded. The intensity showed the same trend, a reduction for high concentrations and an increase for low concentrations. Once again, the drying effect is detected as a reduction of the intensity but, in this case, oxygen at low concentrations produced an increase in intensity. A plausible explanation for this

increase is that the dilution had similar humidity content as the environment and the response of the hologram is mainly due to the oxygen presence. The results are similar to the ones in the preliminary results section (§5.5).

Thus, it has been noted that oxygen gives a response that is masked by the drying effect on the holographic matrix. Figure 5.27 shows the response to varying O_2 concentrations in N_2 for the same conditions as Figure 5.26. Diluting O_2 in N_2 eliminated the variations in humidity because both gases were dry. The drying effect was, nevertheless, invariably present. The aim of this experiment was to determine the effect of oxygen concentrations over the effect of drying. It was found that the intensity decayed and the wavelength changed from negative to positive values as a function of different concentrations of oxygen gas.

Ideally, a response to oxygen without interference from humidity would give the necessary information to determine the oxygen concentration. One way to do this is to work only under moisture-free conditions. In order to achieve this, the membranes were pre-exposed to a copious flow of dry gases to test the holographic response to oxygen concentrations after the holograms have been dried and the atmospheric humidity removed from analyzing chamber. Figures 5.28 and 5.29 correspond to pre-exposures with pure N_2 and O_2 respectively. It was not possible to determine the humidity inside the membranes; thus, it was assumed that this process removed all moisture or at least minimised it.

Since the holograms should not respond to N_2, a response to the varying concentrations of O_2 was expected for the experiments shown in Figure 5.28. However, there was no difference in the responses: All the concentrations yielded the same level for intensity and no response at all for wavelength. The identical intensity response suggests that there was still humidity after the gas pre-exposure. Interestingly, air showed a positive response compared to the dry gases, suggesting again that the hologram reacted to the humidity in the air.

Pre-exposing with O_2 should have given the same response as pre-exposing with N_2, because there was no humidity difference. Indeed, the level of response was similar as it can be seen in Figure 5.29. However, the response to air was different; the change was less pronounced than with the pre-exposure to N_2. It seems that the oxygen in the pre-exposure did not leave any room for the oxygen in air to interact with the membrane and that the response to air in Figure 5.28 carries the response to O_2 as well.
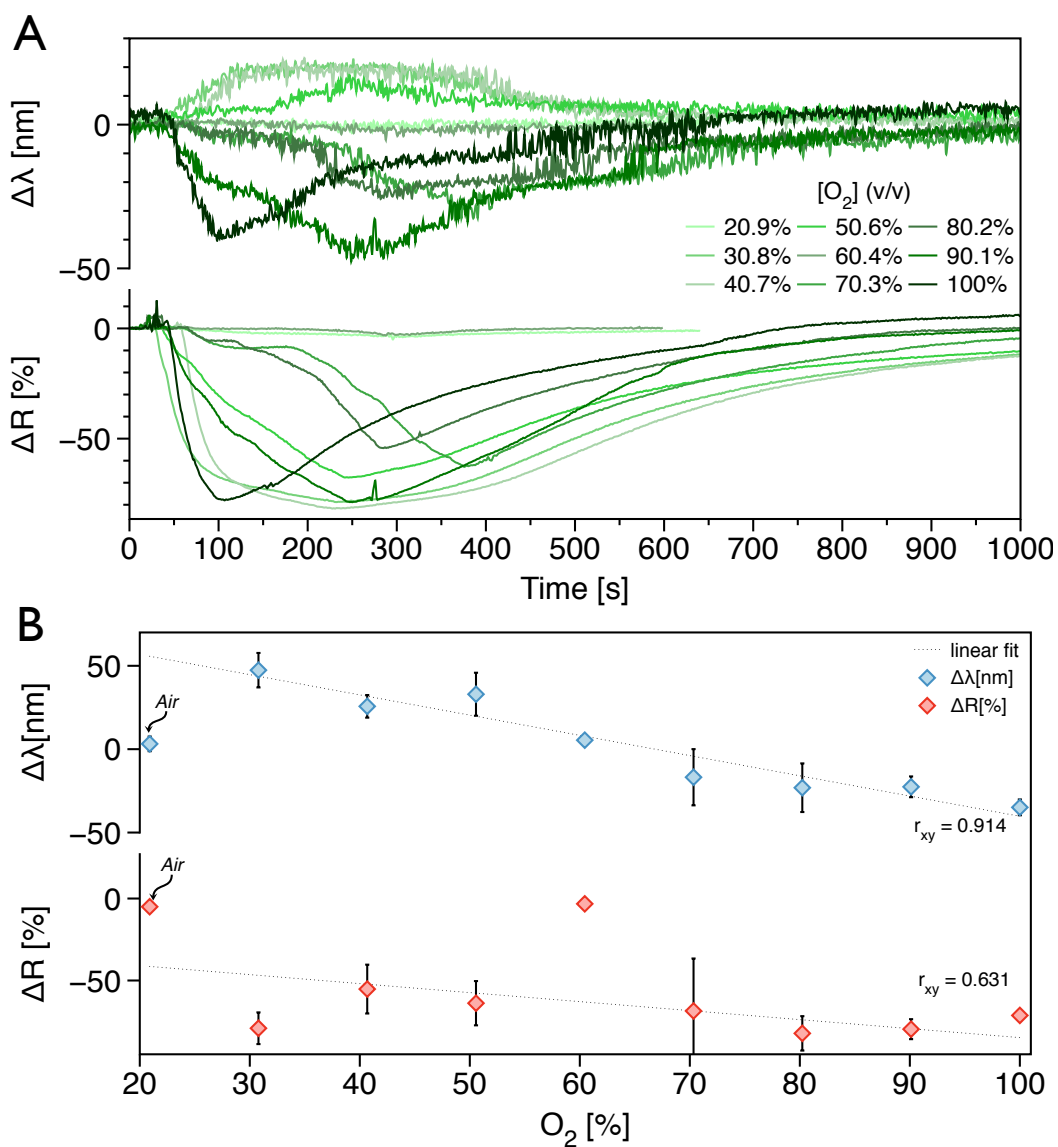
Figure 5.25: Holographic response to O_2 in air for a wet Nafion hologram. λ_0=545nm, I_0=60000. (A) Kinetics of the response for the different concentrations. (B) Peak intensity values, their corresponding wavelength, and correlations with gas concentration.
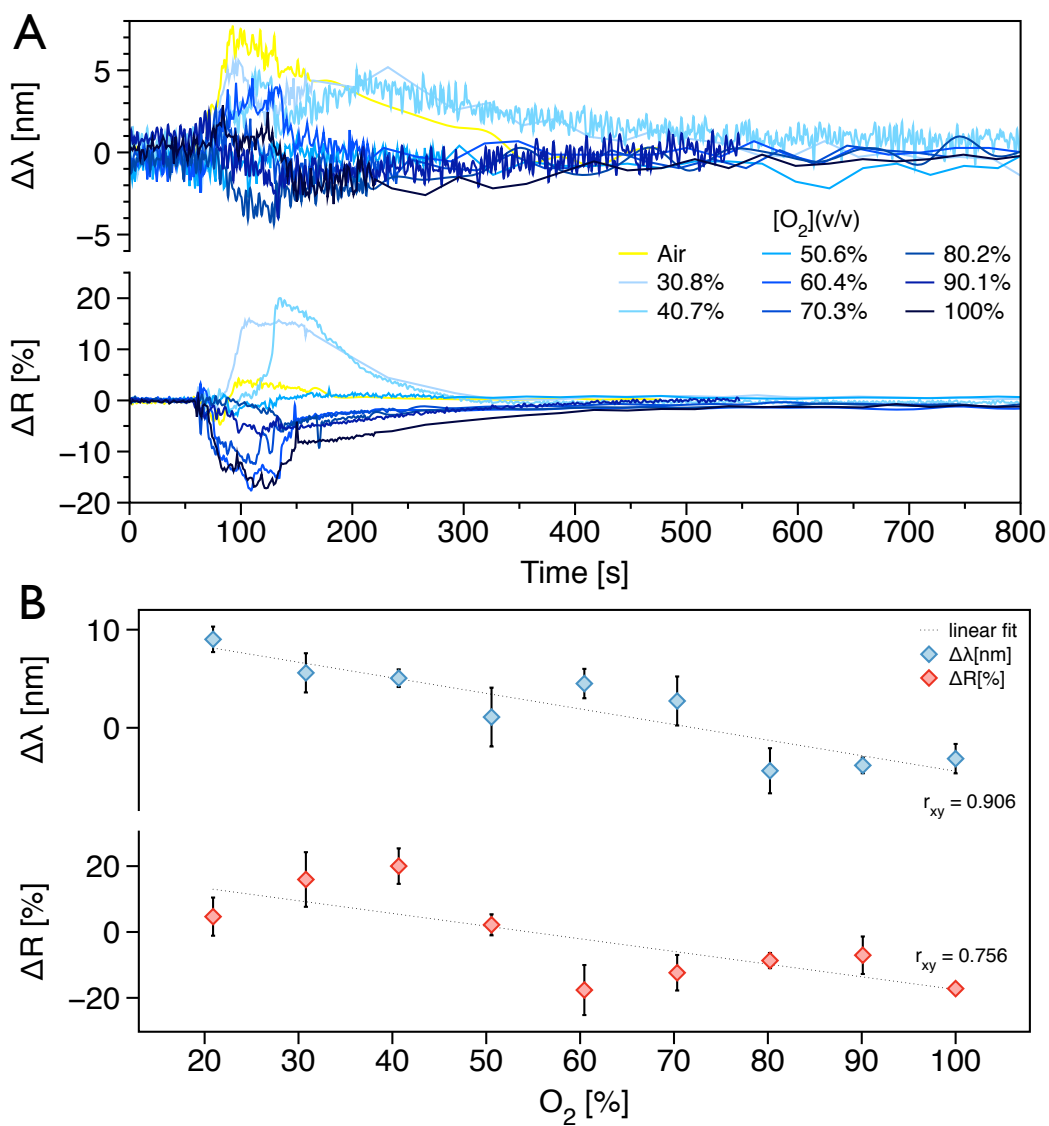
Figure 5.26: Holographic response to O_2 in air for an equilibrated Nafion hologram. λ_0=569nm, I_0=50000. (A) Kinetics of the response for the different concentrations. (B) Peak intensity values, their corresponding wavelength, and correlations with gas concentrations.
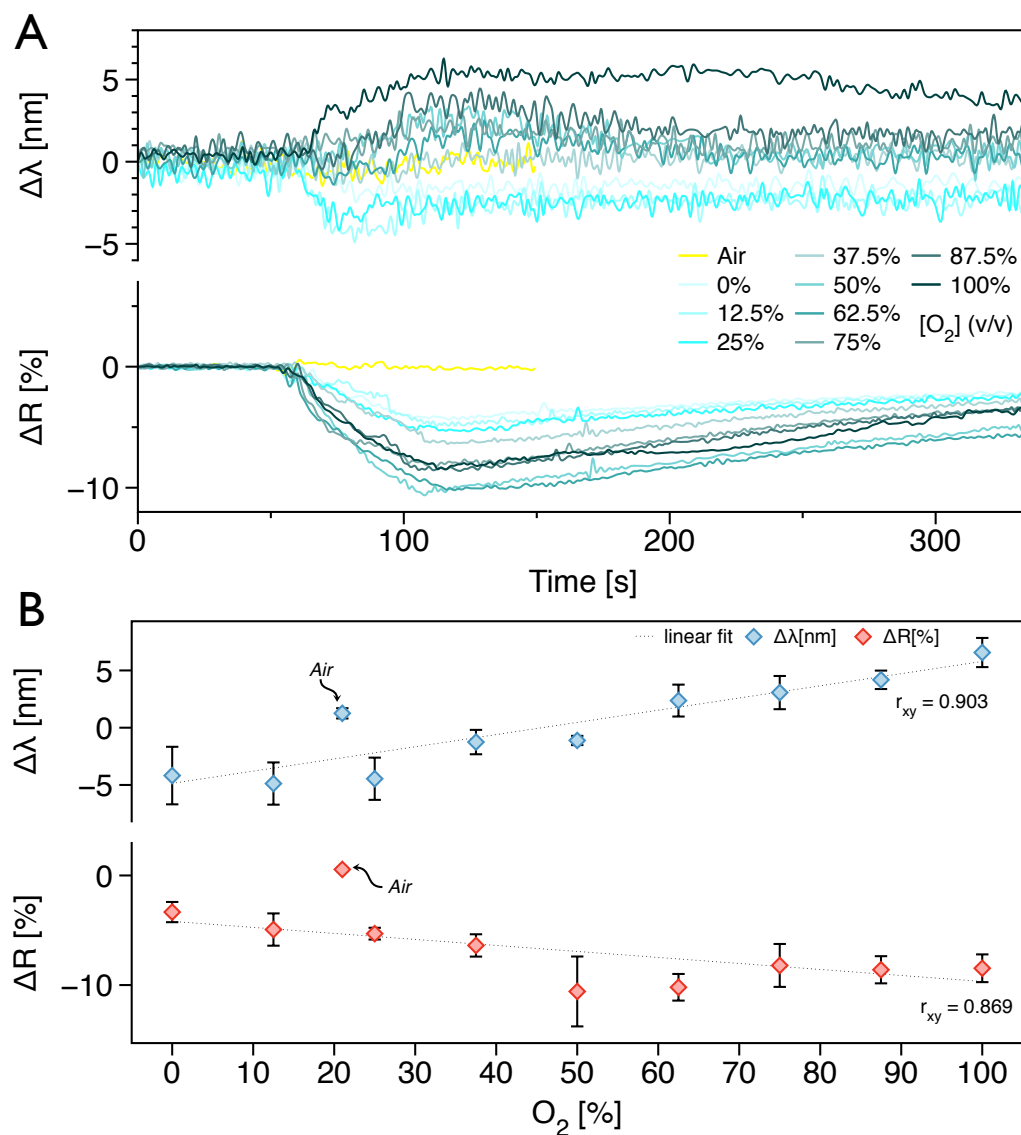
Figure 5.27: Holographic response to O_2 in N_2 for an equilibrated Nafion hologram. λ_0=567nm, I_0=50000. (A) Kinetics of the response for the different concentrations. (B) Peak intensity values, their corresponding wavelength, and correlations with gas concentration.
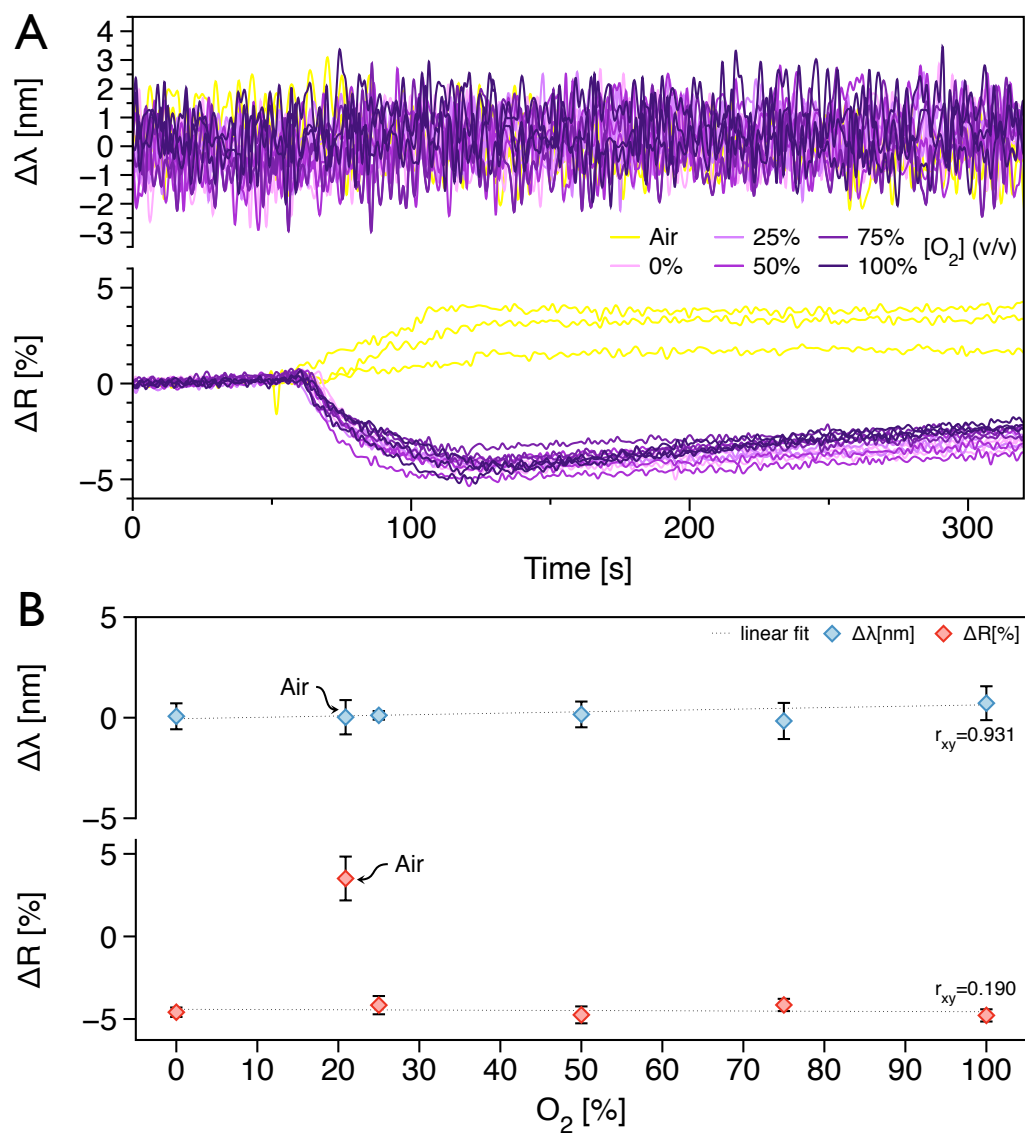
Figure 5.28: Holographic response to O_2 in N_2 for a N_2-dried Nafion hologram. $\lambda_0=561nm$, $I_0=36000$. (A) Kinetics of the response for the different concentrations. (B) Peak intensity values, their corresponding wavelength, and correlations with gas concentration.
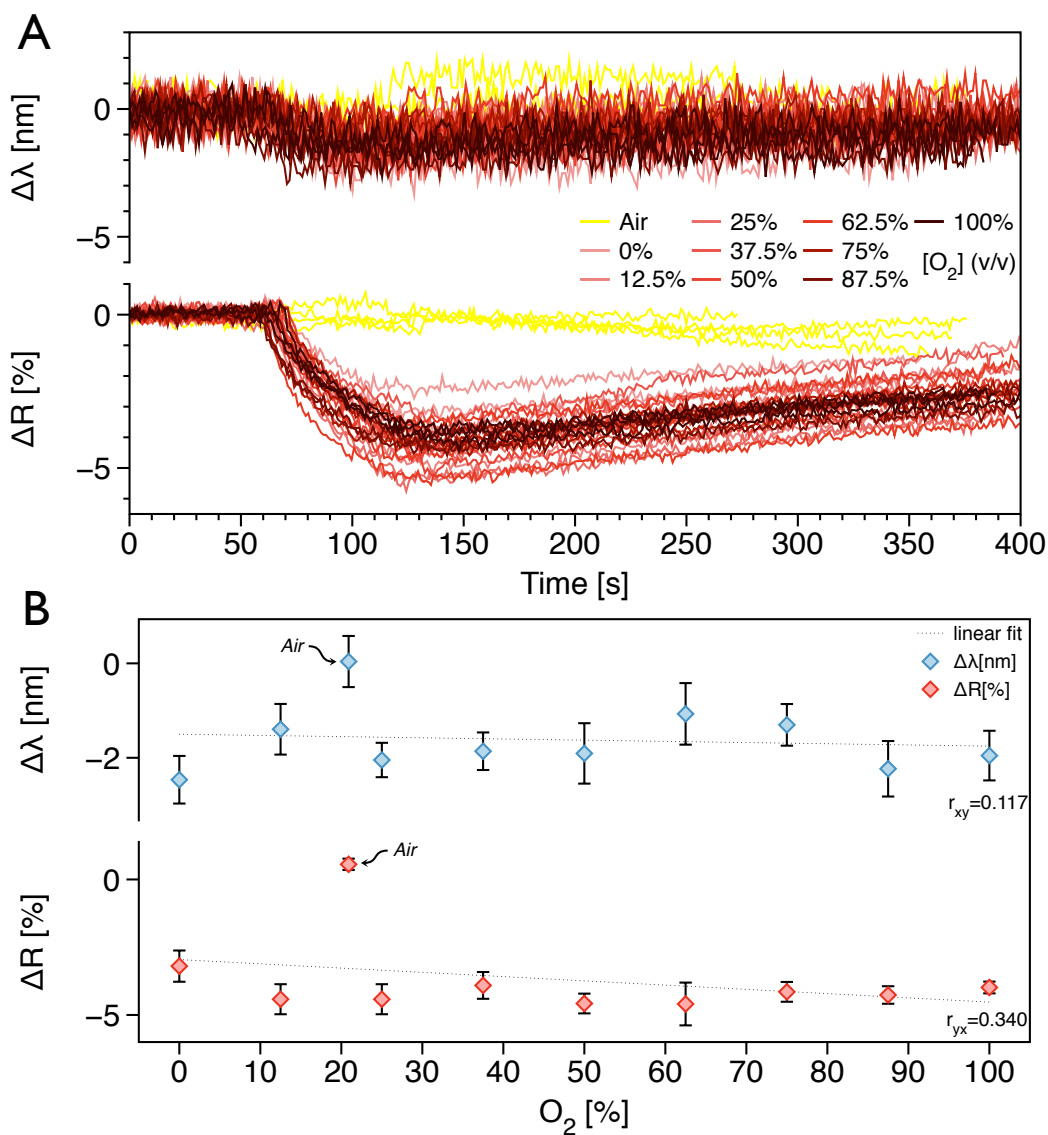
Figure 5.29: Holographic response to O_2 in N_2 for an O_2-dried Nafion hologram. λ_0=562nm, I_0=47000. (A) Kinetics of the response for the different concentrations. (B) Peak intensity values, their corresponding wavelength, and correlations with gas concentration.

Therefore, it can be inferred from all these experiments that that Nafion holograms effectively responded to oxygen concentrations but only in the presence of moisture. An ideal experiment would consist in having O_2 dilutions with the same humidity content as the analyzing chamber which should be in equilibrium with the hologram contained in it. This could be achieved with a humidity controlling device for mixing gases and is recommended for further experiments with oxygen-sensitive Nafion holograms. Nevertheless, having detected different levels of response to oxygen makes Nafion holograms oxygen-sensitive, even though the response was obscured with the humidity and the drying effect. In conclusion, Nafion holograms are oxygen sensors only under specific humidity conditions.

5.7   Holographic sensing of NH_3

The optimized low-exchange Nafion holograms were also exposed to ammonia. The response to this gas was distinct to that for water and oxygen, since $\Delta\lambda$ and ΔR changed in the opposite direction, and it was easier to measure under environmental conditions since there was no interference from water. Nafion holograms were equilibrated with atmospheric humidity for 72h. However, it was noted that for concentrations above 9% (v/v), ammonia appeared to condense on the surface of the holograms, thereby causing a drastic change in the holographic response. Figure 5.30 shows the response to different concentrations of NH_3 up to 12.5% (v/v); above that concentration, the condensation on the surface caused saturation of the response –this is included in Figure A.7 in the Appendix. Figure 5.31 shows the response to concentrations in the range 0.19-1.56% (v/v) not appreciable in Figure 5.30. At lower concentrations, the error from the volume measuring device exacerbates the error in the final measured concentration and the signal. A linear correlation was found for both $\Delta\lambda$ and ΔR with concentration. The wavelength decreased and the reflection intensity increased as the gas concentration increased, although the linear correlation for wavelength was not as satisfactory as the one for reflection intensity, particularly for the lower concentrations.

The sensitivity and detection limits of the holograms were determined from this set of results, taking into account the spectrophotometer resolution. The
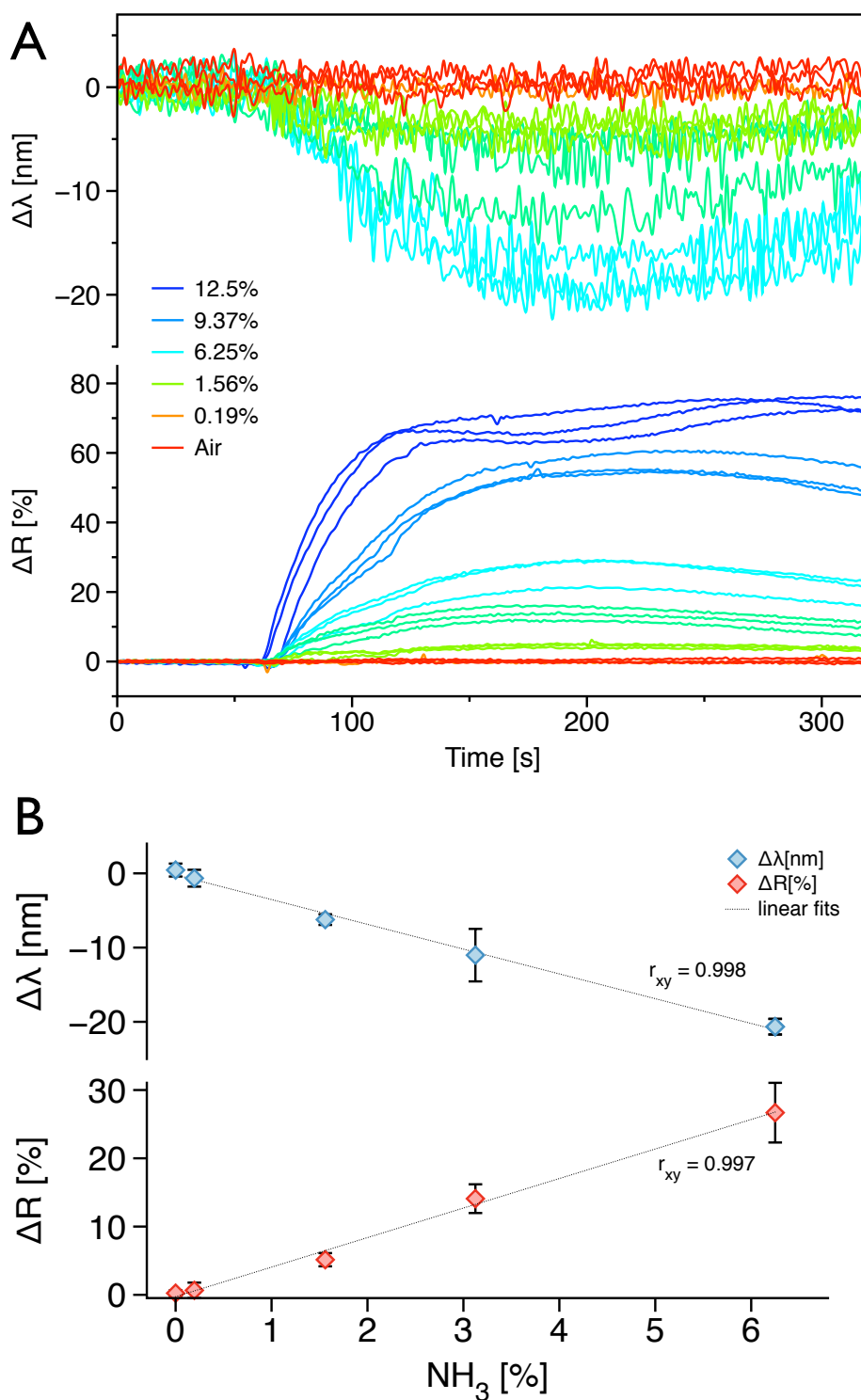
Figure 5.30: Holographic response to high NH_3 concentrations in air for equilibrated Nafion holograms at room temperature. (A) Kinetics of the response for the different concentrations. (B) Peak intensity values, their corresponding wavelength, and correlations with gas concentration.
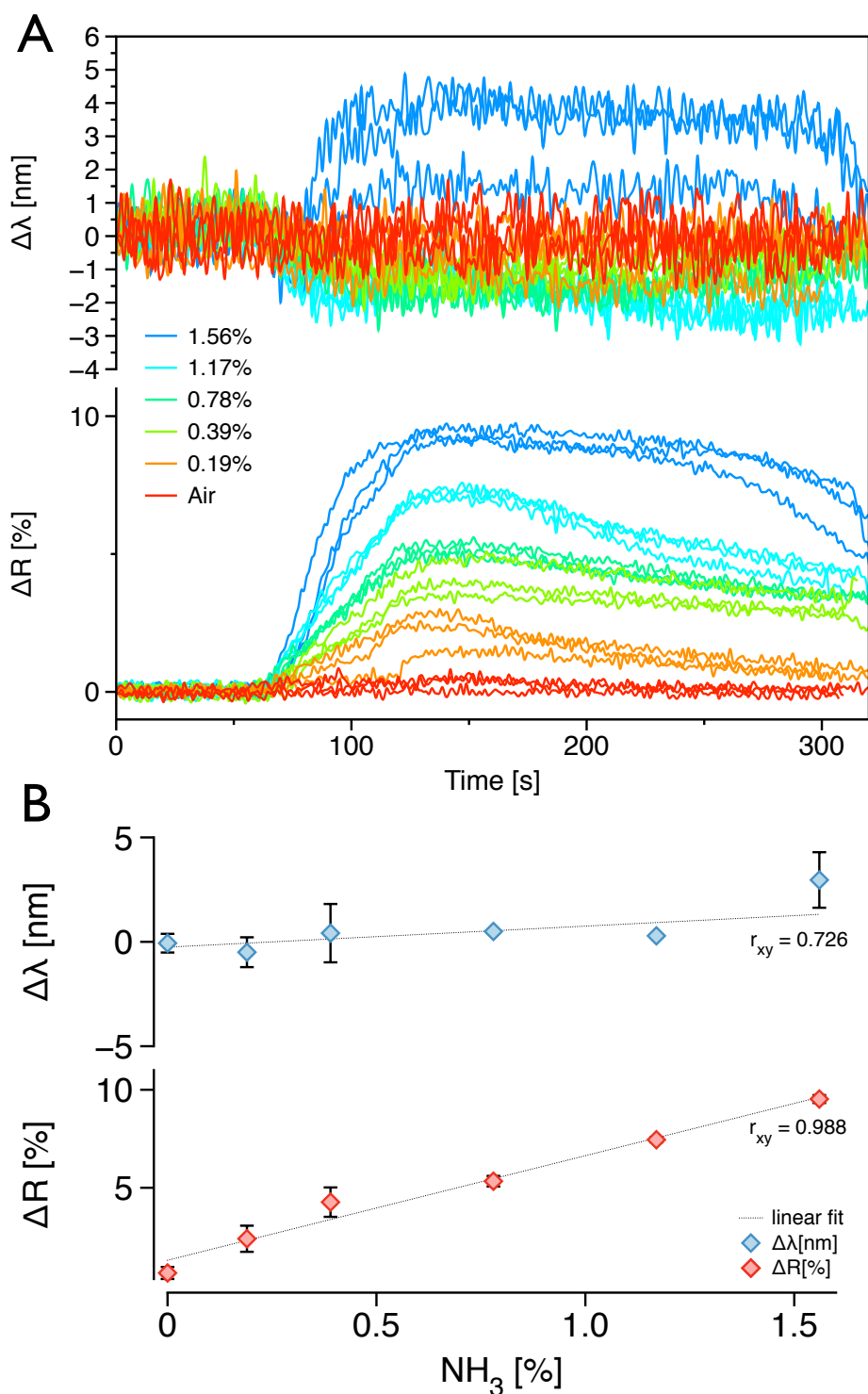
Figure 5.31: Holographic response to low NH_3 concentrations in air for equilibrated Nafion holograms at room temperature. (A) Kinetics of the response for the different concentrations. (B) Peak intensity values, their corresponding wavelength, and correlations with gas concentration. In contrast with the high concentrations experiment, 1.56% (v/v) ammonia gave a positive $\Delta\lambda$ rather than a negative one; an explanation for this is that the hologram reaches a maximum expansion allowing only changes in ΔR (*see* explanation of Figure 5.32).
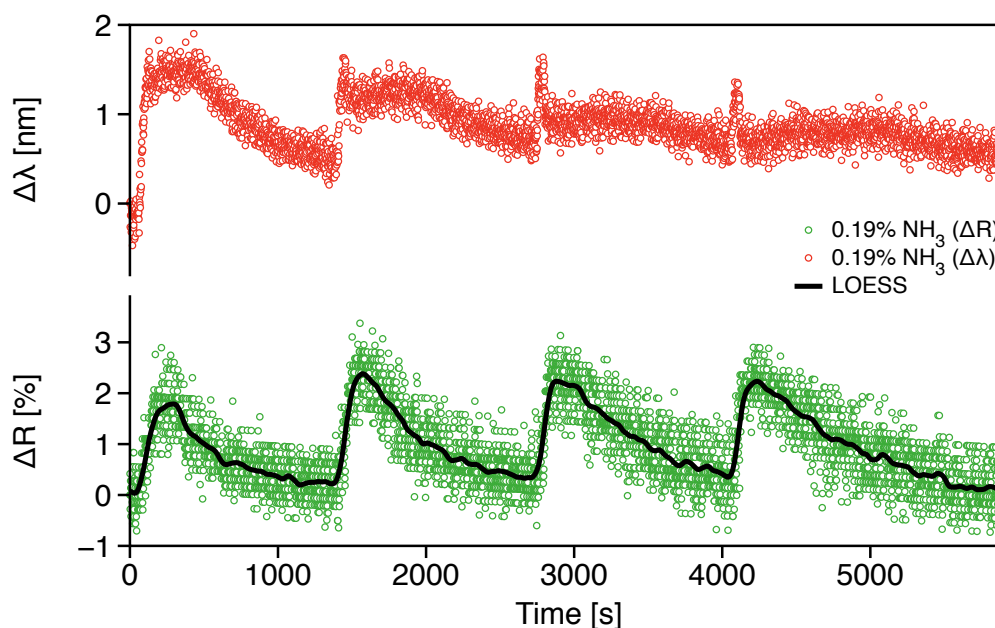
Figure 5.32: Reversibility and repeatability of the holographic response to NH_3 in Nafion holograms. 0.19% (v/v) NH_3 gas flow was injected during 1min after 60s of recording a baseline and the holograms were left open to the atmosphere for 20min. This cycle was repeated 4 times. The black line corresponds a local regression (LOESS) to fit the noisy data points.

sensitivity and detection limits, not only depended on the instrumentation, but also on the noise levels of the signals and the quality of the holographic reflections. The Avantes spectrophotometer signal-to-noise ratio is 200:1 and the specified wavelength resolution is 0.29nm, which in this case corresponds to a ΔR of 0.5% [281]. By interpolating in the linear fits for ΔR and $\Delta \lambda$ in the high concentration plot, the expected sensitivity should be between 0.09% to 0.12% (v/v) of NH_3. However, the holographic signal noise was higher than the spectrophotometer resolution. In practice, only a minimum $\Delta \lambda$ of 3nm and minimum ΔR of 0.7% were detected. This suggests the actual sensitivity and minimum detection limits of the sensor for NH_3 concentrations are ($\Delta \lambda$) 0.89% (v/v) and (ΔR) 0.16% (v/v).

The ΔR response to ammonia was completely reversible and the holograms were operated continuously giving repeatable results as shown in Figure 5.31. This figure shows a continuous measurement of the holographic response to gas injections of 0.19% (v/v) ammonia in air which was detected mainly as a change

167

in R. The time for the signal to recover its original position was $\sim$20min. The concentration at which the hologram acquired a stable wavelength response was found to be $\sim$0.4% (v/v). This could also explain the poor correlation between wavelength shift and concentration for the low concentrations plot in Figure 5.31.

The kinetics of the holographic response to water, ammonia and oxygen gas are summarized in Figure 5.33A and the response rates are compared in Figure 5.33B. All the plots correspond to holograms equilibrated with atmospheric humidity ($\sim$40%). The concentration of ammonia for the comparison with pure oxygen gas and liquid water was 12.5% (v/v). Equilibrium was reached in $\sim$100s for all samples. The response to water is greater than the response to oxygen; therefore, any variations in the local humidity will prevail over a response to O_2. NH_3 on the other hand responded in completely opposite directions to water and O_2. This agrees with the hypothesis above that ammonia has partial positive charges that attract the sulphonate groups causing shrinkage, thus decreasing the wavelength and increasing the reflection efficiency.

There are several physical properties related to charge or polarity that could explain the changes in n and Λ in Nafion holograms, for instance: Ionic strength, octanol-water partition coefficients, molecular polarizability, molecular and polar surface areas, molar refractivity, orbital electronegativities, molecular dipole moment, and the solubility parameter (δ) previously discussed (Equation 4.8).

5.8   Ionic strength tests

Ionic strength is a physical property that could relate to the charge-induced intermolecular forces, and that can be tested experimentally. The ionic strength was originally defined[a] as $\mu_I = 1/2 \sum m_i z_i^2$, where m_i is the molality and z_i the number of charges in the ion. μ_I is used to relate charges and ionic interactions to the activity coefficients of ionic solutions [284]. Thus, if the holographic response depends on the strength of similar dipole-ion interactions, the hologram should respond to various ionic strengths. It should be pointed out that measuring ionic strength requires aqueous solutions, and hence these experiments started at the

---

[a]There is some debate in the literature about the use of this empirical concept in theoretical models and whether the equation should be different [282,283]; the original empirical definition is used in this work.
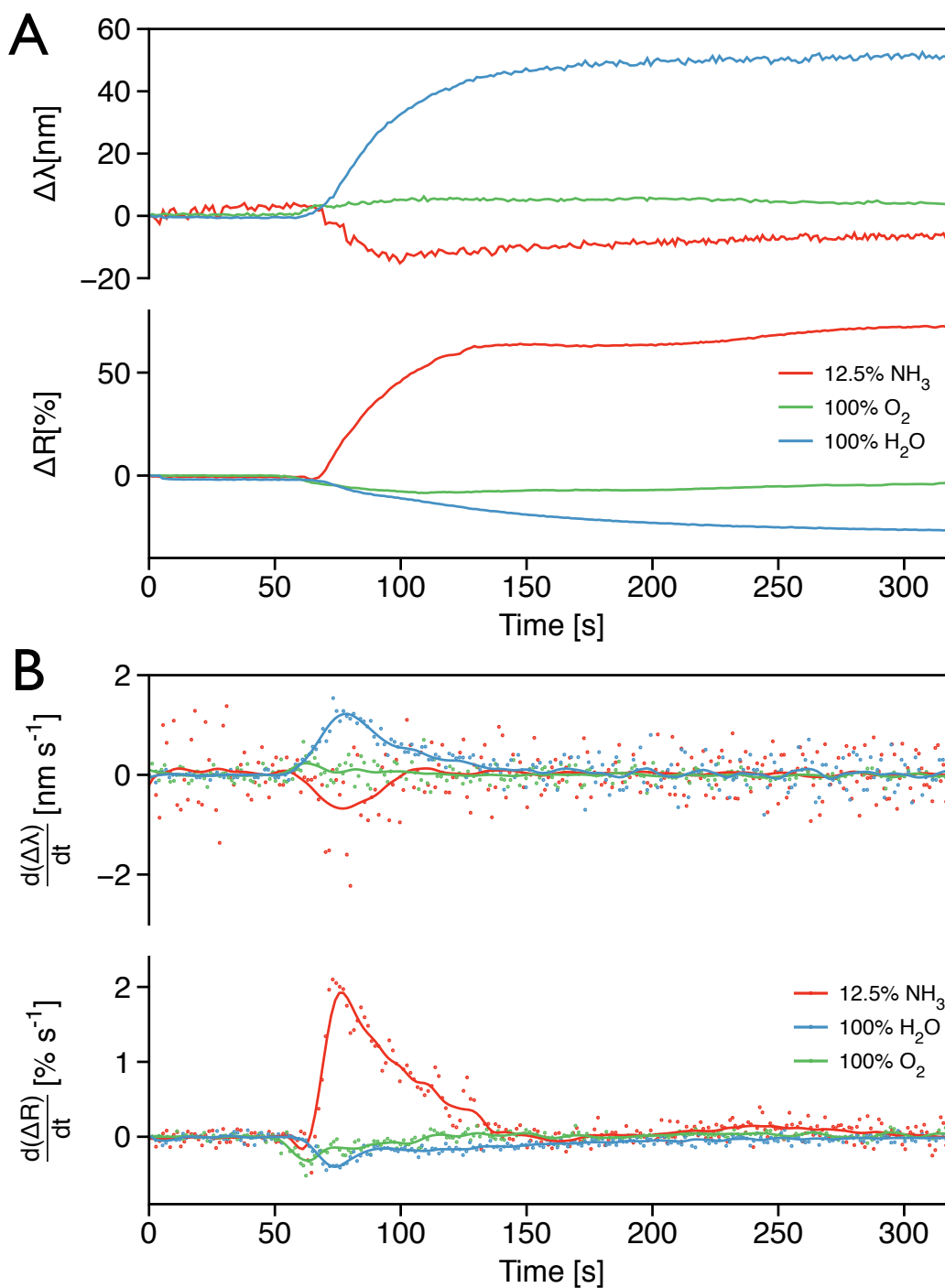
Figure 5.33: Summary of the holographic response kinetics to NH_3, O_2 and water. (A) Evolution of the response over time. (B) Numerical differentiation by centered finite differences of the plots in (A). The analytes injected after recording a baseline for 60s. Equilibrium was reached when $d\Delta\lambda/dt=0$ and $d\Delta R/dt=0$, which is equivalent to 90s of exposure. The solid lines are the local regression (LOESS) that fit the noisy data.

maximum response to water where the baseline was recorded.

The sulphonate groups in the channels of the membrane have hydrophilic negative charges that when hydrated are surrounded by water molecules [257–259]. These water molecules structure themselves around the sulphonate groups causing a change in the local refractive index that can change due to perturbations by interacting counter-ions [255, 258–260, 270]. Therefore, changes in intensity were expected in these experiments. Figure 5.34 shows the holographic signal changes to water and to solutions of NaCl with different ionic strengths. Ionic strength is expressed in terms of molarity[a]. There were some fluctuations at the beginning of each addition caused by the additions of liquid; in order to avoid them, the liquid was instead injected to the initial 5mL covering the hologram. Figure 5.35 shows the control experiment for 1mL additions of water showing no initial disturbance of the signal. In the case of the ionic solutions, an initial large shift was observed; no apparent trend was detected. The plots showing the holographic response to an increase in ionic strength for NaCl, NH_4Cl and NH_4OH ions are included in Figure 5.36. The data points of $\Delta\lambda$ and ΔR for the correction plots were collected before each addition and compared with μ_I, as shown in Figure 5.37.

Na^+ ions were tested as a standard measure of ionic strength and NH_4^+ cations were selected to compare their response with NH_3. Unfortunately, the tests were not reproducible and no significant correlation was found. Nevertheless, water did not show a change to either $\Delta\lambda$ or ΔR. The ionic composition of the sample has an effect on the holographic signals but a correlation with concentration could not be found. A reason for the lack of repeatability of the tests could be that the membranes were transformed into the sodium or ammonium form and remained in that form for the rest of the additions. Conceivably, longer washing times in DI water were required to revert them to the non-protonated form.

An alternative approach was to analyze the charge-induced intermolecular interactions theoretically to try to find and empirical correlation with the observed data. Molecular interactions are the driving force for the holographic signal to change: For example, the holographic response of PDMS holograms was directly correlated to the free energy of mixing. This might not be the case for Nafion,

---

[a]For all the solutions there was only one type of cation of charge +1, and the density of water at room temperature is 1kg/L; therefore, $\mu_I = m_i = M_i$, where M_i is the molarity.
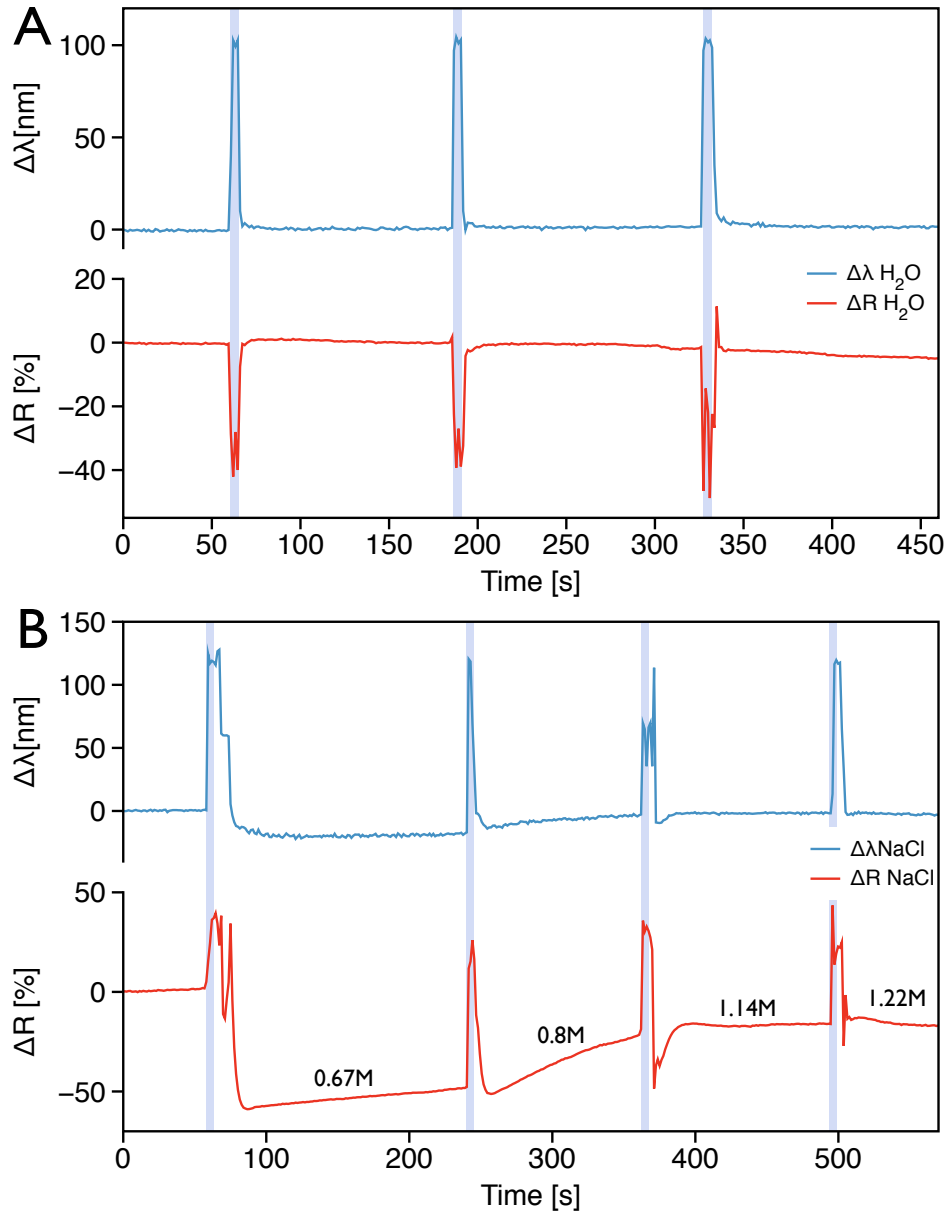
Figure 5.34: The response of Nafion holograms to water and different concentrations of NaCl. (A) Control experiment: Response to water. (B) Response to NaCl. Region shadowed in blue indicates the beginning of the 1mL additions during 20s. The solutions were decanted on top of the initial volume.
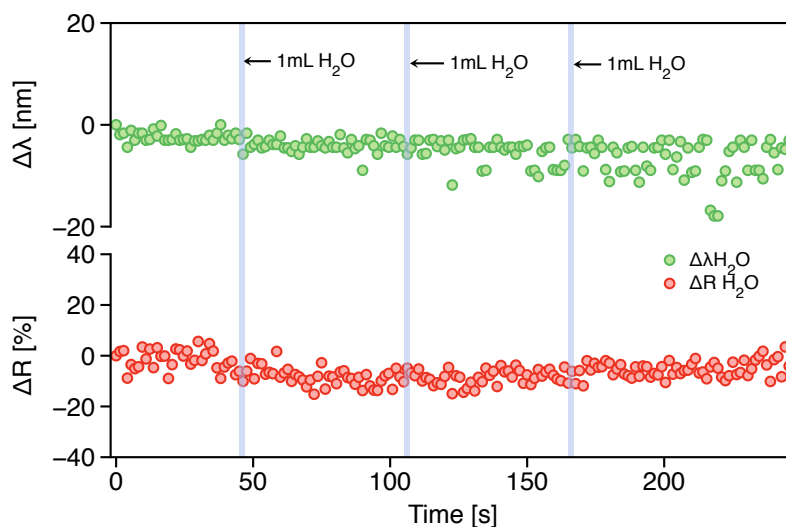
Figure 5.35: Holographic response to water without reflection disturbances. Region shadowed in blue indicates the beginning of the 1mL additions during 20s. The solutions were injected in the initial volume.

although a similar approach was taken by looking at the thermodynamics of the interactions.

5.9 Thermodynamics of Nafion-analyte interactions

Polar hydrophilic interactions with the sulphonate groups in the membrane cavities are postulated to be the cause of the observed changes in λ and R. Their magnitude should depend on the partial charges of the analytes which interact, somehow, with the charges in the sulphonate groups. Physical phenomena such as absorption, diffusion, swelling, and, in the case of Nafion, ionic dissociation may be present [285]. The combination of these processes and the strength of the dipole interactions may form the basis for the holographic response.

A thermodynamic model that relates swelling, absorption, and ionic-exchange equilibria in Nafion membranes has been proposed by Choi [285], based on the Flory-Huggins theory for activity. This model depends on various factors that can be estimated *a priori* and the interaction parameter χ_{12} for which an empirical
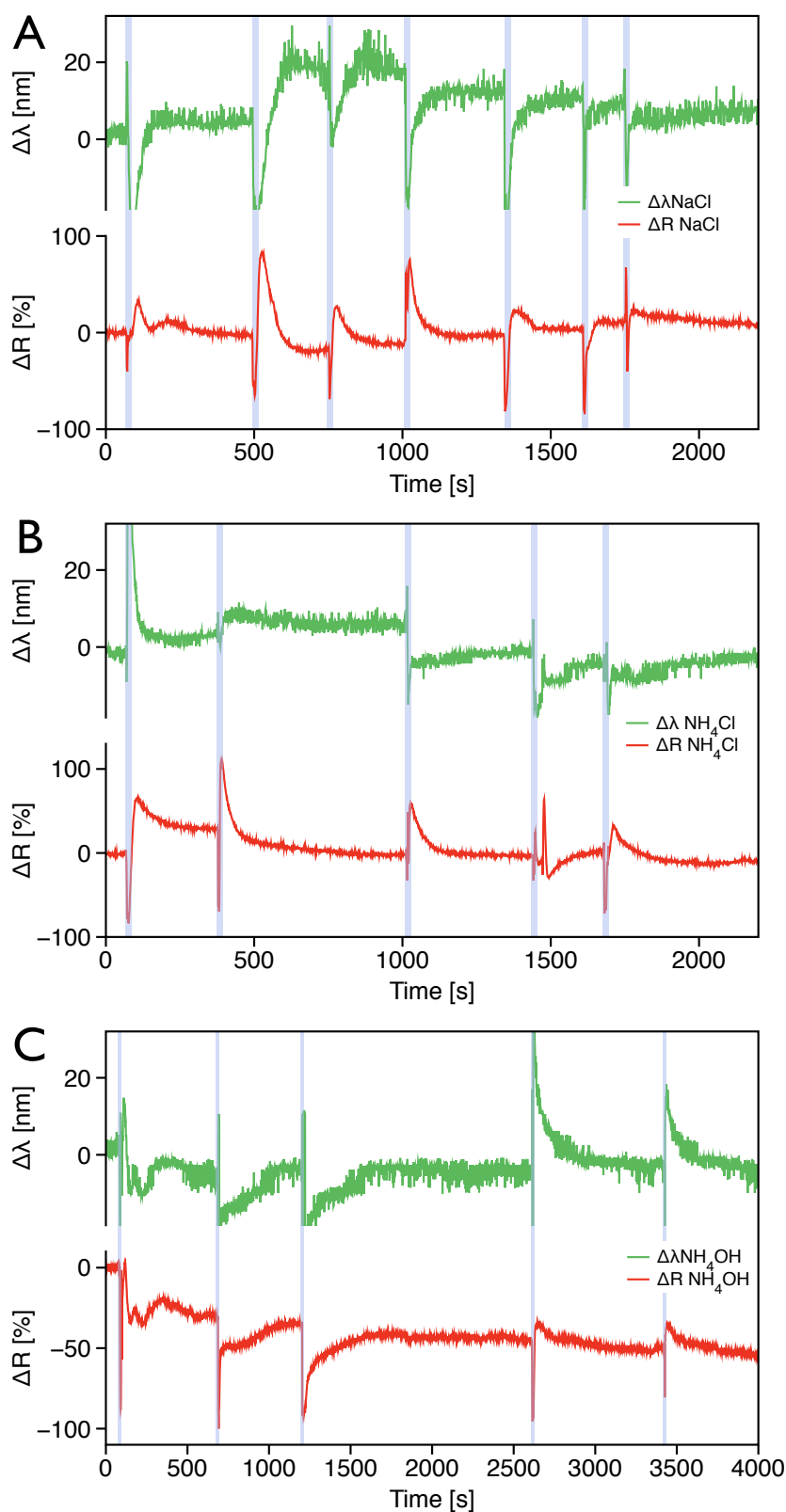
Figure 5.36: The response of Nafion holograms to 1.0M NH_4OH, 0.5M NH_4Cl and 1.0M NaCl at room temperature. (A) NaCl. (B) NH_4Cl. (C) NH_4OH at room temperature. The region shadowed in blue indicates the beginning of the 1mL additions during 20s. The solutions were injected in the initial volume.
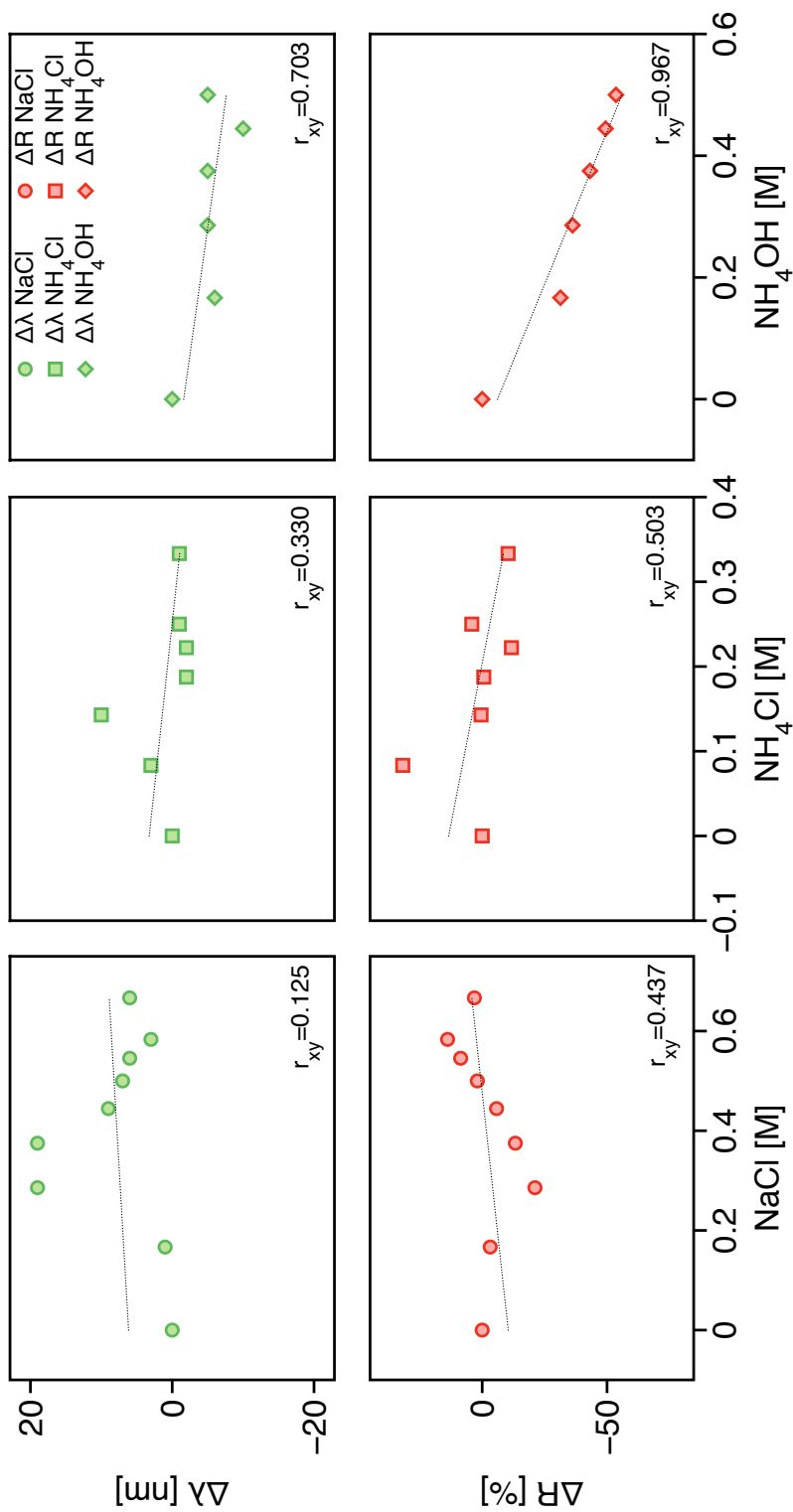
Figure 5.37: Correlation of the holographic response with ionic strength for NH$_4$OH, NH$_4$Cl and NaCl solutions in Figure 5.36.

relation has to be found. As discussed in the previous chapter, χ_{12} depends on concentration and solvent-polymer interactions. These interactions can be expressed in terms of the solubility parameter δ [286]. χ_{12} is also related to the enthalpy of the system (Equation 4.5 p.104), and thus to the free energy which is the driving force for changes in Λ or n. Therefore, finding an empirical correlation with δ is a step closer to predicting and modeling the sensor response to any analyte. However, other physicochemical parameters could also have an effect on the free energy, for instance, refractive index changes can be caused by the complex electron distributions in the materials [287, p.43].

Analyte interactions with Nafion membranes seem to be a complex process that should take into account both the polar and apolar interactions. When the gases interact with the non-polar part of the persulphonic acid polymer, different events may happen, as detailed in the hypotheses promoted in §5.5. Changes in refractive index, wavelength, and the quality of the fringe interfaces occurred simultaneously, and only three different molecular species have given a change in $\Delta\lambda$ and ΔR. Thus, the response in Nafion holograms is likely to have a complex relationship with the molecular properties of the analytes, and may not correlate with any single physicochemical property of the analytes.

In an attempt to find this empirical correlation, the holographic response was plotted against various physicochemical parameters that relate to charges and dipoles in the gas molecules. These include: The solubility parameter δ, the octanol-water partition coefficient K_{ow}, and the solvent accessible surface area A_{SAS}. Other properties considered are:

χ_v The orbital electronegativity of the most acidic atom in the molecule which governs the partial charge distribution in the molecules. It depends on the partial charge of the individual atoms and it is given by $\chi_v = 0.5(I_v + E_v)$, where E_v is the electron affinity[a] of the atom and I_v is the ionization potential[b] [289].

E_π The pi energy which is the sum of bond energy terms for pi orbitals in a molecule given by the sum of the single-electron energies $E_\pi = \sum n_j \epsilon_j$, where n_j is the number of electrons in orbital j and ϵ_j the energy of that

---

[a]Energy required to detach an electron from an ion [288].
[b]Energy required to remove an electron from an atom in its ground state [288].

orbital [290].

$\alpha_{(ahc)}$ The molecular polarizability which measures the tendency to diminish external electric fields by induced dipoles in a molecule; it can also be induced by electrostatic interactions with solvents or ions [291]. It is given by $\alpha_{(ahc)} = 4/N_e \left[\sum_A \tau_A\right]^2$, where N_e is the number of electrons in the molecule and τ_A the polarizability of each atom[a] [292, 293].

A_{PSA} The polar surface area corresponding only to the solvent accessible area of the polar atoms in the molecules.

MR_{calc} The molar refractivity is related to the volume of the molecules and charge distributions at the Van der Waals' surface [294, 295]. It is used to model electrostatic interactions and is given by $\left(\frac{n^2-1}{n^2+2}\right)\frac{MW}{\rho}$, where n is the refractive index, MW the molecular weight, and ρ the density; it is usually calculated from contributions of the individual atoms [296].

μ_x The molecular dipole caused by the uneven distributions of positive and negative charges in the molecules. It is given by the vector sum of the bond dipole moments $\mu_x = \sum_\beta \mu_\beta$, where $\mu_\beta = \varrho\partial$, μ_β is the dipole moment of the βth bond, ∂ the bond distance and ϱ the charge[b] [297].

The plots of these properties versus the holographic response are included in Figure 5.38. The data corresponds to the gas species that exhibited a response: O_2, NH_3 and water; N_2 is included as a control. The values of the physical properties were obtained from reference [291]; Table 5.4 includes all the plotted values.

The holographic response data seems to correlate well with χ_v, μ_x and δ. It has been reported that Nafion membranes have a dual solubility parameter (δ), with one corresponding to the hydrophobic backbone and the other to the hydrophilic sulphonate groups [157, 302]. It has also been reported that the dual solubility parameter is affected by the counter-ion forms of the membrane; it has different values for the H^+ form and the Na^+ form [302]. The values of δ for the untransformed membranes are 20MPa$^{1/2}$ and 34 MPa$^{1/2}$ for the hydrophilic and hydrophobic parts respectively.

---

[a]Tabulated systematically from values based on H_2 [292].
[b]In a bond $\varrho^+ \xrightarrow{\partial} \varrho^-$
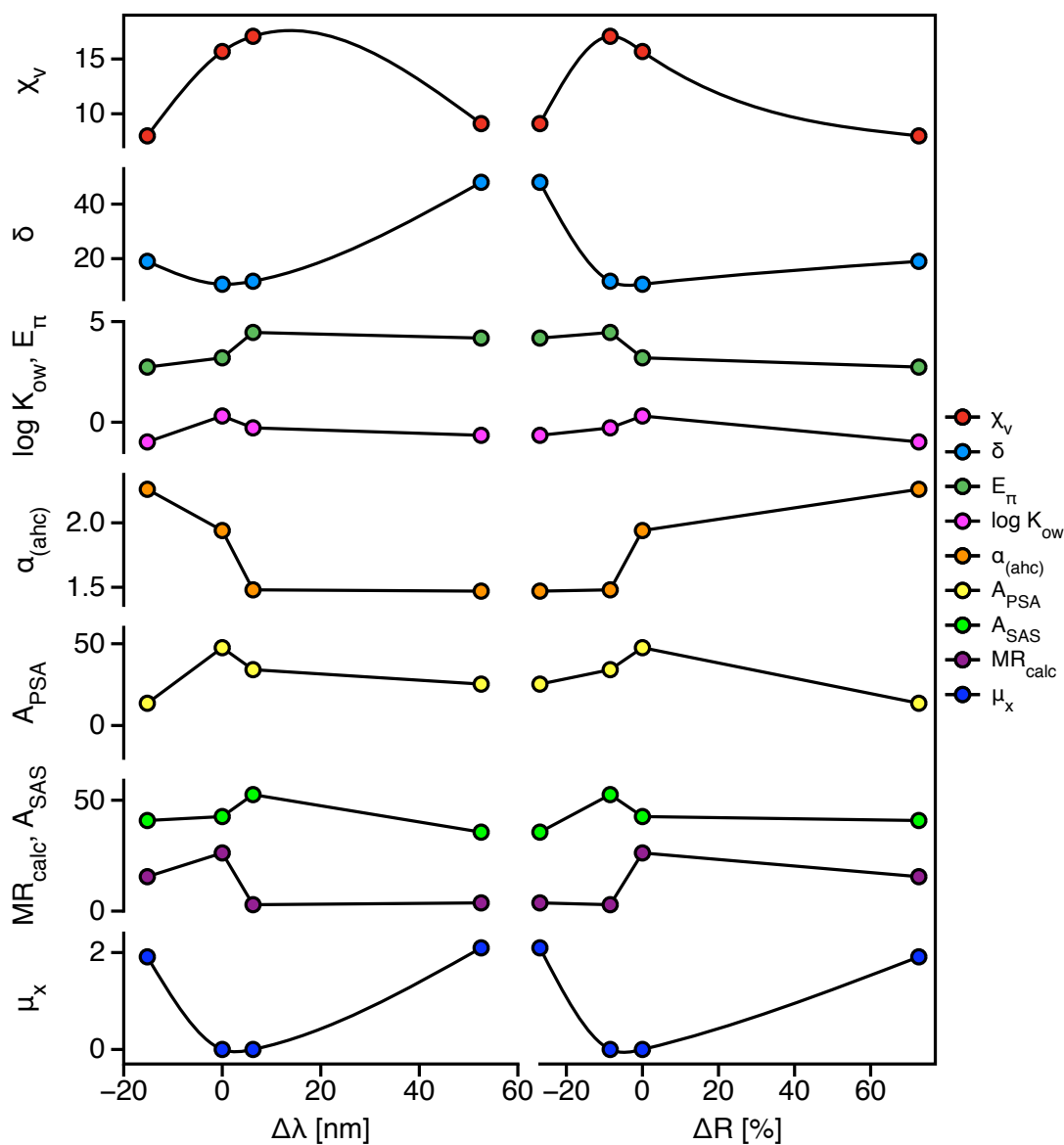
Figure 5.38: Correlation of the holographic response in Nafion holograms with different physicochemical properties. The response values correspond to O_2, N_2, NH_3 and water. The physicochemical properties are: χ_v, orbital electrostatic potentials; δ, solubility paramters; E_π, pi energy; K_{ow}, octanol-water partition coefficient; $\alpha_{(ahc)}$, molecular polarizability; A_{PSA}, polar surface area; A_{SAS}, solvent accessible surface; MR_{calc}, molar refractivity; μ_x, molecular dipole. Areas in Å^2 all other values in SI units.

Table 5.4: Some physicochemical properties of O_2, N_2, NH_3 and water, and their holographic response in Nafion holograms. Areas in Å^2, all other values in SI units unless specified.

Gas	$\Delta\lambda$[nm]	ΔR[%]	$\delta^\star$	$\log K_{ow}$	$\alpha_{(ahc)}$	A_{PSA}	A_{SAS}	MR_{calc}	E_π	χ_v	μ_x
NH_3	-15	73	19	-0.98	2.26	13.6	40.8	15.5	2.7	7.98	1.9
N_2	0	0	10.6	0.31	1.94	47.6	42.6	26.2	3.2	15.7	0
O_2	6.2	-8.5	11.7	-0.28	1.48	34.1	52.5	2.9	4.5	17.1	0
H_2O	52	-27	48	-0.65	1.47	25.3	35.6	3.7	4.2	9.1	2.1

*Solubility parameter values from: [298–301]. All other values from: [291].

Species with values of δ similar to those of Nafion yielded the highest responses. Thus, the correlation seems to follow the dual solubility parameter of Nafion, giving the biggest shift in $\Delta\lambda$ or ΔR for species with similar values to the Nafion hydrophilic and hydrophobic δ. Similarly, species with the highest μ_x and lowest χ_v give the highest response. However, it was not possible to produce an empirical equation because the data points were scarce and the curve lines are just connections between the points. Nonetheless, once the empirical correlation of the holographic response with a physical property is found, it would be possible to relate changes in n and Λ to a thermodynamic model. Hence, in theory, the sensor performance to any analyte could be predicted mathematically. These limitations constrain the depth of analysis that can be made; thus, the holographic response predictions for Nafion membranes is limited to observations.

It is clear that the strength and type of molecular interactions are the cause for changes in fringe spacing and refractive index. The hypothesis that the fringe spacing was modulated by alterations in intermolecular repulsions or attractions, and that the refractive index changes by variations in the electron distributions in the analytes and Nafion now seems plausible. However, an analytical relationship has not yet been found and modeling this complexity might not be possible with current methodologies. Thus, it is recommended that future research focuses on understanding these phenomena, particularly, the refractive index changes caused by intermolecular interactions.

5.10 Summary

Holographic gratings in Nafion membranes were used as transducers for ammonia and oxygen gas concentrations. Furthermore, the holograms exhibited a reversible response. The gases in contact with the grating induced changes in optical properties and acted as the sensing mechanism behind the holographic response.

The response to oxygen was only detected in the presence of moisture. Nafion holograms were able to detect oxygen concentrations in the 0%-100% (v/v) range but their high sensitivity to humidity obscured the independent response to oxygen. The response time was ∼100s and took ∼20min to fully recover. Further investigation is required to improve oxygen sensitivity and understand the mechanisms of the response in the presence of water. Nevertheless, Nafion holograms could be used as oxygen sensors under specific controlled humidity conditions.

On the other hand, the response to ammonia was detected regardless of the presence of moisture in the membranes. Ammonia concentrations in the range 0.16%-12% (v/v) were detected with minimum detection limits of 0.16% (v/v), and with response and recovery times similar to oxygen (100s and 20min). Moreover, the response signal to ammonia did not interfere with $\Delta\lambda$ and ΔR measurements for water or oxygen gas.

It was hypothesized that the holographic-signal changes were caused by the dipole interactions of the gaseous analytes with the sulphonate groups in the Nafion cavities. In order to confirm this hypothesis, an empirical correlation between the holographic response and the intermolecular interactions is needed. The holographic response data agreed with χ_v, μ_x and δ which indicates that dipole interactions are the cause of the change in n and Λ. However, the amount of data was insufficient to properly validate the correlation.

Even if a significant empirical relationship was found, the hypotheses should be analyzed with caution because the interactions could affect n and Λ simultaneously in different ways. Further, the photonic model has some limitations when the quality of the fringes changed; it does not account for reflection efficiency. Nevertheless, the mathematical model for the photonic effect was used to fit the data from the Nafion holograms.

In conclusion, exploiting the intermolecular interactions of ammonia and oxygen with Nafion lead to the production of oxygen and ammonia gas sensors. How-

ever, the challenges of modeling the holographic response based on the analyte's properties, and producing a more selective and sensitive sensors still remain.

Final Discussion

Two new types of holographic sensor have been described in this thesis: Sensors for oxygen and ammonia fabricated in Nafion membranes and sensors for hydrocarbon gases and VOCs made in PDMS films.

In order to record holograms in Nafion and PDMS, a new holographic recording technique has been developed. This technique required the formation of silver nanoparticles ($\sim$18nm) in both PDMS and Nafion. The methodology for inclusion of particles was designed according to the characteristics of the materials and commenced with the perfusion and subsequent reaction of silver salts and a reducing agent inside the polymer matrix, thereby forming metallic nanoparticles. These reagents, however, require chemically compatible solutions with Nafion and PDMS respectively.

PDMS is an apolar material [146], and thus the solutions containing the silver and reducing agent were prepared in organic solvents with high affinity for PDMS. The solvent chosen for this was tetrahydrofuran (THF) and the silver salt soluble in THF was silver pentafluoropropionate (AgPFP). Similarly, hydroquinone (HQ) was chosen as the reducing agent. The amount of silver nanoparticles generated in the films was controlled by the concentration and volume of the solutions used, and the size of the particles was constrained by entanglement in the polymer chains.

In contrast, Nafion is not apolar, and exhibits internal cavities surrounded by charged sulphonic groups [157, 240, 241]. These charges confer on Nafion its permselectivity, allowing only positively charged molecules to permeate into the polymer matrix when it is treated in an aqueous solution [240]. Thus, the solutions used to perfuse the silver and reducing agent were water-miscible and employed only silver cations. $AgNO_3$ in solution was used to load silver ions into the cavities of the membrane and a very strong reducing agent, $NaBH_4$, was used

to reduce the silver cations (Ag^+) to metallic silver (Ag^0) particles. The size of the particles was constrained by the size of the cavities in the membrane, and the amount of silver at the time of imbibing the solutions.

The nanoparticles in both membranes appeared approximately homogeneous in size with average diameters of $\sim$17nm and $\sim$19nm for Nafion and PDMS respectively, and sizes no larger than $\sim$100nm. Furthermore, their distribution in the z-direction beneath the surface was uniform down to a depth of $\sim$20μm for PDMS and $\sim$4.5μm for Nafion. This homogeneity in distribution and sizes of metallic particles in the membranes is the principal requirement for the recording technique which involves ablation of these preformed particles. The 300mJ laser radiation is reflected through the films containing nanoparticles forming constructive interference patterns of high energy laser waves in which the ablation takes place. The result is an ordered stack of layers of film with ablated and non-ablated particles. The ablated regions showed narrower distributions of particle sizes close to the average values. In other words, particles larger than 30nm appear to be more susceptible to ablation.

The ordered layer structure produces a photonic effect filtering the wavelengths that are reflected from the structure; the reflected wavelength (λ) is a function of the grating spacing (Λ), the refractive indices of the alternating layers n_1 and n_2 (average n), the angle of observation ϑ_B and the number of layers L, and this can be described mathematically [116]. Likewise, changes in λ can be used to estimate changes in n and Λ and vice-versa.

A key finding of this work was the correlation between the changes in n and Λ and the analyte interactions with the materials of the sensor. Thermodynamic models for the analyte-polymer interactions suggested that the solubility parameter (δ) is a good indication of the strength of the molecular interactions for polar or apolar molecules (§4.7.1 & §5.9, [218, 220, 221, 285, 286]). The experimental results gave sufficient kinetic data to correlate the sensor response ($\Delta\lambda$) to the thermodynamic parameter, δ. Analytes with similar affinity to Nafion and PDMS gave the highest response. This correlation can be used to predict the response of the sensor for an analyte of which δ is known.

The molecular affinity of Nafion and PDMS for the target analytes was inferred before finding the correlation based on a thorough study of the molecular properties of the analytes and polymers, which was the main reason why they

were chosen as sensor materials. PDMS interacts with apolar substances via hydrophobic interactions [146], and thus it was selected as a suitable material for interacting with hydrocarbons and VOCs. Nafion, on the other hand, is a porous material with hydrophilic cavities which interacts with molecules based on their hydrophilicity or polarity [157, 240, 241], and thus it was deemed suitable for polar molecules such as ammonia and oxygen. Both PDMS and Nafion also form optically transparent films, which is a requirement for the laser ablation methodology.

Nafion is a permselective membrane with nano-metric pore sizes [240, 241]; these constraints determine the type of molecules that permeate into the membrane, *i.e.* small molecules, such as gases. Furthermore, molecules with partial positive charges in their molecular structure are more likely to be attracted by the sulphonic acid charges in Nafion, improving even more the selectivity of this sensor. PDMS also exhibits extra advantages, such as its wide availability, easy fabrication and inertness to corrosive materials or water [146, 171]. PDMS can, therefore, be used in aqueous environments for sensing volatile compounds.

All the experimental evidence suggests that the cause of the change in n and Λ is the strength of the analyte-polymer molecular interactions. However, the mechanisms of the changes are still unknown and different hypotheses were suggested based on previous work [241, 270, 272–275, 277–279], and the findings in this work (§5.9 and §4.7.1).

The hydrophobic interactions between PDMS and the analytes are dominated by Van der Waals' intermolecular forces [167]. Upon interaction, the analytes in continuous movement cede energy (*i.e.* free energy of mixing ΔG_m) to the PDMS polymer chains, thereby changing their conformation and expanding the bulk film, resulting in swelling of the fringe spacing (Λ).

The interactions with charged sulphonic acidic groups in Nafion are caused by electrostatic attraction or repulsion by the partial charges in the molecular structure of the analytes (*i.e.* similarities in δ) [236, 238]. In the case of ammonia, contraction of the fringes is expected due to the attraction of the sulphonate terminated polymer chains towards the cavities. In the case of gaseous oxygen, its partial negative charges were expected to repel the Nafion chains, thus expanding the film and Λ. However, oxygen could not interact with the Nafion membranes in the absence of water, and water changes the refractive index of the cavities.

Thus, the strength of the interactions (δ) affects n and Λ simultaneously.

The significance of these results is that, regardless of the sensor materials or target analytes, the design, fabrication, characterization and modeling methodologies are generic for producing holographic sensors. Sensors for oxygen, ammonia, hydrocarbons and other volatile organic compounds were produced using this methodology, and thereby fulfilled the objectives of the project. The general steps are detailed the section below.

6.1 Generic methodology for the production of holographic sensors

First, it is necessary to select the target analyte for the sensor. A study of the key properties of the analyte such as polarity, electronegativity, molecular structure, conformation, etc. can determine what type of materials are good candidates for the sensor. These materials should promote strong but reversible molecular interactions with the analyte. Not all materials will fulfill the fabrication requirements for holography and identifying a pair that matches the fabrication and interaction requirements is the first key step in the production of holographic sensors.

The sensitivity and selectivity of the sensor are determined by the strength and specificity of the interactions regardless of the sensing platform; the more selective is the material, the more selective will be the sensor, whilst the sensing platform constitutes the means of transducing the interactions into signals. Figure 6.1 illustrates the proposed generic methodology with the key steps identified.

The sensitivity of the sensor materials to the analytes should be preserved through all the hologram formation and recording steps and the materials used should comply to the holographic recording process. Producing a sensitive hologram is not enough for its use as a sensor; it has to be characterized to ensure it gives a significant response as the concentration of the analytes changes. Figure 6.1 also includes these subsequent characterization steps, with the ultimate goal of predicting the holographic response. This is accomplished by coupling the photonic model (§1.2.3) with a thermodynamic model (§4.7.1 and §5.9), relating the strength of the intermolecular interactions with the changes in reflected wavelength and intensity. Coupling these two models requires an empirical cor-
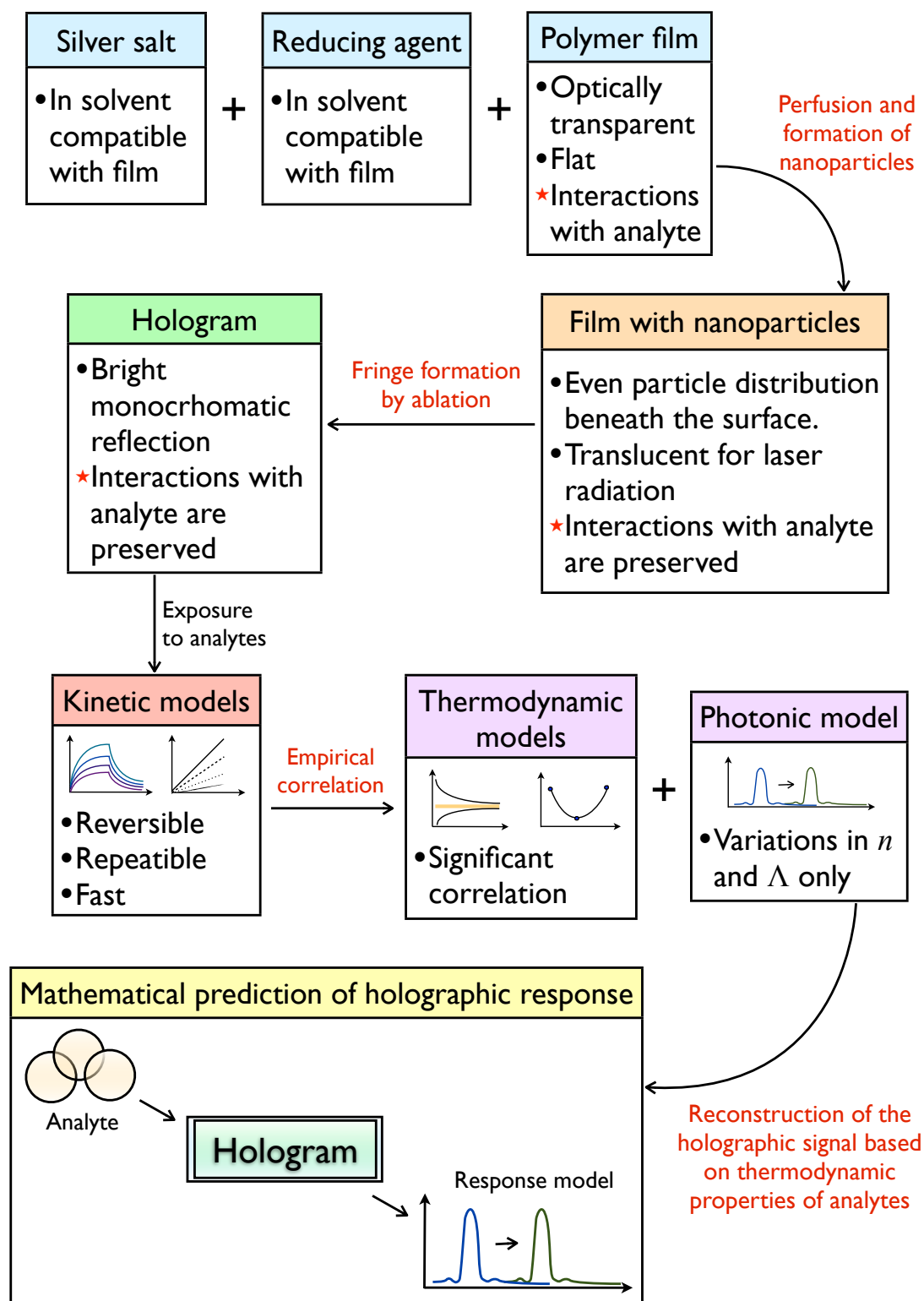
Figure 6.1: Generic methodology for the production of holographic sensors. The key steps and main contributions of the project are highlighted in red. Specific requirements for each step or material are shown as bullet points. The first five blocks represent the fabrication of the sensor and the last four the carachterization. An analogous with Figure 1.2 is represented in the last block: A hologram integrates all the essential components of a sensor.

Table 6.1: Holographic sensor parameters for hydrocarbons.

Parameter	Value
LDL	1% (v/v)
Range	0%-100% (v/v)
Response time	2s (40°C)
	3s (22°C)
	5s (8°C)
Recovery time	300s; flushing with air ≤3s

relation between the holographic response and the thermodynamic properties of the analyte, and finding this correlation is necessary for the analytical prediction, which is the last key step of the common generic methodology.

6.2 Comparison of holographic sensors with other gas-sensing technologies

It is necessary to compare the performance of the holographic sensors with current gas-sensing technologies. Several technologies for measuring the target analytes have been introduced in §1.1.3. This final section of the discussion focuses on comparing the main advantages and disadvantages of the holographic sensors based on the results obtained in this work for each analyte. The parameters that offer a good comparison for the sensor performance include the Lower Detection Limit (LDL), the response time and the range of concentrations over which the sensors operate. The following subsections compare the sensors by type of analyte.

6.2.1 Hydrocarbons and VOCs sensors

There are many examples of hydrocarbon or VOC sensors that are usually unselective and group the analytes as flammables or toxics [12]. Sensitive techniques that require sophisticated equipment are not discussed here; only those which provide an end-point device readable by a final user are considered.

The poor selectivity of VOC sensors offered in the market is often justified by claiming versatility for simultaneous detection of multiple analytes [303]; this

is a potential advantage and disadvantage shared by PDMS sensors. The most common sensors for hydrocarbons are solid state semiconductors that operate at high temperatures ≥200°C [304–308], and require a constant energy consumption by the semiconductor to maintain this temperature. Although the mode of operation of these sensors is different to holographic sensors, it is based on oxidation of their semiconducting layers. The holographic sensors are more competitive in this aspect as they do not require embedded electronics or a power supply.

The detection limits cited for commercial hydrocarbon sensors are as low as 0.2ppm in air for a range of concentrations from 0 to 1% (v/v), response times of ≤30s, and recovery times up to ∼70s [304, 305, 308]. Table 6.1 summarizes the sensor parameters for the PDMS holographic sensor. Holographic sensors cannot compete with the sensitivity of available hydrocarbon sensors in the *ppm* range. Nevertheless, they detect concentrations as low as 1% (v/v) and span over the whole range up to 100%. Moreover, the response times are an order of magnitude faster than commercial sensors. This makes the holographic hydrocarbon sensors unique and competitive if used in an appropriate environment.

Holograms can be used in environments with a high level of exposure to hydrocarbons or VOCs that require no interference with atmospheric gases or water. Therefore, they would be suitable for real-time monitoring of industrial processes (*i.e.* gas production plants, refineries, etc.). There is a copious body of research including conductive polymers in the solid state sensors to increase their selectivity and affinity for hydrocarbons [308].

Sensors for liquid VOCs are designed for different environments and there is a plethora of methodologies available to measure them. A comparison with current technologies should be performed on a case-by-case basis. For example, §4.8 shows that concentrations of toluene in water can be detected accurately down to ∼50ppb with a response time of 5min. Comparing this example with current literature, it is as least as sensitive as optical or amperometric methods, which display detection limits of 10ppm-2500ppm [309–311]. Furthermore, the sensitivity of holographic sensors in aqueous solution compares favourably with catalytic electrodes for gaseous toluene with similar response times and LDLs of 5min and 10ppb respectively [312].

Table 6.2: Holographic sensor parameters for oxygen gas detection.

Parameter	Value
LDL	not possible to determine
Range	0%-100% (v/v)
Response time	100s (22°C)
Recovery time	20min

6.2.2 Oxygen sensors

It was not possible to determine the sensitivity of Nafion holograms to oxygen because the concentration measurements were affected by humidity. Hence, the current holographic oxygen sensor described in this thesis offers no competition to current technologies. Some of the published technologies can sense concentrations as low as 0.5ppb and some detect oxygen within picoseconds of exposure [313,314]. The holographic oxygen sensor parameters are summarized in Table 6.2; it can be operated at all concentrations, but this has also been achieved by other sensing technologies [315]. Furthermore, there is interference with water which makes the holograms unsuitable for most of the applications in which oxygen monitoring is crucial. Nevertheless, the sensor offers the advantages of being a hologram: Reversibility, no need for embedded electronics and facile affordable fabrication.

Further investigation on how to improve the sensitivity of the Nafion holographic sensor to oxygen is required. However, matching the achievements of current sensors is a challenge that might be limited by the fundamentals of the holographic platform.

6.2.3 Ammonia sensors

Currently available sensors for ammonia measure concentrations down to 50ppb and up to 1000ppm in ~1min [52]. This concentration range is ideal for environmental monitoring or health diagnostics applications. It has been found that ammonia concentrations are potential disease markers in exhaled breath [52, 316–318]. Healthy individuals exhale 50-2000ppb ammonia whereas individuals with disease could see this concentration decreased or increased depending on the disease or metabolic regime (*i.e.* renal failure, *H. pylori* infection, protein

Table 6.3: Holographic sensor parameters for ammonia detection.

Parameter	Value
LDL	0.16% (v/v)
Range	0%-12.5% (v/v)
Response time	100s (22°C)
Recovery time	20min

deprivation or starvation, etc.) [9,52,316–321]. The maximum concentrations detected from breath samples in patients with disease rises up to 10000ppb [316,317]. Environmental and industrial monitoring of ammonia, however, requires monitoring concentrations ≥20ppm and up to the lower explosive limit of 15% [52,55]. There is a gap from 1000ppm up to 15% (150,000ppm) that cannot be detected with the current commercial sensors. The fatal exposure limits for humans lies just above 1000ppm and below 10000ppm [50], and falls within this gap.

Nafion holographic sensors for ammonia are beyond the sensitivity required for breath analysis. Also, they need to be operated under constant humidity or oxygen concentrations. As a consequence, they are not yet suitable for breath diagnostics. However, their detection range fills in the gap for ammonia sensors to detect high concentrations and their response times are comparable with those of current sensors. Table 6.3 summarizes the sensing parameters. Holographic ammonia sensors are noteworthy for their potential use in industrial applications where real-time monitoring of dangerous ammonia levels is required. Nevertheless, further investigation on the sensitivity is required for their use in biomedical diagnosis.

Comparing the different analytes confirms that the photonic structure in polymer films is a standard platform with potential use for the detection of various analytes. This platform can be multiplexed by fabricating a sensor array for the analysis of gas mixtures and can be integrated with previously developed holographic sensing technologies. Furthermore, using pulsed lasers requires fractions of a second for recording a hologram; this process can be easily escalated for mass manufacturing given that the polymer films are flat and can be roll-coated on surfaces as discussed in the Materials and Methods section.

Concluding Remarks

Understanding the fundamentals of how a sensor operates enabled the design and production of new sensors under a standard platform. Furthermore, targeting specific gaseous analytes led to the invention of new holographic recording techniques in previously unexplored materials. The final outcome was an ablation technique to record grating layers in an elastomer and a fluoropolymer, which were sensitive to hydrocarbons, volatile organic compounds, oxygen and ammonia.

Knowledge of the fundamentals was also essential for the characterization and theoretical analysis of the response of the sensors: It was possible to relate analytically the thermodynamic properties of the analytes to a photonic model for the prediction of the holographic reflection spectra.

The holographic sensing principle assumes that the molecular interactions cause changes in the properties of the layered structure, which are then observed as a coloured reflection. In the present work, experiments were designed, and an explanation has been given, to validate this assumption. By finding significant correlations, it was pointed out that the intermolecular interactions are likely to be the cause of the changes. However, correlation does not imply causation[a], and –citing David Hume– "*It is only after a long course of uniform experiments in any kind, that we attain a firm reliance and security with regard to a particular event*" [323, p.36]. Thus, it is necessary to leave the question of what causes the sensor signal to change open for future experimentalists.

---

[a]It has been argued that when the observations are detailed enough, a single measurable cause might not exist [322].

Appendix

A.1 Discrimination of response in a group of analytes using principal component discrimination analysis (PCA)

It can be said that the sensor distinguishes between different types of analytes when the PCA components are plotted in non overlapping areas. PCA in 2D was performed for all the kinetic responses of VOCs and hydrocarbons at the different concentrations and temperatures. The data points correspond to one repetition only. The PCA plots were generated by a Matlab® script (Program A.1) which gathers data from the kinetic results (Program A.2). Figures A.1, A.2 and A.3 show the results of the PCA algorithm. There was no overlap between the data points for most of the gas species and VOCs. However, there was a considerable amount of data points that, even if not overlapping, were very close together; this might be of limted use for identifying different species or concentrations. In general, it can be said that the sensor was able to identify a combination of molecules or concentrations but, in practice, it will only respond to certain groups of analytes, or for mixtures in which only a few molecules interact. An example of a real application in which only one component needs to be identified in a binary mixture is discussed in §4.8.

Program A.1: Principal Component Discrimination Analysis algorithm for extracting the F components

```
FILENAME: "pca.m"
function [Y,X1,v,Psi] = pca(X,numvecs, options)
options.null = 0;
Psi = mean(X')';
if isfield(options, 'use_em') && options.use_em==1
    if isfield(options, 'iter')
        iter = options.iter;
    else
        iter = 20;
    end
    [Y,v] = empca(X,numvecs,iter); X1 = Y' * X;
    return;
end
dim = size(X,1);
p = size(X,2);
for i = 1:p
    X(:,i) = X(:,i) - Psi;
end;
if numvecs<=dim && dim<p
    L = X*X'; [Y,v] = eig(L); [Y,v] = sortem(Y,v);
    Y = Y(:,1:numvecs); X1 = Y' * X; v = diag(v);
    return;
end
L = X'*X; [Y,v] = eig(L); [Y,v] = sortem(Y,v);
Y = X*Y; v = diag(v); v = v / (p-1); num_good = 0;
for i = 1:p
    Y(:,i) = Y(:,i)/norm(Y(:,i));
    if v(i) < 0.00001
        v(i) = 0;
        Y(:,i) = zeros(size(Y,1),1);
    else
        num_good = num_good + 1;
    end;
end;
if (numvecs > num_good)
    fprintf(1,'Warning: numvecs is \%d; only \%d exist.\n',numvecs,num_good);
    numvecs = num_good;
end;
Y = Y(:,1:numvecs); X1 = (Y')*X;
function [vectors values] = sortem(vectors, values)
if nargin ~= 2
    error('Must specify vector matrix and diag value matrix')
end;
vals = max(values);
[svals inds] = sort(vals,'descend');
vectors = vectors(:,inds);
values = max(values(:,inds));
```

```
values = diag(values);
function [evec,eval] = empca(data,k,iter,Cinit)
\%[evec,eval] = empca(data,k,iter,Cinit)
[d,N]  = size(data);
data = data - mean(data,2)*ones(1,N);
if(nargin<4) Cinit=[]; end
if(nargin<3) iter=20; end
[evec,eval] = empca_orth(data,empca_iter(data,Cinit,k,iter));
function [C] = empca_iter(data,Cinit,k,iter)
\%[C] = empca_iter(data,Cinit,k,iter)
[p,N] = size(data);
assert(k<=p);
if(isempty(Cinit))
    C = rand(p,k);
else
    assert(k==size(Cinit,2));
    assert(p==size(Cinit,1));
    C = Cinit;
end
for i=1:iter
    x = inv(C'*C)*C'*data;
    C = data*x'*inv(x*x');
end
function [evec,eval] = empca_orth(data,C)
\%[evec,eval] = empca_orth(data,Cfinal)
C = orth(C);
[xevec,eval] = truepca(C'*data);
evec = C*xevec;
function [] = assert(condition,message)
if nargin == 1,message = '';end
if isempty(message),message = 'Assert Failure.'; end
if(~condition) fprintf(1,'!!! \%s !!!\n',message); end
function [evects,evals] = truepca(dataset)
[d,N]  = size(dataset);
mm = mean(dataset')';
dataset = dataset - mm*ones(1,N);
cc = cov(dataset',1);
[cvv,cdd] = eig(cc);
[zz,ii] = sort(diag(cdd));
ii = flipud(ii);
evects = cvv(:,ii);
cdd = diag(cdd);
evals = cdd(ii);
```

Program A.2: Principal Component Discrimination Analysis algorithm for calling kinetic data

```
FILENAME: "PlotPCA.m"
clear clf clc
```

193

```
format short g
format compact
gases=dlmread('gases.csv'); \%92 columns
solvents=dlmread('solvents.csv'); \%21 columns
decay=dlmread('decay.csv'); \%2 columns
S=input('(1)gases, (2)solvents or (3)decay? ');
PCA=input(' PCA 3 or 2 dimensions?');
if S==1
    if PCA==3
        \% 3D PCA
        a=pca(gases',3)
        f=strvcat('  1',' 2',' 3',' 4',' 5',' 6',' 7',' 8',' 9',' 10',' 11',' 12',
        ' 13',' 14',' 15',' 16',' 17',' 18',' 19',' 20',' 21',' 22',' 23',' 24',
        ' 25',' 26',' 27',' 28',' 29',' 30',' 31',' 32',' 33',' 34',' 35',' 36',
        ' 37',' 38',' 39',' 40',' 41',' 42',' 43',' 44',' 45',' 46',' 47',' 48',
        ' 49',' 50',' 51',' 52',' 53',' 54',' 55',' 56',' 57',' 58',' 59',' 60',
        ' 61',' 62',' 63',' 64',' 65',' 66',' 67',' 68',' 69',' 70',' 71',' 72',
        ' 73',' 74',' 75',' 76',' 77',' 78',' 79',' 80',' 81',' 82',' 83',' 84',
        ' 85',' 86',' 87',' 88',' 89',' 90',' 91',' 92');
        plot3(a(:,1),a(:,2),a(:,3),'*')
        text(a(:,1),a(:,2),a(:,3),f,'FontSize',8)
    else
        \% 2D PCA
        b=pca(gases',2)
        g=strvcat('  1',' 2',' 3',' 4',' 5',' 6',' 7',' 8',' 9',' 10',' 11',' 12',
        ' 13',' 14',' 15',' 16',' 17',' 18',' 19',' 20',' 21',' 22',' 23',' 24',
        ' 25',' 26',' 27',' 28',' 29',' 30',' 31',' 32',' 33',' 34',' 35',' 36',
        ' 37',' 38',' 39',' 40',' 41',' 42',' 43',' 44',' 45',' 46',' 47',' 48',
        ' 49',' 50',' 51',' 52',' 53',' 54',' 55',' 56',' 57',' 58',' 59',' 60',
        ' 61',' 62',' 63',' 64',' 65',' 66',' 67',' 68',' 69',' 70',' 71',' 72',
        ' 73',' 74',' 75',' 76',' 77',' 78',' 79',' 80',' 81',' 82',' 83',' 84',
        ' 85',' 86',' 87',' 88',' 89',' 90',' 91',' 92');
        plot(b(:,1),b(:,2),'*')
        text(b(:,1),b(:,2),g,'FontSize',20)
    end
elseif S==2
    if PCA==3
        \% 3D PCA
        c=pca(solvents',3)
        h=strvcat('  1',' 2',' 3',' 4',' 5',' 6',' 7',' 8',' 9',' 10',' 11',' 12',
        ' 13',' 14',' 15',' 16',' 17',' 18',' 19',' 20',' 21');
        plot3(c(:,1),c(:,2),c(:,3),'*')
        text(c(:,1),c(:,2),c(:,3),h,'FontSize',8)
    else
        \% 2D PCA
        d=pca(solvents',2)
        i=strvcat('  1',' 2',' 3',' 4',' 5',' 6',' 7',' 8',' 9',' 10',' 11',' 12',
        ' 13',' 14',' 15',' 16',' 17',' 18',' 19',' 20',' 21');
        plot(d(:,1),d(:,2),'*')
        text(d(:,1),d(:,2),i,'FontSize',8)
```

```
        end
elseif S==3
    if PCA==3
        \% 3D PCA
        e=pca(decay',3)
        j=strvcat('  1',' 2',' 3',' 4',' 5',' 6',' 7',' 8',' 9',' 10',' 11',' 12',
        ' 13',' 14',' 15',' 16',' 17',' 18',' 19',' 20',' 21',' 22',' 23',
        ' 24',' 25',' 26');
        plot3(e(:,1),e(:,2),e(:,3),'*')
        text(e(:,1),e(:,2),e(:,3),j,'FontSize',8)
    else
        \% 2D PCA
        k=pca(decay',2)
        l=strvcat('  1',' 2',' 3',' 4',' 5',' 6',' 7',' 8',' 9',' 10',' 11',' 12',
        ' 13',' 14',' 15',' 16',' 17',' 18',' 19',' 20',' 21',' 22',' 23',
        ' 24',' 25',' 26');
        plot(k(:,1),k(:,2),'*')
        text(k(:,1),k(:,2),l,'FontSize',8)
    end
end
```
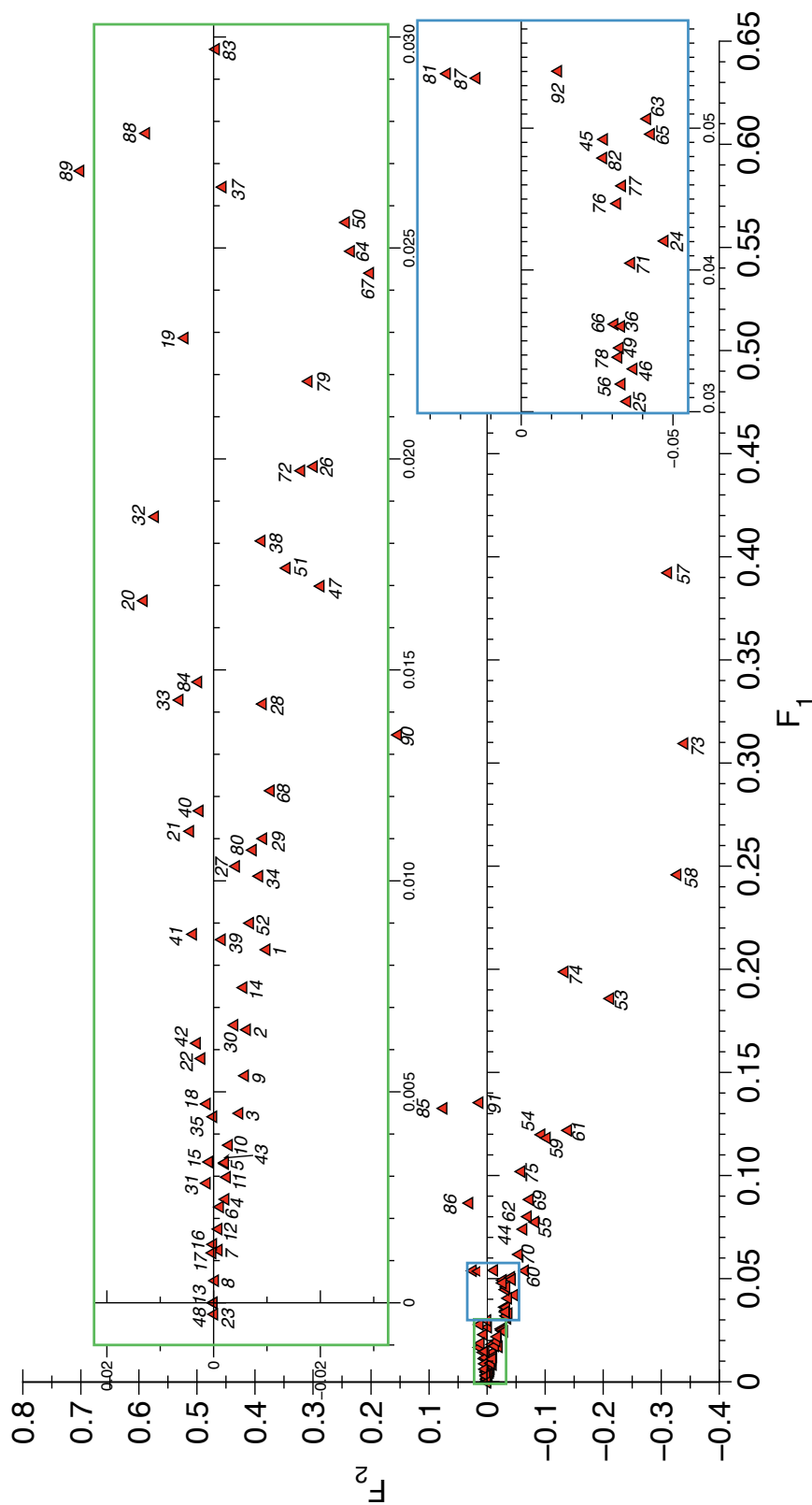
Figure A.1: PCA for gases. The rectangles indicate a magnification of the areas containing many data points. Numbers next to the names are temperature in °C and concentration in % (v/v) after the hyphen: Ethane8-100 (1), Ethane8-75 (2), Ethane8-50 (3), Ethane8-25 (4), Ethane40-100 (5), Ethane40-75 (6), Ethane40-50 (7), Ethane40-25 (8), Ethane22-100 (9), Ethane22-75 (10), Ethane22-50 (11), Ethane22-25 (12), Ethane22-0 (13), Ethye22-100 (14), Ethyne22-75 (15), Ethyne40-100 (16), Ethyne40-100 (17), Ethyne8-100 (18), Propane22-100 (19), Propane22-75 (20), Propane22-50 (21), Propane22-25 (22), Propane22-0 (23), Propane8-100 (24), Propane8-75 (25), Propane8-50 (26), Propane8-25 (27), Propane40-100 (28), Propane40-75 (29), Propane40-50 (30), Propane40-25 (31), Propene22-100 (32), Propene22-75 (33), Propene22-50 (34), Propene22-25 (35), Propene8-100 (36), Propene8-75 (37), Propene8-50 (38), Propene825 (39), Propene40-100 (40), Propene40-75 (41), Propene40-50 (42), Propene40-25 (43), IsoButane22-75 (44), IsoButane22-50 (45), IsoButane22-25 (46), IsoButane22-0 (47), IsoButane40-100 (48), IsoButane40-75 (49), IsoButane40-50 (50), IsoButane40-25 (51), IsoButane8-100 (52), IsoButane8-75 (53), IsoButanee8-50 (54), IsoButane8-25 (55), Butane8-100 (56), Butane8-75 (57), Butane8-50 (58), Butane8-25 (59), Butane22-100 (60), Butane22-75 (61), Butane22-50 (62), Butane22-25 (63), Butane40-100 (64), Butane40-75 (65), Butane40-50 (66), Butane40-25 (67), butene22-100 (68), butene22-75 (69), butene22-50 (70), butene22-25 (71), butene8-100 (72), butene8-75 (73), butene8-50 (74), butene8-25 (75), butene40-100 (76), butene40-75 (77), butene40-50 (78), butene40-25 (80), butyne40-100 (81), butyne22-75 (82), butyne40-50 (83), butyne40-25 (84), butyne22-100 (85), butyne22-75 (86), butyne22-50 (87), butyne22-25 (88), butyne8-100 (89), butyne8-75 (90), butyne8-50 (91), butyne8-25 (92).
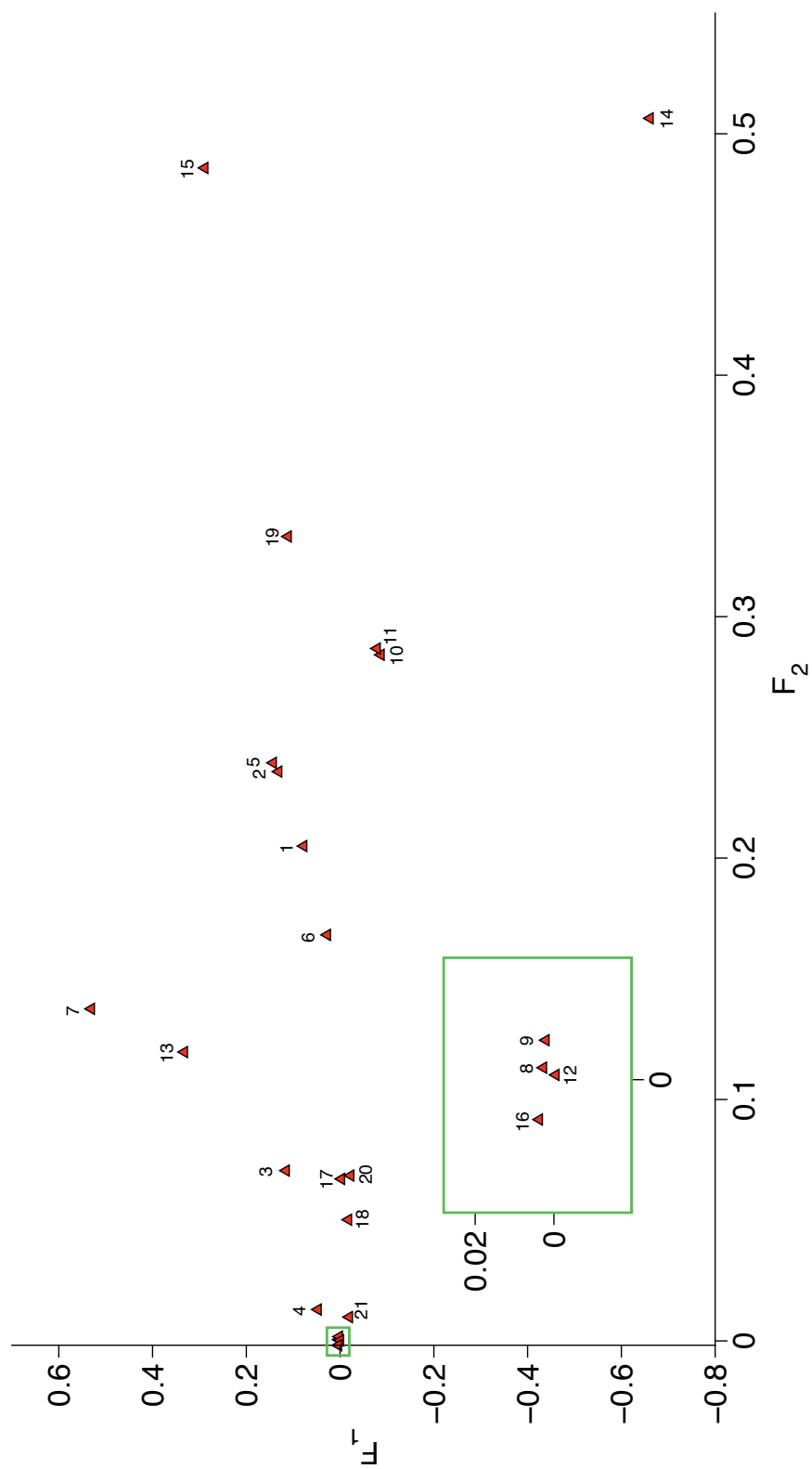
Figure A.2: PCA for liquids:(1) Butanol, (2) Propanol, (3) Ethanol, (4) Methanol, (5) Propan-2-ol, (6) Pentanol, (7) Acetone, (8) Water, (9) 2,3-butanediol, (10) Iso-Pentanol, (11) Iso-Butanol, (12) EthyleneGlycol, (13) Acetaldehyde, (14) Butanone, (15) Ter-butanol, (16) Glycerol, (17) Cyclooctanol, (18) Cycloheptanol, (19) Methylcyclopentanol, (20) Cyclohexanol, (21) PDMS monomer.
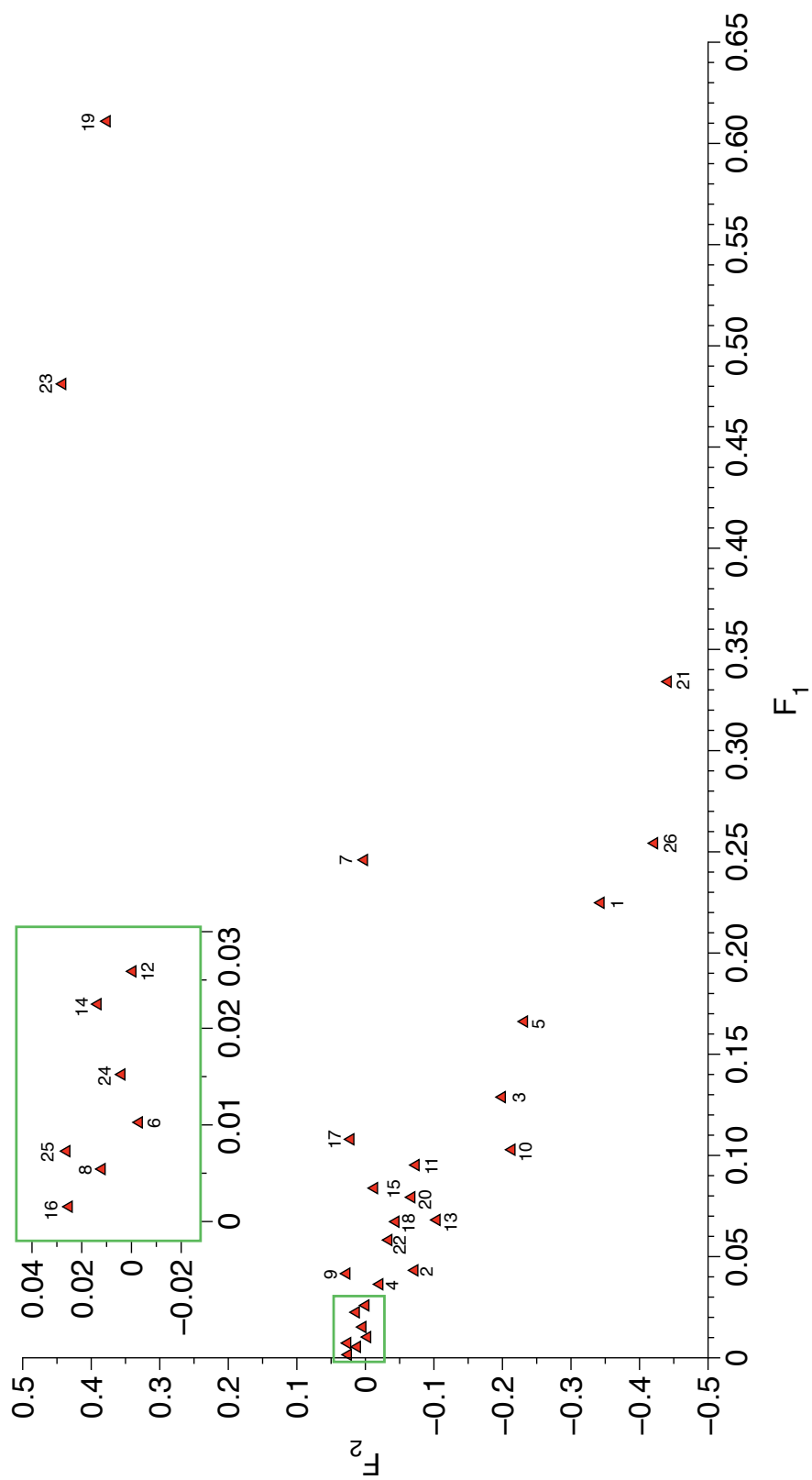
Figure A.3: PCA for the decay of the signal in gases. Temperature in °C next to names: (1) Butane22, (2) Propane22, (3) IsoButane22, (4) Propene22, (5) 1-Butene22, (6) Ethane22, (7) 1-Butyne22, (8) Ethyne22, (9) Propyne/Propadiene22, (10) Propane:Butane22, (11) Butane40, (12) Propane40, (13) IsoButane40, (14) Propene40, (15) 1-Butene40, (16) Ethane40, (17) 1-Butyne40, (18) Propane:Butane40, (19) Butane8, (20) Propane8, (21) IsoButane8, (22) Propene8, (23) 1-Butene8, (24) Ethane8, (25) Ethyne8, (26) Propane:Butane8.

Table A.1: Current gas sensors market. Distribution of sensor types grouped by analyte, multiple analyte sensors also considered. $n = 724$ products.

Gas analyte	Abundance*	Percentage
Oxygen	193	15.55%
Hydrocarbons	111	8.94%
Hydrogen	92	7.41%
Hydrogen Sulfide	86	6.93%
Carbon Monoxide	82	6.61%
Ammonia	49	3.95%
Sulfur Dioxide	45	3.63%
Chlorine	42	3.38%
Carbon Dioxide	41	3.30%
Nitrogen Dioxide	36	2.90%
Ozone	34	2.74%
Hydrogen Chloride	26	2.10%
Hydrogen Cyanide	24	1.93%
Chlorine Dioxide	22	1.77%
Nitric Oxide	20	1.61%
Phosphine	19	1.53%
Hydrogen Fluoride	16	1.29%
Halocarbons	14	1.13%
Arsine	12	0.97%
Silane	11	0.89%
Germane	11	0.89%
Fluorine	11	0.89%
Diborane	11	0.89%
Nitrogen Oxides	10	0.81%
Bromine	10	0.81%
Hydrogen Selenide	9	0.73%
Sulfur Hexafluoride	6	0.48%
Water Vapour	4	0.32%
Mercury Vapour	4	0.32%
Other Chemicals	190	15.31%
Total	1241	(n=724)

*data collected from [18]

Table A.2: Sensor response ($\Delta\lambda$) to maximum concentration of all the hydrocarbons and VOCs tested. Standard deviation, solubility parameters (δ), log of the octanol-water partition coefficients (log K_{ow}), and boiling points.

Compound[*]	$\Delta\lambda$ [nm]	S.D. [nm]	$\delta^{\dagger}$ [MPa$^{1/2}$]	log K_{ow}[‡]	B.P.[‡] [°C]
Ethane	3.0	0.02	11.6	1.8	-89.0
Propane	13.7	0.19	12.7	2.4	-42.0
Butane	62.8	4.54	13.5	2.9	-0.5
Iso-butane	42.5	0.54	12.8	2.8	-11.7
Ethylene	2.1	<0.01	11.3	1.1	-103.7
Butylene	51.0	0.39	13.7	2.4	-6.3
Propylene	11.3	<0.01	12.5	1.8	-47.6
Acetylene	2.7	0.58	11.0	0.4	-84.0
Butyne	76.2	0.15	28.5	1.5	7.8
Butanol	126.5	<0.01	23.3	0.9	117.2
Propanol	146.4	<0.01	24.3	0.3	97.1
Ethanol	52.7	<0.01	26.0	-0.3	78.4
Methanol	16.2	<0.01	29.7	-0.8	64.7
Propan-2-ol	153.9	<0.01	23.7	0.1	82.3
Acetone	181.5	<0.01	20.3	-0.2	56.5
Pentanol	97.7	<0.01	21.7	1.5	138.0
Propyne/diene	14.0	<0.01	29.3	0.9	-48.0
Butanone	267.8	<0.01	19.1	0.29	76.6
2,3-butanediol	1.3	<0.01	22.7	-	180.7
Iso-Pentanol	152.8	<0.01	20.5	1.16	131.2
Iso-Butanol	155.9	<0.01	21.5	0.76	105
Acetaldehyde	119.5	<0.01	21.1	-0.34	18.6
Ethylene Glycol	0.0	<0.01	29.9	-1.36	197.5
t-Butanol	300.0	<0.01	21.0	0.35	84.6
Glycerol	0.0	<0.01	43.2	-1.76	290
Cyclohexanol	34.2	<0.01	23.3	1.23	159.6
Cycloheptanol	36.6	<0.01	-	2.13	181.8
Cyclooctanol	26.9	<0.01	-	2.62	203.2
Methylcyclopen-tanol	231.3	<0.01	-	1.60	137.1
Water	0.0	<0.01	47.9	-1.38	100
PDMS	>60	-	14.9-17.5	12	>200

[*] Other measured substances that exceeded the spetrophotometer detection range were: pentane, pentene, pentyne, heptane, octane, decane, hexane, heptanone, hexanol, pentanol, 4-methyl-2-pentanone, tert-amyl alcohol, iso-amyl alcohol. [†] Values were calculated or obtained from references: [146, 148, 218, 221–223, 298, 324–329] 1MPa$^{1/2}$=2.0455$(cal/cm^3)^{1/2}$. [‡] Values from: [213, 330].
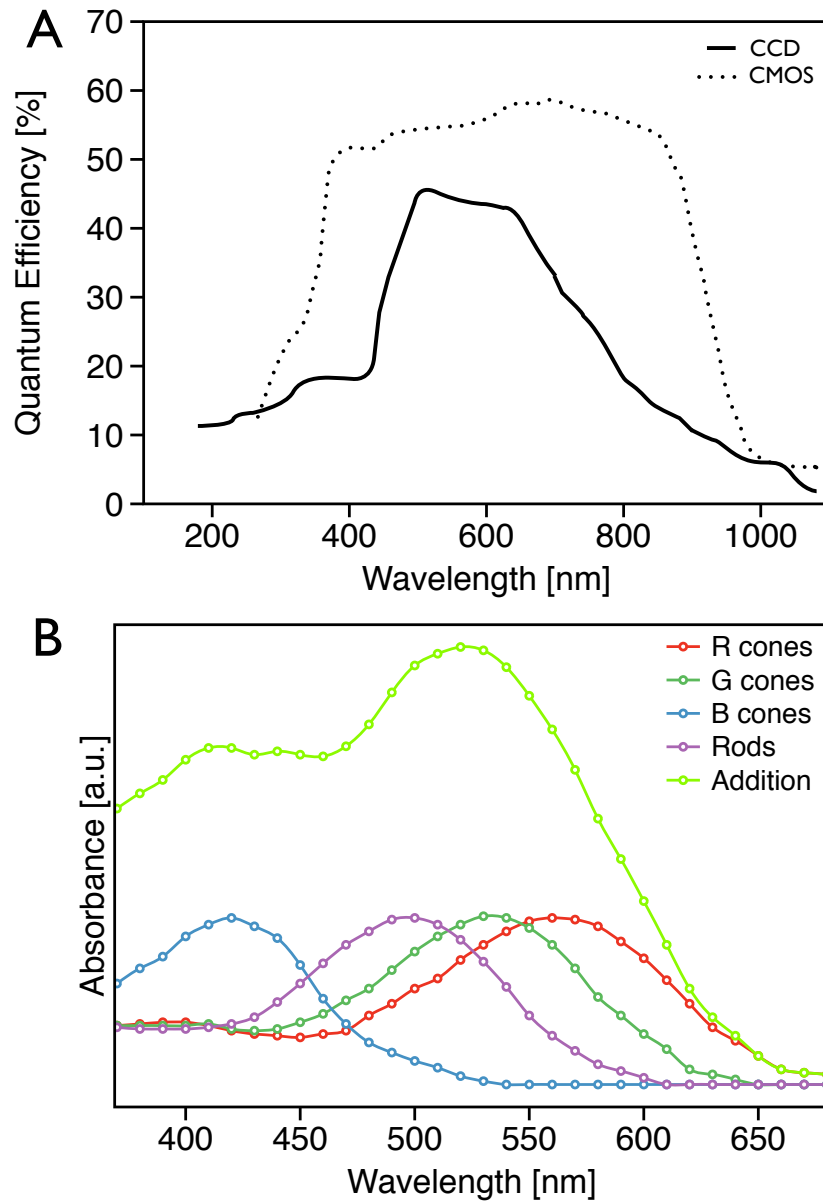
Figure A.4: Comparison between light absorption spectra of rod and cone cells and quantum efficiency spectra of CCD and CMOS sensors. (A) Quantum efficiency for CMOS and CCD sensors of the spectrophotometer used in this study. (B) Absorption spectra of red-sensitive, green-sensitive and blue-sensitive cones, and rods in human eyes. The plots were built with data from references: [331, 332].
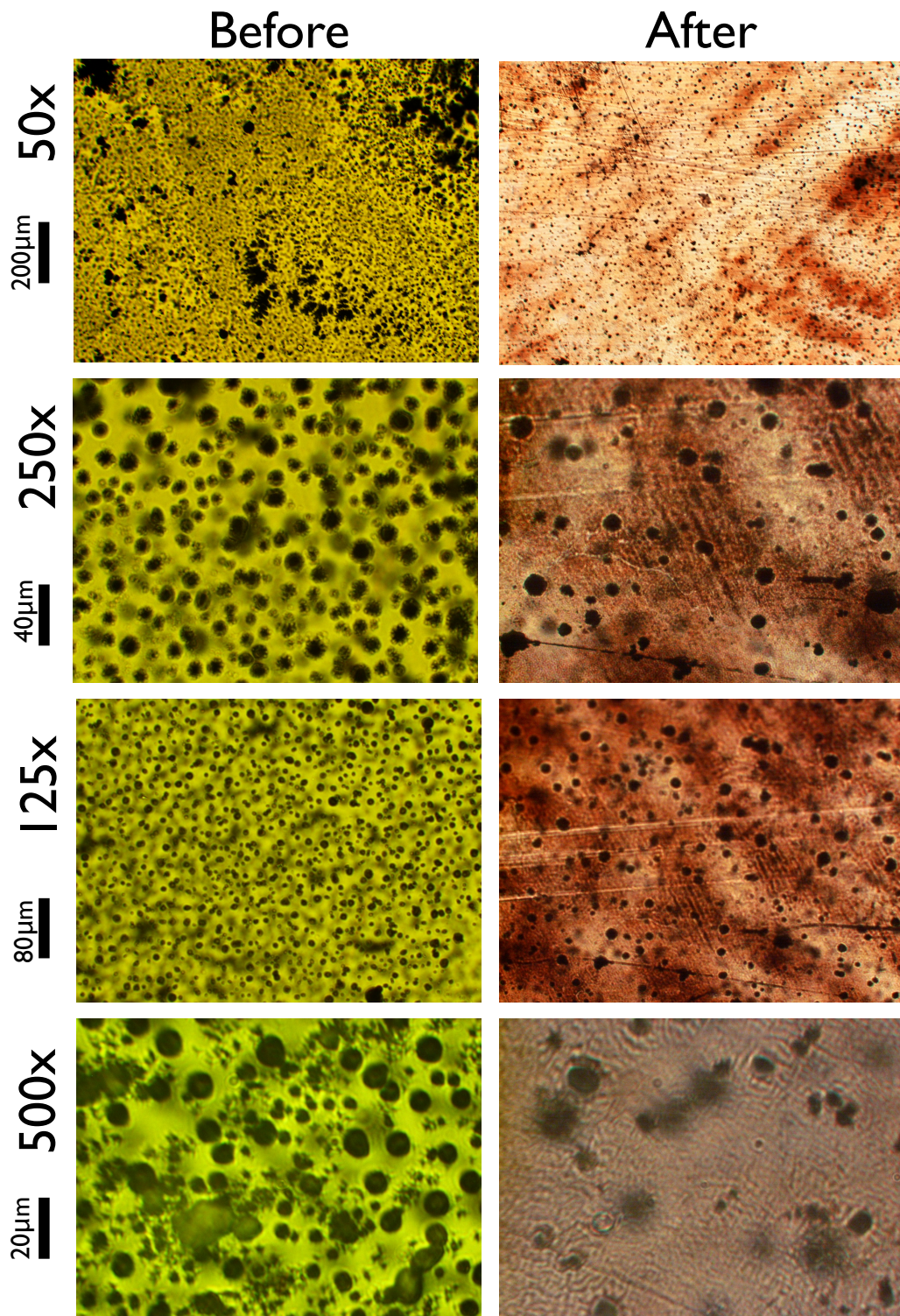
Figure A.5: Microscopy images of the surface of Nafion holograms before and after ablation. The fingerprint like pattern observed in the images is characteristic of the laser optical interference.
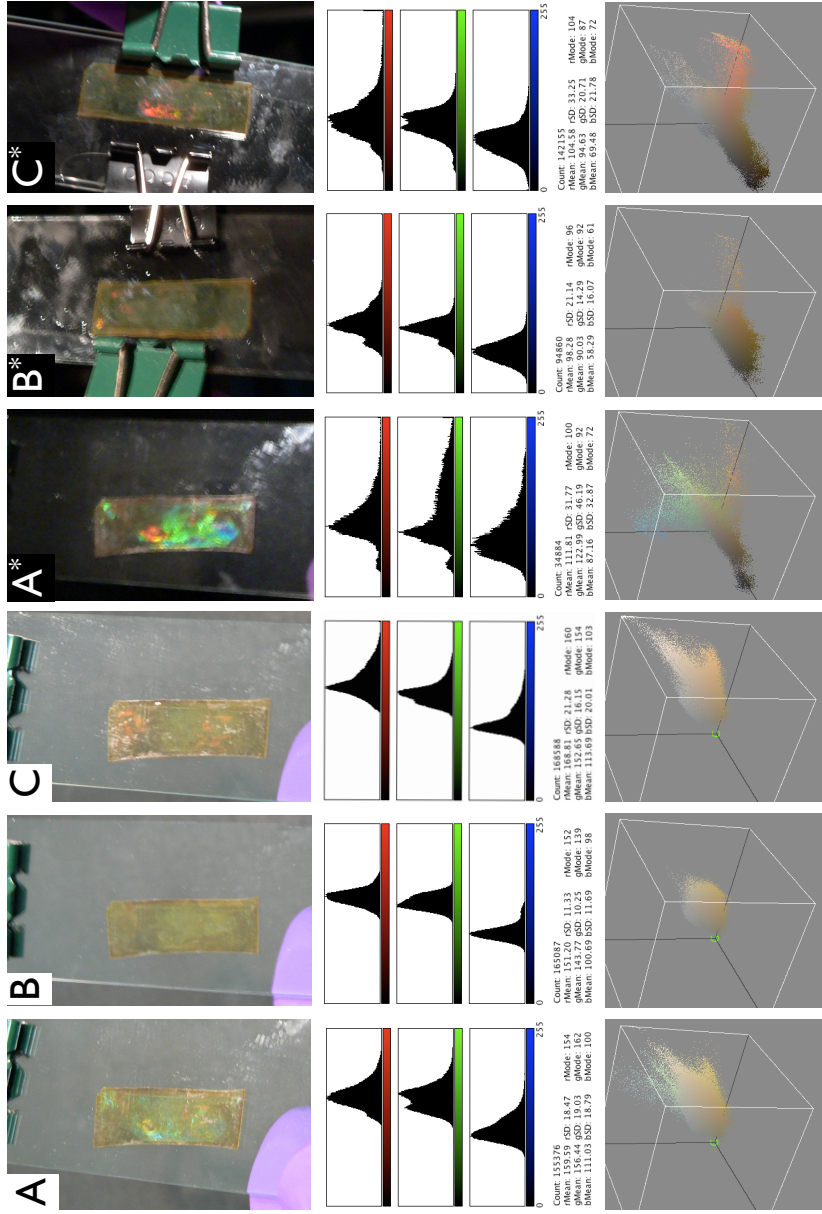
Figure A.6: RGB image analysis of the holographic reflection response to water for Nafion holograms under different light conditions. (A) Holographic reflections at an angle which satisfies maximum reflectivity. (B) Holograms at a non-satisfying. (C) Reflections at the satisfying angle when exposed to liquid water. A, B and C under diffuse light illumination and A*, B* and C* under a spot light.
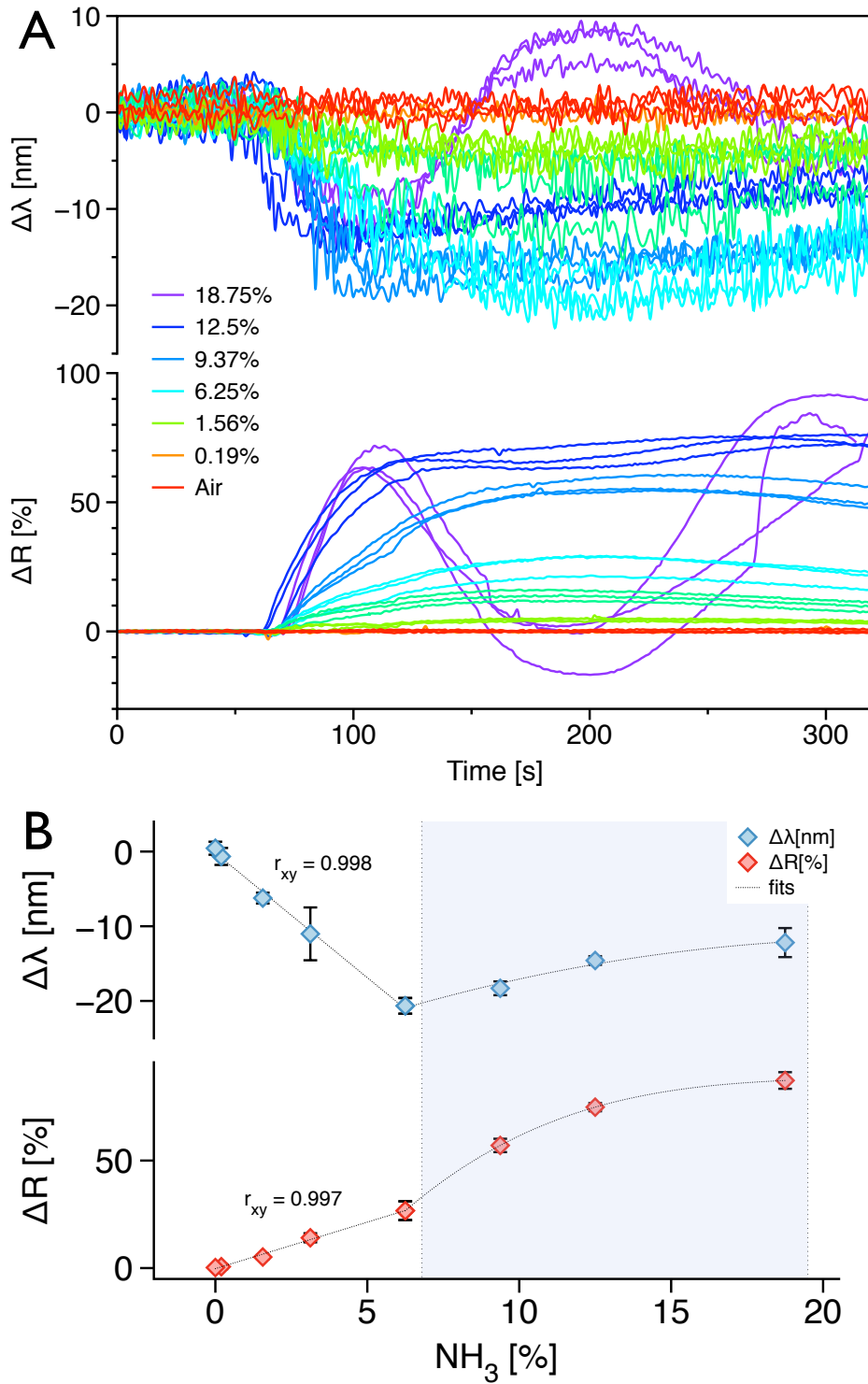
Figure A.7: Holographic response to high concentrations of NH$_3$ in air for equilibrated Nafion holograms and condensation. (A) Kinetics of the response ($\Delta\lambda$, ΔR) for the different concentrations. (B) Peak intensity values and correlation with gas concentration.

Program A.3: Mathematica Yeh Matrix Method

```mathematica
Λ1 := 187; Λ2 := Λ1; N1 := 1.5; N2 := 1.47; L := 150; θ := 20

kθ[n_, ω_, c_, θ_] := n ω/c Cos[θ]

TE[k1_, k2_, a_, b_] :=
 Module[{}, {{Exp[ⅈ k1 a] (Cos[k2 b] + (ⅈ ((k1 / k2) + (k2 / k1)) / 2) Sin[k2 b]),
    -Exp[-ⅈ k1 a] (ⅈ ( (k1 / k2) - (k2 / k1)) / 2) Sin[k2 b]},
   {Exp[ⅈ k1 a] (ⅈ ( (k1 / k2) - (k2 / k1)) / 2) Sin[k2 b],
    Exp[-ⅈ k1 a] (Cos[k2 b] - (ⅈ ((k1 / k2) + (k2 / k1)) / 2) Sin[k2 b])}}]

TM[k1_, k2_, a_, b_, n1_, n2_] := Module[{},

  {{(Cos[k2 b] + (ⅈ (((n2² k1)/(n1² k2)) + (1/ ((n2² k1)/(n1² k2))))) / 2) Sin[k2 b]) Exp[ⅈ k1 a],

    ((ⅈ (((n2² k1)/(n1² k2)) - (1/ ((n2² k1)/(n1² k2))))) / 2) Sin[k2 b]) Exp[-ⅈ k1 a]},

   {(- (ⅈ (((n2² k1)/(n1² k2)) - (1/ ((n2² k1)/(n1² k2))))) / 2) Sin[k2 b]) Exp[ⅈ k1 a],

    (Cos[k2 b] - (ⅈ (((n2² k1)/(n1² k2)) + (1/ ((n2² k1)/(n1² k2))))) / 2) Sin[k2 b]) Exp[-ⅈ k1 a]}}]

KΛ[matrix_] := ArcCos[Tr[matrix] / 2]

CMS[matrix_] := Abs[matrix[[2, 1]]]^2

rqE[a_, b_, n1_, n2_, q_, ω_, θin_] :=
 Module[{matrix, kλ, c = 3. × 10^8, θ1, θ2},

  θ1 = ArcSin[Sin[θin]/n1];

  θ2 = ArcSin[(n1 Sin[θ1])/n2];
  matrix = TE[kθ[n1, ω, c, θ1], kθ[n2, ω, c, θ2], a, b];
  kλ = KΛ[matrix];

  1/(1 + (Abs[Sin[kλ]/Sin[q kλ]]^2)/CMS[matrix])]
```

```
rqM[ a_, b_, n1_, n2_, q_, ω_, θin_] :=
  Module[{matrix, kλ, c = 3. × 10^8, θ1, θ2},

    θ1 = ArcSin[ Sin[θin] / n1 ];

    θ2 = ArcSin[ n1 Sin[θ1] / n2 ];

    matrix = TM[kθ[n1, ω, c, θ1], kθ[n2, ω, c, θ2], a, b, n1, n2];

    kλ = KΛ[matrix];


           1
    ─────────────────────── ]
              Abs[ Sin[kλ] / Sin[q kλ] ]^2
    1 + ──────────────────────────
              CMS[matrix]

Plot[ rqE[ Λ1 / 10^9 2 , Λ2 / 10^9 2 , N1, N2, L, (2 π) 3 × 10^8 / (λ / 10^9) , θ Pi / 180], {λ, 300, 900}]

Plot[ rqM[ Λ1 / 10^9 2 , Λ2 / 10^9 2 , N1, N2, L, (2 π) 3 × 10^8 / (λ / 10^9) , θ Pi / 180], {λ, 300, 900}]


Table[ rqE[ Λ1 / 10^9 2 , Λ2 / 10^9 2 , N1, N2, L, (2 π) 3 × 10^8 / (λ / 10^9) , θ Pi / 180], {λ, 300, 900}]

Table[ rqM[ Λ1 / 10^9 2 , Λ2 / 10^9 2 , N1, N2, L, (2 π) 3 × 10^8 / (λ / 10^9) , θ Pi / 180], {λ, 300, 900}]
```

References

[1] J. H. Seinfeld and S. N. Pandis, *Atmospheric Chemistry and Physics*. J Wiley & Sons Inc., 1998. 1

[2] W. Bischof, P. Fabian, and R. Borchers, "Decrease in CO_2 mixing ratio observed in the stratosphere", *Nature*, vol. 288, pp. 347–348, 1980. 1

[3] R. Stolarski, R. Bojkov, L. Bishop, C. Zerefos, J. Staehelin, and J. Zawodny, "Measured trends in stratospheric ozone", *Science*, vol. 256, no. 5055, pp. 342–349, 1992. 1

[4] M. Coyle, R. Smith, J. Stedman, K. Weston, and D. Fowler, "Quantifying the spatial distribution of surface ozone concentration in the UK", *Atmospheric Environment*, vol. 36, no. 6, pp. 1013 – 1024, 2002. 1

[5] C. Kennedy, J. Steinberger, B. Gasson, Y. Hansen, T. Hillman, M. Havránek, D. Pataki, A. Phdungsilp, A. Ramaswami, and G. V. Mendez, "Greenhouse gas emissions from global cities", *Environmental Science & Technology*, vol. 43, no. 19, pp. 7297–7302, 2009. 1

[6] EIGA, "Our industry products and services", www.eiga.org, European Industrial Gases Association, EU, 2008. 1

[7] G. P. Gurinovich, "Molecular oxygen photonics", *Journal of Applied Spectroscopy*, vol. 54, no. 3, pp. 403–411, 1991. 2, 7, 122

[8] A. S. Modak, "Single time point diagnostic breath tests: a review", *Journal of Breath Research*, vol. 4, no. 1, p. p17002, 2010. 2

[9] A. Díaz-Aguilar, E. Forzani, L. Nagahara, I. Amlani, R. Tsui, and N. J. Tao, "A breath ammonia sensor based on conducting polymer nanojunctions", *IEEE Sensors Journal*, vol. 8, no. 3, pp. 269–273, 2008. 2, 122, 189

[10] R. Rego, R. Caetano, R. Vale, and A. Mendes, "Development of a new gas sensor for binary mixtures based on the permselectivity of polymeric membranes 1. application to oxygen/nitrogen mixture", *IEEE Sensors Journal*, vol. 8, no. 3, pp. 269–273, 2008. 2

[11] R. Bogue, "The UK gas sensor industry", *Sensor Review*, vol. 2, no. 21, pp. 98–103, 2001. 2

[12] N. Yamazoe and K. Shimanoe, "Overview of gas sensor technology", in *Science and technology of chemiresistor gas sensors* (D. Aswal and S. Gupta, eds.), Nova Publishers, 2007. 2, 4, 8, 84, 186

[13] H. Guo, S. C. Lee, L. Y. Chan, and W. M. Li, "Risk assessment of exposure to volatile organic compounds in different indoor environments", *Environmental Research*, vol. 94, no. 1, pp. 57–66, 2004. 2, 8

[14] TFG, "Chemical sensors", tech. rep., The Freedonia Group, Cleveland, OH. USA, 2008. 2

[15] MNT, "Mnt gas sensor road map", report from the gas sensors forum, Micro & Nano Technology Network, London, UK, 2006. 2, 3

[16] N. Schröder, "Sensor markets 2008", tech. rep., Intechno Consulting, Basel, Switzerland, 2008. 2

[17] J. Gomes, "Gas sensors and gas metering: Applications and markets", tech. rep., BCC research, Norwalk, CT. USA, 2009. 2

[18] GlobalSpec, "Sensors and transducers suppliers", tech. rep., Global Spec the engineering search engine, 2010. 3, 199

[19] E. Comini, G. Faglia, and G. Sberveglieri, *Solid state gas sensing*. Elsevier, 2008. 4, 8

[20] C. R. Lowe, "Chemoselective biosensors", *Current Opinion in Chemical Biology*, no. 3, pp. 106–111, 1999. 6

[21] N. Yamazoe, "Toward innovations of gas sensor technology", *Sensors and Actuators B*, no. 108, pp. 2–14, 2005. 6

[22] P. Hudson and C. Souriau, "Engineered antibodies", *Nature Medicine*, no. 9, pp. 129–134, 2003. 6

[23] E. Ellington and S. Szostack, "In vitro selection of RNA molecules that bind specific ligands", *Nature*, no. 346, pp. 818–822, 1990. 6

[24] C. Tuerk and L. Gold, "Systematic evolution of ligands by exponential enrichment: RNA ligands to bacteriophage T4 DNA polymerase", *Science*, no. 249, pp. 505–, 1990. 6

[25] X. Yang, M. Lee, F. Sartain, X. Pan, and C. Lowe, "Designed boronate ligands for glucose selective holographic sensors", *Chemistry a European Journal*, no. 12, pp. 8491–8497, 2006. 6, 24

[26] N. W. Turner, C. W. Jeans, K. R. Brain, C. J. Allender, V. Hlady, and D. W. Britt, "From 3D to 2D: A Review of the Molecular Imprinting of Proteins", *Biotechnology Progress*, vol. 22, no. 6, pp. 1474–1489, 2006. 6

[27] E. Niederhoffer, J. timons, and A. Martell, "Thermodynamics of oxygen binding in natural and synthetic dioxygen complexes", *Chemical Reviews*, vol. 84, no. 2, pp. 137–203, 1991. 6, 7, 122

[28] C. Kumar, *Nanomaterials for Biosensors.* Wiley-VCH, 2007. 6

[29] F. Mao, N. Mano, and A. Heller, "Long tethers binding redox centers to polymer backbones enhance electron transport in enzyme 'wiring' hydrogels.", *Journal of the American Chemical Society*, vol. 16, no. 125, pp. 4951–4957, 2003. 6

[30] N. Pchelintsev and P. Millner, "Development of surface activated screen-printed carbon transducers for biosensors application", *Analytical Letters*, vol. 7, no. 40, pp. 1317–1332, 2007. 6

[31] M. Lelerc, "Optical and electromechanical transducers based on functionalized conjugated polymers", *Advanced Matter*, no. 11, pp. 1491–1498, 199. 6

[32] J. C. Vidal, E. Garcia-Ruiz, and J. R. Castillo, "Recent advances in electropolymerized conducting polymers in amperometric biosensors", *Microchimica Acta*, no. 143, pp. 93–11, 2003. 6

[33] S. A. Pieltsky and A. P. Turner, "Electrochemical sensors based on molecular imprinted polymers", *Electroanalysis*, no. 14, pp. 317–323, 2002. 6

[34] J. Wang, G. Liu, and Y. Lin, "Amperometric choline biosensor fabricated though elecrostatic assembly of bienzyme/polyelectrolyte hybrid layers on carbon nanotubes", *Analyst*, no. 131, pp. 477–483, 2006. 6

[35] A. P. F. Turner, "Biosensors sense and sensitivity", *Science*, vol. 290, no. 5495, pp. 1315–1317, 2000. 7

[36] T. P. Labuza and W. M. Breene, "Application of active packaging for improvement of shelf-life and nutritional quality of fresh and extended shelf-life foods.", *Journal of Food Process Preservation*, vol. 13, pp. 1–69, 1989. 7

[37] Y. Lee and G. Tsao, "Dissolved oxygen electrodes", in *Advances in Biochemical Engineering, Volume 13* (T. Ghose, N. Blakebrough, and A. Fiechter, eds.), vol. 13 of *Advances in Biochemical Engineering/Biotechnology*, pp. 35–86, Springer Berlin / Heidelberg, 1979. 7

[38] E. R. Carraway, J. N. Demas, B. A. DeGraff, and J. R. Bacon, "Photophysics and photochemistry of oxygen sensors based on luminescent transition-metal complexes", *Analytical Chemistry*, vol. 63, pp. 337–342, 1991. 7, 123

[39] P. Payra and P. K. Dutta, "Development of a dissolved oxygen sensor using tris(bipyridyl) ruthenium (II) complexes entrapped in highly siliceous zeolites", *Microporous and Mesoporouns Materials*, vol. 64, pp. 109–118, 2003. 7, 123

[40] R. E. Slovacek and J. K. Sullivan, "Oxygen sensing membranes and methods for making the same". US Patent 5863460, January 1999. 7, 123

[41] R. Machyda, E. Kimura, and M. Kodama, "Dioxygen uptake by cobalt (II) complexes of mcrocyclic polyamines. Effects of chelate ring size and substituents", *Inorganic Chemistry*, vol. 22, pp. 2055–2061, 1983. 7, 122

[42] A. Mills, G. Doyle, A. Peiro, and J. Durrant, "Demonstration of a novel flexible photocatalytic oxygen-scavenging polymer film", *Journal of Photochemistry and Photobiology A: Chemistry*, vol. 1016, pp. 328–331, 2006. 7, 123

[43] F. Navarro-Villoslada, G. Orellana, M. C. Moreno-Bondi, T. Vick, G. Hilderbrand, and K. Liefeith, "Fiber-optic luminescent sensors with composite oxygen-scavenging layers and anti-biofouling coatings", *Analytical Chemistry*, vol. 73, pp. 5150–5156, 2001. 7, 123

[44] S. Kitahara and K. Terada, "Oxygen absorber". US Patent 2007/0123647 A1, May 2007. 7

[45] J. E. Dickens, *Fluorescent Sensing and Process Analytical Applications*, pp. 337–352. John Wiley & Sons, Ltd, 2010. 7

[46] P. Korytar, H.-G. Janssen, E. Matisova, and U. A. Brinkman, "Practical fast gas chromatography: methods, instrumentation and applications", *Trends in Analytical Chemistry*, vol. 21, no. 9-10, pp. 558 – 572, 2002. 8

[47] H. J. Hubschmann, *Introduction*, pp. 2–3. Wiley-VCH, 2009. 8

[48] C. Malins, A. Doyle, B. D. MacCraith, F. Kvasnik, M. Landl, P. Simon, L. Kaldova, R. Lukas, K. Pufler, and I. Badusik, "Personal ammonia sensor for industrial environments", *Journal of Environmental Monitoring*, no. 5, pp. 417–422, 2003. 8

[49] E. P. Felix and A. A. Cardoso, "Colorimetric determination of ammonia in air using a hanging drop", *Instrument Science and Technology*, vol. 3, no. 31, pp. 283–294, 2008. 8

[50] OSHA, "Exposure limits", report, Occupational Safety and Health Administration, US Dept. of Labor, Cincinnati, US, 2008. 8, 9, 189

[51] B. Tarkington, A. Harris, P. Barton, B. Chandler, and P. Goad, "Effectiveness of common shelter-in-place techniques in reducing ammonia exposure following accidental release", *Journal of Occupational and Environmental Hygiene*, vol. 6, pp. 248–255, 2009. 8

[52] B. Timmer, W. Olthuis, and A. van den Berg, "Ammonia sensors and their applications: A review", *Sensors and Actuators B: Chemical*, vol. 107, no. 2, pp. 666 – 677, 2005. 8, 122, 123, 188, 189

[53] W. Cao and Y. Duan, "Optical fiber-based evanescent ammonia sensor", *Sensors and Actuators B*, no. 110, pp. 252–259, 2005. 9

[54] P. S. Kumar, A. V. Scaria, C. P. G. Vallabhan, V. P. Nampoori, and P. Radhakrishnan, "Long-period grating in multimode fiber for ammonia gas detection", *Proceedings of the SPIE*, vol. 5279, no. 1, pp. 331–335, 2004. 9

[55] RAE, "Measuring ammonia (NH_3) with photoionization detectors", application note ap-201, RAE Systems Inc, San Jose, CA, USA, 2011. 9, 189

[56] A. M., K. T., and H. M., "Optical co detection by use of CuO/Au composite films", *Sensors and Actuators B: Chemical*, vol. 25, no. 1, pp. 851–853, 1995. 10

[57] Z. Gu and P. Liang, "Novel optical film sensor design based on p-polarized reflectance", *Optics & Laser Technology*, vol. 36, no. 3, pp. 211 – 217, 2004. 10

[58] K. Shinbo, M. Minagawa, H. Takasaka, K. Kato, F. Kaneko, and T. Kawakami, "Electrical and luminescent properties due to gas adsorption in electroluminescent device of metal-free phthalocyanine", *Colloids and Surfaces A: Physicochemical and Engineering Aspects*, vol. 198-200, no. 0, pp. 905 – 909, 2002. 10

[59] Y. A., I. K., and M. M., "Detection of ammonia in the ppt range based on a composite optical waveguide pH sensor", *Sensors and Actuators B: Chemical*, vol. 88, no. 3, pp. 239–245, 2003. 10

[60] J. Homola, S. S. Yee, and G. Gauglitz, "Surface plasmon resonance sensors: review", *Sensors and Actuators B: Chemical*, vol. 54, no. 1-2, pp. 3 – 15, 1999. 10

[61] N. Agbor, J. Cresswell, M. Petty, and A. Monkman, "An optical gas sensor based on polyaniline Langmuir-Blodgett films", *Sensors and Actuators B: Chemical*, vol. 41, no. 1-3, pp. 137 – 141, 1997. 10

[62] W. Liang, Y. Huang, Y. Xu, R. K. Lee, and A. Yariv, "Highly sensitive fiber Bragg grating refractive index sensors", *Applied Physics Letters*, vol. 86, no. 15, p. 151122, 2005. 10

[63] M. Mierla, R. Schwenn, L. Teriaca, G. Stenborg, and B. Podlipnik, "Analysis of the Fe X Fe XIVe width in the solar corona using LASCO-C1 spectral data", *Astronomy & Astrophysics*, vol. 480, no. 2, pp. 509–514, 2008. 10

[64] S. A. Asher, J. Holtz, L. Liu, and Z. Wu, "Self-assembly motif for creating submicron periodic materials. polymerized crystalline colloidal arrays", *Journal of the American Chemical Society*, vol. 116, no. 11, pp. 4997–4998, 1994. 10

[65] J. H. Holtz, J. S. W. Holtz, C. H. Munro, and S. A. Asher, "Intelligent polymerized crystalline colloidal arrays: Novel chemical sensor materials", *Analytical Chemistry*, vol. 70, no. 4, pp. 780–791, 1998. 10

[66] M. M. Hawkeye and M. J. Brett, "Glancing angle deposition: Fabrication, properties, and applications of micro- and nanostructured thin films", *Journal of Vacuum Science & Technology A*, vol. 25, no. 5, pp. 1317–1326, 2007. 10

[67] M. M. Hawkeye, K. M. Krause, and M. J. Brett, "Ambient humidity monitoring using a 1D photonic crystal sensor fabricated with glancing angle deposition", *Proceedings of SPIE*, vol. 7356, pp. 73560G–73560G–8, 2009. 10

[68] O. Hennig, Y. Beregovskii, R. Clemens, S. Mendes, M. Fallahi, and N. Peyghambarian, "Distributed Bragg reflector laser-based sensor for chemical detection", *Optics Communications*, vol. 156, no. 4-6, pp. 311–315, 1998. 10

[69] J. Hu, X. W. Zhao, Y. J. Zhao, J. Li, W. Y. Xu, Z. Y. Wen, M. Xu, and Z. Z. Gu, "Photonic crystal hydrogel beads used for multiplex biomolecular detection", *Journal of Materials Chemistry*, vol. 19, pp. 5730–5736, 2009. 10, 15

[70] N. Gayraud, U. W. Kornaszewski, J. M. Stone, J. C. Knight, D. T. Reid, D. P. Hand, and W. N. MacPherson, "Mid-infrared gas sensing using a photonic bandgap fiber", *Applied Optics*, vol. 47, no. 9, pp. 1269–1277, 2008. 11

[71] T. M. Geppert, S. L. Schweizer, J. Schilling, C. Jamois, D. P. A. V. Rhein, R. Glatthaar, P. Hahn, A. Feisst, A. Lambrecht, and R. B. Wehrspohn, "Photonic crystal gas sensors", *Proceedings of the SPIE*, vol. 5511, no. 61, 2004. 11

[72] E. Austin, A. van Brakel, M. N. Petrovich, and D. J. Richardson, "Fibre optical sensor for C_2H_2 gas using gas-filled photonic bandgap fibre reference cell", *Sensors and Actuators B: Chemical*, vol. 139, no. 1, pp. 30–34, 2009. 11

[73] T. Sunner, T. Stichel, S. H. Kwon, T. W. Schlereth, S. Hfling, M. Kamp, and A. Forchel, "Photonic crystal cavity based gas sensor", *Applied Physics Letters*, vol. 92, no. 26, p. 261112, 2008. 11

[74] C. Lin, K. Chen, C. Hsiao, S. Lin, and C. Lee, "Design and fabrication of an alternating dielectric multi-layer device for surface plasmon resonance sensor", *Sensors and Actuators B: Chemical*, vol. 113, no. 1, pp. 169–176, 2006. 11

[75] E. E. McKenzie, *A second course on light*. Cambridge University Press, 1959. 11

[76] J. W. S. Rayleigh, "On the remarkable phenomenon of crystalline reflexion described by Prof. Stokes", *Philosophical Magazine*, no. 26, pp. 256–265, 1888. 12

[77] E. Yablonovitch, "Photonic band-gap structures", *J. Opt. Soc. Am. B*, vol. 10, no. 2, pp. 283–295, 1993. 13

[78] J. Joannopoulos, S. Johnson, J. Winn, and R. Meade, *Photonic Crystals: Molding the flow of light*. Princeton University Press, 2008. 13, 21

[79] P. Vukusic and D. G. Stavenga, "Physical methods for investigating structural colours in biological systems", *J R Soc Interface*, vol. 6, pp. S133–S148, 2009. 13, 22

[80] S. G. Johnson and J. D. Joannopoulos, "Block-iterative frequency-domain methods for Maxwell's equations in a planewave basis", *Optics Express*, vol. 8, pp. 183–190, 2001. 13, 22

[81] D. Gabor, "Microscopy by reconstructed wave fronts", *Proceedings of the Royal Academy of Sciences*, no. 197, pp. 457–484, 1949. 13

[82] R. Paschotta, *Encyclopedia of laser physics and technology.* WILEY-VCH, 2008. 13, 18

[83] G. Lippmann, "La photographie des couleurs", *Comptes Rendus Hebdomadaires des Sances de l'Acadmie des Sciences*, no. 112, pp. 274–275, 1891. 14

[84] G. Lippmann, "La photographie des couleurs [deuxieme note]", *Comptes Rendus Hebdomadaires des Sances de l'Acadmie des Sciences*, no. 114, pp. 961–962, 1892. 14

[85] G. Lippmann, "Sur la théorie de la photographie des couleurs simples et composées par la méthode interférentielle", *Journal du Physique*, no. 3, pp. 97–107, 1894. 14

[86] A. Einstein, "On a heuristic viewpoint concerning the production and transformation of light", *Annalitycal Physik*, vol. 132, no. 17, pp. 91–107, 1905. 14

[87] A. Einstein, "On the quantum theory of radiation", *Physika Zeitschrift*, no. 18, pp. 121–129, 1917. 14

[88] T. H. Maiman, "Stimulated optical radiation in ruby", *Nature*, no. 187, pp. 493–494, 1960. 14

[89] Y. Denisyuk, "On the reflection of optical properties of an object in a wave field of light scattered by it", *Journal of the Soviet Academy of Sciences*, vol. 6, no. 144, pp. 1275–1278, 1962. 14

[90] J. Upatnieks, J. Marks, and R. Fedorwicz, "Color holograms for white light reconstruction", *Applied Physics Letters*, vol. 8, no. 11, pp. 286–287, 1966. 14

[91] J. Goodman, *Introduction to Fourier optics.* McGraw-Hill physical and quantum electronics series, Roberts & Co., 2005. 14

[92] P. Hariharan, *Basics of holography.* Cambridge Univ Press, 2002. 14

[93] G. K. Ackermann, J. Eichler, and J. Eichler, *Holography: A Practical Approach.* Wiley-VCH, 2008. 15

[94] J. Blyth, "Smart holograms", *The Holographer*, vol. Materials, April 2004. 15, 24

[95] J. Blyth, A. G. Mayes, R. B. Millington, and C. R. Lowe, "A novel method for producing silver halide-based holographic recording materials", *Imaging Science Journal*, vol. 47, pp. 87–91, 1999. 15

[96] H. Bjelkhagen, *Silver-halide recording materials: for holography and their processing*, vol. 66. Springer Verlag, 1995. 15, 71

[97] B. A. Budkevich, A. M. Polikanin, V. A. Pilipovich, and N. Y. Petrochenko, "Amplitude-phase hologram recording on $FeCl_2$-PVA films", *Journal of Applied Spectroscopy*, vol. 50, pp. 621–624, 1989. 15

[98] R. Fontanilla-Urdaneta, A. Olivares-Pérez, and I. Fuentes-Tapia, "Real-time holographic gratings modulate with voltage by different thickness film", *Optical Engineering*, vol. 50, 2011. 15

[99] A. Olivares-Pérez, M. P. Hernández-Garay, I. Fuentes-Tapia, and J. C. Ibarra-Torres, "Holograms in polyvinyl alcohol photosensitized with $CuCl_2(H_2O)$", *Optical Engineering*, vol. 50, 2011. 15

[100] K. Curtis and D. Psaltis, "Recording of multiple holograms in photopolymer films", *Applied Optics*, vol. 31, pp. 7425–7428, 1992. 15, 18

[101] R. J. Carlson and S. A. Asher, "Characterization of optical diffraction and crystal structure in monodisperse polystyrene colloids", *Applied Spectroscopy*, vol. 38, pp. 297–304, 1984. 15

[102] C. G. Reese, J. Weissman, K. Lee, and S. A. Asher, "Synthesis of highly charged, monodisperse polystyrene colloidal particles for the fabrication of photonic crystals", *J. Colloid and Interface Science*, vol. 232, pp. 76–80, 1984. 15

[103] H. Kogelnik, "Coupled wave theory for thick hologram gratings", *The Bell System Technical Journal*, vol. 48, no. 9, pp. 2909–2947, 1969. 16

[104] P. Phariseau, "On the diffraction of light by progressive supersonic waves", *Proceedings of the Indian Academy of Sciences*, vol. 44, no. A, pp. 165–170, 1956. 16

[105] E. J. Saccocio, "Application of the dynamical theory of x-ray diffraction to holography", *Journal of Applied Physics*, vol. 38, no. 10, pp. 3994–3998, 1967. 17

[106] T. Jannson, I. Tengara, Y. Qiao, and G. Savant, "Lippmann-Bragg broadband holographic mirrors", *Journal of the Optical Society of America*, vol. 8, no. 1, pp. 201–211, 1991. 18

[107] C. Sheppard, "Approximate calculation of the reflection coefficient from a stratified medium", *Pure and Applied Optics: Journal of the European Optical Society Part A*, vol. 4, p. 665, 1995. 18

[108] W. Sellmeier, "Zur erklrung der abnormen farbenfolge im spectrum einiger substanzen", *Annalen der Physik und Chemie*, vol. 219, pp. 272–282, 1871. 18, 19

[109] L. Davis and M. Deutsch, "Surface plasmon based thermo-optic and temperature sensor for microfluidic thermometry", *arXiv.org [physics.optics]*, p. arXiv:1009.4904v1, 2010. 18

[110] D. Jundt, "Temperature-dependent Sellmeier equation for the index of refraction, n_e, in congruent lithium niobate", *Optics Letters*, vol. 22, no. 20, pp. 1553–1555, 1997. 18, 19

[111] I. Dolev, A. Ganany-Padowicz, O. Gayer, and A. Arie, "Temperature and wavelength dependent refractive index equation for stochiometric lithium tantalite", in *Electrical and Electronics Engineers in Israel, 2008. IEEEI 2008. IEEE 25th Convention of*, pp. 308–312, IEEE, 2008. 18, 19

[112] J. Owens, "Optical refractive index of air: dependence on pressure, temperature and composition", *Applied Optics*, vol. 6, no. 1, pp. 51–59, 1967. 18, 19

[113] A. Bashkatov and E. Genina, "Water refractive index in dependence on temperature and wavelength: a simple approximation", in *Proc. SPIE*, vol. 5068, pp. 393–395, 2003. 18, 19

[114] V. Boriskin, M. Ayzatsky, S. Boriskina, Y. Machehin, and A. Semenov, "Theoretical and experimental study of temperature-dependent spectral properties of multi-layer metal-dielectric nano-film structures", in *Transparent Optical Networks, 2007. ICTON'07*, vol. 4, pp. 279–282, IEEE, 2007. 18

[115] H. Macleod, *Thin-film optical filters*. Series in optics and optoelectronics, CRC Press/Taylor & Francis, 2009. 19

[116] A. Y. Pochi Yeh, *Optical waves in crystals*, ch. 6 Electromagnetic propagation in periodic media, pp. 155–219. NY, USA: Wiley-Interscience, 1984. 20, 21, 72, 182

[117] J. D. Jackson, *Classical Electrodynamics*. Wiley, 3rd ed., 1999. 21

[118] D. Chigrin, A. Lavrinenko, D. Yarotsky, and S. Gaponenko, "All-dielectric one-dimensional periodic structures for total omnidirectional reection and partial spontaneous emission control", *IEEE Journal of lightwave technology*, vol. 17, no. 11, pp. 2018 – 2024, 1999. 21

[119] H. M. Ng, "Distributed Bragg reflectors based on AIN/GaN multilayers", *Applied Physics Letters*, vol. 74, no. 7, pp. 1036–1038, 1999. 22

[120] L. R. Brovelli and U. Keller, "Simple analytical expressions for the reflectivity and the penetration depth of Bragg mirror between arbitrary media", *Optics Communications*, no. 116, pp. 343–350, 1995. 22

[121] E. F. Pen, Y. Rodinov, and V. Shelkovnikov, "Modeling the spectral characteristics of reflection holograms in photopolymer materials", *Russian Physics Journal*, vol. 44, no. 10, pp. 1074–1076, 2001. 22

[122] C. Pond, "Holographic angle sensor". US Patent 4,227,807, Jan 1980. 23

[123] I. Cin, "Holographic pressure sensor". US Patent 6,590,640, Sept 1971. 23

[124] R. Jones and C. Wykes, *Holographic and speckle interferometry*. Cambridge University Press, 1989. 23

[125] R. K. Kostuk and J. W. Goodman, "Refractive index modulation mechanism in bleached silver halide holograms", *Applied Optics*, vol. 30, pp. 369–371, 1991. 23

[126] R. B. Millington, A. G. Mayes, J. Blyth, and C. R. Lowe, "A holographic sensor for proteases", *Analytical Chemistry*, vol. 67, no. 23, pp. 4229–4233, 1995. 24

[127] J. Blyth, R. B. Millington, A. G. Mayes, E. R. Frears, and C. R. Lowe, "Holographic sensor for water in solvents", *Analytical Chemistry*, vol. 68, no. 7, pp. 1089–1094, 1996. 24

[128] J. Blyth, "Holographic sensors and their production". WO Patent 1999/063,408, January 1999. 24

[129] A. G. Mayes, J. Blyth, M. Kyrlinen-Reay, R. B. Millington, and C. R. Lowe, "A holographic alcohol sensor", *Analytical Chemistry*, vol. 71, no. 16, pp. 3390–3396, 1999. 24

[130] A. G. Mayes, J. Blyth, R. B. Millington, and C. R. Lowe, "Metal ion-sensitive holographic sensors", *Analytical Chemistry*, vol. 74, no. 15, pp. 3649–3657, 2002. 24

[131] A. J. Marshall, J. Blyth, C. A. B. Davidson, and C. R. Lowe, "pH-Sensitive Holographic Sensors", *Analytical Chemistry*, vol. 75, no. 17, pp. 4423–4431, 2003. 24

[132] A. J. Marshall, D. S. Young, S. Kabilan, A. Hussain, J. Blyth, and C. R. Lowe, "Holographic sensors for the determination of ionic strength", *Analytica Chimica Acta*, vol. 527, no. 1, pp. 13–20, 2004. 24

[133] I. Naydenova, J. Raghavendra, S. Martin, and V. Toal, *Humidity Sensors*, ch. 3. Holographic Humidity Sensors pp. 117-142. Dublin, IE: Nova Science Publishers, Inc., 2011. 24

[134] A. J. Marshall, D. S. Young, J. Blyth, S. Kabilan, and C. R. Lowe, "Metabolite-sensitive holographic biosensors", *Analytical Chemistry*, vol. 76, no. 5, pp. 1518–1523, 2004. 24, 94

[135] M. C. Lee, S. Kabilan, A. Hussain, X. Yang, J. Blyth, and C. R. Lowe, "Glucose-sensitive holographic sensors for monitoring bacterial growth", *Analytical Chemistry*, vol. 76, no. 19, pp. 5748–5755, 2004. 24

[136] S. Kabilan, A. J. Marshall, F. K. Sartain, M.-C. Lee, A. Hussain, X. Yang, J. Blyth, N. Karangu, K. James, J. Zeng, D. Smith, A. Domschke, and C. R. Lowe, "Holographic glucose sensors", *Biosensors and Bioelectronics*, vol. 20, no. 8, pp. 1602–1610, 2005. 24

[137] A. Domschke, W. F. March, S. Kabilan, and C. Lowe, "Initial clinical testing of a holographic non-invasive contact lens glucose sensor", *Diabetes Technology and Therapeutics*, vol. 8, no. 1, pp. 89–93, 2006. 24

[138] X. Yang, X. Pan, J. Blyth, and C. R. Lowe, "Towards the real-time monitoring of glucose in tear fluid: Holographic glucose sensors with reduced interference from lactate and pH", *Biosensors and Bioelectronics*, vol. 23, no. 6, pp. 899–905, 2008. 24

[139] A. G. Mayes, J. Blyth, R. B. Millington, and C. R. Lowe, "A holographic sensor based on a rationally designed synthetic polymer", *Journal of Molecular Recognition*, vol. 11, no. 1-6, pp. 168–174, 1998. 24

[140] S. Kabilan, J. Blyth, M. C. Lee, A. J. Marshall, A. Hussain, X.-P. Yang, and C. R. Lowe, "Glucose-sensitive holographic sensors", *Journal of Molecular Recognition*, vol. 17, no. 3, pp. 162–166, 2004. 24

[141] A. M. Horgan, A. J. Marshall, S. J. Kew, K. E. Dean, C. D. Creasey, and S. Kabilan, "Crosslinking of phenylboronic acid receptors as a means of glucose selective holographic detection", *Biosensors and Bioelectronics*, vol. 21, no. 9, pp. 1838–1845, 2006. 24

[142] X. Yang, M.-C. Lee, F. Sartain, X. Pan, and C. R. Lowe, "Designed boronate ligands for glucose-selective holographic sensors", *Chemistry A European Journal*, vol. 12, no. 33, pp. 8491–8497, 2006. 24

[143] F. K. Sartain, X. Yang, and C. R. Lowe, "Holographic lactate sensor", *Analytical Chemistry*, vol. 78, no. 16, pp. 5664–5670, 2006. 24

[144] E. Leite, I. Naydenova, S. Mintova, L. Leclercq, and V. Toal, "Photopolymerizable nanocomposites for holographic recording and sensor application", *Applied Optics*, vol. 49, no. 19, pp. 3652–3660, 2010. 24

[145] B. Adhikari and S. Majumdar, "Polymers in sensor applications", *Progress in Polymer Science*, vol. 29, no. 7, pp. 699 – 766, 2004. 24

[146] A. C. M. Kuo, *Polymer Data Handbook*, ch. Poly(dimethylsiloxane). Oxford, UK: Oxford University Press, 1999. 26, 46, 47, 106, 110, 181, 183, 200

[147] C. W. Mayer, "Coating machine". US Patent 1043021, November 1912. 26

[148] J. NgLee, C. Park, and G. Whitesides, "Solvent compatibility of poly(dimethylsiloxane)-based microfluidic devices", *Anal. Chem.*, vol. 75, no. 23, pp. 6544–6554, 2003. 27, 50, 200

[149] F. Hajiesmaeilbaigi, A. Mohammadalipour, J. Sabbaghzadeh, S. Hoseinkhani, and H. Fallah, "Preparation of silver nanoparticles by laser ablation and fragmentation in pure water", *Laser Physics Letters*, vol. 3, no. 5, pp. 252–256, 2005. 27, 30, 135

[150] F. Mafune, J.-y. Kohno, Y. Takeda, T. Kondow, and H. Sawabe, "Structure and stability of silver nanoparticles in aqueous solution produced by laser ablation", *The Journal of Physical Chemistry B*, vol. 104, no. 35, pp. 8333–8337, 2000. 27, 30

[151] F. Mafune, J.-y. Kohno, Y. Takeda, T. Kondow, and H. Sawabe, "Formation and size control of silver nanoparticles by laser ablation in aqueous solution", *The Journal of Physical Chemistry B*, vol. 104, no. 39, pp. 9111–9117, 2000. 27, 30

[152] T. Tsujia, N. Watanabeb, and M. Tsujia, "Laser induced morphology change of silver colloids: formation of nano-size wires", *Applied Surface Science*, vol. 211, no. 1-4, pp. 189 – 193, 2003. 27, 30

[153] A. Goswami, A. Acharya, and A. K. Pandey, "Study of self-diffusion of monovalent and divalent cations in Nafion-117 ion-exchange membrane", *The Journal of Physical Chemistry B*, vol. 105, no. 38, pp. 9196–9201, 2001. 28

[154] Y. P. Sun, P. Atorngitjawat, Y. Lin, P. Liu, P. Pathak, J. Bandara, D. Elgin, and M. Zhang, "Nanoscale cavities in ionomer membrane for the formation of nanoparticles", *Journal of Membrane Science*, vol. 245, no. 1-2, pp. 211 – 217, 2004. 29, 124, 128

[155] A. Sachdeva, S. Sodaye, A. K. Pandey, and A. Goswami, "Formation of silver nanoparticles in poly(perfluorosulfonic) acid membrane", *Analytical Chemistry*, vol. 78, no. 20, pp. 7169–7174, 2006. 30, 124, 128

[156] M. Saito, K. Yasukawa, T. Umeda, and Y. Aoi, "Copper nanoparticles fabricated by laser ablation in polysiloxane", *Optical Materials*, vol. 30, no. 7, pp. 1201 – 1204, 2008. 30

[157] R. S. Yeo, "Dual cohesive energy densities of perfluorosulphonic acid (Nafion) membrane", *Polymer*, vol. 21, no. 4, pp. 432 – 435, 1980. 32, 123, 124, 176, 181, 183

[158] M. D. Abramoff, P. J. Magalhẽs, and S. J. Ram, "Image processing with Image J", *Biophotonics international*, vol. 11, no. 7, pp. 36–42, 2004. 34

[159] BD, "Technical data sheet", BD Plastipak^{TM} syringe without needle - Sterile, BD Medical - Medical Surgical Systems, Belgium, 2009. 41

[160] B. Li, F. Pan, Z. Fang, L. Liu, and Z. Jiang, "Molecular dynamics simulation of diffusion behavior of benzene/water in PDMS-calix[4]arene hybrid pervaporation membranes", *Industrial and Engineering Chemistry Research*, vol. 47, no. 13, pp. 4440–4447, 2008. 45, 116

[161] J.-H. Zhou, R.-X. Zhu, J.-M. Zhou, and M.-B. Chen, "Molecular dynamics simulation of diffusion of gases in pure and silica-filled poly(1-trimethylsilyl-1-propyne) [ptmsp]", *Polymer*, vol. 47, no. 14, pp. 5206 – 5212, 2006. 45

[162] F. Pan, F. Peng, L. Lu, J. Wang, and Z. Jiang, "Molecular simulation on penetrants diffusion at the interface region of organic–inorganic hybrid membranes", *Chemical Engineering Science*, vol. 63, no. 4, pp. 1072–1080, 2008. 45

[163] F. Pan, F. Peng, and Z. Jiang, "Diffusion behavior of benzene/cyclohexane molecules in poly(vinyl alcohol)-graphite hybrid membranes by molecular dynamics simulation", *Chemical Engineering Science*, vol. 62, no. 3, pp. 703 – 710, 2007. 45

[164] D. Wu, S. J. Paddison, J. A. Elliott, and S. J. Hamrock, "Mesoscale modeling of hydrated morphologies of 3M perfluorosulfonic acid-based fuel cell electrolytes", *Langmuir*, vol. 26, no. 17, pp. 14308–14315, 2010. 45

[165] T. Schlick and M. Overton, "A powerful truncated newton method for potential energy minimization", *Journal of Computational Chemistry*, vol. 8, no. 7, pp. 1025–1039, 1987. 45

[166] H. Sun, "COMPASS: An ab Initio Force-Field Optimized for Condensed-Phase ApplicationsOverview with Details on Alkane and Benzene Compounds", *The Journal of Physical Chemistry B*, vol. 102, no. 38, pp. 7338–7364, 1998. 45

[167] C. Drummond and D. Chan, "van der waals interaction, surface free energies, and contact angles: dispersive polymers and liquids", *Langmuir*, vol. 13, no. 14, pp. 3890–3895, 1997. 46, 183

[168] E. Grulke, J. Brandrup, and E. Immergut, *Polymer handbook*. Wiley-Blackwell, 1999. 46

[169] I. F. Vankelecom and P. A. Jacobs, "Dense organic catalytic membranes for fine chemical synthesis", *Catalysis Today*, vol. 56, no. 1-3, pp. 147 – 157, 2000. 47, 48, 110, 111

[170] S. Z. Wu and J. E. Mark, "Some simulations and theoretical studies on poly(dimethylsiloxane)", *Polymer Reviews*, vol. 47, no. 4, pp. 463–485, 2007. 47, 48, 110

[171] DowCorning, "Siloxanes rheology", silicone technology / materials science / rheology, Dow Corning Inc, US, 2009. 47, 110, 183

[172] G. Schmid, "Large clusters and colloids. Metals in the embryonic state", *Chemical Reviews*, vol. 92, no. 8, pp. 1709–1727, 1992. 50

[173] L. M. Liz-Marzan, "Nanometals: Formation and color", *Materials Today*, vol. 7, no. 2, pp. 26 – 31, 2004. 50

[174] M. Lehmann, *Holography: technique and practice.* Focal Press, 1970. 52

[175] F. Sartain, *Design of a holographic lactate sensor.* PhD thesis, University of Cambridge. Institute of Biotechnology, 2006. 53

[176] V. Jain, R. Sahoo, J. Jinschek, R. Montazami, H. Yochum, F. Beyer, A. Kumar, and J. Heflin, "High contrast solid state electrochromic devices based on ruthenium purple nanocomposites fabricated by layer-by-layer assembly", *Chemical Communications*, no. 31, pp. 3663–3665, 2008. 53

[177] V. Jain, M. Khiterer, R. Montazami, H. Yochum, K. Shea, and J. Heflin, "High-contrast solid-state electrochromic devices of viologen-bridged polysilsesquioxane nanoparticles fabricated by layer-by-layer assembly", *ACS Applied Materials & Interfaces*, vol. 1, no. 1, pp. 83–89, 2009. 53

[178] H. I. Bjelkhagen, "New recording materials for holography", *De Montfort University, Centre for Modern Optics*, vol. 3D imaging and photography group, 2011. 54

[179] F. Lednicky, E. Coufalova, J. Hromadkova, A. Delong, and V. Kolarik, "Low-voltage tem imaging of polymer blends", *Polymer*, vol. 41, no. 13, pp. 4909 – 4914, 2000. 54

[180] A. Courty, A. I. Henry, N. Goubet, and M. P. Pileni, "Large triangular single crystals formed by mild annealing of self-organized silver nanocrystals", *Nature Materials*, vol. 6, pp. 900–907, 11 2007. 56, 57

[181] H. Hofmeister, G. Tan, and M. Dubiel, "Shape and internal structure of silver nanoparticles embedded in glass", *Journal of materials research*, vol. 20, no. 06, pp. 1551–1562, 2005. 56, 57, 131, 133

[182] Z. Zhang and M. Han, "Template-directed growth from small clusters into uniform silver nanoparticles", *Chemical physics letters*, vol. 374, no. 1, pp. 91–94, 2003. 56

[183] F. Giessibl, "Advances in atomic force microscopy", *Reviews of modern physics*, vol. 75, no. 3, p. 949, 2003. 61

[184] M. Born, E. Wolf, and A. Bhatia, *Principles of Optics: Electromagnetic Theory of Propagation, Interference and Diffraction of Light.* Cambridge University Press, 1999. 63

[185] J. Silfies, S. Schwartz, and M. Davidson, "The diffraction barrier in optical microscopy", tech. rep., Nikon Inc, 2012. 63

[186] D. Chang Yen, R. Eich, and B. Gale, "A monolithic PDMS waveguide system fabricated using soft-lithography techniques", *Journal of Lightwave Technology*, vol. 23, no. 6, pp. 2088–2093, 2005. 66, 71, 72

[187] S. Moiseev, "Optical properties of a Maxwell-Garnett composite medium with nonspherical silver inclusions", *Russian Physics Journal*, vol. 52, no. 11, pp. 1121–1127, 2009. 66, 71, 72, 138

[188] K. G. Stamplecoskie and J. C. Scaiano, "Light emitting dioded irradiation can control the morphology and optical properties of silver nanoparticles", *Journal of the American Chemical Society*, vol. 132, pp. 1825–1827, 2010. 66, 69, 127

[189] S. Malynych and G. Chumanov, "Light-induced coherent interactions between silver nanoparticles in two dimensional arrays", *Journal of the American Chemical Society*, vol. 125, pp. 2896–2898, 2003. 66, 69, 127

[190] J. Hu, W. Lee, W. Cai, L. Tong, and H. Zeng, "Evolution of the optical spectra of an Ag/mesoporous SiO_2 nanostructure heat-treated in air and H_2 atmospheres", *Nanotechnology*, vol. 18, p. 185710, 2007. 66, 126

[191] A. O. Pinchuk, "Angle dependent collective surface plasmon resonance in an array of silver nanoparticles.", *The Journal of Physical Chemistry A*, vol. 113, no. 16, pp. 4430–4436, 2009. 66, 126

[192] S. Thomas, S. K. Nair, E. M. A. Jamal, S. H. Al-Harthi, M. R. Varma, and M. R. Anantharaman, "Size-dependent surface plasmon resonance in silver silica nanocomposites", *Nanotechnology*, vol. 19, no. 7, p. 075710, 2008. 66, 126

[193] G. D. Bothun, "Hydrophobic silver nanoparticles trapped in lipid bilayers: Size distribution, bilayer phase behavior, and optical properties", *Journal of Nanobiotechnology*, vol. 6, no. 13, 2008. 66, 126

[194] NanoComposix, "Silver nanoparticles: Optical properties", tech. rep., NanoComposix Inc, San Diego, CA, 2012. 66, 69

[195] A. Ziaeemehr and R. Poursalehi, "Optical properties of silver nanoparticle dispersed in polymer matrix", *Department of Physics, Shahed University, Theran, Iran*, 2011. 71, 138

[196] T. Saranti and C. Carter, "Multilayer photonic bandgap". Wolfram Demonstrations Project, 2011. 73

[197] E. Gutierrez and A. Groisman, "Measurements of elastic moduli of silicone gel substrates with a microfluidic device", *PLoS ONE*, vol. 6, p. e25534, 09 2011. 79

[198] A. Douglas, "Properties of polymers: Young Modulus of Sylgard 184", tech. rep., Sandia National Laboratories, 2010. 79

[199] V.-M. Graubner, R. Jordan, O. Nuyken, T. Lippert, M. Hauer, B. Schnyder, and A. Wokaun, "Incubation and ablation behavior of poly(dimethylsiloxane) for 266 nm irradiation", *Applied Surface Science*, vol. 197-198, no. 0, pp. 786 – 790, 2002. 81

[200] C. Dupas-Bruzek, O. Robbe, A. Addad, S. Turrell, and D. Derozier, "Transformation of medical grade silicone rubber under Nd:YAG and excimer laser irradiation: First step towards a new miniaturized nerve electrode fabrication process", *Applied Surface Science*, vol. 255, no. 21, pp. 8715 – 8721, 2009. 81

[201] P. J. Mohr and B. N. Taylor, "CODATA recommended values of the fundamental physical constants: 1998", *Rev. Mod. Phys.*, vol. 72, pp. 351–495, Apr 2000. 87

[202] D. R. Lide, *Handbook of Chemistry and Physics*. CRC Press, 2008. 88

[203] Y. Ho, "Review of second-order models for adsorption systems", *Journal of hazardous materials*, vol. 136, no. 3, pp. 681–689, 2006. 93

[204] H. Hu, M. Trejo, M. Nicho, J. Saniger, and A. Garcıa-Valenzuela, "Adsorption kinetics of optochemical NH_3 gas sensing with semiconductor polyaniline films", *Sensors and Actuators B: Chemical*, vol. 82, no. 1, pp. 14–23, 2002. 93

[205] M. Nicho, L. Hechavarría, and H. Hu, "Similarity between optical response kinetics of conducting polymer thin film based gas sensors and electrochromic devices.", *Revista mexicana de fisica*, vol. 50, no. 5, pp. 471–477, 2004. 93

[206] D. Jenkins, "Desorption as a rate limiting step for gas permeation through a polymer membrane", *The Journal of Physical Chemistry B*, vol. 108, no. 50, pp. 19325–19329, 2004. 93

[207] Y. Lilach, I. Danziger, and M. Asscher, "Second order isothermal desorption kinetics", *Catalysis letters*, vol. 76, no. 1, pp. 35–39, 2001. 93

[208] P. Puri, Q. Liu, and D. De Kee, "Diffusion through swelling membranes with a robin boundary condition", *Journal of Applied Polymer Science*, vol. 108, no. 1, pp. 47–51, 2008. 93

[209] Q. Liu and D. De Kee, "Mass transport through PDMS/clay nanocomposite membranes", *The Canadian Journal of Chemical Engineering*, vol. 85, no. 1, pp. 36–44, 2007. 93

[210] Q. Liu and D. De Kee, "Modeling of diffusion through nanocomposite membranes", *Journal of non-newtonian fluid mechanics*, vol. 131, no. 1, pp. 32–43, 2005. 93

[211] C. Labruyère, G. Gorrasi, F. Monteverde, M. Alexandre, and P. Dubois, "Transport properties of organic vapours in silicone/clay nanocomposites", *Polymer*, vol. 50, no. 15, pp. 3626–3637, 2009. 93

[212] D. Bhatta, G. Christie, B. Madrigal-Gonzalez, J. Blyth, and C. Lowe, "Holographic sensors for the detection of bacterial spores", *Biosensors and Bioelectronics*, vol. 23, no. 4, pp. 520 – 527, 2007. 94

[213] R. S. of Chemistry, "Predicted and experimental octanol-water partition coefficients". RSC Chemspider.com, 2010. 95, 97, 200

[214] S. Hirono, Q. Liu, and I. Moriguchi, "High correlation between hydrophobic free energy and molecular surface area characterized by electrostatic potential", *Chemical Pharmaceutical Bulletin*, pp. 3106–3109, 1991. 98

[215] G. Peyre, "Principal component discrimination analysis". Toolbox Non-Local Means, 2006. 102

[216] H. Sundgren, F. Winquist, I. Lukkari, and I. Lundstrom, "Artificial neural networks and gas sensor arrays: quantification of individual components in a gas mixture", *Measurement Science and Technology*, vol. 2, no. 5, p. 464, 1999. 102

[217] B. Li, D. Xu, X. Zhang, Z. Jiang, Y. Wang, J. Ma, X. Dong, and H. Wu, "Rubbery polymer-inorganic nanocomposite membranes: Free volume characteristics on separation property", *Industrial and Engineering Chemistry Research*, vol. 49, no. 24, pp. 12444–12451, 2010. 102

[218] J. Fried, *Conformation, Solutions and Molecular Weight*, ch. 3, pp. 87–151. Prentice Hall, 2nd ed., 2003. 103, 104, 105, 106, 182, 200

[219] L. Boltzmann, *Vorlesungen über Gastheorie*, vol. 1. JA Barth, 1896. 103

[220] J. Prausnitz, R. Lichtenthaler, and E. de Azevedo, *Molecular thermodynamics of fluid-phase equilibria.* Prentice Hall, 1998. 105, 182

[221] J. Hildebrand, "An improvement in the theory of regular solutions", *Proceedings of the National Academy of Sciences*, vol. 76, no. 12, pp. 6040–6041, 1979. 105, 182, 200

[222] J. E. Mark, *Physical properties of polymers Handbook.* Springer, 1990. 106, 200

[223] A. F. Barton, *Handbook of polymer liquid interaction parameters and solubility parameters.* CRC Press, 1990. 106, 200

[224] M. Belmares, M. Blanco, W. Goddard III, R. Ross, G. Caldwell, S. Chou, J. Pham, P. Olofson, and C. Thomas, "Hildebrand and Hansen solubility parameters from molecular dynamics with applications to electronic nose polymer sensors", *Journal of computational chemistry*, vol. 25, no. 15, pp. 1814–1826, 2004. 108

[225] M. L. Connolly, "Molecular surfaces: A review", *Network Science*, 1996. 108

[226] A. Murata, S. Shibata, and M. Saito, "Continuous analyzer for volatile organic compounds in air and water", *Yokogawa technical report - English edition*, pp. 1–4, 2001. 113

[227] T. Ohshima, T. Miyata, T. Uragami, and H. Berghmens, "Cross-linked smart poly(dimethylsiloxane) membranes for removal of volatile organic compounds in water", *Journal of Molecular Structure*, vol. 739, no. 1–3, pp. 47–55, 2005. 116

[228] U. E. P. Agency, "Basic information about toluene in drinking water". Drinking Water Contaminants, 1996. 116

[229] L. P, S. N, A. C, H. S-J, A. E, R. K, and C. S, "Proposed EQS for Water Framework Directive Annex VIII substances: toluene", SNIFFER Report: WFD52(xiv) SC040038/SR14, UK Environment Agency, 2007. 116

[230] C. Bohren, E. Clothiaux, and E. Clothiaux, *Fundamentals of atmospheric radiation: an introduction with 400 problems*. Wiley-VCH, 2006. 118

[231] D. Yang, H. Min, B. Fowler, A. E. Gamal, M. Beiley, and K. Cham, "Test structures for characterization and comparative analysis of CMOS image sensors", *Proceedings of the SPIE*, pp. 8–17, 1996. 118

[232] P. C. Lee and M. A. J. Rodgers, "Kinetic properties of singlet oxygen in a polymeric microheterogeneous system", *The Journal of Physical Chemistry*, vol. 88, no. 19, pp. 4385–4389, 1984. 122, 123, 124

[233] M. C. Liu, C. L. Dai, C. H. Chan, and C. C. Wu, "Manufacture of a polyaniline nanofiber ammonia sensor integrated with a readout circuit using the CMOS-MEMS technique", *Sensors*, vol. 9, pp. 869 – 880, 2009. 122

[234] C. Preininger, I. Klimant, and O. Wolfbeis, "Optical fiber sensor for biological oxygen demand", *Analytical Chemistry*, vol. 66, no. 11, pp. 1841–1846, 1994. 122

[235] S. Banerjee and D. E. Curtin, "Nafion perfluorinated membranes in fuel cells", *Journal of Fluorine Chemistry*, vol. 125, pp. 1211 – 1216, 2004. 123

[236] U. Bohner and G. Zundel, "Proton potentials and proton polarizability of hydrogen bonds in sulfonic acid-oxygen base systems as a function of the δpka", *The Journal of Physical Chemistry*, vol. 89, pp. 1408–1413, 1985. 123, 183

[237] V. A. Sethuraman, S. Khan, J. S. Jur, A. T. Haug, , and J. W. Weidner, "Measuring oxygen, carbon monoxide and hydrogen sulfide diffusion coefficient and solubility in Nafion membranes", *Electrochimica Acta*, vol. 54, no. 27, pp. 6850–6860, 2009. 123

[238] W. Phillip, E. Martono, L. Chen, and M. Hillmyer, "Seeking an ammonia selective membrane based on nanostructured sulfonated block copolymers", *Journal of Membrane Science*, vol. 337, no. 1-2, pp. 39–46, 2009. 123, 183

[239] R. Halseid, P. J. S. Vie, and R. Tunold, "Influence of Ammonium on Conductivity and Water Content of Nafion 117 Membranes", *Journal of The Electrochemical Society*, vol. 151, no. 3, pp. A381–A388, 2004. 123

[240] R. A. Huggings, *Advanced Batteries: Materials science aspects*, ch. 14 Liquid Electrolytes, pp. 325–328. Standford, CA, USA: Springer, 2008. 123, 124, 125, 181, 183

[241] K.-D. Kreuer, S. J. Paddison, E. Spohr, and M. Schuster, "Transport in proton conductors for fuel-cell applications: Simulations, elementary reactions, and phenomenology", *Chemical Reviews*, vol. 104, no. 10, pp. 4637–4678, 2004. 124, 125, 147, 181, 183

[242] T. D. Gierke, G. E. Munn, and F. C. Wilson, "The morphology in nafion perfluorinated membrane products, as determined by wide- and small-angle x-ray studies", *Journal of Polymer Science: Polymer Physics Edition*, vol. 19, no. 11, pp. 1687–1704, 1981. 124, 126, 135

[243] W. Y. Hsu and T. D. Gierke, "Ion transport and clustering in Nafion perfluorinated membranes", *Journal of Membrane Science*, vol. 13, no. 3, pp. 307 – 326, 1983. 124, 126, 135

[244] H. W. Rollins, F. Lin, J. johnson, J. J. Ma, J. T. Liu, M. H. Tu, D. D. DesMarteau, and Y. P. sun, "Nanoscale cavities for nanoparticles in perfluorinated ionomer membranes", *Langmuir*, vol. 16, p. 8031, 2000. 124, 126, 135

[245] H. Ablat, A. Yimit, M. Mahmut, and K. Itoh, "Nafion Film/K^+-Exchanged Glass Optical Waveguide sensor for BTX Detection", *Analytical Chemistry*, vol. 80, no. 20, pp. 7678–7683, 2008. 124

[246] Sigma-Aldrich, "Nafion$^{®}$ 117 solution". Catalog Product Information, 2012. 124

[247] N. Pantelic, C. M. Wansapura, W. R. Heineman, and C. J. Seliskar, "Dynamic in situ spectroscopic ellipsometry of the reaction of aqueous Iron(II) with 2,2'-bipyridine in a thin Nafion film", *Journal of Physical Chemistry B*, vol. 109, pp. 13971–13979, 2005. 124, 139, 140

[248] T. Hasegawa, T. Strunskus, V. Zaporotjenko, F. Faupel, and M. Mizuhata, "Preparation of silver nanoparticles-Nafion membrane composite by photoreduction process", *ECS Transactions*, vol. 41, no. 30, pp. 9–18, 2012. 124, 138

[249] L. L. Beecroft and C. K. Ober, "Nanocomposite materials for optical applications", *Chem. Mater.*, vol. 9, no. 6, pp. 1302–1317, 1997. 137

[250] K. Sathiyamoorthy, C. Vijayan, and M. P. Kothiyal, "Design of a low power optical limiter based on a new nanocomposite material incorporating silica-encapsulated phthalocyanine in naon", *J. Phys. D: Appl. Phys*, vol. 40, no. 6, p. 61216128, 2007. 137

[251] J. He, W. Ji, G. H. Ma, S. H. Tang, E. S. W. Kong, S. Y. Chow, X. H. Zhang, Z. L. Hua, and J. L. Shi, "Ultrafast and large third-order nonlinear optical properties of CdS nanocrystals in polymeric film", *The Journal of Physical Chemistry B*, vol. 109, no. 10, pp. 4373–4376, 2005. 137

[252] M. B. Satterfield and J. B. Benziger, "Viscoelastic properties of Nafion at elevated temperature and humidity", *Journal of Polymer Science Part B: Polymer Physics*, vol. 47, no. 1, pp. 11–24, 2009. 138

[253] Q. Zhao, P. Majsztrik, and J. Benziger, "Diffusion and Interfacial Transport of Water in Nafion", *The Journal of Physical Chemistry B*, 2011. 138

[254] A. Leis, S. Schlicher, H. Franke, and M. Strathmann, "Optically transparent porous medium for nondestructive studies of microbial biofilm architecture and transport dynamics", *Applied and environmental microbiology*, vol. 71, no. 8, pp. 4801–4808, 2005. 139, 140

[255] K. Kreuer, "On the development of proton conducting polymer membranes for hydrogen and methanol fuel cells", *Journal of Membrane Science*, vol. 185, no. 1, pp. 29–39, 2001. 139, 170

[256] G. Scherer, *Fuel Cells I.* Advances in Polymer Science, Springer, 2008. 139

[257] T. Zawodzinski Jr, C. Derouin, S. Radzinski, R. Sherman, V. Smith, T. Springer, and S. Gottesfeld, "Water uptake by and transport through Nafion® 117 membranes", *Journal of the Electrochemical Society; US*, vol. 140, no. 4, 1993. 139, 170

[258] M. Rubner, R. Cohen, A. Nolte, *et al.*, *Fundamental studies of polyelectrolyte multilayer films: optical, mechanical, and lithographic property control.* PhD thesis, Massachusetts Institute of Technology, 2007. 139, 170

[259] M. Laporta, M. Pegoraro, and L. Zanderighi, "Perfluorosulfonated membrane (Nafion): FT-IR study of the state of water with increasing humidity", *Phys. Chem. Chem. Phys.*, vol. 1, no. 19, pp. 4619–4628, 1999. 139, 170

[260] F. Bauer, S. Denneler, and M. Willert-Porada, "Influence of temperature and humidity on the mechanical properties of Nafion® 117 polymer electrolyte membrane", *Journal of Polymer Science Part B: Polymer Physics*, vol. 43, no. 7, pp. 786–795, 2005. 139, 170

[261] K. Sendhil, C. Vijayan, and M. Kothiyal, "Nonlinear optical properties of a porphyrin derivative incorporated in Nafion polymer", *Optical Materials*, vol. 27, no. 10, pp. 1606 – 1609, 2005. 144

[262] E. Roberti, G. Carlotti, S. Cinelli, G. Onori, A. Donnadio, R. Narducci, M. Casciola, and M. Sganappa, "Measurement of the Young's modulus of Nafion membranes by Brillouin light scattering", *Journal of Power Sources*, vol. 195, no. 23, pp. 7761 – 7764, 2010. 144

[263] P. Winsemius, F. Kampen, H. Lengkeek, and C. Went, "Temperature dependence of the optical properties of Au, Ag and Cu", *Journal of Physics F: Metal Physics*, vol. 6, p. 1583, 1976. 144

[264] R. Karimzadeh and N. Mansour, "The effect of concentration on the thermo-optical properties of colloidal silver nanoparticles", *Optics & Laser Technology*, vol. 42, no. 5, pp. 783–789, 2010. 144

[265] R. Karimzadeh and N. Mansour, "Thermo-optic nonlinear response of silver nanoparticle colloids under a low power laser irradiation at 532 nm", *Physica Status Solidi (B)*, vol. 247, no. 2, pp. 365–370, 2010. 144

[266] J. Zamir Anvari, R. Karimzadeh, and N. Mansour, "Thermo-optic properties and nonlinear responses of copper nanoparticles in polysiloxane oil", *Journal of Optics*, vol. 12, p. 035212, 2010. 144

[267] J. Beckman and W. Koppenol, "Nitric oxide, superoxide, and peroxynitrite: the good, the bad, and ugly", *American Journal of Physiology-Cell Physiology*, vol. 271, no. 5, pp. C1424–C1437, 1996. 144

[268] P. Gray and A. Yoffe, "The reactivity and structure of nitrogen dioxide", *Chemical Reviews*, vol. 55, no. 6, pp. 1069–1154, 1955. 144

[269] A. Carvalho, F. Mendon a, and M. Piedade, "Acid-base reactions with carbon dioxide", *Journal of chemical education*, vol. 79, no. 12, p. 1464, 2002. 146

[270] V. Tychinsky, "High electric susceptibility is the signature of structured water in water-containing objects", *Water Journal*, vol. 3, pp. 95–99, 2011. 147, 170, 183

[271] V. Renteria-Tapia and J. Garcia-Macedo, "Influence of oxygen on the optical properties of silver nanoparticles", *Journal of Nanoscience and Nanotechnology*, vol. 8, no. 12, pp. 6545–6550, 2008. 148

[272] G. Kaye, T. Laby, and NPL-UK, *Kaye & Laby Tables of Physical & Chemical Constants*, ch. 2 General physics: Radiation and optics: 2.5.7 Refractive index of gases. National Physical Laboratory, 1995. 148, 151, 183

[273] M. Vera, A. Saint-Jalmes, and D. Durian, "Scattering optics of foam", *Applied optics*, vol. 40, no. 24, pp. 4210–4214, 2001. 148, 183

[274] J. Fuller, "A molecular dynamics simulation study of oxygen within hydrated Nafion-117 for fuel cell application". BSc Thesis, 2012. 148, 183

[275] T. Okada, G. Xie, O. Gorseth, S. Kjelstrup, N. Nakamura, and T. Arimura, "Ion and water transport characteristics of Nafion membranes as electrolytes", *Electrochimica acta*, vol. 43, no. 24, pp. 3741–3747, 1998. 148, 183

[276] D. Schinca, L. Scaffardi, F. Videla, G. Torchia, P. Moreno, and L. Roso, "Silver–silver oxide core–shell nanoparticles by femtosecond laser ablation: core and shell

sizing by extinction spectroscopy", *Journal of Physics D: Applied Physics*, vol. 42, p. 215102, 2009. 148

[277] K. Jones, *Comprehensive Inorganic Chemistry*, vol. 2, ch. Ammonia, pp. 199–227. Pergamon Press, 1973. 151, 183

[278] I. Mavrovic, "Method of controlling urea system". US Patent 3,940,440, February 1976. 151, 183

[279] EPA, "Ammonia", environmental health research series, Subcommittee on Ammonia, Environmental Protection Agency, Washington, DC, US, 1977. 151, 183

[280] DAIKIN, "Split system air conditioning". Operation Manual FAQ100BUV1B, 2008. 154

[281] AVANTES, "AvaSpec-ULS2048 StarLine Versatile Fiber-optic Spectrometer". Spectrophotometers p. 30-32, 2012. 167

[282] M. Sastre de Vicente, "The concept of ionic strength eighty years after its introduction in chemistry", *Journal of chemical education*, vol. 81, no. 5, p. 750, 2004. 168

[283] T. Solomon, "The definition and unit of ionic strength", *Journal of Chemical Education*, vol. 78, no. 12, p. 1691, 2001. 168

[284] G. Lewis and M. Randall, "The activity coefficient of strong electrolytes", *Journal of the American Chemical Society*, vol. 43, no. 5, pp. 1112–1154, 1921. 168

[285] P. Choi, *Investigation of Thermodynamic and Transport Properties of Proton-Exchange Membranes in Fuel Cell Applications.* PhD thesis, Worcester Polytechnic Institute, 2004. 172, 182

[286] R. E. Fernandez, *Polymer Data Handbook*, ch. Perfluorinated ionomers. Oxford, UK: Oxford University Press, 1999. 175, 182

[287] J. Peatross and M. Ware, *Physics of light and optics.* Brigham Young Unversity, Department of Physics and Astronomy, 2011. 175

[288] A. McNaught and A. Wilkinson, *IUPAC compendium of chemical terminology*, vol. 2. Blackwell Scientific Publications, 1997. 175

[289] R. Mulliken, "A new electroaffinity scale; together with data on valence states and on valence ionization potentials and electron affinities", *The Journal of Chemical Physics*, vol. 2, p. 782, 1934. 175

[290] L. Schaad and B. Hess Jr, "A comparison of recent theoretical aromaticity indices", *J. Am. Chem. Soc*, vol. 93, p. 305, 1971. 176

[291] ChemAxon, "Chemical properties viewer". chemicalize.org, 2012. 176, 178

[292] K. Miller and J. Savchik, "A new empirical method to calculate average molecular polarizabilities", *Journal of the American Chemical Society*, vol. 101, no. 24, pp. 7206–7213, 1979. 176

[293] K. Bonin and V. Kresin, *Electric-dipole polarizabilities of atoms, molecules, and clusters.* World Scientific Pub Co Inc, 1997. 176

[294] A. Ghose, A. Pritchett, and G. Crippen, "Atomic physicochemical parameters for three dimensional structure directed quantitative structure-activity relationships III: Modeling hydrophobic interactions", *Journal of Computational Chemistry*, vol. 9, no. 1, pp. 80–90, 1988. 176

[295] J. Padrón, R. Carrasco, and R. Pellón, "Molecular descriptor based on a molar refractivity partition using randic-type graph-theoretical invariant", *J. Pharm. Pharmaceut. Sci*, vol. 5, no. 3, pp. 258–265, 2002. 176

[296] S. Wildman and G. Crippen, "Prediction of physicochemical parameters by atomic contributions", *Journal of chemical information and computer sciences*, vol. 39, no. 5, pp. 868–873, 1999. 176

[297] T. Gierke, H. Tigelaar, and W. Flygare, "Calculation of molecular electric dipole and quadrupole moments", *Journal of the American Chemical Society*, vol. 94, no. 2, pp. 330–338, 1972. 176

[298] A. F. Barton, *Handbook of solubility parameters and other cohesion parameters.* CRC Press, 1991. 178, 200

[299] J. Gladysz, D. Curran, and I. Horvath, *Handbook of Fluorous Chemistry.* Wiley, 2006. 178

[300] R. Winslow, *Blood Substitutes.* Elsevier Academic Press, 2006. 178

[301] J. Gjaldbaek, "The solubility of hydrogen, oxygen, and carbon monoxide in some non-polar solvents", *Acta chem. scand*, vol. 6, pp. 623–633, 1952. 178

[302] R. Yeo and C. Cheng, "Swelling studies of perfluorinated ionomer membranes", *Journal of applied polymer science*, vol. 32, no. 7, pp. 5733–5741, 1986. 176

[303] L. White, *Hazardous Gas Monitoring: A Guide for Semiconductor and Other Hazardous Occupancies.* Safety, Health & Hygiene, William Andrew Publishing, 2000. 186

[304] N. Taniguchi, Y. Nakagiri, T. Gamou, K. Ohara, and M. Kawamura, "Hydrocarbon sensor". US Patent 5,935,398, August 1999. 187

[305] T. Okabayashi, T. Fujimoto, I. Yamamoto, K. Utsunomiya, T. Wada, Y. Yamashita, N. Yamashita, and M. Nakagawa, "High sensitive hydrocarbon gas sensor utilizing cataluminescence of γ-Al_2O_3 activated with Dy^{3+}", *Sensors and Actuators B: Chemical*, vol. 64, no. 1, pp. 54–58, 2000. 187

[306] T. Hibino and H. Iwahara, "A hydrocarbon sensor using a high temperature-type proton conductor", *Journal of applied electrochemistry*, vol. 24, no. 3, pp. 268–270, 1994. 187

[307] T. Poteat and B. Lalevic, "Pd-MOS hydrogen and hydrocarbon sensor device", *Electron Device Letters, IEEE*, vol. 2, no. 4, pp. 82–84, 1981. 187

[308] K. Arshak, E. Moore, G. Lyons, J. Harris, and S. Clifford, "A review of gas sensors employed in electronic nose applications", *Sensor Review*, vol. 24, no. 2, pp. 181–198, 2004. 187

[309] Y. Fujii, S. Honma, M. Morisawa, and S. Muto, "Development of new optical fiber toluene sensor", in *Proceedings of SPIE, the International Society for Optical Engineering*, pp. 68291Z–1, Society of Photo-Optical Instrumentation Engineers, 2008. 187

[310] V. Matejec, M. Chomát, D. Berkova, J. Mrazek, R. Ardeleanu, V. Harabagiu, M. Pinteala, and B. Simionescu, "Detection of toluene dissolved in water by using PCS fibers excited by an inclined collimated beam", *Sensors and Actuators B: Chemical*, vol. 90, no. 1, pp. 204–210, 2003. 187

[311] K. Cherif, S. Hleli, A. Abdelghani, N. Jaffrezic-Renault, and V. Matejec, "Chemical detection in liquid media with a refractometric sensor based on a multimode optical fibre", *Sensors*, vol. 2, no. 6, pp. 195–204, 2002. 187

[312] T. Sato, M. Breedon, and N. Miura, "Improvement of toluene selectivity via the application of an ethanol oxidizing catalytic cell upstream of a YSZ-based sensor for air monitoring applications", *Sensors*, vol. 12, no. 4, pp. 4706–4714, 2012. 187

[313] U. Liebl, L. Bouzhir-Sima, M. Négrerie, J. Martin, and M. Vos, "Ultrafast ligand rebinding in the heme domain of the oxygen sensors FixL and Dos: General regulatory implications for heme-based sensors", *Proceedings of the National Academy of Sciences*, vol. 99, no. 20, pp. 12771–12776, 2002. 188

[314] I. Analytical industries, "Pico-ion ppb oxygen sensors". Product specifications, 2010. 188

[315] R. Ramamoorthy, P. Dutta, and S. Akbar, "Oxygen sensors: materials, methods, designs and applications", *Journal of materials science*, vol. 38, no. 21, pp. 4271–4282, 2003. 188

[316] L. Narasimhan, W. Goodman, and C. Patel, "Correlation of breath ammonia with blood urea nitrogen and creatinine during hemodialysis", *Proceedings of the National Academy of Sciences*, vol. 98, no. 8, pp. 4617–4621, 2001. 188, 189

[317] S. Davies, P. Spanel, and D. Smith, "Quantitative analysis of ammonia on the breath of patients in end-stage renal failure.", *Kidney international*, vol. 52, no. 1, p. 223, 1997. 188, 189

[318] N. Marczin and M. Yacoub, *Disease markers in exhaled breath: basic mechanisms and clinical applications*, vol. 346. Ios PressInc, 2002. 188, 189

[319] D. Smith, P. Spanel, and S. Davies, "Trace gases in breath of healthy volunteers when fasting and after a protein-calorie meal: a preliminary study", *Journal of applied physiology*, vol. 87, no. 5, pp. 1584–1588, 1999. 189

[320] A. Diskin, P. Španěl, and D. Smith, "Time variation of ammonia, acetone, isoprene and ethanol in breath: a quantitative SIFT-MS study over 30 days", *Physiological measurement*, vol. 24, no. 1, p. 107, 2003. 189

[321] K. Wells, J. Vaughan, T. Pajewski, S. Hom, L. Ngamtrakulpanit, A. Smith, A. Nguyen, R. Turner, and J. Hunt, "Exhaled breath condensate pH assays are not influenced by oral ammonia", *Thorax*, vol. 60, no. 1, pp. 27–31, 2005. 189

[322] J. Aldrich, "Correlations genuine and spurious in pearson and yule", *Statistical Science*, pp. 364–376, 1995. 190

[323] D. Hume, *Essays and treatises on several subjects*, vol. 2, ch. An Enquiry Concerning Human Understanding. London: davidhume.org, 1777. 190

[324] H. Harris and J. Prausnitz, "Thermodynamics of solutions with physical and chemical interactions. solubility of acetylene in organic solvents", *Industrial & Engineering Chemistry Fundamentals*, vol. 8, no. 2, pp. 180–188, 1969. 200

[325] L. E. W, E. C. A, and P. J. M, "Generalized liquid volumes and solubility parameters for regular solutions application", *Chemical Engineering Science*, vol. 20, no. 7, pp. 703–706, 1965. 200

[326] M. L. Bradford and G. Thodos, "Solubility parameters of hydrocarbons", *The Canadian Journal of Chemical Engineering*, vol. December, pp. 345–348, 1966. 200

[327] R. Kiyama and H. Hiraoka, "The Solubilities of compressed acetylene gas in liquids, I, II, III, IV", *Rev. Phys. Chem. Japan*, vol. 25, pp. 16–20, 1955. 200

[328] M. Alam, K. Tadasa, T. Maeda, and H. Kayahara, "Correlation of inhibition of thermolysin by water-miscible alcoholic solvents with their physicochemical parameters and the status of monoalcoholic character of water in the peptide synthesis of Z-Phe-Phe-OMe in water organic one-phase reaction system", *Biotechnology letters*, vol. 19, no. 11, pp. 1129–1133, 1997. 200

[329] A. Vetere, "An empirical method to evaluate the solubility of several gases in polar and non-polar solvents", *Fluid phase equilibria*, vol. 132, no. 1-2, pp. 77–91, 1997. 200

[330] W. Bruggeman, D. Weber-Fung, A. Opperhuizen, J. VanDerSteen, A. Wijbenga, and O. Hutzinger, "Absorption and retention of polydimethylsiloxanes (silicones) in fish: Preliminary experiments", *Toxicological & Environmental Chemistry*, vol. 7, no. 4, pp. 287–296, 1984. 200

[331] J. K. Bowmaker and H. J. Dartnall, "Visual pigments of rods and cones in a human retina", *The Journal of Physiology*, vol. 298, no. 1, pp. 501–511, 1980. 201

[332] NewportCorp, "LineSpec^{TM} CMOS and CCD Array Spectrometers", tech. rep., NewportCorp, 2012. 201